RAYSTATION 2024A

Reference Manual

Traceback information:
Workspace Main version a834
Checked in 2023-12-19
Skribenta version 5.6.015

Disclaimer

For information on functionality not available for regulatory reasons, see the Regulatory Information in the RayStation Instructions for Use.

Declaration of conformity

CE 2862

Complies with Medical Device Regulation (MDR) 2017/745. A copy of the corresponding Declaration of Conformity is available on request.

Safety notices

This user documentation contains WARNINGS concerning the safe use of the product. These must be followed.

WARNING!

The general warning sign informs you of a risk for bodily harm. In most cases the risk is related to mistreatment of the patient.

Note: *The note gives additional information concerning a specific topic, for example, things to consider when performing a certain step in an instruction.*

Copyright

This document contains proprietary information that is protected by copyright. No part of this document may be photocopied, reproduced or translated to another language without prior written consent of RaySearch Laboratories AB (publ).

All Rights Reserved. © 2023, RaySearch Laboratories AB (publ).

Printed material

Hard copies of Instructions for Use and Release Notes related documents are available upon request.

Trademarks

RayAdaptive, RayAnalytics, RayBiology, RayCare, RayCloud, RayCommand, RayData, RayIntelligence, RayMachine, RayOptimizer, RayPACS, RayPlan, RaySearch, RaySearch Laboratories, RayStation, RayStore, RayTreat, RayWorld and the RaySearch Laboratories logotype are trademarks of RaySearch Laboratories AB (publ)*.

Third-party trademarks as used herein are the property of their respective owners, which are not affiliated with RaySearch Laboratories AB (publ).

RaySearch Laboratories AB (publ) including its subsidiaries is hereafter referred to as RaySearch.

* Subject to registration in some markets.

RaySearch Laboratories

TABLE OF CONTENTS

1 INTRODUCTION 13

2 PATIENT GEOMETRY 15

2.1 Precautions 16
2.2 Outline and dose grid 20
2.3 CT mapping 21
2.3.1 Mass density mapping 21
2.3.2 CT to material properties mapping 22
2.3.3 Stopping-power ratio mapping for protons and light ions 25
2.4 Effective density in collapsed cone computations 27
2.4.1 The effective density in relation to the mass density 27
2.5 Material override 30
2.5.1 Support, Fixation and Bolus ROIs 32
2.6 RBE cell types 33
2.7 Dose grid effects when interpreting CT values 34
2.7.1 Dose grid effect on the External ROI 35
2.7.2 Dose grid effects for ROIs of type Bolus, Support and Fixation 35
2.7.3 Dose grid effects for ion PBS plans 37
2.8 Material handling for BNCT dose calculation 38
2.9 CBCT conversion 41
2.9.1 Corrected CBCT 41
2.9.2 Virtual CT 43

3 BRACHYTHERAPY DOSE CALCULATION 45

3.1 Overview of the TG43 dose calculation formalism 47
3.2 TG43 parameter data 50
3.3 Interpolation and extrapolation of TG43 data 51
3.4 RayStation TG43 dose computation details 52
3.5 TG43 dose engine accuracy and limitations 53
3.5.1 TG43 dose engine acceptance criteria 53
3.5.2 TG43 dose engine limitations 54

4 PHOTON DOSE CALCULATION 57

4.1 Precaution 58
4.2 Brief overview of the dose computation 59
4.3 Fluence computation – CyberKnife and C-arm LINACs 60
4.3.1 Overview of the LINAC head model 61
4.3.2 Normalization 69
4.3.3 Flattening filter 74
4.3.4 Source projection 75

4.4 Fluence computation - TomoTherapy LINACs ... 76
4.4.1 Physical LINAC head components ... 77
4.4.2 Fluence output ... 77
4.4.3 Collimators ... 77
4.4.4 Transverse profile ... 80
4.4.5 Fluence calculation ... 81
4.4.6 Differences between the Accuray model and the RayStation model ... 81
4.5 Collapsed cone dose computation ... 83
4.5.1 RayTracing ... 84
4.5.2 Radiological depths and intersection lengths ... 85
4.5.3 Energy distribution ... 86
4.5.4 TERMA computation ... 87
4.5.5 Point spread kernels ... 90
4.5.6 Superposition/convolution ... 94
4.5.7 Dose engine speed-ups ... 96
4.5.8 Modulated arc therapy/VMAT ... 99
4.5.9 Conformal arc ... 101
4.5.10 Static arc ... 101
4.5.11 Collapsed arc ... 102
4.5.12 DMLC ... 102
4.5.13 TomoHelical ... 102
4.5.14 TomoDirect ... 103
4.5.15 CyberKnife ... 103
4.5.16 Algorithm weaknesses ... 103
4.6 Monte Carlo dose computation ... 111
4.6.1 Overview ... 112
4.6.2 Dose to medium ... 112
4.6.3 Sampling of particles from fluence ... 112
4.6.4 Photon transport ... 112
4.6.5 Electron transport ... 113
4.6.6 Discrete interactions ... 114
4.6.7 Condensed history ... 114
4.6.8 Statistical uncertainty ... 116
4.6.9 Post-processing ... 117
4.6.10 Algorithm weaknesses ... 117
4.7 Dose-to-water, dose-to-medium, or dose-to-tissue ... 119
4.8 Electron contamination ... 123
4.8.1 Electron energy fluence ... 124
4.8.2 Electron energy distribution ... 124
4.8.3 Contamination electron dose ... 124
4.9 Wedges ... 129
4.9.1 Wedge angle ... 130
4.9.2 Wedge orientation ... 131
4.9.3 Wedge factor ... 131

4.9.4 Maximum field size ... 132
4.9.5 Physical wedges ... 132
4.9.6 Dynamic wedges ... 137
4.10 Blocks ... 141
4.11 Circular cones for C-arm LINACs ... 142
4.12 Circular Cones for CyberKnife LINACs ... 143
4.13 Beam commissioning ... 144
4.13.1 Measurement conditions ... 145
4.13.2 Detector width ... 145
4.13.3 Detector height and depth offset ... 145
4.14 GPU computation ... 147
4.15 SVD dose computation ... 148

5 ELECTRON DOSE CALCULATION ... 151

5.1 Accelerator electron beam line design ... 153
5.1.1 The accelerator electron beam line design ... 154
5.1.2 The primary and secondary scattering foils ... 155
5.1.3 The ion chamber and collimators ... 155
5.1.4 The applicator and cutout ... 155
5.2 Electron dose calculation algorithm ... 157
5.2.1 Background and rationale ... 158
5.2.2 Modeling the electron beam phase space ... 160
5.2.3 In-patient energy transport and energy scoring ... 168
5.2.4 Dose reporting, dose-to-water ... 168
5.2.5 Electron density weighted depth ... 168
5.2.6 Algorithm weaknesses ... 169
5.3 Statistical uncertainty ... 170

6 PROTON DOSE CALCULATION ... 171

6.1 Beam modeling of proton beams ... 173
6.2 General algorithms ... 174
6.2.1 Stopping power ... 175
6.2.2 Linear Energy Transfer (LET) ... 175
6.2.3 Energy loss straggling ... 175
6.2.4 Water equivalent depth at beam dose specification point ... 176
6.2.5 Compensator physical thickness at beam dose specification point ... 176
6.3 Beam model parameters ... 177
6.3.1 Beam model parameters ... 177
6.3.2 Interpolation of beam model parameters ... 178
6.4 Pencil Beam dose engine ... 180
6.4.1 Initialization and tracing of phase space parameters ... 181
6.4.2 Energy loss and radiological depth ... 182
6.4.3 Multiple Coulomb Scattering ... 182
6.4.4 Nuclear scattering ... 184

6.4.5 Calculation of the integrated depth dose in water ... 186
6.4.6 Scoring of dose ... 187
6.5 Pencil Beam dose calculation for PBS beams ... 188
6.5.1 Beam model ... 189
6.5.2 Scoring of dose in the patient (PBS) ... 193
6.5.3 Modeling of a range shifter ... 195
6.5.4 Modeling of an aperture ... 196
6.5.5 Modeling of an energy selector ... 197
6.6 Pencil Beam dose calculation for US/SS/DS/Wobbling beams ... 198
6.6.1 Beam model ... 199
6.6.2 Transport through aperture and compensator ... 202
6.6.3 Scoring of dose in patient ... 206
6.6.4 Absolute dosimetry ... 208
6.7 Pencil beam dose calculation for Mitsubishi Electric Corporation US beams ... 209
6.7.1 Introduction ... 210
6.7.2 RayStation dose engine ... 210
6.8 Pencil beam dose computation for Sumitomo Wobbling beams ... 213
6.8.1 About Sumitomo Wobbling ... 214
6.8.2 Dose engine adjustments ... 214
6.9 Monte Carlo Dose calculation ... 216
6.9.1 Overview ... 217
6.9.2 Statistical uncertainty ... 218
6.9.3 Sampling of source protons ... 218
6.9.4 Transport mechanics ... 220
6.9.5 Stopping power and energy loss integration ... 221
6.9.6 Energy loss straggling ... 222
6.9.7 Multiple scattering ... 223
6.9.8 Nuclear reactions ... 223
6.9.9 Handling of range shifters ... 226
6.9.10 Handling of energy selector ... 226
6.9.11 Handling of apertures ... 226
6.9.12 Scoring of dose-averaged LET ... 227
6.10 Dose engine accuracy and limitations ... 229
6.10.1 PBS Pencil beam and Monte Carlo dose engine acceptance criteria ... 230
6.10.2 PBS Pencil beam dose calculation limitations ... 231
6.10.3 PBS Monte Carlo dose calculation limitations ... 235
6.10.4 US/SS/DS/Wobbling Pencil beam dose calculation acceptance criteria ... 237
6.10.5 US/SS/DS/Wobbling Pencil beam dose calculation limitations ... 239
6.11 Optimization and dose calculation for Line Scanning ... 250
6.11.1 Optimization of a Line Scanning plan ... 250
6.11.2 Repainting for Line Scanning beams ... 251
6.11.3 Dose calculation for Line Scanning beams ... 251
6.11.4 Clinical and Approximate dose for Line Scanning ... 252
6.11.5 Sumitomo MU rounding algorithm ... 252

6.11.6 Limitations on line segment lengths ... 253
6.12 Optimization and dose calculation for Mevion Hyperscan ... 255
6.12.1 Computation of aperture contours ... 255
6.12.2 Optimization of a Hyperscan plan ... 256
6.12.3 Dose calculation for Hyperscan beams ... 256
6.12.4 Clinical and approximate dose for Hyperscan ... 257
6.12.5 Validation of a Mevion Hyperscan system ... 258
6.12.6 Mevion Spot Map Converter version ... 259
6.13 Optimization with spot dose cache ... 260
6.13.1 Memory consumption of the Spot dose cache ... 261
6.14 Optimization with LET functions ... 262
6.14.1 Dose threshold for the Max LET_d function ... 262

7 LIGHT ION DOSE CALCULATION ... 265

7.1 General models and algorithms ... 267
7.1.1 Stopping power ... 267
7.1.2 Linear Energy Transfer (LET) ... 267
7.1.3 Energy loss and radiological depth ... 268
7.1.4 Water equivalent depth at beam dose specification point ... 268
7.1.5 Multiple Coulomb Scattering ... 268
7.1.6 Nuclear scattering ... 270
7.1.7 Machine model parameters ... 270
7.1.8 Light ion pencil beam dose algorithm ... 272
7.2 Light ion dose calculation input data ... 276
7.2.1 Integrated Depth Doses (*idds*) ... 276
7.2.2 Particle energy spectra ... 276
7.2.3 Nuclear scattering (halo) parameters ... 278
7.3 Dose and RBE-weighted dose calculation for PBS beams ... 286
7.3.1 Beam model ... 286
7.3.2 Scoring of dose and RBE-weighted dose in the patient ... 287
7.3.3 The trichrome approximation ... 288
7.3.4 Scoring of dose-averaged LET ... 289
7.4 Dose engine accuracy and limitations ... 291
7.4.1 Dose engine acceptance criteria ... 291
7.4.2 Algorithm limitations ... 292
7.5 Initial RBE computation in the Local Effect Model ... 295
7.5.1 Local Effect Model ... 295
7.5.2 Calculation of the initial slope of the cell survival curve ... 299
7.6 Import of initial RBE tables for the user-defined Local Effect Model ... 300
7.7 The (modified) Microdosimetric Kinetic Model ... 302
7.8 Import of tables for the user-defined MKM ... 304
7.9 MKM dose computation ... 306
7.10 RBE-weighted dose algorithms for LEM ... 308
7.10.1 The LEM "Classic" algorithm ... 308

7.10.2 The LEM low dose approximation ... 310
7.11 RBE Model limitations ... 312
7.11.1 General RBE Model limitations ... 312
7.11.2 Local Effect Model limitations ... 314
7.11.3 Microdosimetric Kinetic Model limitations ... 318
7.12 Optimization with LET functions ... 321

8 ION MACHINE ALGORITHMS ... 323

8.1 Automatic range shifter selection ... 324
8.2 Automatic proton beam parameters using Treat and Protect ... 325
8.2.1 Aperture ... 326
8.2.2 Compensator ... 326
8.2.3 SOBP field ... 327
8.2.4 Snout position ... 328
8.3 MLC leaf positions for ion machines ... 329
8.4 Spot handling for ion machines ... 331
8.4.1 Spot selection ... 331
8.4.2 Spot selection for robust optimization ... 332
8.4.3 Spot sorting and filtering ... 333

9 ROBUST OPTIMIZATION ... 337

9.1 Precautions ... 338
9.2 Optimization formulation ... 339
9.2.1 Systematic errors ... 339
9.2.2 Interfraction (random) uncertainty ... 339
9.2.3 Intrafraction (e.g., breathing) organ motion ... 340
9.2.4 Combinations of systematic and interfraction errors ... 340
9.2.5 Combinations of systematic errors and intrafraction organ motion ... 341
9.2.6 Combinations of interfraction uncertainty and intrafraction organ motion ... 341
9.2.7 Treatment course scenario dose calculation ... 342
9.3 Scenarios ... 343
9.3.1 Setup error scenarios ... 343
9.3.2 Density error scenarios ... 343
9.3.3 Patient image scenarios ... 344
9.3.4 Scenario dose computation ... 344
9.4 Robust dose mimic ... 345

10 VOLUME HANDLING ... 347

10.1 Algorithms for visualization of ROIs ... 348
10.1.1 General information ... 348
10.1.2 Input ... 349
10.1.3 Output ... 349
10.1.4 Description ... 350

10.2 Algorithms for representing ROIs in the dose grid **355**
10.2.1 Introduction 355
10.2.2 Converting ROIs to dose grid ROIs 355
10.2.3 Computing dose statistics 356
10.2.4 Visualizing dose 357
10.2.5 Summary 357
10.3 Slice indicator gadget in BEV/DRR **358**

11 BIOLOGICAL MODELS REFERENCE INFORMATION **361**

11.1 Precautions **362**
11.2 Summary **363**
11.2.1 The TCP-PoissonLQ model 363
11.2.2 The general EQD_2 363
11.2.3 The NTCP-PoissonLQ model 364
11.2.4 The NTCP-LKB model 364
11.3 Introduction to biological models **365**
11.4 Cell survival models **366**
11.4.1 The linear cell survival model 366
11.4.2 The linear-quadratic (LQ) cell survival model 366
11.5 EQD_2 ..... **371**
11.5.1 Computing EQD_2 dose distribution 371
11.5.2 EQD_2 including incomplete repair 372
11.5.3 EQD_2 including accelerated repopulation 372
11.5.4 EQD_2 including both incomplete repair and accelerated repopulation 373
11.6 Protons **376**
11.7 Dose-response model **377**
11.7.1 The linear dose-response model 378
11.7.2 The linear-quadratic (LQ) dose-response model 380
11.8 Tumor and normal tissue response **383**
11.8.1 TCP-PoissonLQ 383
11.8.2 NTCP 384
11.9 Composite TCP and NTCP models **386**
11.9.1 Composite TCP 386
11.9.2 Composite NTCP 386
11.9.3 P+ 386
11.10 Parameters of the biological models **388**

APPENDIX A - DEFINITIONS **389**

APPENDIX B - REWRITING OF LINEAR DOSE-RESPONSE MODELS **391**

APPENDIX C - DOSE ENGINE VERSION NUMBER **393**

REFERENCES **395**

1 INTRODUCTION

About this manual

This manual is an algorithm reference manual for the RayStation 2024A system. The following information is included in this manual:

- *Chapter 2 Patient geometry* - describes the patient geometry and density.
- *Chapter 3 Brachytherapy dose calculation* - describes the algorithms used in the brachytherapy dose computation.
- *Chapter 4 Photon dose calculation* - describes the algorithms and the beam model parameters used in the photon dose computation and beam commissioning. It also describes the collapsed cone dose engine and beam modifiers such as blocks and wedges.
- *Chapter 5 Electron dose calculation* - describes the algorithms used in the electron dose computation. It also describes the design of the accelerator electron beam line.
- *Chapter 6 Proton dose calculation* - describes the algorithms used in the proton dose computation.
- *Chapter 7 Light ion dose calculation* - describes the algorithms used in the carbon ion dose computation, including the computation of relative biological effectiveness (RBE).
- *Chapter 8 Ion machine algorithms* - describes different algorithms to determine machine parameters in ion therapy.
- *Chapter 9 Robust optimization* - describes the basis for the robust optimization in RayStation.
- *Chapter 10 Volume handling* - describes the algorithms associated with volume handling such as visualization of ROIs and representing the ROIs in the dose grid.
- *Chapter 11 Biological models reference information* - describes the biological models used for radiobiological treatment planning in RayStation 2024A.

The approximate dose computation used during photon plan optimization, the singular value decomposition (SVD) dose engine, is described in section *section 4.15 SVD dose computation on page 148*.

RayStation 2024A contains other algorithms, such as machine parameter optimization, multi criteria optimization, grid deformation computation, dose deformations, model based segmentation, mentioning a few. These are not described in this manual.

For information about the dose engine version number, see *Appendix C Dose engine version number*.

For information about the display of coordinates, movements and scales during treatment planning, refer to *RSL-D-RS-2024A-IFU, RayStation 2024A Instructions for Use*.

WARNING!

Ensure that doses computed with different dose engines are compatible. Combining or comparing doses computed with different dose engines (e.g., in fall-back, co-optimization, background doses, summation of doses) must be handled with care if the dose convention differs between algorithms and the plan is sensitive to dose in high Z materials.

The electron and the proton Monte Carlo dose engines report dose to water with radiation transport in medium. The proton and light ion pencil beam dose engines report dose to water. The photon collapsed cone dose engine computes dose to water with radiation transport in different density water, a property which is in between dose to water and dose to medium when computed in medium. The photon Monte Carlo dose engine for RayStation 2024A reports dose to medium with radiation transport in medium. When transported in medium, differences between dose to water and dose to medium for photons have been found to be small for tissues other than bone (1-2%), but the difference can become relatively large for bone (10%) or other high Z materials.

The dose convention for imported doses is unknown to RayStation, and should be handled with care if the plan is sensitive to dose in high Z materials and if the dose is used as background dose or for dose-mimicking.

(409909)

2 PATIENT GEOMETRY

The patient and problem geometry is defined using CT images, regions of interests (ROIs), material overrides and the dose grid.

In this chapter

This chapter contains the following sections:

2.1	Precautions	p. 16
2.2	Outline and dose grid	p. 20
2.3	CT mapping	p. 21
2.4	Effective density in collapsed cone computations	p. 27
2.5	Material override	p. 30
2.6	RBE cell types	p. 33
2.7	Dose grid effects when interpreting CT values	p. 34
2.8	Material handling for BNCT dose calculation	p. 38
2.9	CBCT conversion	p. 41

2.1 PRECAUTIONS

WARNING!

Dose computation region. The dose computation region is confined to the intersection of the dose grid and the region consisting of dose computation ROIs. The dose computation ROIs include the External ROI, Support and Fixation ROIs included in the beam set, as well as Bolus ROIs assigned to external photon and electron beams. No dose will be scored in the region outside the dose computation region.

External beam therapy

For external beam therapy, all material information from image data will be omitted outside the dose computation region. For all modalities except electrons and BNCT, the volume outside of the dose computation region is treated as vacuum in the radiation transport (no interactions). For BNCT the volume outside the dose computation region is handled by the external dose computation engine.

For electrons, air is used instead of vacuum, with scattering and energy loss in the radiation transport. RayStation will not be able to compute a correct dose if any part of a beam intersects image data that is not included in the dose computation region. This could occur if the dose computation ROIs do not cover all relevant image data, or if the dose grid does not encompass the relevant volumes of the dose computation ROIs.

Large errors in dose are expected if any part of the beam enters a dose computation ROI surface which is not covered by the dose grid. An error in dose is also expected at the exit edges of the dose grid if a too small dose grid is used, since scatter from outside the dose grid is not accounted for. There is no warning in RayStation if the dose grid does not cover the appropriate region at the exit edges.

Brachytherapy (TG43 dose engine)

The TG43 brachytherapy dose computation is a data-driven model based on measurements and simulations in water. The dose computation disregards any material information and treats the full volume as water both inside and outside the dose computation region. This has two implications with respect to the dose computation region:

- Dose on the surface of a dose computation ROI may be incorrect, since an infinite scattering medium is assumed, and the low-density interface is neglected.
- If the dose grid does not cover the entire External ROI (or any other dose computation ROI), the dose will still be correct at the edges of the dose grid, given that all active dwell points are inside the dose grid. In RayStation, it is not possible to compute dose if there are active dwell points outside of the External ROI. Inside of the External ROI, the dose grid must cover all active dwell points including at least a 3 cm margin to make sure that high dose values close to the sources are accounted for.

(9361)

WARNING!

Pixel padding. If pixel padding is present in the region used for dose computation, the calculated dose may be incorrect. Make sure that the pixel padded Hounsfield Units map to the desired density or make sure to add a material override to the pixel padded region.

If the CT-image has excluded material which will be present at treatment and which is inside the radiation scatter region, it is not recommended to use pixel padded values. Instead, add a material override to each material to include them in the dose computation. Failure to do so might lead to errors in the dose computation.

If everything that is important for radiation transport is inside the CT-image, but the External ROI covers image parts with pixel padding values that correspond to high density Hounsfield Units, this could also lead to errors in the dose computation.

(9354)

WARNING!

Material override for multiple structure sets. If material override is defined for an ROI which does not have any geometry defined in the used image set, there will be no warning when computing dose.

(9353)

WARNING!

For imported dose, no assumptions on how the dose was calculated are made. The dose will not be invalidated when data that is used for calculating dose in RayStation is different from the data the imported dose was calculated on. This applies even if the imported dose was originally calculated in RayStation. For example, if the structure set is modified with density overrides or with changes to the External ROI, the imported dose will not be invalidated.

(224134)

WARNING!

Bolus ROIs need to be assigned to beam(s). Bolus ROIs are regarded as beam properties. In order for a bolus ROI to be used for radiation transport and dose computation for a certain beam, it must be explicitly assigned to that beam. If a bolus is to be used for all beams, it must be assigned to all beams individually. A bolus which is not assigned to any beam in a plan is not going to be included in the dose computation at all. (136280)

2.2 OUTLINE AND DOSE GRID

The patient and problem geometry is defined using CT images, regions of interests (ROIs), material overrides and the dose grid.

The entire computation problem is bounded by the dose grid, i.e. the density computation, the radiation transport and the dose computation is only performed inside the dose grid.

The computation problem is also bounded by the External ROI (which is required for all plans) and all present boli, support and fixation ROIs. The boli, support and fixation ROIs can be specified with material overrides, otherwise density from the CT image will be used.

This means that everything in the CT images which lies outside of the External ROI or the dose grid is regarded as vacuum. Boli, support and fixation ROIs will however add density outside of the External ROI. In terms of radiological depth, vacuum is practically the same as air. For electron dose calculations, air is used instead of vacuum with scattering and energy loss in the radiation transport outside of the External ROI and bolus, support and fixation ROIs.

The voxel grid resolution must lie in the interval 1-5 mm.

Note: *The bolus, support or fixation ROI material is disregarded when computing the source-to-skin distance (SSD). It is however always taken into account when computing physical and water equivalent depths.*

WARNING!

Dose grid resolution affects dose. Both dose output and shape can be significantly affected by dose grid resolution and alignment. Make sure to use an appropriate dose grid considering factors such as e.g., field size, modulation and patient geometry.

(2305)

2.3 CT MAPPING

The CT-images provide information about the photon attenuation in the patient density expressed in Hounsfield Units (HU). Hounsfield units scale with the linear attenuation coefficient at the CT-scanner energy (typically 50-150 keV). The Hounsfield scale is defined with -1000 as air and 0 as water.

$$HU = 1000 \times \frac{\mu - \mu_{H_2O}}{\mu_{H_2O} - \mu_{air}} \qquad \text{[Eq. 1]}$$

where μ is the linear attenuation coefficient.

To be able to use the CT-images for dose computation, the HU values have to be converted to relevant physical properties. The main mapping method is based on a user-defined CT-to-density-table, also known as an HU-to-density-table. For protons and light ions, a CT-to-stopping-power-ratio-table (or HU-to-SPR-table) can alternatively be used. The HU values provided by the CT-scan are first resampled to the dose grid and, for each voxel inside the External ROI, converted to either mass density or stopping-power ratio.

2.3.1 Mass density mapping

The CT-to-density table can be created by the user in the CT Commissioning module and it should then represent mass density behavior over the full range from air, over lung and soft tissue to low-density and high-density bone and metal inserts. If the CT-images have voxels with higher HU than contained in the table, the density is undetermined and assumed to be identical to the density for the highest HU in the table. It is therefore important to ensure that the table covers all Hounsfield values that will appear on the CT-scans. Similarly voxels with HU lower than the lowest HU entry are given the density for the lowest HU in the table.

The HU for a given mass density may vary from CT-scanner to CT-scanner, and may even depend on scan protocol settings such as tube potential and field-of-view, or patient geometry. If this is the case, different CT-to-density tables shall be created and the correct one used for planning.

The *RSL-D-RS-2024A-USM, RayStation 2024A User Manual* describes the density handling of cone beam CT-images (CBCT). The use of CBCT images is only supported for photon dose computations, due to limited accuracy when used for electron, proton and light ion dose computations. The CBCT-to-density mapping shall be evaluated before clinical use. This evaluation should entail, not only density, but also dose comparisons using the same plan on CT and CBCT for the type of plan, CBCT-scanner, protocol and patient geometry that is intended for clinical use.

Typical tissue HU and density values

The Generic CT is a table with typical tissue HU and mass densities (ICRU 44 [31] and ICRP 23 [33]).

Table 2.1: The Generic CT is a table with typical tissue HU and relative mass densities.

Name	Hounsfield units	Density [g/cm^3]
Air (outside patient)	-992	0.00121
Air (inside patient)	-976	0.00121
Lung (ICRU 44)	-480	0.5
Adipose (ICRU 44)	-96	0.95
Muscle (ICRU 44)	48	1.05
Bone	230	1.15
Cortical bone	1170	1.82
Aluminum	1850	2.71
Titanium	6400	4.51
Stainless steel	10500	8.0

2.3.2 CT to material properties mapping

For the photon Monte Carlo dose engine, the electron dose engine and all proton and light ion dose engines, a full description of the material composition expressed as mass density, mass fraction of atomic elements $w(Z)$, and mean ionization energy (I) for each voxel of the patient is required. For voxels covered by ROIs associated with a material override, this data is directly given by the properties of the override material. For the other voxels, the material information is interpreted from the CT data. This section describes how this interpretation is performed, when an HU-to-density table is defined. (The interpretation is similar when using an HU-to-SPR table, which is described in *section 2.3.3 Stopping-power ratio mapping for protons and light ions on page 25*.)

The properties stored for each voxel in the dose calculation are the mass density, as obtained either from the Hounsfield numbers or an override material, and a reference to a material in an internal material list. This list is composed of a number of fixed materials used for the CT interpretation, and the materials of the ROI overrides. The applicable dose engine algorithms will use the mass density of the voxel as well as the elemental composition and mean ionization energy of the referenced material (note that the mass density of the referenced material is not used here). There are about 75 fixed materials in the list, whose properties have been interpolated from 16 established core materials that are expected to be found in a patient. The properties of these core materials are given in Table 2.2 and an example of how HU can map to the 16 base materials is shown in Figure 1. The x-axis in this figure depends on which CT-to-density table that used. Because of the relatively slow dependence of the relevant physical quantities (e.g. mass stopping power) on the elemental composition, 75 fixed materials have been shown to be sufficient for patient-like geometries. The material closest in mass density will be associated with a CT based voxel.

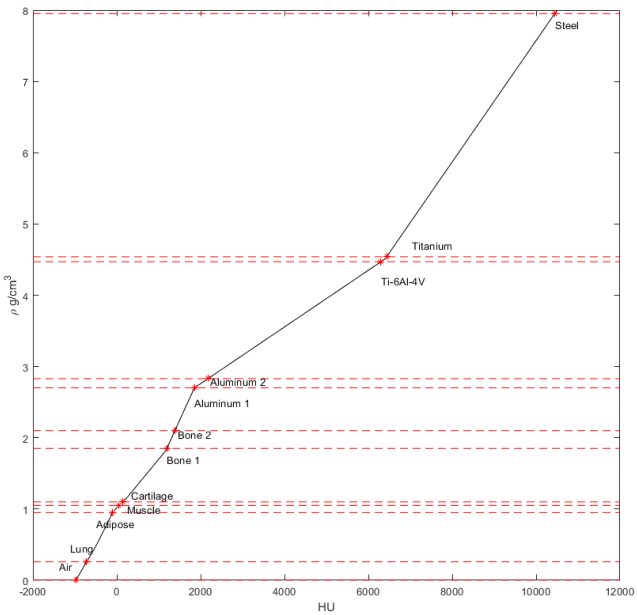

Figure 1. An example of an HU-to-density table. In red is the mapping from mass density to a subset of the core materials used for the photon Monte Carlo dose engine, the electron dose engine and all proton and light ion dose engines. The labels Bone 1 and Bone 2 refer to the core materials Bone and Bone+, and Aluminum 1 and Aluminum 2 refer to the core materials Aluminum and Aluminum+.

Material interpolation

A number of fixed materials are created by interpolation from a number of well-established core materials (Table 2.2). The materials are interpolated with respect to their mass density. The elemental composition $w(Z)^c$ and mean ionization energy I^c for a material C with mass density ρ^c, interpolated between the core materials $A(\rho^a, w(Z)^a, I^a)$ and $B(\rho^b, w(Z)^b, I^b)$ are calculated according to:

$$w(Z)^c = w^a w\,(Z)^a + w^b w\,(Z)^b\,,$$

$$\ln I^c = \frac{w^a < Z/A >^a \ln I^a + w^b < Z/A >^b \ln I^b}{< Z/A >^c} \qquad \text{[Eq. 2]}$$

where $< Z/A >^x$ is the number of electrons to molecular weight ratio of the material x and the weights w_a and w_b are calculated as:

$$w^a = \frac{f^a \rho^a}{\rho^c}, \quad w^b = \frac{f^b \rho^b}{\rho^c}$$

$$f^a = \frac{V^a}{V^a + V^b} = \frac{\rho^b - \rho^c}{\rho^b - \rho^a} \quad , f^b = 1 - f^a$$

[Eq. 3]

f^a and f^b are the relative volume fractions and V^a and V^b are the relative volumes of materials A and B.

Table 2.2: The mass density, the mean ionization energies (I), and the atomic mass composition (%) of the template materials used in RayStation for the photon Monte Carlo dose engine, the electron dose engine and all proton and light ion dose engines (ICRU49 [65], ICRU44 [31] and ICRP 23 [33] [162] [163]).

Name	Density [g/cm³]	I (eV)	Composition
Air	0.00121	85.7	N (75.5%), O (23.2%), Ar (1.3%)
Lung	0.26	75.3	H (10.3%), C (10.5%), N (3.1%), O (74.9%), Na (0.2%), P (0.2%), S (0.3%), Cl (0.3%), K (0.2%)
Adipose	0.95	63.2	H (11.4%), C (59.8%), N (0.7%), O (27.8%), Na (0.1%), S (0.1%), Cl (0.1%)
Muscle	1.05	74.7	H (10.2%), C (14.3%), N (3.4%), O (71%), Na (0.1%), P (0.2%), S (0.3%), Cl (0.1%), K (0.4%)
Cartilage	1.1	75.0	H (9.6%), C (9.9%), N (2.2%), O (74.4%), Na (0.5%), P (2.2%), S (0.9%), Cl (0.3%)
Bone (ICRP23)	1.85	106.4	H (4.7234%), C (14.433%), N (4.199%), O (44.6096%), Mg (0.22%), P (10.497%), S (0.315%), Ca (20.993%), Zn (0.01%)
Bone (ICRP23)+	2.1	106.4	H (4.7234%), C (14.433%), N (4.199%), O (44.6096%), Mg (0.22%), P (10.497%), S (0.315%), Ca (20.993%), Zn (0.01%)
Aluminum	2.7	166	Al (100%)
Aluminum+	2.83	166	Al (100%)
Ti-6Al-4V	4.4705	227.7	H (0.015%), C (0.08%), N (0.05%), O (0.2%), Al (6.125%), Ti (89.225%), V (4%), Fe (0.3%), Y (0.005%)
Titanium	4.54	233	Ti (100%)
Steel	7.952	286.62	Cr (18%), Fe (65.5%), Ni (14%), Mo (2.5%)
CoCrMo	8.3	290.9	Cr (28%), Mn (0.5%), Fe (0.375%), Co (64.625%), Ni (0.5%), Mo (6%)
Silver	10.49	470	Ag (100%)
Tantalum	16.654	718	Ta (100%)
Gold	19.32	790	Au (100%)

2.3.3 Stopping-power ratio mapping for protons and light ions

For protons and for light ions, the CT values can be mapped directly to stopping-power ratios. The stopping-power ratio for a reference particle at a reference energy is defined as the stopping power

in the material divided by the stopping power in water. As for the HU-to-density table, the HU-to-SPR table is created in the CT Commissioning module. The same precautions as described for the definition of HU-to-density tables in *section 2.3.1 Mass density mapping on page 21* must be taken when using stopping-power ratio. Stopping-power ratio mapping is not implemented for CBCT images.

The CT to material properties mapping is similar when using an HU-to-SPR table as when using an HU-to-density table, but with the following differences:

- The stopping-power ratio is computed for each of the interpolated materials using the same reference particle and energy as specified for the HU-to-SPR table.
- The material closest in stopping-power ratio is associated with the CT based voxel.
- After associating the voxel with a material, the mass density of the voxel is adjusted, so that the stopping-power ratio computed from the material properties at the reference energy and the adjusted mass density equals the stopping-power ratio obtained from the CT.

The stopping power used in the dose computation is computed in the same way regardless of how the mass density and material properties are obtained. It is based on the density and material properties of the voxel, as well as the transported particle type and energy. This is described in detail in *section 6.2.1 Stopping power on page 175* for protons and *section 7.1.1 Stopping power on page 267* for light ions

Note: *For CT scanners that provide SPR values directly (typically a Dual Energy CT), the HU to SPR curve in RayStation is simply defined to scale the imported SPR values to absolute SPR.*

2.4 EFFECTIVE DENSITY IN COLLAPSED CONE COMPUTATIONS

To compute the radiological depth and the attenuation of a voxel inside the patient, one needs information about the photon attenuation at radiation treatment energies. This can differ from attenuation at CT energies. For energies between 0.1 MeV and 10 MeV, the attenuation is dominated by Compton scattering (which scales with the electron density of the material). The electron density is related to the mass density as

$$\rho_e = < Z/A > \rho \qquad \text{[Eq. 4]}$$

where $< Z/A >$ is the weighted mean nuclear ratio. The weight for each element corresponds to the mass fraction of that element in the material.

In the upper end of the energy spectrum, around 10 MV and above, pair-production becomes important, resulting in an attenuation coefficient which increases with energy and atomic number (see *Linear attenuation coefficient on page 88*). To account for this process a conversion from mass density to effective density is made.

For a mono-energetic photon beam the effective density is defined as:

$$\frac{\rho_{eff-material}}{\rho_{eff-water}} = \frac{\rho_{e-material}}{\rho_{e-water}} \frac{1+\alpha\cdot(1+<Z>_{material})\ln E\cdot E}{1+\alpha\cdot(1+<Z>_{water})\ln E\cdot E} \qquad \text{[Eq. 5]}$$

where E is the photon energy given in MeV and <Z> is the weighted mean nuclear Z defined as

$$< Z > = \frac{\sum_{i=atomtypes} f_i (Z^2/A)_i}{<Z/A>} \qquad \text{[Eq. 6]}$$

where f_i is the weight fraction of atom type i in the material [24]. The parameter α equals $1.775 \cdot 10^{-3}$ and is obtained through a fit of the equivalent path lengths of photons in a set of tissue materials (Table I in [24]) as well as to certain water-like materials (Table II in [24]). For photon energies between 0.5 MeV and 20 MeV, the fit errors are less than 1%.

2.4.1 The effective density in relation to the mass density

In RayStation 2024A, the effective density is implemented as follows: Equation 5 is summed over the beam energy spectrum at isocenter in air, giving a table which relates the effective density to the mass density. In the construction of this table, only the materials listed in Table 2.3 are used. An extra data point for mass density and effective density equal to zero is added to the table. For each voxel inside the External the mass density is converted to effective density using linear interpolation in this table. The transformation is applied over the patient dose grid. For voxels where a material override applies, the effective density is computed using <Z> from the material in question, not from interpolation in the table.

Table 2.3: The mass density relative to water and the atomic mass composition (%) of tissue materials used in RayStation 2024A for effective density calculation.

	$\frac{\rho_{m-material}}{\rho_{m-water}}$	H	C	N	O	Na	Mg	P	S	Cl	Ar	K	Ca
Z		1	6	7	8	11	12	15	16	17	18	19	20
Z/A		0.992	0.5	0.5	0.5	0.478	0.494	0.484	0.499	0.479	0.451	0.486	0.499
Air	0.001203			75.5	23.2						1.3		
Lung	0.26	10.3	10.5	3.1	74.9	0.2		0.2	0.3	0.3		0.2	
Adi-pose	0.95	11.4	59.8	0.7	27.8	0.1			0.1	0.1			
Tissue	1	10.12	11.1	2.6	76.18								
Muscle	1.05	10.2	14.3	3.4	71	0.1		0.2	0.3	0.1		0.4	
Carti-lage	1.1	9.6	9.9	2.2	74.4	0.5		2.2	0.9	0.3			
Bone	1.85	3.4	15.5	4.2	43.5	0.1	0.2	10.3	0.3				22.5
Alu-minum	2.7												
Iron	7.87												
Gold	19.32												
Osmi-um	22.57												

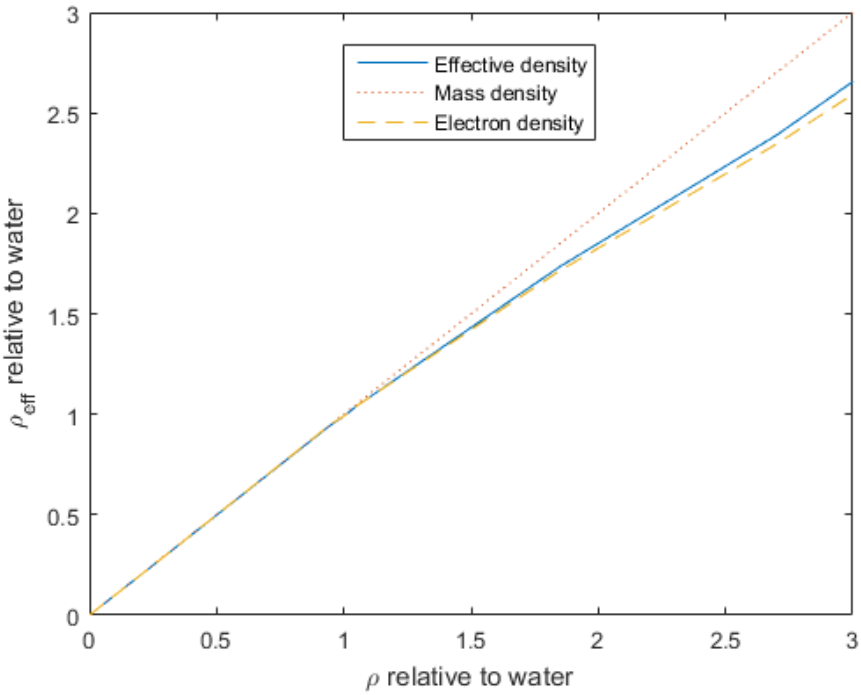

Figure 2. A typical conversion from mass density to electron and effective density for a 6 MV beam. The effective density is used both in TERMA-tracing, point spread kernel tracing and electron dose computation.

2.5 MATERIAL OVERRIDE

The CT image generally provides a means to extract the mass density (or stopping power ratio map) of the patient. However, phantom materials, prostheses or inserts, which do not follow the HU-to-density (or HU-to-SPR) curve, should be outlined as material override ROIs for a more accurate dose computation. Override materials are defined by their mass density, atomic composition and mean ionization energy (also when using a 16-bit CT scanner). When applicable, the stopping power ratio of the material is derived from these properties. (It is currently not possible to specify a stopping power ratio value directly for a material override.)

In general, material override ROIs are not allowed to overlap. If they do, ROI algebra can be used to separate the regions to obtain the desired material override. However, in the special case where the External ROI has material override, it is still allowed for ROIs inside the External ROI to have material override as long as they only overlap the External ROI and not each other. The material override for the inner ROI will be used for the voxels fully covered by it. For voxels that are partly covered by the inner ROI and fully covered by the External ROI, the density of each voxel will be the weighted average of the inner ROI material density and the External ROI material density.

When two ROIs of type Support or Fixation outside the patient overlap, where one has a material override and one uses CT density, RayStation behaves in the same way as with material overrides inside the patient, i.e., the override material is used in the overlap region.

The density (or stopping power ratio) for a voxel which is partly overlapped by a material override ROI is computed as the weighted average density (or stopping power ratio) of all material override ROIs that overlap the voxel. This is done on dose grid resolution. If the sum of overlap between a voxel and all material override ROIs is less than 100%, the remaining density (or stopping power ratio) is taken from the CT. For the mass density, this can be formulated as:

If

$$\sum_{i=material} \Delta V_i < 1, \qquad \text{[Eq. 7]}$$

then

$$\rho = \sum_{i=material} \Delta V_i \rho_i + (1 - \sum_{i=material} \Delta V_i)\rho_{CT}$$

and if

$$1 \leq \sum_{i=material} \Delta V_i < 1.99, \qquad \text{[Eq. 8]}$$

then

$$\rho = \frac{\sum_{i=material} \Delta V_i \rho_i}{\sum_{i=material} \Delta V_i}$$

and if

$$1.99 \leq \sum_{i=material} \Delta V_i, \qquad \text{[Eq. 9]}$$

dose computation is not allowed.

Here, ΔV_i is the fractional voxel coverage of material override ROI i. Material override ROIs with the same material are allowed to overlap; in this case the overlap region is regarded as having the density of the material override ROI counted only once. Common material override ROIs must be completely enclosed inside the External ROI; if they are not, dose computation is not allowed. Bolus ROIs must be completely outside the External, and Support and Fixation ROIs can be partly inside and partly outside the External ROI.

Note: *There is no special handling of contrast fluids or CT-pixel padding. If the patient CT has regions with high constrast material, these will be treated as high density regions unless an override is applied.*

Note: *Synthetic phantoms with water material override are exported from Oncentra MasterPlan as having mean Z=1, mean A=1 and density 1 g/cm^3. When importing such a phantom, it is necessary to change the material override to RayStation water in order to obtain a correct attenuation and dose.*

Note: *Material overrides from Syngo are exported with electron density only. When they are imported to RayStation these are treated as water with the electron density specified in the structure set file in the photon dose computations. This is shown in ROI properties.*

If this was not the intention, please change the material override to give the correct radiation transport.

Note: *The test for overlapping ROIs with material override is performed on dose grid resolution. This means that contours that visually overlap in the patient views may still be allowed for dose computation when represented on the dose grid.*

Note: *The BNCT dose computation is performed by an external dose engine and the material handling differs in some aspects from what has been described above. See section 2.8 Material handling for BNCT dose calculation on page 38 for details.*

2.5.1 Support, Fixation and Bolus ROIs

The DICOM standard defines SUPPORT and FIXATION ROIs as regions with external patient support, fixation or immobilization devices. Support and Fixation ROIs in RayStation are intended to be used for such devices to allow for material outside the patient outline to be included in dose computation. The treatment couch is an example of a Support ROI. Template Support and Fixation models need to be dosimetrically validated, since they will influence the calculated dose. It is particularly important to use an appropriate geometry, material description and positioning in relation to the patient for the part of the ROI which is intersected by the beam in the entrance region. Errors in the exit region influence dose only through backscattering in the photon case.

In RayStation, ROIs of type Support, and Fixation are not allowed to be fully contained within the External ROI. There may be examples where it is difficult to segment External, Support and Fixation ROIs without overlap. The effect of incorrect use of Support, or Fixation ROIs is described in *section 2.7.2 Dose grid effects for ROIs of type Bolus, Support and Fixation on page 35*.

Bolus, supports and fixation devices will cause the same photon and electron interactions as in the patient. For Collapsed Cone, TERMA is deposited and contamination electrons are attenuated in these regions just like in the patient. When in doubt on what material to choose, the effective density is the property of interest for the radiation transport in support and fixation devices; it is close to the electron density and is computed from the mass density and the atomic composition of the material as stated in *section 2.4 Effective density in collapsed cone computations on page 27*. For photon and electron Monte Carlo, beam transport through ROIs of type Bolus, Support and Fixation is identical to the transport through the patient geometry.

For protons and light ions, beam transport through ROIs of type Support and Fixation is identical to the transport of the ions through the patient geometry with the difference that dose is not scored outside the External ROI.

2.6 RBE CELL TYPES

For light ion and BNCT planning it is possible to select an RBE cell type for any ROI. This is used for RBE dose computation. The RBE is computed per dose grid voxel and depends on the RBE cell type defined in the voxel. For BNCT, each dose grid voxel containing a non-zero volume of the External ROI is assigned exactly one ROI, from which the corresponding material and cell type information are obtained, as described in detail in *section 2.8 Material handling for BNCT dose calculation on page 38*. For light ion dose calculation, the cell type defined in every dose grid voxel within the patient is assumed to be the RBE cell type defined for the External ROI, except in those voxels partially or completely covered by another ROI with defined RBE cell type. These voxels will instead be assigned the RBE cell type of the non-External ROI, regardless of how much of the voxel volume is covered by that ROI.

In general, two ROIs different to the External ROI and with an associated RBE cell type are not allowed to overlap. ROI algebra may be used to separate the two regions. The overlap is checked per dose grid voxel, which means that it is not allowed to have a dose grid voxel completely covered by two ROIs with associated cell types (excluding the External ROI). However, it is still allowed to have multiple ROIs with associated RBE cell types partially covering a voxel, even if they overlap within the voxel. In that case, the RBE cell type selected for the voxel is the one corresponding to the ROI with the greatest occupancy in that voxel. For BNCT that includes the External ROI (see *section 2.8 Material handling for BNCT dose calculation on page 38* for details), while for light ions the External ROI is always given a lower priority regardless of occupancy, and its cell type will never be assigned to a voxel that also contains other ROIs with an associated RBE cell type.

Note: *The test for overlapping ROIs with specified RBE cell types is performed on dose grid resolution. This means that contours that visually overlap in the patient views may still be allowed for dose computation when represented on the dose grid.*

Note: *The dose statistics for a given ROI always include voxels both partially and fully covered by the ROI. When different cell types are assigned to different ROIs covering the same voxel, it is the ROI with the greatest occupancy in the voxel that determines the cell type of the voxel. For partially covered voxels, this could lead to a mismatch between the cell type assigned to the ROI and the cell type assigned to the voxel, which in turn will affect the evaluation of dose statistics. Especially in cases where there are large differences between adjacent cell types, this may lead to effects such as apparent cold or hot spots that are only a consequence of the discretization of the dose grid. In such cases, the dose statistics should be treated with great caution. This applies to dose statistics in a broader sense, i.e., including DVHs, dose statistics tables, clinical goals, prescription evaluation and objective function evaluation (see section 10.2.3 Computing dose statistics on page 356).*

2.7 DOSE GRID EFFECTS WHEN INTERPRETING CT VALUES

The dose grid resolution influences the dose already when extracting the CT values. First, the Hounsfield units are resampled from the CT grid to the dose grid. Then, resampled Hounsfield units are used to get mass densities (or stopping-power ratios). CT to material mapping (see *section 2.3.2 CT to material properties mapping on page 22*) or effective density computation (see *section 2.4 Effective density in collapsed cone computations on page 27*) is subsequently performed for each dose grid voxel. The following description assumes that mass densities are used, but the effects are identical for stopping-power ratios.

As described in *section 2.5 Material override on page 30*, material overrides modify the mass density distribution after it has been resampled to dose grid resolution. For a single material override ROI, overlapping a voxel with a fraction of the volume ΔV (where ΔV is between 0 and 1), the density of the voxel would be computed as:

$$\rho_{voxel} = \Delta V \cdot \rho_{material\ override} + (1-\Delta V) \cdot \rho_{before\ material\ override} \qquad \text{[Eq. 10]}$$

Let us look at a voxel at the border between a region with density ρ_2 and Hounsfield unit HU_2 and a region with density ρ_1 and Hounsfield unit HU_1. The voxel fraction inside the region with density ρ_2 is ΔV, and the remaining part is inside the region with density ρ_1. The resampled Hounsfield unit of such a voxel is computed as:

$$HU_{resampled} = \Delta V \cdot HU_2 + (1-\Delta V) \cdot HU_1 \qquad \text{[Eq. 11]}$$

The same expression, but with Hounsfield units replaced with densities, is not necessarily valid since the Hounsfield units to density mapping is only piecewise linear. However, if the densities are close enough, or if the table is linear over a larger region, Equation 11 can be written using ρ_1 and ρ_2 instead of HU_1 and HU_2.

$$\rho_{resampled} = \Delta V \cdot \rho_2 + (1-\Delta V) \cdot \rho_1 \qquad \text{[Eq. 12]}$$

Assume that we wish to take away the region with ρ_2 by exactly covering it with a material override with density $\rho_{material\ override}$. According to Equation 10, the resulting density is computed as:

$$\rho_{computed} = \Delta V \cdot \rho_{material\ override} + (1-\Delta V) \cdot \rho_{resampled} \qquad \text{[Eq. 13]}$$

Without the first resampling step (Equation 12) one would have a better density estimate in:

$$\rho_{ideal} = \Delta V \cdot \rho_{material\ override} + (1-\Delta V) \cdot \rho_1 \qquad \text{[Eq. 14]}$$

The error in this case is:

$$\rho_{error} = \rho_{computed} - \rho_{ideal} = \Delta V(1-\Delta V)(\rho_2 - \rho_1) \quad \text{[Eq. 15]}$$

This error is not dependent on the material override, but it is dependent on the density difference between the two original materials.

2.7.1 Dose grid effect on the External ROI

The External ROI defines the volume within which the CT data will be interpreted to patient material considered by the dose calculation. With the possible exception of any bolus, support and fixation ROIs, all volumes outside of the external ROI is treated as vacuum. However, the CT values of the surface voxels, i.e. the voxels that are only partially covered by the External ROI, will be determined as the mean value of the CT data for the entire voxel, disregarding the actual position of the external surface in the voxel. This treatment will be fully correct as long as the external ROI defines the border between the patient and the surrounding air. On the other hand, if the external ROI is used to mask non air volumes in the CT images, the interpreted density of the surface voxels may be larger than anticipated.

2.7.2 Dose grid effects for ROIs of type Bolus, Support and Fixation

This section describes dose grid effects for composite mass densities computed from CT data and ROIs of type Bolus, Support and Fixation. Analogous effects are present also when stopping power ratios (SPRs) are used to interpret the CT data.

If an ROI of type Bolus, Support or Fixation only partially covers a voxel that in turn is only partially covered by the External ROI (i.e., a patient surface voxel) the resulting mass density of that voxel may not be completely as expected. For dose calculation, the mass density distribution, as interpreted from the patient images, is first resampled to dose grid resolution. The composite mass density of a dose grid voxel is then calculated as a weighted average of the density from the CT data and the density of any material override ROIs that overlap the voxel.

Dose grid effects can occur for the composite density in two different situations when using ROIs of type Bolus, Support and Fixation: (1) if there is a mismatch between the relative volume of the External ROI and the resampled CT density in a voxel, or (2) if the Bolus/Support/Fixation ROI overlaps with the External ROI. These two situations are described below.

Mismatch between density and relative volume of the External ROI

As explained in *section 2.7.1 Dose grid effect on the External ROI on page 35*, the External ROI is in general only used to determine which dose grid voxels will be included in the dose computation, disregarding the relative volume of the External for that voxel. This handling is correct when the External ROI marks the border between the patient and the surrounding air. When a Bolus, Support or Fixation ROI is present, this approach could lead to unexpected density values in surface voxels, if there is a mismatch between the External relative volume and the CT density resampled to the dose grid voxel resolution. Surface voxels with combined densities from the External ROI and from Bolus/Support/Fixation ROIs are therefore treated using a slightly adjusted method.

This method is based on the assumption that the density inside the External ROI is 1.0 g/cm3, which will be a good approximation for skin or soft tissue. For border voxels covered by both a Bolus/Support/Fixation ROI and the External ROI, the relative volume of the External is adjusted so that the density of the part of the voxel that is inside the External equals 1.0 g/cm3. As an example, a resampled CT density of 0.4 g/cm3 in a surface dose grid voxel would always result in an updated External relative volume of that voxel of 0.4, regardless of the actual position of the External contour. The method for adjusting the External relative volume returns correct results if the density inside the External is close to 1.0 g/cm3 and the density of the Bolus/Support/Fixation ROI is equal to 1.0 g/cm3 or lower. In cases where the Bolus/Support/Fixation ROI is higher than 1.0 g/cm3, the combined density can be slightly overestimated.

Overlap between Bolus/Support/Fixation ROI and the External ROI

In situations where a Bolus/Support/Fixation ROI and the External ROI overlap, the combined density may not be as intended. A few examples of situations with mixed density between Bolus/Support/Fixation ROI and the External are depicted in Figure 3. If the Bolus/Support/Fixation ROI is completely outside the External ROI, the density will be correct (Case 1), since there is no overlap. However, if a Bolus/Support/Fixation ROI inside the External ROI overlaps the External ROI in a surface voxel, the air part of the voxel is not correctly taken into account, resulting in a too high density in that voxel (Case 3 and 4). If the overlapping voxel does not contain any air, the density will be correct (Case 2).

The combined density of the surface voxel can be overestimated by a factor of up to 0.5 relative the density of the External ROI material in the surface voxel. The impact depends on the material in the External ROI and the amount of air in the affected voxel. For photon and electron treatments, the effect is negligible. For proton or light ion treatments, the range may be affected.

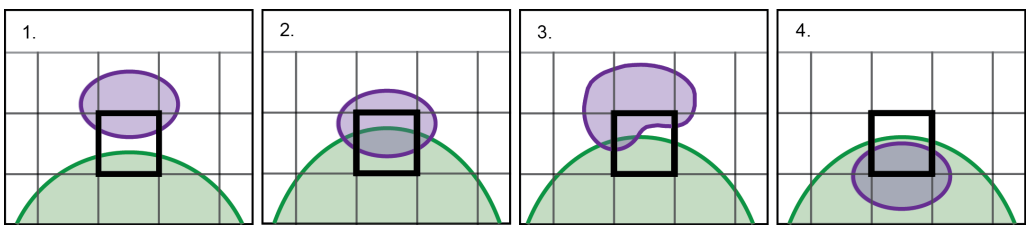

Figure 3. Case 1) The density will be correct. Case 2) The density will be correct. Case 3) The density will be incorrect in the affected voxel, but since it only affects a single voxel, the effect on overall dose will be negligible. Case 4) The density will be incorrect in the affected voxel. For a Bolus/Support/Fixation ROI mainly inside the External ROI, many surface voxels may be affected, which may result in a non-negligible effect on the overall dose.

2.7.3 Dose grid effects for ion PBS plans

Precaution

WARNING!

Dose grid effects for proton and light ion PBS plans. The Pencil Beam dose engines in RayStation calculate the average dose to a voxel along the integrated depth dose (IDD) and the dose to the center point of each voxel laterally and lets this dose value represent the dose in the entire voxel, while the RayStation Monte Carlo dose engine calculates the average dose deposited to a voxel. This means that any variation in dose that occurs on a resolution that is finer than that of the current dose grid may be lost in the dose calculation. The user has the responsibility to choose a dose grid resolution that is suitable for each plan. However, for low energy proton fields, and light ion fields without a ripple filter, the Bragg peak may be so sharp that even the highest dose grid resolution in RayStation (0.5 mm) is insufficient to resolve the Bragg peak, leading to a systematic underestimation of computed dose in relation to delivered dose. This may generate treatment plans that give a higher delivered dose than expected.

Be aware of this limitation in the dose calculation. To determine if this discrepancy is on a significant level, be extra careful in the patient-specific QA process.

(439)

2.8 MATERIAL HANDLING FOR BNCT DOSE CALCULATION

The BNCT dose computation is performed by an external dose engine and the material handling differs in some aspects from the other dose engines for external beam radiotherapy (EBRT) which are fully integrated in RayStation. No CT image information is used in the material handling, instead the information is exclusively obtained from ROI material overrides. It is therefore required that the External ROI has a material override. Other ROIs inside the External ROI can also be assigned material overrides as long as they only overlap the External ROI and not each other. Note that the material override handling as described in *section 2.5 Material override on page 30* does not apply for BNCT dose calculation.

For BNCT, each dose grid voxel containing a non-zero volume of the External ROI is assigned exactly one ROI, from which the corresponding material and cell type information are obtained and used by the external dose engine, assuming the entire voxel to have these properties. The material and cell type information per voxel is communicated to the external dose engine through a dedicated DICOM interface.

As explained in *section 2.5 Material override on page 30*, two ROIs with a material override are not allowed to overlap (with the exception of overlaps with the External ROI). ROI algebra may be used to separate overlapping regions. Overlaps are checked per dose grid voxel, which means that it is not allowed to have a dose grid voxel completely covered by two ROIs with material override (see Equation 9). As for the other EBRT dose computations, it is also for BNCT allowed to have multiple ROIs with material override partially covering a voxel (see first part of Equation 8). However, if a voxel contains two or more ROIs, no interpolation is performed for BNCT. Instead, the ROI with the largest relative volume in the voxel is assigned to the entire voxel. The relative volume of the External ROI in a voxel equates to the remaining relative voxel volume after subtracting the relative volumes of the other ROIs with material override.

A consequence of the material handling for BNCT is that ROIs, or parts of ROIs, that are small compared to the size of the dose grid voxels may not be included in the dose calculation. This could for example happen for narrow, elongated structures (see Figure 4).

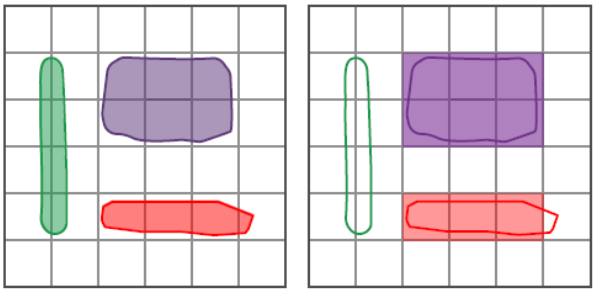

Figure 4. Illustration of material handling for BNCT for ROIs or parts of ROIs that are small compared to the size of the dose grid voxels. *Left*: ROIs in the patient view. Each of these ROIs has been given a material override, as has the underlying External ROI. *Right*: Materials assigned to the corresponding dose grid voxels. None of the voxels received the material of the left-most ROI since it does not have the largest relative volume in any voxel. For the bottom ROI, the right-most voxel did not receive its material since in this voxel the ROI does not have the largest relative volume.

Another major difference compared to the other EBRT dose computations is the handling of voxels on the border of the External ROI, i.e., the patient surface voxels. These will always be assigned the material and cell type of the External ROI (or potentially any other ROI with larger relative voxel volume than the External ROI), regardless of how large part of the voxel is covered by the External ROI. This behavior is inherited from the other EBRT dose engines, where the External ROI is used as a binary mask to define which voxels should be considered for dose computation. It will give a correct representation of the actual patient outline when using pure CT data or the material override interpolation procedure described in *section 2.5 Material override on page 30*. For BNCT, the different handling of the External ROI border voxels will result in a less accurate representation of the patient surface as is illustrated in Figure 5.

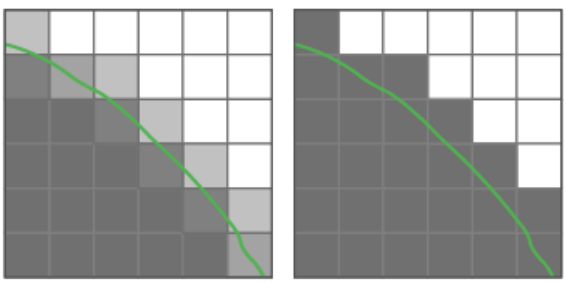

Figure 5. Handling of voxels at the edge of the External ROI for other EBRT dose computation (left) and for BNCT (right). The green line indicates the border of the External ROI. The darkest shade of gray corresponds to the material assigned to the External ROI. For the other EBRT dose computation, voxels on the edge of the External ROI are assigned an interpolated material based on the proportion of their volume that is within the External ROI. For BNCT, all voxels that contain a non-zero volume of the External ROI are assigned the material assigned to the External ROI.

Note: *The test for overlapping ROIs with material overlap is performed on dose grid resolution. This means that contours that visually overlap in the patient views may still be allowed for dose computation when represented on the dose grid.*

Note: *For the BNCT dose computation, any ROI assigned a material override must also be assigned an RBE cell type and vice versa.*

Note: *The dose statistics for a given ROI always include voxels both partially and fully covered by the ROI. When different materials and cell types are assigned to different ROIs covering the same voxel, it is the ROI with the greatest occupancy in the voxel that determines the material and cell type of the voxel. For partially covered voxels, this could lead to a mismatch between the material and cell type assigned to the ROI and the material and cell type assigned to the voxel, which in turn will affect the evaluation of dose statistics. Especially in cases where there are large differences between adjacent materials or cell types (such as very different cell type-to-blood boron concentration ratios), this may lead to effects such as apparent cold or hot spots that are only a consequence of the discretization of the dose grid. In such cases, the dose statistics should be treated with great caution. This applies to dose statistics in a broader sense, i.e., including DVHs, dose statistics tables, clinical goals, prescription evaluation and objective function evaluation (see section 10.2.3 Computing dose statistics on page 356).*

WARNING!

BNCT material handling. For BNCT dose computation, each dose grid voxel is assigned exactly one ROI from which the corresponding material and cell type information is obtained and used by the external dose engine, assuming the entire voxel to have these properties. The ROI with the largest relative volume is assigned to the entire voxel. ROIs, or parts of ROIs, that are small compared to the size of the dose grid voxels may therefore not be included in the dose calculation. Care should be taken to choose the dose grid voxel size accordingly.

Note that the voxels on the patient surface will be assigned the ROI with largest coverage in that voxel, even if the ROI only covers a small part of the voxel. The result is that the interpretation of the patient surface in the dose computation can become larger than in the image data. The user must be aware of this limitation for BNCT dose computation.

(724224)

2.9 CBCT CONVERSION

RayStation includes two algorithms for image conversion, corrected CBCT and virtual CT.

2.9.1 Corrected CBCT

The corrected CBCT algorithm works in an iterative manner with two main stages, conversion and correction. These stages are alternated until convergence, where improvement in one stage leads to more accurate results in the other. The purpose of the conversion stage is to find a conversion between the CBCT intensity scale and the HU intensity scale of the reference CT (usually the planning CT). The purpose of the correction stage is to find a correction map that removes low-frequency artifacts for each CBCT voxel. Low-frequency artifacts affect dose computations the most since they are correlated over large regions, and therefore errors will accumulate along the path trajected by the incident radiation. Using the provided deformable registration, the reference CT is deformed to match the CBCT geometry prior to these two stages.

In the conversion stage, a joint histogram between the reference CT and the CBCT is created (see Figure 6). In this joint histogram, the peaks correspond to different patient tissues. By finding the peak locations, a list of tissue value pairs is obtained. Based on these value pairs, a conversion function can be constructed by interpolating between these.

For bone tissues, no clear peaks in the joint histogram are present. In this region, three connecting lines are successively found by searching for the line (connecting to the last tissue value pair) that includes the most counts within a certain margin. For each line, the region in the joint histogram for which counts are considered is restricted to correspond to higher and higher bone density.

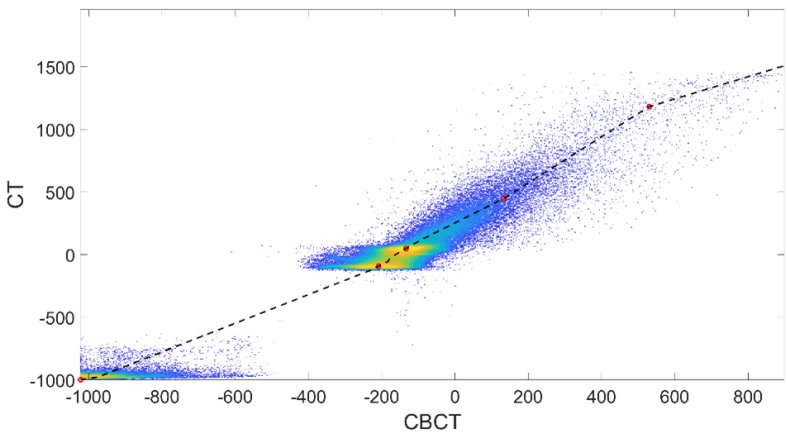

Figure 6. The CBCT and CT joint histogram shows peaks corresponding to different tissue types. The found conversion function is overlayed on the joint histogram.

In the correction stage, a mask excluding anatomical differences is generated in an iterative way by adaptive thresholding. As the correction and conversion stages improve during the iterations, so does the mask. After the conversion, and given a mask, a difference map between the reference CT and the CBCT can be created including only differences within this mask.

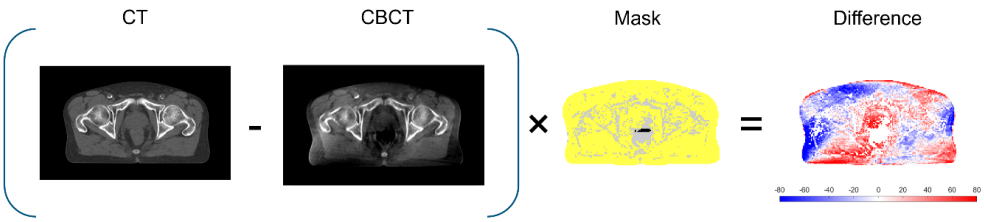

Figure 7. The masked difference image is created by only taking the differences between the images inside the mask.

This masked difference image can be used to estimate the low frequency artefacts in the CBCT and thus the correction map needed. The correction map is created by smoothing the masked difference image with an adaptive Gaussian kernel, compensating for the information lost by applying the mask. The corrected CBCT is then obtained by adding the correction map to the CBCT image.

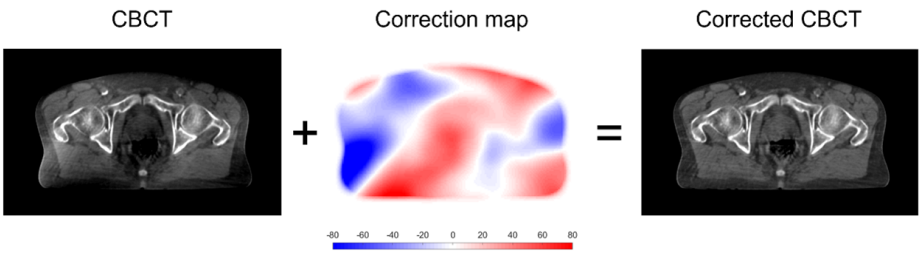

Figure 8. The corrected CBCT is obtained by adding the correction map to the CBCT image.

If the method is given a field-of-view ROI (that is present on the CBCT) as input, values outside this ROI will be mapped from the reference CT to the corrected CBCT using the provided deformable registration.

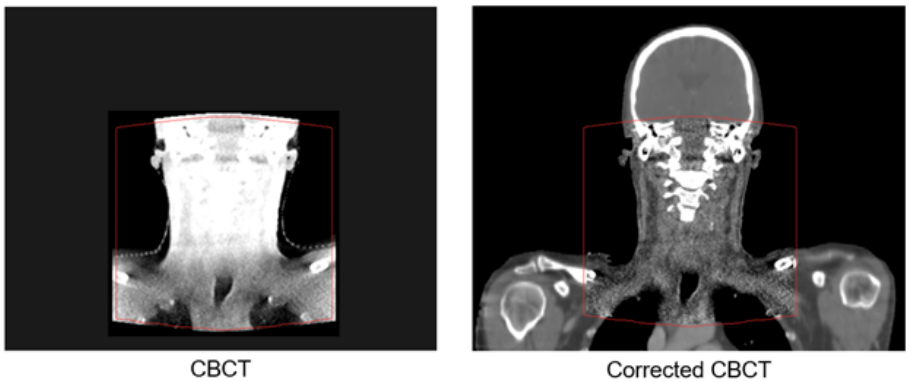

Figure 9. Regions outside of the field-of-view ROI of the CBCT are mapped from the reference CT to the corrected CBCT using the deformable registration.

2.9.2 Virtual CT

The virtual CT is created by first deforming the reference CT to the CBCT. Then the algorithm checks for mismatching low-density (air/lung) regions between the reference CT and a corrected CBCT that is created in the background. The mismatching air/lung regions in the deformed reference CT are replaced with values from the corrected CBCT, yielding the virtual CT. The replacement of low-density mismatches is needed, since these may introduce large dose errors, arising from the large differences in density they pertain to. Other mismatches are not replaced, since the associated dose errors in general are smaller and the replacement method could introduce secondary errors.

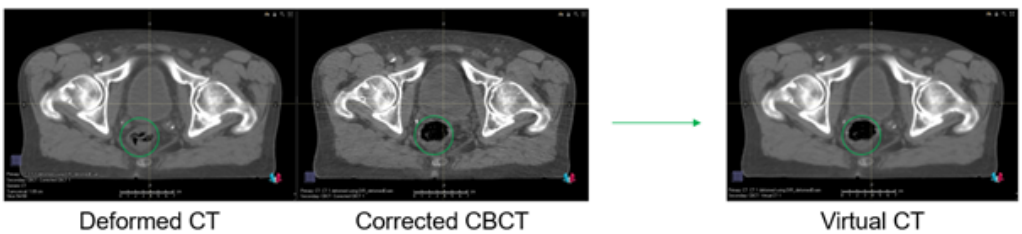

Figure 10. The virtual CT method takes most of the image from the deformed CT, apart from low density regions such as air or lung that are taken from the corrected CBCT.

3 BRACHYTHERAPY DOSE CALCULATION

The brachytherapy dose computation in RayStation follows the general TG43 (AAPM Task Group No. 43) 2D formalism as outlined in Nath et al. (1995) [148] and further refined in Rivard et al. (2005) [150]. In this formalism, the full patient geometry is treated as water and any heterogeneities in the patient volume are disregarded. The formalism was originally developed for low-energy LDR sources, such as I and Pd isotopes. It was further extended in the HEBD (High Energy Brachytherapy Source Dosimetry) Working Group report [149] to include sources with higher energies (e.g., Ir, Cs and Co isotopes), mainly used in HDR (High Dose Rate) and PDR (Pulsed Dose Rate) brachytherapy. The original TG43 report includes both a 1D and 2D formalism, but for high-energy sources only the 2D formalism is recommended [149], and therefore the implementation in RayStation follows the 2D formalism only.

The in-patient absolute positions and orientations of the radioactive source in HDR brachytherapy, referred to as dwell points, are determined from relative positions in the channels. The geometry and positions of the channels are commonly determined from medical imaging data, either by manual or automatic reconstruction. The dose rate is calculated for each of the dwell points and scaled with the corresponding dwell time. The full dose distribution is retrieved through summation of the contributions from each of the dwell points. The correctness of the in-patient dose distribution strongly depends on the accuracy in positioning of the channels and the dwell points.

The TG43 dose calculation is based on a number of assumptions: (1) all tissue around the sources are water-equivalent, (2) each source must be surrounded by a sufficiently large patient volume to keep the validity of the consensus data set, and (3) any shielding effects can be neglected. Situations when these assumed conditions are not met include: plans where the source is close to air cavities or metal implants, setups including applicator shielding and sources placed closed to the skin.

Several retrospective studies, where already delivered plans created using the TG43 formalism have been recomputed using a model-based dose calculation, have been performed to quantify the TG43 limitations in patients. These studies indicate that there are small dosimetric changes (<5%) for unshielded applicators in cervical cancer patients ([146], [145]), while clinically significant differences are observed when a shielded applicator is used [147]. Furthermore, computed doses can be higher than delivered doses close to the air-tissue interface in breast cancer brachytherapy, where the sources are located close to the skin [144]. Other treatment sites where the TG43 dose computation limitations are anticipated to appear include, for example, head-and-neck treatments due to the presence of air cavities.

In this chapter

This chapter contains the following sections:

3.1	Overview of the TG43 dose calculation formalism	p. 47
3.2	TG43 parameter data	p. 50
3.3	Interpolation and extrapolation of TG43 data	p. 51
3.4	RayStation TG43 dose computation details	p. 52
3.5	TG43 dose engine accuracy and limitations	p. 53

3.1 OVERVIEW OF THE TG43 DOSE CALCULATION FORMALISM

For brachytherapy TG43 dose computations, the dose rate from each source is determined at the point of calculation, P. RayStation implements the TG43 2D formalism for cylindrically symmetric line sources, where the point P is given in a polar coordinate system by the radius r and the angle θ between the line source center and the direction to P (see Figure 11).

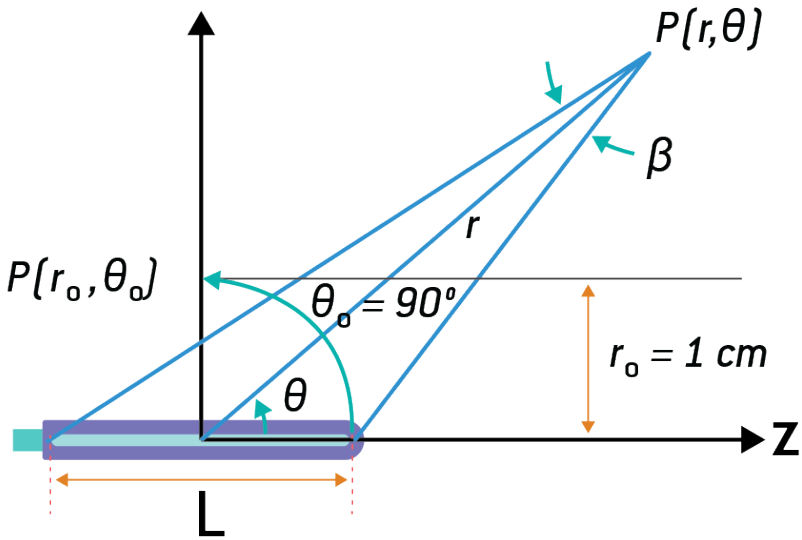

Figure 11. Coordinate system used for the brachytherapy TG43 dose calculation.

In this coordinate system, the dose rate, $\dot{D}(r,\theta)$, is given by

$$\dot{D}(r,\theta) = S_K \cdot \Lambda \cdot \frac{G_L(r,\theta)}{G_L(r_0,\theta_0)} \cdot g_L(r) \cdot F(r,\theta), \qquad \text{[Eq. 16]}$$

where S_K is the air-kerma strength, Λ is the dose-rate constant, G_L is the geometry function, g_L the radial dose function and $F(r,\theta)$ the anisotropy function. The point $P(r_0,\theta_0)$ is the reference point given by $r_0 = 1\ \mathrm{cm}$ and $\theta_0 = 90°$ (see Figure 11).

The air-kerma strength gives a measure of the brachytherapy source strength *in vacuum* and is typically measured at a calibration distance of 1 m from the source along the transverse axis. The source strength at a given reference date is stated in the source certificate provided by the vendor. It is either given as the air-kerma strength, or more commonly as the reference air-kerma rate (RAKR) at 1 m [mGy h^{-1}]. The air-kerma strength, S_K, relates to the air-kerma rate in vacuum, $\dot{K}_\delta(d)$, as

$$S_K = \dot{K}_\delta(d)\, d^2, \qquad \text{[Eq. 17]}$$

where d is the distance from the source. At a distance of 1 m, S_K is numerically identical to $\dot{K}_\delta(d)$, but with different units (S_K [mGy m^2 h^{-1}]; $\dot{K}_\delta(d)$ [mGy h-1]). The source strength is entered into the commissioning module of RayPhysics in terms of the reference air-kerma rate at 1 m from the source center in the transverse plane, together with the reference date. When the source is used in a brachytherapy plan, both the reference air-kerma rate and the reference date are exported in the DICOM RTPlan. These values are used by the afterloader control system to scale up the dwell times from the treatment plan to account for the decreasing activity of the radioactive sources. Even though the source strength is provided by the manufacturer, it is the responsibility of the user to verify the source strength before the first use of the source.

The dose-rate constant, Λ, is defined as the dose rate to water at the reference point $P(r_0, \theta_0)$ divided by the air-kerma strength:

$$\Lambda = \frac{\dot{D}(r_0, \theta_0)}{S_K}, \qquad \text{[Eq. 18]}$$

The dose-rate constant unit is cm^{-2}.

The geometry function, G_L, provides an effective inverse square law correction and reduces to r^{-2} for a point source. For a line source, the geometry function is given by

$$G_L(r, \theta) = \begin{cases} \beta/(Lr\sin\theta), & \theta \neq 0^\circ \\ (r^2 - L^2/4)^{-1}, & \theta = 0^\circ \end{cases} \qquad \text{[Eq. 19]}$$

where β is the angle from the reference point to the virtual tips of the line source and L is the active length (length of the radioactive portion) of the source (see Figure 11).

Neither scattering nor attenuation are included in the geometry function, but this is accounted for by the radial dose function, g_L, and the 2D anisotropy function, $F(r, \theta)$. The radial dose function is given by

$$g_L(r) = \frac{\dot{D}(r, \theta_0)}{\dot{D}(r_0, \theta_0)} \frac{G_L(r_0, \theta_0)}{G_L(r, \theta_0)}, \qquad \text{[Eq. 20]}$$

and the 2D anisotropy function is given by

$$F(r,\theta) = \frac{\dot{D}(r,\theta)}{\dot{D}(r,\theta_0)} \frac{G_L(r,\theta_0)}{G_L(r,\theta)} . \qquad \text{[Eq. 21]}$$

The radial dose function describes the dose rate as a function of distance r from the source center in the traverse plane, relative to the dose rate at distance $r = r_0$, and is therefore equal to unity at $r = r_0 = 1\ \mathrm{cm}$ and have dimensionless units. The anisotropy function describes the dose rate variation out from the transverse plane, relative to the dose rate at angle $\theta = \theta_0$, and is therefore equal to unity at $\theta = \theta_0 = 90^\circ$ and have dimensionless units. It typically decreases when the radius increases and θ approaches 0° or 180°. For consistency, the same active length must be used in the derivation of the radial dose function and the anisotropy function as in the geometry function.

3.2 TG43 PARAMETER DATA

The dose rate constant, the radial dose function and the anisotropy function can all be retrieved from measurements or Monte Carlo simulations. However, it is recommended that consensus reference data sets are used with data compiled from a large number of measurements and simulations. For high-energy brachytherapy sources, relevant data is tabulated in the HEBD report [149] [1]. All TG43 parameters can be entered into the RayPhysics Beam commissioning module.

Rivard et al. (2004) [150] and Perez-Calatayud et al. (2012) [149] provide recommended parameter ranges for which the radial dose function and the anisotropy function should be given. For the 2D anisotropy function for high-energy sources the recommendation is that values are tabulated at distances 0.5, 1.0, 2.0, 3.0, 5.0, 7.0 and 10.0 cm. The polar angle resolution should use 2° increments in the intervals $[0^\circ, 10^\circ]$ and $[170^\circ, 180^\circ]$, 5° increments in the intervals $[10^\circ, 30^\circ]$ and $[140^\circ, 170^\circ]$, and 10° increments in the interval $[30^\circ, 140^\circ]$. For the radial dose function, the recommendations are vaguer with the requirement to be able to perform log-linear interpolation between data points with at least a ±2% accuracy. It is the recommendation from RaySearch to adhere to the published parameter range recommendations. However, all tabulated consensus data does not include all data points and therefore the import of the $F(r, \theta)$ data into RayPhysics only requires that the distances must include 1.0, 2.0, 3.0, 5.0 and 10.0 cm and polar angles must have at least a 10° resolution from 0° to 180°.

As stated in Rivard et al. (2004) [150], it is the responsibility of the user to verify that the TG43 parameters are entered correctly into the system, whether the vendor or the user actually enters the data, as well as to check the accuracy of the dose calculation algorithm using the entered parameters.

1 If new measurements or simulations of parameters are to be performed, the HEBD report recommends using an effectively unbounded spherical phantom radius of 40 cm to be able to assume full scatter conditions. The HEBD report provides a methodology to convert data sets from bounded to unbounded phantom sizes. It is not possible to specify the phantom size in RayPhysics and all TG43 parameters entered into the system are expected to be retrieved from such an unbounded phantom.

3.3 INTERPOLATION AND EXTRAPOLATION OF TG43 DATA

The TG43u1 and HEBD reports give recommendations on how to interpolate and extrapolate values from the tabulated data in the radial dose function and the anisotropy function. These recommendations are essentially followed and the methods for interpolation and extrapolation in the RayStation TG43 dose engine are given in Table 3.1.

Table 3.1: Interpolation and extrapolation methods used in the RayStation TG43 dose engine.

Parameter	$r < r_{min}$ (Extrapolation)	$r_{min} < r \leq r_{max}$ (Interpolation)	$r > r_{max}$ (Extrapolation)
$g_L(r)$	Nearest neighbor extrapolation	Log-linear interpolation	Log-linear extrapolation (using the two last points)
$F(r,\theta)$	Nearest neighbor extrapolation	Bilinear interpolation	Nearest neighbor extrapolation

The tabulated data for $F(r,\theta)$ and $g_L(r)$ are commonly given defined for distances r up to 10 cm. Further away, the dose rate is very low, but if dosimetric data is required at those distances to correctly assess low dose to critical organs, the users should refer to the original Monte Carlo publications [149].

3.4 RAYSTATION TG43 DOSE COMPUTATION DETAILS

As stated in Rivard et al. (2004) [150], treatment planning systems can either be fully compliant with the TG43 formalism or not. Compliance is defined as using Equation 16 together with appropriate values of the active length, dose-rate constant, the radial dose function and the anisotropy function. RayStation is fully compliant with TG43 according to this definition, but for computation performance reasons implementation details may differ from other TG43 compliant systems.

The TG43 formalism contains a mathematical singularity in the form of a line segment at the center of the source. To avoid the singularity, and also to avoid reporting very high doses inside and in the region very close to the physical source, a cylindrical avoidance region is used. The region has a diameter of 0.1 cm and is 0.1 cm longer than the active length of the source. Any dose computation inside the region is carried out for the closest point on the cylinder surface.

For performance reasons the TG43 formalism is not used directly when computing dose. Instead, it is used to compute a 2D away-along kernel which is used for dose scoring. The kernel is defined on a cartesian grid with 0.5 mm resolution to a maximum radius of 30 cm and is evaluated in the center of each voxel using bilinear interpolation. Any dose computation outside the maximum radius uses the nearest away-along kernel value at maximum radius. No dose will be scored outside the dose computation region, which is confined to the intersection of the dose grid and the region consisting of ROIs of type External, Support and Fixation.

The dose grid resolution must be set to 1 mm in all directions to obtain a clinical dose in RayStation. This follows the recommendations from Rivard et al. (2004) [150]. For larger voxel sizes than 1 mm, the dose is set to *Approximate*. This limit is present to ensure that the dose is reported on a sufficiently accurate level.

3.5 TG43 DOSE ENGINE ACCURACY AND LIMITATIONS

3.5.1 TG43 dose engine acceptance criteria

Comparison to QA along-away data

The following accuracy requirements shall apply when comparing to published QA along-away data for HDR sources:

- 97% of the computed dose values shall be within 2% of the published data.
- 99% of the computed dose values shall pass local gamma(1%,1mm) < 1.

Comparison to EQUAL-ESTRO measurement

The following accuracy requirement shall apply when comparing to the measurement point in the EQUAL-ESTRO laboratory procedure:

- The computed dose value shall be within 5% of the measurement.

Comparison to computation with independent TG43 system for SagiNova afterloading system

The following accuracy requirement shall apply when comparing to independent systems, implementing the TG43 formalism:

- 98% of the computed dose values shall pass local gamma(1%/1mm) < 1 for a low-dose threshold set to 5% of the prescribed dose.

The given accuracy requirement shall apply to comparison to single dwell positions, as well as to full treatment plans for relevant patient cases.

Comparison to computation with independent TG43 system for Flexitron afterloading system

The following accuracy requirement shall apply when comparing to dose computed with the independent TPS Oncentra Brachy, implementing the TG43 formalism:

- 98% of the computed dose values shall pass local gamma(1%/1mm) < 1 for a low-dose threshold set to 5% of the prescribed dose.

The given accuracy requirement shall apply to comparison to a plan for the Flexitron afterloader, containing four dwell positions.

Comparison to independent Monte Carlo computation

The following accuracy requirement shall apply when comparing to an independent Monte Carlo computation:

- 98% of the points shall pass local gamma(3%/2 mm) < 1 for a low-dose threshold set to 20% of the prescribed dose.

- 90% of the points shall pass local gamma(1%/1mm) < 1 for a low-dose threshold set to 50% of the prescribed dose.

3.5.2 TG43 dose engine limitations

The user should be aware of the following limitations in the TG43 dose computation:

WARNING!

Validity of TG43 dose calculation. The TG43 dose calculation is based on a number of assumptions: (1) all tissue around the sources are water-equivalent, (2) each source must be surrounded by a sufficiently large patient volume to keep the validity of the consensus data set, and (3) any shielding effects can be neglected. Situations when these assumed conditions are not met include: plans where the source is close to air cavities or metal implants, setups including applicator shielding and sources placed close to the skin.

The user must be aware of these assumptions and how they will affect the dose computation.

(283360)

WARNING!

Correctness of TG43 parameters. The accuracy of the brachytherapy TG43 dose computation is strongly dependent on the correctness of the TG43 parameters used. If available for the current source, it is strongly recommended to use published consensus data from the HEBD report (Perez-Calatayud et al., 2012) or similar reports. The resolution of the radial dose function and the anisotropy function should follow the recommendations given in the TG43u1 report (Rivard et al. 2004) and in the HEBD report. It is the responsibility of the user to verify that the TG43 parameters have been entered correctly, regardless of whether it is the user or the manufacturer that has entered the data. The user must also check the accuracy of the dose calculation algorithm using the entered parameters.

(283358)

WARNING!

Brachytherapy dwell point positioning. The correctness of the in-patient dose distribution strongly depends on the accuracy in positioning of the channels and dwell points. It is the responsibility of the user to verify that the channels are correctly positioned for each patient and that the representation of dwell points inside the channels is correct.

(283361)

WARNING!

Transit doses in brachytherapy. Doses delivered in between dwell positions, as well as entrance and exit doses from and to the afterloader, are not accounted for in the dose computation. These transit doses are dependent on the source strength and the actual movement (speed and acceleration) of the source within the HDR brachytherapy channels. The transit doses can reach clinically significant levels in some cases, especially for high source strengths, slow source movement and when the number of HDR brachytherapy channels is large, resulting in the source spending a significant portion of the time in transit. The user should be aware of this limitation and assess in which cases transit doses might become an issue for each afterloader and source.

(331758)

WARNING!

HDR brachytherapy delivery in magnetic fields. If the HDR brachytherapy treatment is performed in a magnetic field (e.g. delivery during MRI), there might be large discrepancies between delivered dose and dose computed using the TG43 formalism. The derivation of published TG43 parameters does not include magnetic fields and any effect on the dose distribution will thus be disregarded in the dose computation. The user must be aware of this limitation if the treatment is to be delivered in a magnetic field. Special care should be taken for ^{60}Co sources and for magnetic field strengths larger than 1.5 T.

(332358)

4 PHOTON DOSE CALCULATION

This chapter describes the beam model and the energy fluence computation for photons. It also describes the collapsed cone dose engine, the photon Monte Carlo dose engine and beam modifiers such as blocks and wedges.

In this chapter

This chapter contains the following sections:

4.1	Precaution	p. 58
4.2	Brief overview of the dose computation	p. 59
4.3	Fluence computation – CyberKnife and C-arm LINACs	p. 60
4.4	Fluence computation - TomoTherapy LINACs	p. 76
4.5	Collapsed cone dose computation	p. 83
4.6	Monte Carlo dose computation	p. 111
4.7	Dose-to-water, dose-to-medium, or dose-to-tissue	p. 119
4.8	Electron contamination	p. 123
4.9	Wedges	p. 129
4.10	Blocks	p. 141
4.11	Circular cones for C-arm LINACs	p. 142
4.12	Circular Cones for CyberKnife LINACs	p. 143
4.13	Beam commissioning	p. 144
4.14	GPU computation	p. 147
4.15	SVD dose computation	p. 148

4.1 PRECAUTION

WARNING!

Independent dose calculation. Ensure that the independent dose calculation system that is used really is independent. There are systems that may appear to be suitable for independent dose calculation that are in fact not independent at all since the dose engine is manufactured by RaySearch and uses the same algorithm for photon dose computation and possibly also the same code as RayStation (e.g., Compass (IBA)). (6669)

4.2 BRIEF OVERVIEW OF THE DOSE COMPUTATION

Clinical dose computation can be separated into 2D energy fluence computation and 3D dose scoring. The energy fluence computation is shared between the collapsed cone and photon Monte Carlo dose engine. It uses sources projected through collimator openings.

Dose scoring for the collapsed cone dose engine is performed in two steps:

1. the TERMA (total energy released per unit mass) computation
2. the point spread kernel tracing (dose computation)

The TERMA and dose computation uses linear mass attenuation and pre-computed Monte Carlo point spread kernels. An electron contamination component is computed separately and added to the dose.

$$D_{tot} = D_{photon} + D_{electron} \quad \text{[Eq. 22]}$$

The electron dose computation is described in *section 4.8 Electron contamination on page 123*.

Dose scoring for the photon Monte Carlo dose engine uses a Class II algorithm to transport photons, electrons and positrons.

4.3 FLUENCE COMPUTATION – CYBERKNIFE AND C-ARM LINACS

This section describes the beam model and the energy fluence computation for photons for CyberKnife and C-arm LINACs. Ring gantry LINACs with an isocentric configuration such as BrainLab Vero and Varian Halcyon are treated as C-arm LINACs in terms of beam modeling and fluence computation.The beam model contains a number of parameters which are entered and fixed by the user at the beam commissioning stage, to give the best description of a specific linear accelerator (LINAC) system. Some of the machine parameters are actual physical quantities obtained from the LINAC vendor while others are adapted during the modeling process to provide the best fit possible to imported beam scans. The data in this case can be depth dose curves, profiles, absolute calibration and output factors. Modeled machine parameters cannot be changed during the planning process.

In this section

This section contains the following sub-sections:

4.3.1	Overview of the LINAC head model	p. 61
4.3.2	Normalization	p. 69
4.3.3	Flattening filter	p. 74
4.3.4	Source projection	p. 75

4.3.1 Overview of the LINAC head model

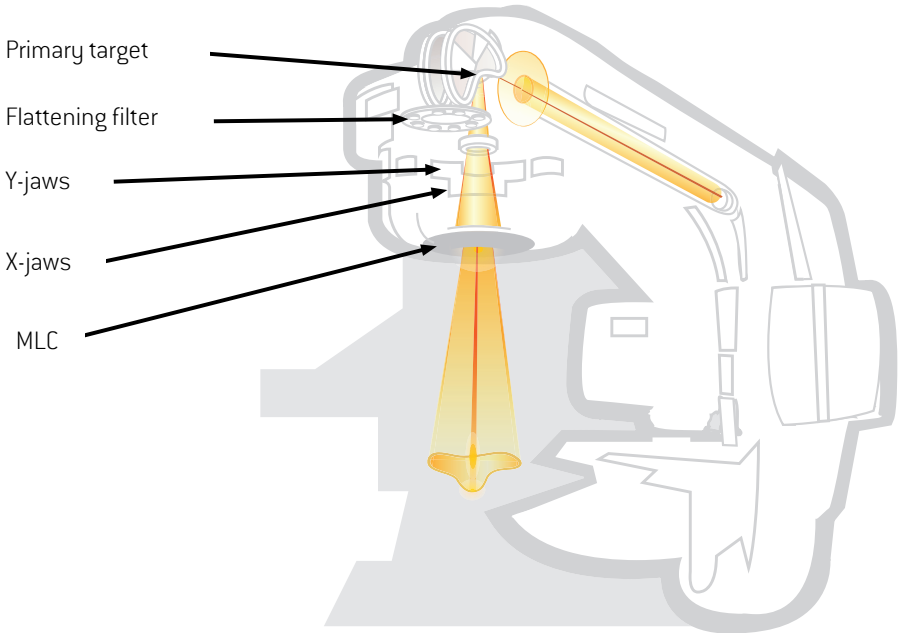

Figure 12. Physical LINAC components and corresponding beam model components.

Fluence plane

The energy fluence Φ is calculated from the beam model by projecting each source through the collimators onto the fluence plane, the isocenter plane. The energy fluence is defined as a scalar field on a flat surface, the separation into different energy components is performed later, during dose computation. The resolution of the fluence grid is 1 mm x 1 mm when projecting the primary photon source and 3 mm x 3 mm for the other sources. The coarser grid for the non-primary sources is resampled to 1 mm x 1 mm after projection, before TERMA computation.

Sources

The beam model has two or three different photon sources:

- the primary source which has a small spot-size and a high intensity.
- the scatter source (also known as the flattening filter source or the secondary source) which has a large spot-size and lower intensity.
- the wedge scatter source (only for plans with physical wedges).

The primary photon source is positioned at the Bremsstrahlung target at a distance from isocenter known as the source-axis-distance (SAD). The secondary photon source is generally positioned close to the bottom of the flattening filter but the position is an effective parameter which can be adjusted during beam commissioning.

In addition, there is a model for the contamination of electrons arising in interactions between the photons and the treatment head and the air; this will be discussed further in *section 4.8 Electron contamination on page 123*.

The sources are modeled as flat with elliptical or circular isointensity lines. The primary source has an elliptical Gaussian intensity profile with the main axes along the x- and the y-directions; hence it is characterized by its widths in the x- and y-directions (perpendicular to the beam). The width of a source is equal to the standard deviation of a Gaussian distribution. The primary source is fixed in the gantry system, i.e. it does not rotate with the collimator. This is taken into account in the fluence calculation. The scattering source has a circular Gaussian intensity profile and is characterized by only one width, the distance from the primary source is fixed during beam commissioning. Weights are assigned to the sources; they are chosen such that the sum of the weights of the primary source and the flattening filter photon source is equal to one, for the case when there are no wedges. The weights when using wedges are described in *Wedge scatter on page 135*. The electron sources are explained in detail in *section 4.8.1 Electron energy fluence on page 124*.

Collimators

The beam model can contain three collimators: two jaws and one multi-leaf collimator (MLC). The MLC can run in the x- or in the y-direction. If there is an add-on MLC and an internal MLC, it is the add-on MLC that is included in the beam model. The order and position along the isocenter axis is entered in beam commissioning. The Varian Halcyon MLC has two layers at different z-position.

It is possible to exclude the MLC from the model, using only the two sets of jaws, and for Siemens LINACs and Elekta LINACs with the Agility head there is the option to deselect the backup jaw (x-jaw) and only have a y-jaw and an MLC. The z-position for all three collimators and the transmission of the MLC and the x-jaw (y-jaw for machines with MLC in the y-direction) are beam model parameters fixed at the beam commissioning. The jaws in the y-direction (in the x-direction for machines with MLC in the y-direction) are regarded as fully opaque. The MLC transmission should be the average transmission, including interleaf leakage. Some additional MLC parameters are described further in sections *Tongue-and-groove on page 64*, *Leaf tip width on page 64*, *Corner region where the leaf tip and the tongue-and-groove intersects on page 65* and *Collimator position calibration – offset, gain and curvature on page 66*.

The collimator geometry and transmission are mapped geometrically onto the collimator planes. In areas with no collimator, the transmission is one and where the fully opaque jaws are situated, the transmission is zero.

MLC - Multi leaf collimator

A multi leaf collimator is comprised of a number of opposing leaves which can be retracted from or extended into the beam region. In 3DCRT, the leaves create an opening which conforms to the target in two dimensions. In IMRT a number of segments with different MLC settings are used to build up a fine energy fluence map which for several beams conforms to the target in three dimensions. The LINAC head model includes an MLC with adjacent opposing leaf-pairs.

MLC regions

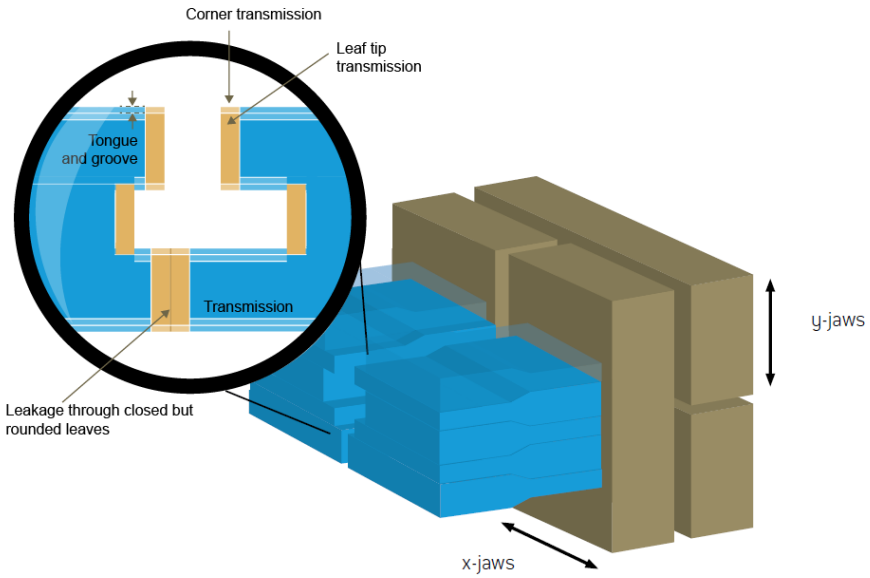

Figure 13. The MLC regions.

The MLC is a rather complicated device which has different regions with characteristics which will be explained further below:

- MLC leaves
- Open areas
- MLC leaf sides (tongue-and-groove)
- MLC leaf tips

In the energy fluence and dose computation, the MLC is treated as flat but a set of parameters are used to correct for 3D-effects. These are parameters associated with the tongue-and-groove region (*Tongue-and-groove on page 64*), the leaf tip region (*Leaf tip width on page 64*), the corner region where the tongue-and-groove and the leaf tip intersect (*Corner region where the leaf tip and the tongue-and-groove intersects on page 65*) and the fine-tuning of the collimator position (*Collimator position calibration – offset, gain and curvature on page 66*). Even though some of the parameters have small influence on large open fields, their effects add up over many small fields as in IMRT or VMAT. Therefore, tuning of these parameters requires more measurements than the usual rectangular field depth dose curves and profiles. Recommendations can be found in the *RSL-D-RS-2024A-RPHY, RayStation 2024A RayPhysics Manual*.

Tongue-and-groove

Some MLC leaves have a step, or a tongue-and-groove leaf side (see Figure 13), designed to reduce radiation leakage between the MLC leaves. The step profile differs between MLC models and vendors and some models have an inclined interface instead of a step profile. Examples of MLCs with stepped tongue-and-groove are Varian Millennium, HD120 and Halcyon. Examples of MLCs with a tilted leaf side are Agility and MLCi2. In the RayStation dose computation, areas which are covered by only a tongue or only a groove are given a transmission coefficient which is the square root of the MLC transmission parameter. The spatial extent of the tongue-and-groove region projected onto the isocenter plane is one of the parameters which can be tuned at beam commissioning. In RayStation, the tongue-and-groove region is centered at the leaf edge, and extends with the size of the tongue and groove parameter on both sides of the leaf edge so that the total tongue and groove region will be twice the size of the entered parameter.

As an example, a 1% MLC-transmission gives a 10% tongue-and-groove transmission. This is higher than the MLC transmission but lower than 100% and therefore the overall effect of increasing the tongue-and-groove width is a reduction in overall fluence. Tongue-and-groove regions are only added for MLC leaf edges where the edge is exposed into the MLC opening. Overlapping tongue-and-groove regions of adjacent leaves are handled as closed MLC regions. If there is extra leakage in this area (interleaf leakage), RayStation considers this as part of the MLC transmission, which therefore should be seen as an areal average.

Leaf tip width

The tips of the MLC leaves are generally rounded in the xz-plane in the beam limiting device coordinate system (yz-plane for a machine with MLC in the y-direction), see Figure 14. The rounding reduces the MLC thickness at the tip, giving a gradually decreasing transmission from the open 100% to the closed MLC transmission. The RayStation dose computation allows for a leaf tip region to be added just outside the open field. The width of the region is set by the Leaf tip width and the transmission by the parameter Leaf tip transmission. For RayStation 12A and earlier the Leaf tip transmission was not separately editable but instead set to the square root of the MLC transmission. The leaf tip width is defined at the projection onto the isocenter plane. Since the leaf tip region is positioned from the nominal tip position toward the leaf base, the effect of increasing the width is to increase the width of the low dose region just outside the penumbra along the MLC leaf motion direction.

RayStation also offers the possiblity to add extra fluence at the leaf tip using the Collimator position calibration (see *Collimator position calibration – offset, gain and curvature on page 66*).

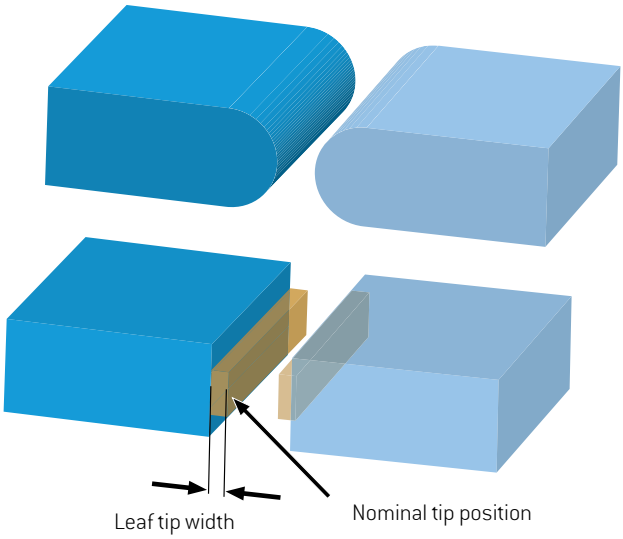

Figure 14. The leaf tip width.

Corner region where the leaf tip and the tongue-and-groove intersects

From RayStation 2023B there is the option to adjust the transmission also in the small corner region where the leaf tip intersects the tongue-and-groove. This is done slightly differently for single and dual layer MLCs (see Figure 15 and Figure 16).

For all single layer MLC linacs, the small region that is covered by both a leaf tip and a tongue and groove from the same leaf is divided into two regions with different transmission. The part extending from the leaf edge into the leaf in the Y-direction (in the X-direction for a machine with MLC in the Y-direction) is treated as leaf tip. For RayStation 12A and earlier the part extending from the leaf edge towards the open region was treated as open. From RayStation 2023B and later the transmission of this region can be adjusted using the Corner transmission parameter.

The small region that is covered by a leaf tip and two tongue-and-grooves is similarly divided into two regions. The part extending from the leaf edge into the leaf in the Y-direction (in the X-direction for a machine with MLC in the Y-direction) is treated as leaf tip. The part extending from the leaf edge towards the closed leaf is treated as closed.

For information about dual layer MLC, see *Dual layer MLC (Varian Halcyon) on page 67*.

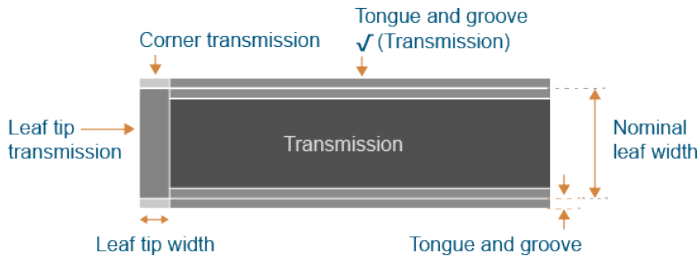

Figure 15. Right leaf bank MLC transmission regions from the beams-eye-view for a single layer MLC.

Collimator position calibration – offset, gain and curvature

The RayStation MLC calibration parameters are the offset, the gain and the curvature. For the MLC, these parameters correct the nominal leaf position to an effective leaf position that better match the measurement. The nominal leaf position is used in beam lists, reports, beams-eye-view and RTPlan DICOM-files. The effective leaf position is used in dose computation. The correction is polynomial and x-symmetric, where x is the nominal position expressed in IEC 61217 field coordinate system.

$$x_{effective} = x{-}offset + gain \cdot x{-}curvature \cdot x^2 \quad left\ MLC\ bank \qquad \text{[Eq. 23]}$$

$$x_{effective} = x + offset + gain \cdot x + curvature \cdot x^2 \quad right\ MLC\ bank \qquad \text{[Eq. 24]}$$

The coordinates are defined at the projection of the respective collimators onto the isocenter plane. A positive offset enlarges the field. A positive gain shifts the leaf position outwards by an increasing amount with the distance from the origin. The shift will be to the left if the leaf is to the left of the origin independent of the leaf bank, and vice versa for the right side. A positive curvature moves the left MLC leaves to the left and the right MLC leaves to the right. This type of three- parameter calibration can be applied to the MLC in the x-direction and the jaws in the x- and y-direction. In the y-direction, the MLC leaves are calibrated with a gain term only. A position correction with negative offset and/or curvature could in some cases give overlapping effective positions of the opposing leaves; the leaves are then simply treated as fully closed.

For a machine with MLC in the y-direction, the opposite applies, i.e., there is offset, gain and curvature in the y-direction and only a gain term in the x-direction.

Since the impact of the MLC calibration on the standard beam-profiles is limited, it may be necessary to study other sets of measurements to establish a correct calibration. Refer to *RSL-D-RS-2024A-RPHY, RayStation 2024A RayPhysics Manual* for recommendations.

If one knows how the MLC control system interprets DICOM, one can let that knowledge influence what MLC calibration parameters to start the tuning from. For instance, Agility interprets the RTPlan MLC positions as field edge positions and employs an MLC correction table (as it happens a second degree polynomial in leaf position) to translate DICOM positions to physical leaf tip parameters at the MLC center plane. This table should **not** be used to set the offset, gain and curvature in RayStation, which has the same DICOM definition as Agility.

WARNING!

Collimator calibration. The collimator calibrations (offset, gain and curvature) are used to shift the collimator positions from the plan positions (shown in the Beam's Eye View, in beam lists, in reports, exported in DICOM etc.) to an effective position used in dose computation. For dose curves this only shifts the penumbra, but for a VMAT, SMLC or DMLC field with many segments adding up, this can change the overall dose level significantly. Ensure that the collimator shift in the beam model is really intended. Be extra careful with gain and curvature shifts which increase with increasing distances from the origin. Results from the auto-modeling collimator calibration step must be reviewed before clinical use.

(9368)

Dual layer MLC (Varian Halcyon)

For dual layer MLCs the fluence computation take the following regions into account: open areas, regions which are covered by the tongue-and-groove region of one leaf, regions which are covered by the leaf tip region of one leaf, regions which are at the intersection of the tongue-and-groove and the leaf tip region of one leaf and regions which are covered by a single layer. Regions which are covered by two layers, or one layer and a tongue-and-groove or one layer and a leaf-tip are considered opaque. The opaque region starts where the nominal side of the leaf is.

The intersection of the leaf tip and the tongue-and-groove of one layer for dual layer MLCs is handled as a separate region. It extends over the double-tongue-and-groove width (the same as the tongue-and-groove) in one direction and the leaf tip width in the other. For RayStation 12A and earlier the corner transmission was 35%, for RayStation 2023B and later the corner transmission is an adjustable parameter.

The tongue-and-groove, leaf tip width and collimator calibrations can be set per MLC layer. The transmissions are the same for both layers and the upper MLC position is used in the source projection.

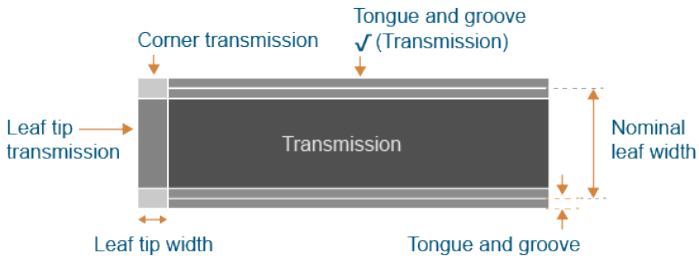

Figure 16. Right leaf bank MLC transmission regions from the beams-eye-view for a dual layer MLC.

CyberKnife

A CyberKnife equipped with MLC is modeled as a LINAC with fixed jaws in the fluence computation. The fixed x-jaws model the patient plane shield in the x-direction, behind which closed MLC leaves are parked. The fixed y-jaws model the side protection plates of the MLC, which begin at the edge of the first and last MLC leaf and effectively act as one additional, closed MLC leaf pair.

When a CyberKnife is equipped with fixed or iris cones, neither MLC nor jaws are included in the fluence computation. In this case, the fluence projection is only performed through the circular cone opening. There is no cone transmission included in the fluence computation.

4.3.2 Normalization

Calibration dose

In beam commissioning, the normalization of the measured curves is specified using the dose in the reference point for the reference field size and one monitor unit, this is called the calibration dose. The reference point is a selected point on the isocenter axis; described by the source-surface-distance, SSD, and the depth. The source-surface-distance is generally 90 cm or 100 cm, and the depth is preferably well below the electron contamination range, recommended depths are 5 cm or 10 cm for 6 MV (see *section 4.8.3 Contamination electron dose on page 124* for electron ranges for different energies). The reference field size is 10 cm x 10 cm for all LINACs which are capable of creating that field-size. Elekta LINACs with beam modulators have the jaws fixed at 21 cm x 16 cm and create fields using the MLC only. For Elekta BM the reference field size is 9.6 cm x 9.6 cm, 9.6 cm x 10.4 cm, 10.4 cm x 9.6 cm or 10.4 cm x 10.4 cm. For CyberKnife, the 6 cm fixed cone is used as reference field size. The calibration dose is specified at beam commissioning to set the global scale of measured dose curves but it is not a multiplicative factor in the dose computation.

In RayStation, the absolute normalization of the computed dose is given by the application of the beam model as described in this chapter. The beam model is tuned to give computations which match measurement and therefore to give the right output for different fields.

Monitor units

Inside the LINAC head, there is a monitor chamber (an ionization chamber) which keeps track of the fluence passing through, counted in beam monitor units (MU). Generally, the counter is calibrated such that it shows 100 monitor units when the dose obtained in water in the reference point for the reference field size (*Calibration dose on page 69*) is 1 Gy, but this is a matter of choice during beam monitor calibration. The number of MUs is a multiplicative factor in the energy fluence computation and the dose calculation.

Output factors – measured input to the beam model

The dose on the central axis corresponding to a specified number of measured beam monitor units varies with the field size; this dependence is expressed in the output factors. The output factor corresponding to a given collimator setting is defined as the measured dose in a specific point for that collimator setting divided by the corresponding dose for the reference field at the same point (SSD and depth). Therefore the output factor for the reference field is always 1.0, the output factors are measured for a set of field settings resulting in a table of output factors versus field size. The output factor reference point can be different than the absolute calibration reference point, but it must still be on the axis from source to isocenter and the same depth recommendations apply. The table is machine and beam quality dependent and must be provided by the user at beam commissioning. The output factors normally increase with increasing field size.

Some treatment planning systems use output factors as multiplicative factors when computing dose. This is not the case for RayStation 2024A.

The output factors are not part of the beam model, and are hence not used in dose or fluence computations. Instead they are used to set the scale for the imported measured dose curves and become part of the beam model when the beam model is tuned to match measurement.

Output factor corrections – used in energy fluence computations

There are several factors that influence the output versus field size in RayStation. Part of the output factor increase with field size is caused by increased secondary scattering of energy from the sides into the center of the field (phantom scatter); this effect is part of the radiation transport in the collapsed cone dose calculation (*section 4.5 Collapsed cone dose computation on page 83*). A smaller part (for Varian, Elekta and Siemens LINACs) of the field size dependence is caused by the projection of extended sources through the collimators (head scatter). The phantom scatter and head scatter is generally not sufficient to completely describe the output factor variation. The remaining field size dependence is called the output factor correction, and it is introduced into the energy fluence and dose computation to account for effects such as backscattering from collimators into the beam monitor. The output factor correction can be normalized to 1.0 for the reference field size; it generally increases slightly with field size. The output factor corrections are fitted in commissioning to give a best fit to dose curves and output factor measurements. When computing the fluence for a segment the output factor corrections are computed using the field measure (*Field measure on page 70*).

Field measure

The field measure is calculated from the jaw or MLC openings, $l_{x\text{-jaw/MLC}}$ and $l_{y\text{-jaw/MLC}}$, using an equivalent square formula. The openings are given on the isocenter plane.

Field measure calculations for LINACs equipped with x-jaws

For machines that are equipped with x-jaws, the field measure is calculated with the equivalent square field formula defined as

$$Fieldmeasure = \frac{2l_{x-jaw/MLC} \cdot l_{y-jaw/MLC}}{l_{x-jaw/MLC} + l_{y-jaw/MLC}} \qquad \text{[Eq. 25]}$$

For a square field, the field measure is equivalent to the field side at the isocenter.

For machines where the jaws are closest to the source, for example Varian LINACs except for Varian Halcyon, the $l_{x\text{-jaw/MLC}}$ and $l_{y\text{-jaw/MLC}}$ are obtained from the x-jaw and y-jaw openings.

For machines where the MLC is closest to the source, for example Elekta LINACs and for Varian Halcyon, $l_{x\text{-jaw/MLC}}$ is obtained from the maximum MLC leaf pair opening and $l_{y\text{-jaw/MLC}}$ is obtained from the sum of leaf widths for the open MLC leaf pairs, considering only those MLC leaves that are not covered by the jaws. For dual layer MLCs with fixed jaws (Varian Halcyon), the maximum x-opening and the y-summation is performed over half-widths, and only parts that are fully open are taken into account.

For machines where there are only fixed jaws, for instance Elekta LINACs with Beam Modulators and CyberKnife LINACs, the $l_{x\text{-jaw/MLC}}$ is obtained from the maximum MLC leaf pair opening within the field and $l_{y\text{-jaw/MLC}}$ is obtained from the sum of leaf widths for the open MLC leaf pairs multiplied with the MLC leaf width.

When deciding the number of open MLC leaf pairs, only leaf pairs that have an opening larger than the applicable minimum tip gap entered during beam commissioning will be considered as open.

Depending on the beam type and whether the **Use minimum dynamic tip gap for static fields** check box has been checked, either the Minimum dynamic tip gap or Minimum static tip gap will be used.

Field measure calculations for LINACs that are not equipped with x-jaws

For machines that are not equipped with x-jaws, for example Siemens LINACs and Elekta LINACs with the Agility head, the field measure is calculated with the equivalent square field formula defined in [36] as

$$Fieldmeasure = \frac{(1+k) \cdot l_{lower} \cdot l_{upper}}{k \cdot l_{lower} + l_{upper}} \qquad \text{[Eq. 26]}$$

The quantity k is calculated from both

- the distances from the top of the jaw/MLC to the source plane: $d1lower$ for the lower collimator closest to the isocenter plane and $d1upper$ for the upper collimator closest to the source

  and

- the distances from the top of the jaw/MLC to the isocenter plane: $d2lower$ for the lower collimator closest to the isocenter plane and $d2upper$ for the upper collimator closest to the source

  according to

$$k = \frac{d1lower/d2lower}{d1upper/d2upper} \qquad \text{[Eq. 27]}$$

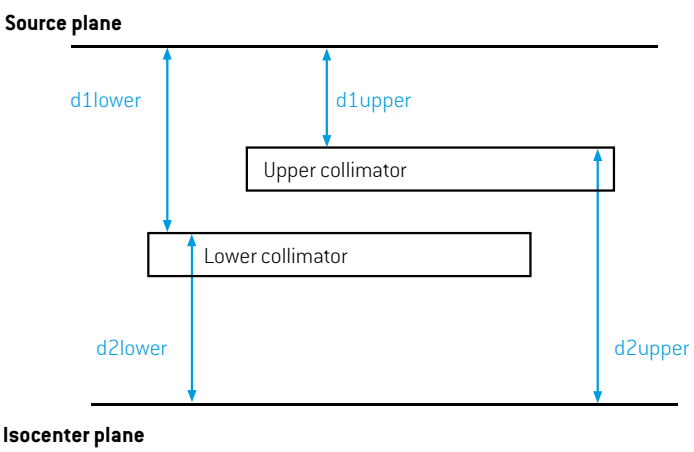

Figure 17. Illustration of the distances used to calculate quantity k: d1lower, d1upper, d2lower and d2upper.

For a square field, the field measure is equivalent to the field side at the isocenter. The length $l_{y\text{-jaw}}$ is obtained from the y-jaw opening and l_{MLC} is obtained from the maximum individual MLC leaf pair opening, considering only the leaves which are not covered by the y-jaws.

The position of the top of the collimators is calculated by adding the collimator thickness to the bottom collimator position entered in MLC properties and Jaw properties during beam commissioning. In RayStation 2024A, it is mandatory to enter collimator thickness and bottom positions for LINACs not equipped with x-jaws.

Influence of output factors and reference dose on computed output

The measured calibration dose (*Monitor units on page 69*) and the measured output factors (*Output factors – measured input to the beam model on page 69*) are only a part of the dose computation in so far as they are the base for determining the beam model. Nevertheless, once the beam model has been adjusted so that computation matches the data, the computed output can be related to measured input.

The overall normalization is therefore such that:

$$N \cdot OFC(reference\ field) = \frac{D_{meas.}(d_{ref}, reference\ field)}{D_{comp.}(d_{ref}, N = 1, OFC = 1, reference\ field)} \qquad \text{[Eq. 28]}$$

N is the normalization factor, independent of field setup. The output factor correction, OFC, varies with field size (collimation). It is generally set to 1 for the reference field. $D_{meas.}(d_{ref}, referencefield)$ is the measured calibration dose at the reference depth, d_{ref}. The expression $D_{comp.}(d_{ref}, N = 1, OFC = 1, referencefield)$ is the dose that would be obtained from the dose computation at the reference point for the reference field if $N = 1$ and $OFC = 1$, where the number of MUs is the same as used in the measurement.

The dose to a point is computed as:

$$D_{comp.}(x, y, z, collimation, MU) = MU \cdot N \cdot OFC(FM(collimation)) \cdot D_{comp.}(x, y, z, MU = 1, N = 1, OFC = 1, collimation) \qquad \text{[Eq. 29]}$$

where $OFC(FM(collimation))$ is the output factor correction, OFC, computed for the field measure, FM, corresponding to the field collimation (*Field measure on page 70*). $D_{comp.}(x, y, z, MU = 1, N = 1, OFC = 1, collimation)$ is the computed dose to the point for $MU = 1$, $N = 1$ and $OFC = 1$.

When the beam model is perfectly adjusted to the data, the output factor corrections $OFC(FM(collimation))$ have been adjusted such that:

$$OFC(FM(collimation)) = \frac{D_{meas}(d_{OF}, collimation)}{D_{comp.}(d_{OF}, N, OFC = 1, collimation)}$$
$$= OF(d_{OF}, collimation) \cdot D_{meas.}(d_{ref}, referencefield) \cdot \frac{PDD^{ref}(d_{OF})}{PDD^{ref}(d_{ref})} \cdot \frac{1}{D_{comp.}(d_{OF}, N, OFC = 1, collimation)} \quad \text{[Eq. 30]}$$

where OF are the output factors, which are a measured quantity defined as:

$$OF(d_{OF}, collimation) = \frac{D_{meas.}(d_{OF}, collimation)}{D_{meas.}(d_{OF}, referencefield)} \quad \text{[Eq. 31]}$$

see *Output factors – measured input to the beam model on page 69*. Note that the measured output factors describe the full measured dose variation that is due to both phantom scatter and collimator scatter. This means that they are equivalent to the total measured scatter correction factors $S_{cp,measured}$.

The output factor depth, d_{OF}, does not need to be the same as the reference depth for the calibration point, d_{ref}. If they differ, the depth dose curve (PDD) is used to convert between depths as described above. If the same depth is used to measure the reference dose and the output factors, $d_{OF} = d_{ref}$, the equation simplifies to:

$$OFC(FM(collimation)) = \frac{OF(d_{ref}, collimation) \cdot D_{meas}(d_{ref}, reference\ field)}{D_{comp.}(d_{ref}, N, OFC = 1, collimation)} \quad \text{[Eq. 32]}$$

If we define a computed total scatter correction as:

$$S_{cp,comp.}(OFC = 1, collimation) \equiv \frac{D_{comp.}(d_{ref}, N, OFC = 1, collimation)}{D_{comp.}(d_{ref}, N, OFC = 1, reference\ field)} \quad \text{[Eq. 33]}$$

then, also using Equation 28 and Equation 29, the output factor corrections are:

$$\frac{OFC(FM(collimation))}{OFC(referencefield)} = \frac{S_{cp,meas.}(collimation)}{S_{cp,comp.}(collimation, OFC = 1)} \quad \text{[Eq. 34]}$$

To summarize, the collapsed cone algorithm handles the dose increase with field size due to phantom scatter. The extended sources in the fluence model handle dose increase with field size due to head scatter. Given this, the OFCs are assumed to describe backscatter into the monitor chamber. However, in practice, the OFCs are fitting parameters that can absorb both algorithm and parameter imperfections and the best values are the ones that best recreate data for treatment fields.

4.3.3 Flattening filter

The interactions in a flattening filter are taken into account by the introduction of the flattening filter photon source, an electron source (*section 4.8 Electron contamination on page 123*), the off-axis softening (*section 4.5.3 Energy distribution on page 86*) and finally a radially varying beam profile correction.

Beam profile correction

The fluence that originates in the primary source is scaled with a radial beam profile correction. The radial beam profile correction is used to obtain the characteristic central field dip of conventional Elekta LINACs, or to model the forward peaked energy fluence of flattening filter free beams. It can also be used to model more subtle effects; one example being the primary collimator which can decrease the fluence at the corners of large fields. Note that the beam profile correction is a radial scaling, this means that values at radii larger than 20 cm influence the corners of the fields directly but the x- and y-profiles only through phantom scatter.

Some LINACs have a circular primary collimator close to the source which limits the field to a circular shape which is smaller than the diagonal of the largest square fields, such that the corners are cut off. To model this, start by setting the Beam Profile to zero (or close to zero) from the primary collimator radius onwards. The exact shape shall be tuned to match diagonal measurements. The Beam Profile correction and the Off Axis Softening at radii larger than the largest profile can be validated and adjusted by comparing Beam 3D modeling doses to measurements in the corner.

The energy fluence map is given by the primary Gaussian source projected through the collimators and multiplied with the beam profile correction, plus the secondary photon source from the flattening filter without beam profile correction. The radius is defined in the projection onto the isocenter plane. The beam profile correction is defined as a look-up table with linear interpolation between points.

WARNING!

Beam profile correction and off-axis softening at large field radii.The photon beam model parameters *Beam profile correction* and *Off-axis softening* cannot be evaluated at large radii in the Beam commissioning module without having imported diagonal profiles which extend to the corners of the field. Special care must be taken when using auto-modeling for the *Beam profile correction* and *Off-axis softening* parameters if there are only x- and y-profile curves imported into the Beam commissioning module. Be aware that manual adjustments of these parameters at large radii will be necessary after using auto-modeling without diagonal curves. The Beam 3D modeling module can be used to check the calculated dose of the entire field, including corners, before commissioning a machine (not available for CyberKnife LINACs).

(3438)

4.3.4 Source projection

In RayStation the sources are projected through collimators using back projection.

In back projection, for each central pixel point in the fluence plane, integration is performed over the visible part of the sources. When projecting the sources through the collimators, the collimator z positions specified in the **Fluence** tab in beam commissioning are used.

When the source size is small, on the scale of a few fluence pixels, the approximation that the average fluence in the pixel is the same as the fluence in the center of the pixel no longer holds. In that case an integration over the pixel has to be performed. This integration is performed by convolving the source distribution with the size of the pixel in the source plane.

To increase computational efficiency, some simplifications are used. The assumption is made that there is no electron transmission through the MLC leaves and the electron source is not projected through closed MLC leaves nor through the MLC leaf tips or the tongue-and-groove region of the MLC. The flattening filter and wedge scatter sources are projected through closed MLC leaves but not through the MLC leaf tips or the tongue-and-groove region. For most machines, these sources are extended sources (not point-like) and the MLC regions are small. The effect of projecting extended sources through small regions is negligible.

The projection is done separately for the primary photon source, secondary (flattening filter) photon source, electron source and wedge scatter source considering the jaws and the MLC settings and block or circular cone openings when applicable.

The projection of extended sources widens the penumbra, and influences the output and fluence shape when the fields are small enough. Small fields are mainly influenced by the primary source. Larger fields are increasingly influenced by the flattening filter source as well.

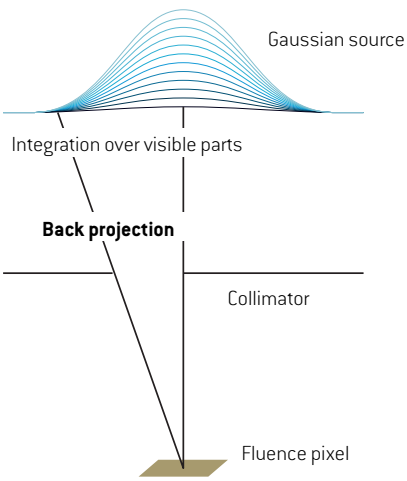

Figure 18. Source projection.

4.4 FLUENCE COMPUTATION - TOMOTHERAPY LINACS

This section describes the beam model and energy fluence computation for TomoTherapy LINACs. The beam model contains a number of parameters, most of which are equal to corresponding parameters used by Accuray.

In this section

This section contains the following sub-sections:

4.4.1	Physical LINAC head components	p. 77
4.4.2	Fluence output	p. 77
4.4.3	Collimators	p. 77
4.4.4	Transverse profile	p. 80
4.4.5	Fluence calculation	p. 81
4.4.6	Differences between the Accuray model and the RayStation model	p. 81

4.4.1 Physical LINAC head components

The TomoTherapy LINAC head is similar to C-arm LINACs (*section 4.3 Fluence computation – CyberKnife and C-arm LINACs on page 60*). The TomoTherapy LINAC does not have a flatting filter, resulting in a non-flat beam profile. The collimators of TomoTherapy LINACs consist of one pair of jaws in the y-direction and one MLC where each leaf can either be fully open or fully closed at a given time.

4.4.2 Fluence output

The output of the energy fluence comes from:

- EFIOT - energy fluence per ideal open time
- Dose normalization
- Jaw fluence output factors
- Projection time of the treatment plan

The EFIOT value is read from the Accuray model and tells the dose rate of the TomoTherapy LINAC. The dose normalization is an additional mutliplicative factor which is unique for RayStation and sets the correct output of the calculated fluence for a particular TomoTherapy beam model. The jaw fluence output factors are multiplicative output factors for a particular jaw width.

The projection time, i.e., the time it takes to deliver one segment, is related to the output since more dose can be delivered during a segment if the segment lasts for a longer time.

RayStation defines jaw output factors for central fields for all jaw widths supported by the machine. Output factors for jaw widths W in-between supported jaw widths (W0 and W1) are interpolated as:

$$Jaw\ output(W) = e^{\left(\frac{(W1-W)}{(W1-W0)} ln(Jawoutput(W0)) + \frac{(W-W0)}{(W1-W0)} ln(Jawoutput(W1))\right)} \quad \text{[Eq. 35]}$$

The interpolated jaw output factors are used for segments with dynamic jaws.

4.4.3 Collimators

Jaws

The jaw pair, called the front and back jaw, are described by a set of jaw filters for different jaw positions. The jaw filters describe the jaw penumbra at that jaw position. Jaw filters are a function of y. For dynamic jaws, interpolated jaw filters are used. First, the adjacent jaw filters at Y0 and Y1 are shifted in y to get the field edges at the new y position. Then, a jaw at position Y is interpolated from the adjacent jaw filters as:

$$Jawfilter(y, Y) = \frac{Y1-Y}{Y1-Y0} Jawfilter(y-(Y-Y0)) + \frac{Y-Y0}{Y1-Y0} Jawfilter(y-(Y-Y1)) \quad \text{[Eq. 36]}$$

The front and the back jaws are combined such that:

$$Total\ jaw\ filter(y) = Jaw\ filter\ back(y) + Jaw\ filter\ front(y) - 1 \qquad \text{[Eq. 37]}$$

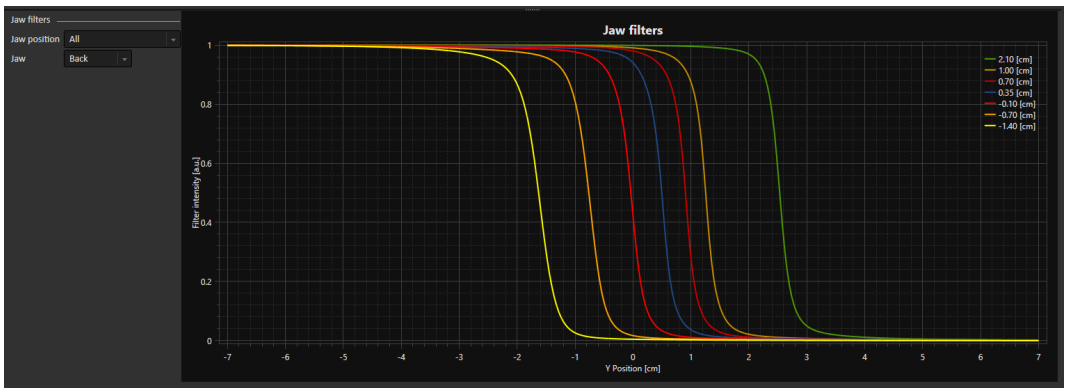

Figure 19. Jaw filters for different jaw positions.

MLC

The MLC is described by a set of MLC filters (three for each leaf) which gives the MLC penumbra depending on if the neighbors of the leaf are open or closed.

1. The filter used when the leafs left neighbor is open, the leaf is open, and the leafs right neighbor is closed is called the Open-Closed filter (OC)
2. The filter used when the leafs left neighbor is closed, the leaf is open, and the leafs right neighbor is closed is called the Closed-Closed filter (CC)
3. The filter used when the leafs left neighbor is closed, the leaf is open, and the leafs right neighbor is open is called the Closed-Open filter (CO)

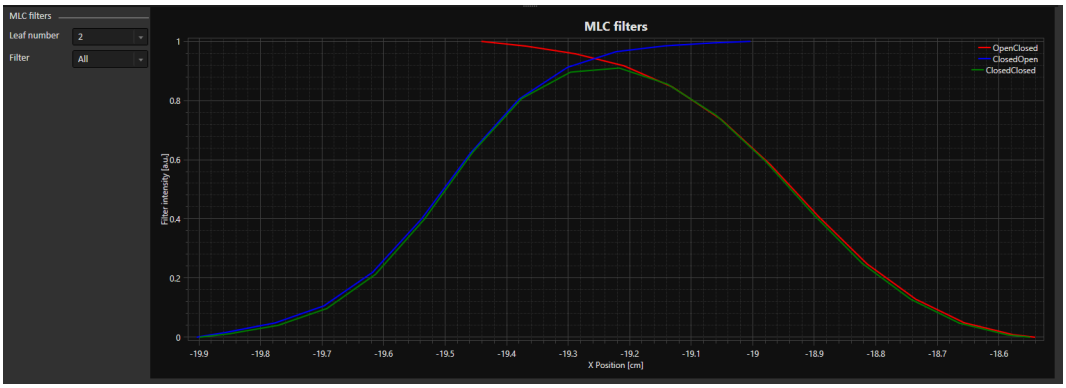

Figure 20. The MLC filters which gives the MLC penumbra depending on if the neighbors of the leaf are open or closed. The figure shows all three filters for one leaf.

An MLC leaf may be open no part of a segment, the entire segment or part of a segment. This is called the leaf open time t, and is described by a leaf open fraction between 0 (closed the entire segment) and 1 (open the entire segment). If the leaf is open part of the segment, the assumption is made that the open time is centered in the middle of the segment. MLC filters are combined such that:

$$Sum\ of\ MLC\ filter = \sum_{i=leaves} \left(t_{OC} \cdot Filter^{i}_{OC} + t_{CC} \cdot Filter^{i}_{CC} + t_{CO} \cdot (Filter^{i}_{CO} - 1)\right) \quad \text{[Eq. 38]}$$

The MLC leaves do not open and close instantaneously. The relation between the programmed (ideal) leaf open time, which is displayed in the RayStation user interface and transferred to IDMS for delivery, and the real resulting leaf open time during delivery is expressed as leaf latencies.

Leaf latencies are listed for different projection times and consist of a slope and an offset. The relationship between programmed time and real time for a certain projection time is:

*realTime = slope * programmedTime + offset*

If a leaf latency is not available for a certain projection time, the slope and offset values are linearly interpolated from accessible values.

During fluence calculation, the leaf open times in the treatment plan are corrected for leaf latencies and the real time is used during fluence calculation.

For leaves that are fully closed or fully open during a projection, leaf latencies are not applied.

For short leaf open times and almost fully open leaves, the leaf latency correction relationship breaks down, see Westerly [121]. This means that for short leaf open times and almost open leaves, the dose calculation will not be correct with respect to leaf latencies, leading to differences between computed and delivered dose.

WARNING!

TomoTherapy dose computation accuracy for short leaf open times and short leaf close times. For TomoHelical and TomoDirect plans with a large number of short leaf open times or a large number of short leaf close times, the delivered dose may differ significantly from the computed dose. The reason is that for fast leaf movements, the treatment machine will not open/close the leaves in accordance with the model used in the dose computation.

To avoid short leaf open times and short leaf close times when creating plans in RayStation, use the beam model parameters *Minimum leaf open time* and *Minimum leaf close time*. The issue will occur with certain machine-specific leaf open/close time characteristics, but around 50 ms can normally be an appropriate value for both *Minimum leaf open time* and *Minimum leaf close time*.

To find the appropriate values for *Minimum leaf open time* and *Minimum leaf close time* for each TomoTherapy treatment unit, leaf latency data can be measured as described in *Westerly DC, Soisson E, Chen Q, Woch K, Schubert L, Olivera G and Mackie TR, Treatment planning to improve delivery accuracy and patient throughput in helical tomotherapy, Int J Radiat Oncol Biol Phys. 2009;74(4):1290–1297*. Another option is to use scripting to create a set of test plans with a constant leaf open time for all open leaves and then examine the relation between measured dose and opening time.

(7551)

4.4.4 Transverse profile

The TomoTherapy LINAC does not have a flattening filter, resulting in a non-flat beam profile. This is described by the transverse profile which is applied at the fluence level.

The transverse profile is imported from the Accuray machine model where it is referred to as the cone filter. It can however be modified to adapt to the RayStation dose computation.

The transverse profile is defined along the x-axis and is generally slightly asymmetric around the origin. It is applied as:

$$\begin{aligned} \mathit{Cone\ filter}\ (x,y) &= \frac{1}{2} \times \left(\mathit{Cone\ filter}\ (r) + \mathit{Cone\ filter}\ (-r)\right) \\ &+ \frac{x}{2r} \times \left(\mathit{Cone\ filter}\ (r) - \mathit{Cone\ filter}\ (-r)\right) \end{aligned} \qquad \text{[Eq. 39]}$$

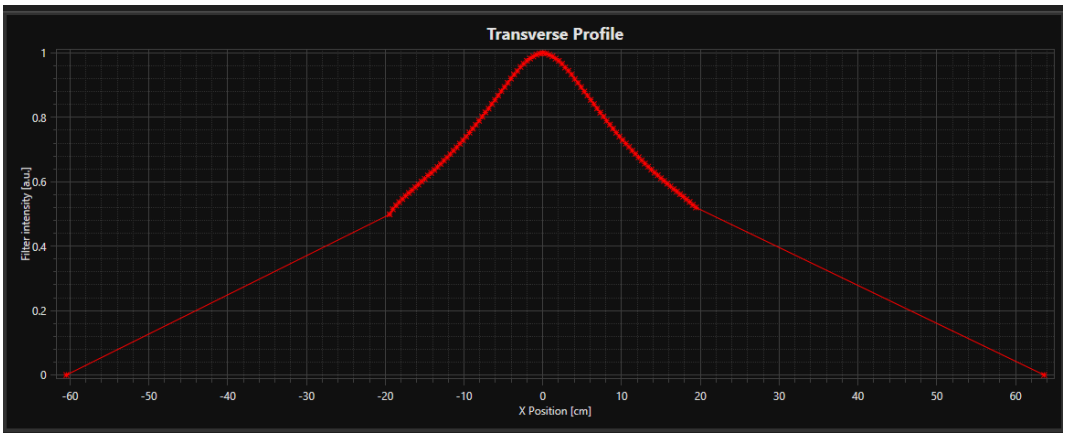

Figure 21. The transverse profile for TomoTherapy LINACs.

4.4.5 Fluence calculation

The energy fluence is defined as a scalar field on a flat surface, the separation into different energy components is performed later, during dose computation. The resolution of the fluence grid is 1 mm x 1 mm. The fluence for TomoHelical and TomoDirect beams only consists of primary photon fluence, no secondary photon fluence or electron contamination fluence is used.

The energy fluence is calculated from the beam model by applying:

- The correct jaw filters based on the front and back jaw positions, interpolating if necessary.
- The transverse profile.
- The correct jaw fluence output factor based on the front and back jaw positions, interpolating if necessary.
- MLC filters for each leaf, depending on the leaf open fraction and if the neighboring leaves are open or closed. Leaf latencies are taken into account for the leaf open fractions.
- EFIOT to the output.
- Dose normalization to the output.
- Projection time to the output.

4.4.6 Differences between the Accuray model and the RayStation model

The RayStation fluence and dose calculation model closely mimics the Accuray model, but there are a few parameters unique to RayStation and a few things that differ.

Dose normalization

The dose normalization is a factor used only by RayStation to get the correct absolute output of the beam model.

Energy spectrum

The energy spectrum model used by RayStation to calculate dose for a TomoTherapy LINAC does not mimic the Accuray model. Instead, the same principle as for C-arm LINACs (see *section 4.5.3 Energy distribution on page 86*) is used, but since there is no inverse square law de-scaling of TERMA and rescaling of dose used for TomoTherapy dose computation, the shape of the energy spectrum will differ from C-arm LINACs.

Jaw fluence output factors

In the Accuray model, different jaw fluence output factors can be used for central and off-axis fields. However, in the Accuray model the same value is usually used for all fields with the same field width and the RayStation model is limited to using the same jaw fluence output factor for all fields with the same field width, regardless of the position of the field.

In the Accuray model, it is also possible to specify jaw fluence output factors for field widths which are not among the field widths that can be used for planning. This is not the case in the RayStation model, where the jaw fluence output factors are limited to the field widths of the fields used for planning.

Off-axis jaw filter penumbras not used

In the Accuray model, different jaw filter penumbras are used for different off-axis positions. Due to the small differences normally seen in the jaw filter penumbras for different off-axis positions, RayStation only uses one jaw filter for each jaw position to save computation time. RayStation uses the central (x = 0) jaw filter penumbra.

Leakage not used

In the Accuray model, it is possible to specify all-slice leakage (general leakage when the beam is on) and in-slice leakage (leakage through MLC leaves). In practice, these values are always set to zero in the Accuray model, meaning that there is no leakage, and in the RayStation model the leakage is omitted.

4.5 COLLAPSED CONE DOSE COMPUTATION

The collapsed cone dose engine calculates the dose by means of a collapsed cone method. The basic principle of the collapsed cone method is described in literature by, for example, Ahnesjö [1] and Mackie [16], [17], [18]. The main idea behind this method is to separately consider the primary photon transport and the secondary transport of photons and electrons which are created in the primary photon interaction.

Dose is computed from the energy fluence in two steps:

- a TERMA (total energy released per mass unit) distribution is first determined by a ray trace of primary radiation through the patient, taking inhomogeneities into account.
- a superposition of point spread kernels (PSK) collapsed along radial rays in a spherical coordinate system, again taking inhomogeneities into account. This is called the collapsed cone algorithm, its accuracy is superior to for instance pencil beam algorithms in that it takes lateral energy transport into account without assuming homogeneity.

In this section

This section contains the following sub-sections:

4.5.1	RayTracing	p. 84
4.5.2	Radiological depths and intersection lengths	p. 85
4.5.3	Energy distribution	p. 86
4.5.4	TERMA computation	p. 87
4.5.5	Point spread kernels	p. 90
4.5.6	Superposition/convolution	p. 94
4.5.7	Dose engine speed-ups	p. 96
4.5.8	Modulated arc therapy/VMAT	p. 99
4.5.9	Conformal arc	p. 101
4.5.10	Static arc	p. 101
4.5.11	Collapsed arc	p. 102
4.5.12	DMLC	p. 102
4.5.13	TomoHelical	p. 102
4.5.14	TomoDirect	p. 103
4.5.15	CyberKnife	p. 103
4.5.16	Algorithm weaknesses	p. 103

4.5.1 RayTracing

The TERMA is determined through a ray trace where each ray in the ray trace grid is followed from the primary source position through the patient. A set of calculations is performed for each intersected voxel in the dose grid. From the surface downwards the beam divergence is approximated to originate in the primary source spot.

For each intersected voxel the following quantities are calculated:

- effective density, ρ_{eff} (described further in *section 2.4 Effective density in collapsed cone computations on page 27*).
- geometric intersection length, Δr.
- radiological intersection length, Δd (described further in *section 4.5.2 Radiological depths and intersection lengths on page 85*).
- total radiological depth, d, as the weighted average over rays which intersect the voxel (described further *section 4.5.2 Radiological depths and intersection lengths on page 85*).
- TERMA based on the energy and material dependent mass attenuation (*Linear attenuation coefficient on page 88*).

These entities are all used in the next step of the dose calculation, which is the application of point spread kernels.

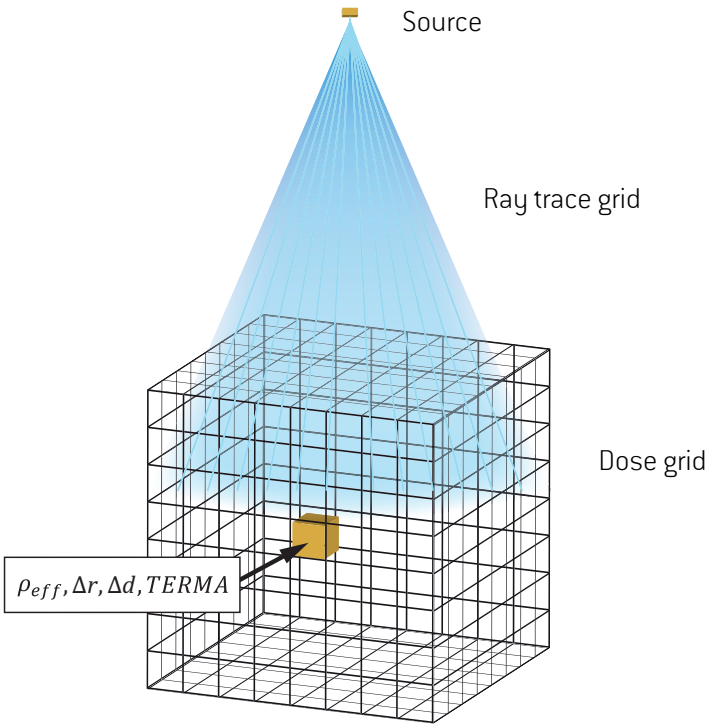

Figure 22. The dose and TERMA grid.

4.5.2 Radiological depths and intersection lengths

The radiological depth d is defined as

$$d(\overline{r}) = \int_{r_0}^{r} \rho_{effective}(\overline{r}'(l), E_i) / \rho_{effectiveH_2O} \, dl \qquad \text{[Eq. 40]}$$

integrated over the geometric distance *l* from the point where the photon ray crosses the surface $\overline{r}_0$ to the position $\overline{r}$.

Keeping track of the radiological depth d of a volume unit (a voxel) makes it possible to easily calculate the energy fluence for a specific geometric depth. It also facilitates finding the proper energy spectrum for the TERMA deposit and the point spread kernels at each specific voxel. Since the radiological depths are used to find the energy spectrum, it must take the off-axis softening into account and not only the depth in patient; hence the patient and the off-axis softening depth range (between -100 cm and 200 cm radiological depth relative to patient surface at central-axis) is divided into 600 steps and for each of these steps the mass attenuation coefficient and the multi-energetic point spread kernels are computed. Physical wedges can also change the energy

spectrum, this is incorporated in the radiological depth as described in *Wedge beam hardening on page 135*.

Similarly, radiological intersection lengths are defined as the geometric intersection lengths between rays and voxels times the effective density relative to water. The radiological intersection lengths are used in the TERMA computation and in the point spread kernel tracing.

4.5.3 Energy distribution

The photon energy fluence, described in *section 4.3 Fluence computation – CyberKnife and C-arm LINACs on page 60*, is the summed energy of all beam photons impinging on a unit area in one plane, expressed as a scalar field. The photon spectrum of this field is used when computing effective densities, water linear attenuation and poly-energetic point spread kernels.

Discretized photon energy spectrum

The particle fluence distribution as a function of energy at the isocenter in air, is visualized in the beam commissioning. It is a sum of mono-energetic components from the set E = [0.5, 1, 1.5, 2, 2.5, 3, 3.5, 4, 5, 6, 7, 8, 9, 10, 12, 14, 16, 18, 20] MeV, where the photon energy must be lower than the original electron energy (for example 6 MeV for a 6 MV beam). Since the spacing of the energy components is non-constant the visualized weights do not follow the shape of the continuous distribution. During dose and energy fluence computation, there is no interpolation between the specified energy points and no extrapolation towards lower energies for the 0.5 MeV-component. The energy distribution can be normalized such that

$$\sum_{i=Energylevel} weight_i \cdot Energy_i = 1 \qquad \text{[Eq. 41]}$$

Note that the RayPhysics energy spectrum specifies particle fluence and not energy fluence per MeV, where the latter is a common way of plotting photon spectra in typical medical physics papers.

The available mono-energetic components in the energy spectrum in RayPhysics depend on the selected dose computation energy of the beam quality. The dose computation energy may differ from the nominal energy of the beam depending on selected photon energy definition. Refer to the *RSL-D-RS-2024A-RPHY, RayStation 2024A RayPhysics Manual* for more information about dose computation energy and nominal energy.

Off-axis softening

For flattened beams, the primary photon source is attenuated by a flattening filter which is thicker on the central axis and thinner at larger radii. Since low energy photons are more strongly attenuated than higher energy photons in most materials, the attenuation in the flattening filter results not only in a flatter dose profile but also in a hardening of the energy spectrum on the central axis, i.e., a shift of the energy spectrum towards higher energies. But, since the energy spectrum is usually measured at the isocenter axis, the effect is called off-axis softening. The off-axis softening is expressed as a geometric profile (in water equivalent thickness) of the flattening filter as a function of radius defined at the isocenter plane. The distribution is offset such that the thickness is zero at the center and negative otherwise. The off-axis softening is applied to the total photon energy fluence, both the photons from the primary source and the photons from the flattening filter. It changes how the

fluence is separated into different energy components, but the summed energy of all components is not changed. The off-axis softening is defined as a look-up table with linear interpolation between points and constant extrapolation towards larger radii.

For flattening filter free beams the off-axis softening should be close to zero for all radii. Note that the off-axis softening and the beam profile corrections (*Beam profile correction on page 74*) are separated inputs to the model even though both are connected to the flattening filter.

Depth hardening

The off-axis softening and the depth hardening are physically identical phenomena. As the beam penetrates the body, energy is delivered to the tissue and the remaining beam is attenuated. The photon components with lower energies are more strongly attenuated than higher energies leading to a hardening of the attenuated beam at larger depths. This depth hardening is taken into account in the TERMA deposit step by using different linear attenuation depending on radiological depth. It is also taken into account in the dose computation step by selecting poly-energetic point spread kernels with a spectrum, which depends on the radiological depth of the point spread kernels (*section 4.5.5 Point spread kernels on page 90*).

4.5.4 TERMA computation

Individual high energy photons can traverse several decimeters of material without interacting, and for a whole beam the number of photons that have not interacted follows a negative exponential with depth. The typical energy attenuation of primary MeV photons in water is approximately 3% per cm; this is the linear energy absorption in the figure in *Primary photon attenuation and divergence on page 87*. The typical primary interaction probability is higher, 6% per cm; this is the linear attenuation in Figure 24.

The primary energy release in the first interaction is expressed in the TERMA, total energy release per mass unit. This interaction is most likely a Compton scattering. The initial state particles in a Compton scattering are the primary photon and an electron in the material. The final state particles in the Compton scattering are a free energetic electron and a scattered lower energy photon. For 6 MV beams the free electron releases its energy locally, within the first centimeter (electron interactions are described further in *Components in the point spread kernels on page 91*). But a large portion of the energy released travels with the secondary photon in a distribution which again ranges several decimeters.

Primary photon attenuation and divergence

The total energy released per mass unit (TERMA) is the product of the mass attenuation coefficient, μ/ρ_m, and the energy fluence [11].

$$TERMA(\overline{r}) = \int \frac{\mu(\overline{r},E)}{\rho_m(\overline{r})} \cdot \Psi_r\left(\overline{r},E\right) dE \qquad \text{[Eq. 42]}$$

The mass attenuation coefficient depends both on material, here expressed as a spatial dependence, and energy.

If the spectrum is discretized into mono-energetic components, each component of beam energy fluence for a parallel beam at position $\overline{r}$ can be written as

$$\Psi(\overline{r}, E_i) = \Psi_0(E_i) \cdot exp\left(-\int_{\overline{r}_0}^{\overline{r}} \mu(\overline{r}(l), E_i)\, dl\right) \qquad \text{[Eq. 43]}$$

where Ψ_0 is the incident energy fluence at $\overline{r}_0$ and the integration is performed along the fluence ray from the patient surface to $\overline{r}$. The same expression would describe the fluence per space angle for an isotropic divergent beam.

The parallel energy fluence equation (Equation 43) does not take divergence into account. Beam divergence from a point source is introduced by application of the inverse square law:

$$\Psi(\overline{r}, E_i) = \Psi_0(E_i) \cdot \frac{\overline{r}_0^2}{\overline{r}^2} \cdot exp\left(-\int_{\overline{r}_0}^{\overline{r}} \mu(\overline{r}(l), E_i)\, dl\right) \qquad \text{[Eq. 44]}$$

where Ψ_0 is the unattenuated energy fluence at $\overline{r}_0$. The fluence plane for RayStation is positioned at isocenter.

When computing the energy fluence, each source is given its position along the z-axis. When tracing the fluence to TERMA, the fluence for a pixel is back-traced toward the primary source only and then traced from the same primary source into the patient.

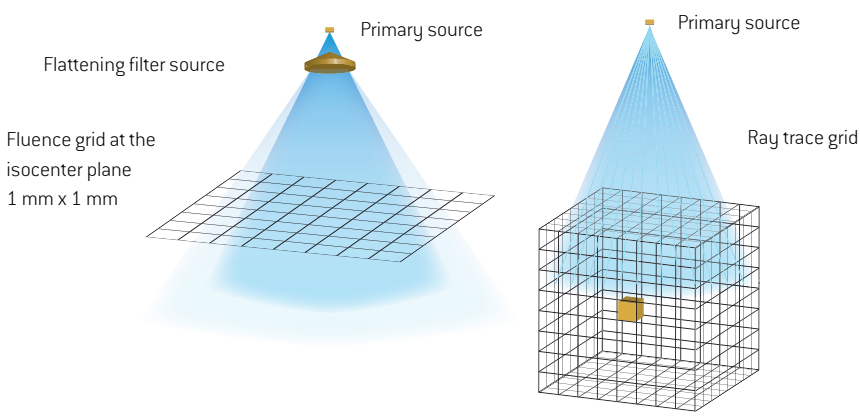

Figure 23. TERMA is computed using the fluence, tracing it back to the surface and then down into the patient as if all rays originate at the primary source.

Linear attenuation coefficient

The linear attenuation coefficient describes the removal of photons from the beam fluence. When computing TERMA, RayStation uses the linear attenuation of water from NIST [8] . This is shown in Figure 24.

The first energy bin in the TERMA computation is 0.5 MeV. The figure still shows the linear attenuation down to ~25 keV where the photoelectric effect becomes important and the linear attenuation increases strongly. At 10 keV the photon linear attenuation is 5 cm^{-1}, i.e. the photon fluence is reduced by a fraction e^{-1} in 2 mm. Since these low energy photons are not part of the dose computation they tend to become part of the electron contamination through the modeling step.

For materials other than water the linear attenuation is rescaled using the effective density. The linear attenuation is expressed relative to water as

$$\mu(\overline{r}, E) = \mu_0(E) \cdot \rho_{effective}(\overline{r}, E)/\rho_{effectiveH_2O}(E) \qquad \text{[Eq. 45]}$$

where $\mu_0(E)$ is the energy dependent attenuation coefficient of water. In media with an atomic number similar to water, the effective density is approximately the same as the electron density.

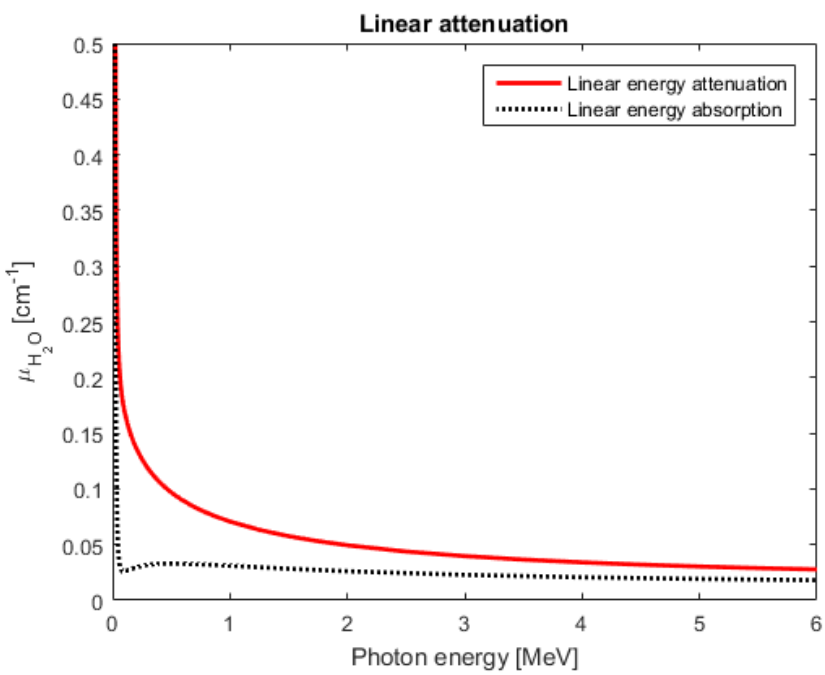

Figure 24. The linear attenuation used for TERMA deposit.

The effective density, $\rho_{effective}(\overline{r}, E)/\rho_{effectiveH_2O}(E)$, is computed using the beam energy spectrum at isocenter in air, without taking off-axis softening or beam hardening into account.

The linear attenuation for water, $\mu_0(E)$, uses the energy spectrum in the TERMA-voxel taking off-axis softening and beam hardening into account.

4.5.5 Point spread kernels

The primary photon interaction is usually a Compton scattering, resulting in a short range free electron that ionizes tissue in a surrounding volume and a long-range lower energy photon. The statistical energy deposit distribution of the full process is contained in the point spread kernel (PSK). It is defined as the spatial energy distribution resulting from one unit of primary energy loss at the origin from a photon energy fluence directed in the $\theta = 0^\circ$ direction. The point spread kernels have been pre-computed using the EGSnrc simulation package: one simulation per energy level. The kernel is cylindrically symmetric and is therefore stored on a two dimensional polar grid with the radius and the polar angle along the two axes, $PSK(r, \theta, E)$. The kernels are computed in water, when applied to a heterogeneous geometry the radial distance r is exchanged by the radiological distance d.

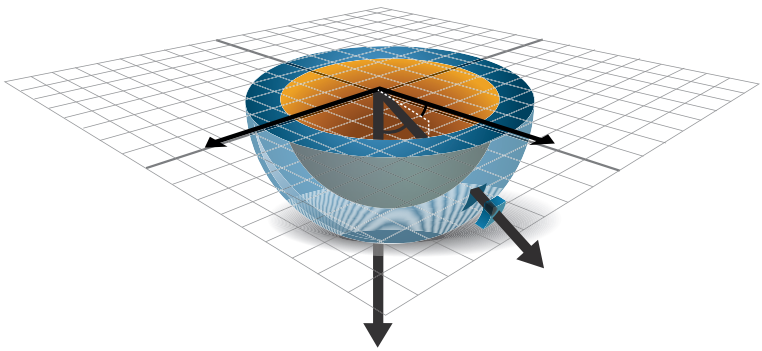

Figure 25. Point spread kernel discretization. The point spread kernel describes the energy distribution in a 3D spherical grid from a primary energy deposit. The figure shows a volume element in the spherical grid defined by its radial, azimuthal and polar interval. The origin of the spherical coordinate system is the interaction point. The photon enters the plot from above.

EGSnrc

The EGSnrc system is a package for the Monte Carlo simulation of coupled electron-photon transport. EGSnrc is developed and maintained by the National Research Council of Canada. EGSnrc is an extended and improved version of the EGS4 package originally developed for high-energy physics simulations at Stanford Linear Accelerator Center [11], [12].

In RayStation 2024A, the photon point spread kernels and the electron pencil kernels were both computed using the EDKnrc user code included with EGSnrc (V4r2-3-1) [16], [23]. When generating the point spread kernels[2], a homogenous sphere with radius 90 cm of the material "H20521ICRU" was used, where the primary photon was forced to interact in the center of the sphere. Only the

2 During development, two minor geometry-related problems were noted in the user codes and changed. The kernels used are generated with these code changes made.

innermost 59.6 cm sphere is stored and used for scoring; it is divided into 1192 radial shells and 200 polar angular cones. The electron transport cut-off energy was set to 521 keV, the photon cut-off energy was set to 10 keV, fractional electron energy loss 10%, exact boundary crossing, PRESTA-II for electron steps, spin effects on, KM Bremsstrahlung angular sampling, simple pair angular sampling, photoelectron angular sampling, Rayleigh scattering and atomic relaxations enabled.

Components in the point spread kernels

The forced first scatter event in the Monte Carlo is most often a Compton scattering giving rise to a lower energy photon and a free electron. As mentioned earlier, the electron has a short range which can be seen as the peak at small radii in the figures below. The fluence of secondary photons decreases exponentially due to attenuation on the way through the patient, this is the long-range part of the point spread kernels. The figures below show that there is some leakage of energy even out through a 59.6 cm water sphere.

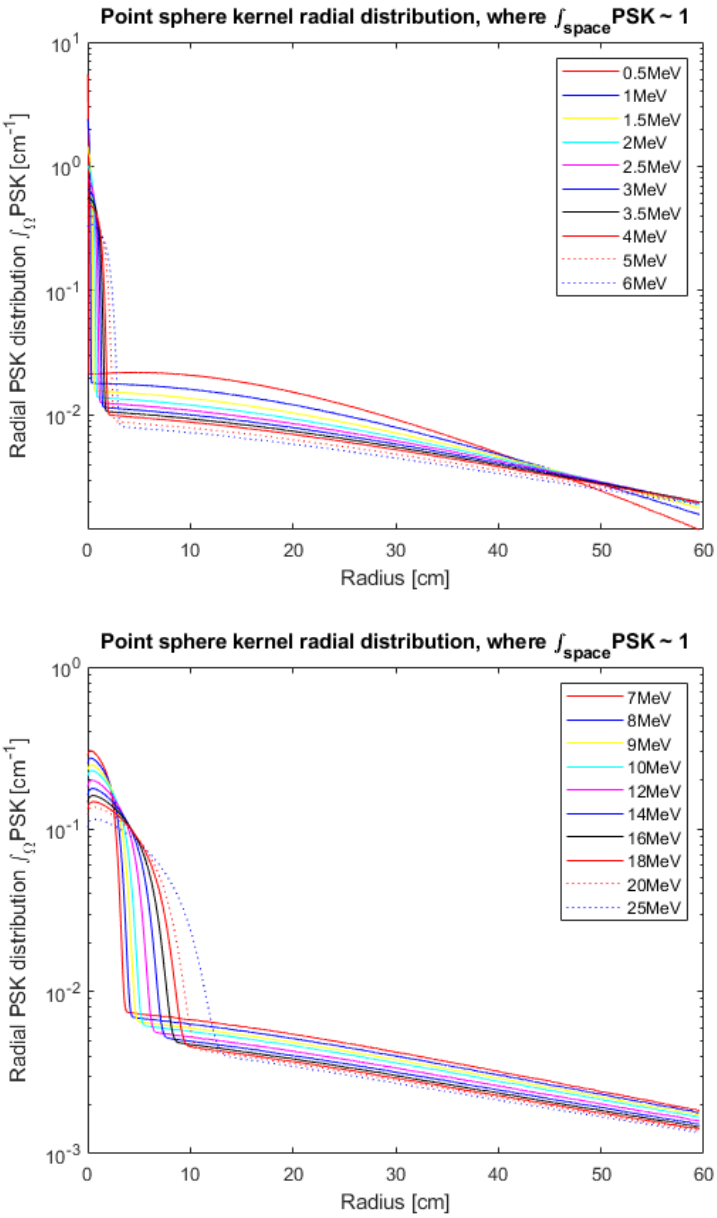

Figure 26. Point sphere kernels, $PSK(r, \theta, E)$, integrated over θ and φ .

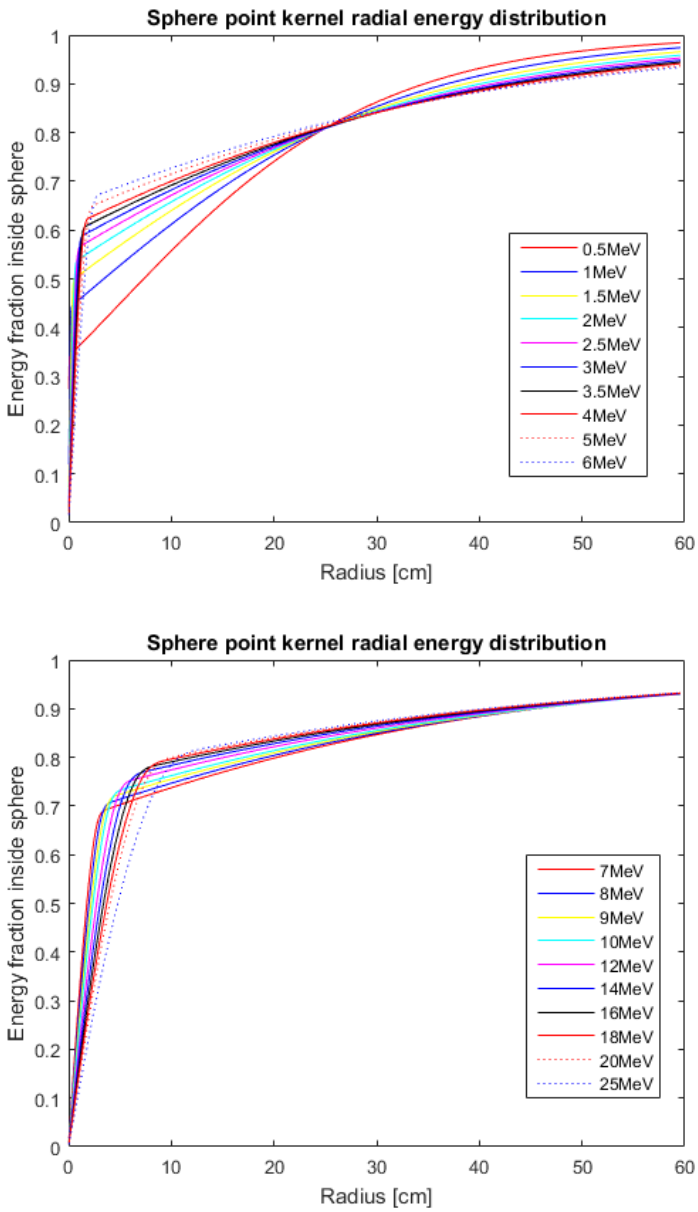

Figure 27. Point sphere kernels, $PSK(r, \theta, E)$, integrated over θ and φ, and accumulated up to each radius. This gives the integrated fractional energy inside a spherical shell around the primary interaction point.

Poly-energetic kernels

The mono-energetic point spread kernels are combined into poly-energetic point spread kernels, weighted so that they correspond to the beam energy distribution at different radiological depths [7], [22] (*section 4.5.3 Energy distribution on page 86*). A range of poly-energetic kernels are computed for 600 different radiological depths (between -100 cm and 200 cm radiological depth relative to patient surface at central-axis). Normally only part of these poly-energetic kernels are used for a given problem. In a cubic phantom with a wizard's hat off-axis softening, one finds the lowest mean energy at the surface at the most softened radius. The highest mean energy is found at the exit surface at isocenter. For geometries with physical wedges the radiological depths are adjusted to account for the wedge as well. In short, the process takes the variations in energy spectrum due to off-axis softening (radial dependence) and depth hardening (depth dependence) into full account [22].

Point spread kernel trace directions

The trace directions are chosen so as to distribute the energy evenly between eight angular intervals in θ, for the isocenter spectrum in air. With 16 perfectly symmetric angular intervals in φ one gets a total of 128 rays, $PSK(r, \theta_i, \varphi_j, d_{TERMA-voxel})$. Since more energy is distributed in the forward direction, the intervals are smallest near the polar angle zero. From momentum conservation low energy point spread kernels have more energy transport towards larger angles and high energy point spread kernels have more energy towards smaller angles. With off-axis softening at large radii there is more energy deposited along the large angle rays at the surface at some distance from the isocenter axis. On the isocenter axis at some depth more energy is deposited along the forward rays.

To achieve adequate dose accuracy for the lowest beam energies, 12 angular intervals are used in θ for energies below 6 MV, resulting in 192 rays in total.

4.5.6 Superposition/convolution

Dose point-of-view point spread kernel tracing

The point spread kernel superposition algorithm uses the dose point-of-view, or receiving point-of-view, which means that for each dose voxel, a ray trace is performed towards a set of different angular directions (*Point spread kernel trace directions on page 94*) to collect the dose contributions from the intersected voxels [18].

When tracing out from the dose voxel, dose contributions are accumulated using point spread kernels for the respective TERMA-voxels.

Each dose contribution is computed as the TERMA multiplied with the point spread kernel energy deposit from voxel entry to voxel exit. The radiological distance between the dose voxel center and the TERMA-voxel entry and exit is used.

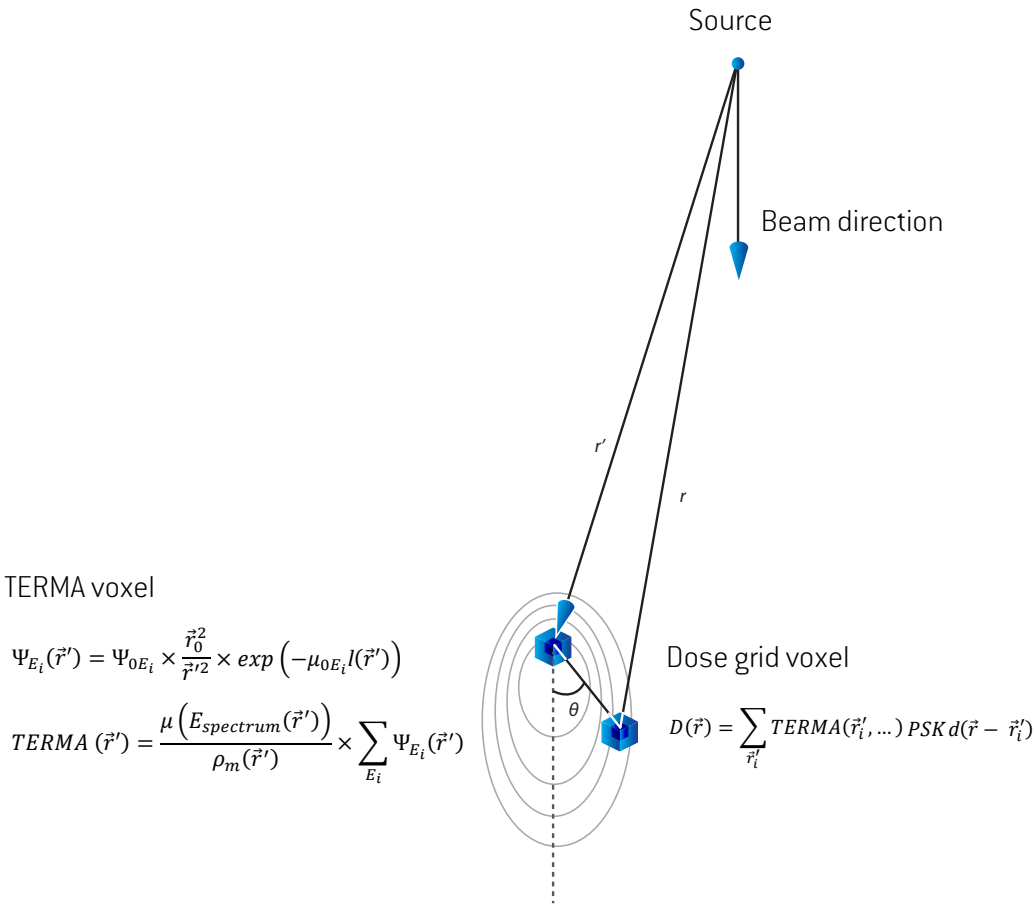

Figure 28. The photon dose is computed as a two-step process: the photon fluence, Ψ, is in the first step used to calculate the TERMA, and in the second step the TERMA is combined with the point spread kernels, to obtain the dose.

Kernel tilt

The angular distribution of secondary photons and electrons from a Compton scattering are directed in the forward direction of the initial photon. In the point spread kernel tracing in RayStation 2024A, all kernels are aligned with the central beam axis, making intersection length re-use possible and saving considerable computation time. This is the well-established no-tilt approximation, or parallel kernel approximation [22], [25]. This approximation is acceptable for most clinical situations, but for larger fields and very small SSDs the no-tilt approximation could lead to dose errors larger than 3% on the central axis (overestimation), off-axis and outside the field edge (underestimation) [20], [22], [25]. Therefore, this is in part corrected by an inverse square law de-scaling of TERMA and rescaling of the dose as proposed in [22], lowering the error.

4.5.7 Dose engine speed-ups

The collapsed cone algorithm, as any algorithm, is sensitive to resolution. The dose engine is designed to balance computational speed with accuracy as outlined below.

Resolution

The dose grid determines the resolution of the dose computation. Too high resolution can lead to memory problems and seriously slow down the dose computation, and too low resolution smears the dose, in particular in regions with high density gradients or high primary fluence gradient. The system allows dose grids with resolution between 1 and 5 mm. The full grid calculation time scales with the inverse grid resolution to the power of four and with the number of point spread kernel rays linearly

$$Calculation\ time \propto (N_x N_y N_z)^{4/3} N_\theta N_\varphi \qquad \text{[Eq. 46]}$$

Here N_x is the number of voxels in the x-direction and similarly for y and z; N_θ is the number of rays in the θ direction and similarly for φ. It is therefore tempting to reduce resolution to increase the computation speed, but a coarser grid than 5 mm is not recommended [3].

Note: *The computed dose is discretized and the dose in the user interface is interpolated.*

Calculation mask

Unnecessary computation is avoided by application of a calculation mask around the TERMA region; when no additional relevant TERMA contribution lies in the trace direction from the dose voxel outwards the ray trace is terminated. This happens when there is no TERMA above 0.5% of the maximum TERMA within 5 cm radiological distance along the ray. For voxels which are farther than 5 cm radiological distance from other voxels with TERMA>0.005 · $TERMA_{max}$, the dose is simply taken as the TERMA. That means that the dose just outside the volume defined by the surface where TERMA>0.005 · $TERMA_{max}$ plus a 5 cm expansion in radiological distance (along all patient coordinate system axes) can be under or overestimated depending on the collimation; a typical 6 MV beam with x-jaw and MLC gives a maximum overestimation of 0.6% of dose maximum, in water. The dose in the region between the surface defined by TERMA>0.005 · $TERMA_{max}$ and the 5 cm radiological expansion is slightly underestimated since here the rays are traced only in some of the 128 directions (192 directions for energies below 6 MV); the underestimation is <0.2% of dose maximum for the same typical 6 MV beam in water.

The calculation mask is determined in a pre-computation step where the TERMA distribution is browsed in the positive x, y, z and the negative x, y, z-directions. The trace directions are divided into eight regions, with increasing or decreasing x, y, and z respectively. The calculation mask is applied such that a ray which has increasing x, y and z is traced from a voxel if it reaches within the next 5 cm radiological distances in positive x, y or z- TERMA>0.005 · $TERMA_{max}$ direction.

The calculation mask is not used for dual layer MLC's, for example Varian Halcyon.

Adaptive dose interpolation

The principle of the adaptive dose interpolation is to first calculate the TERMA using the dose grid, compute the dose only for some voxels and then examine the TERMA and the low resolution dose to identify regions with significant dose gradients. For each voxel it is then determined if the dose value shall be interpolated or not.

The resolution level is identical in all three dimensions and the coarsest possible resolution where interpolation is performed is just below 5.1 mm. If the fine resolution is Δx in x-direction and similarly for y and z, the start distance between dose voxels is determined as:

If...	then...
$\Delta x > 0.26$ cm or $\Delta y > 0.26$ cm or $\Delta z > 0.26$ cm and $\Delta x \leq 0.51$ cm and $\Delta y \leq 0.51$ cm and $\Delta z \leq 0.51$ cm	First dose is computed in every second voxel in each dimension.
$\Delta x \leq 0.26$ cm and $\Delta y \leq 0.26$ cm and $\Delta z \leq 0.26$ cm	First dose is computed in every fourth voxel in each dimension.

For the remaining voxels, the dose is interpolated as the mean over the adjacent computed voxels if:

$$TERMA_{voxel} - \frac{\sum_{adjacentvoxels} TERMA}{numberofadjacentvoxels} \leq 0.2\% \cdot TERMA_{max} \qquad \text{[Eq. 47]}$$

$$Dose_{maxoveradjacentvoxels} - Dose_{minoveradjacentvoxels} \leq$$
$$\leq 5\% Dose_{maxovercomputedvoxelsinthemostcoarseresolution} \qquad \text{[Eq. 48]}$$

If the TERMA variation is high or the dose variation is high, the voxel dose is computed from point spread kernel tracing instead of interpolation. Before this step the beam divergence has been removed from the TERMA as described in *Kernel tilt on page 95*. The voxels which are selected for dose comparison and dose interpolation are two, four or eight depending on the position of the voxel with respect to the already computed voxels. The case when every second voxel in each direction was computed in the first step is depicted below. Starting with every fourth voxel in each dimension the scheme is similar, only that every second voxel in each dimension is simply disregarded in the first interpolation/computation step.

The blue/filled boxes indicate voxels where dose has been computed in the first step from point spread kernel tracing. For white boxes the dose comparison and the possible dose interpolation are made from the two adjacent blue voxels. For the green voxels the dose comparison and the possible dose interpolation are made from the four diagonal voxels in the same plane. For the red voxel the dose comparison and the possible dose interpolation is made from eight diagonal voxels in space.

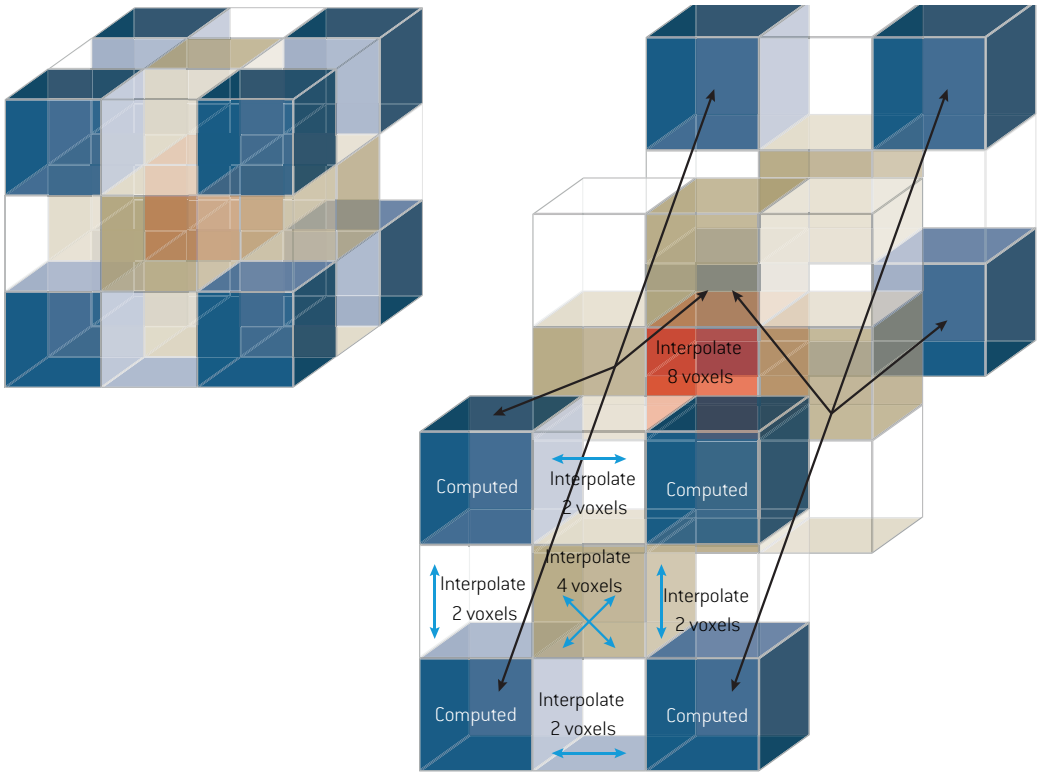

Figure 29. The adaptive dose interpolation.

The TERMA criterion is always (apart from voxel at the edges of the grid) evaluated as for the red box, using the eight adjacent voxels. This is possible at all resolution levels since the TERMA is computed at the finest resolution already from the start.

At the edges of the dose grid, TERMA is averaged over the existing voxels of the eight possible voxels, and the dose maximum and interpolation is obtained from the existing voxels of the two, four or eight voxels.

The rationale behind computing dose at more points where there are large dose gradients is obvious. The TERMA test is designed to identify density gradients and fast fluence variations. With a simple 10 cm x 10 cm, 6 MV beam in water the dose with adaptive interpolation has a correlation with the dose without interpolation which is higher than 0.99999 and a maximum dose error of +/-2% in the beam penumbra.

4.5.8 Modulated arc therapy/VMAT

The dose computation for rotational therapy is separated into segments. An arc segment represents the region between two control points. Depending on the leaf motion within an arc segment, the arc segment may be divided into sub-segments in the fluence calculation. Each sub-segment within an arc segment is equally long. Within each sub-segment the maximum leaf travel is never more than 1.5 cm. All collimator positions are interpolated to the center position of the sub-segment, and the MU of the arc segment is distributed over the sub-segments. To capture the leaf motion the fluence of each sub-segment within an arc segment is calculated and summed to obtain the arc segment fluence. The arc segment fluence is applied at the middle of the arc segment for the dose computation. For each arc segment TERMA is found by tracing the fluence into the patient at the mean gantry angle within the interval. TERMA is accumulated over 10 degree gantry angle intervals. Point spread kernel tracing is performed for each 10 degree section using the middle direction of the accumulated region. This saves computation time at a small cost of accuracy.

Example

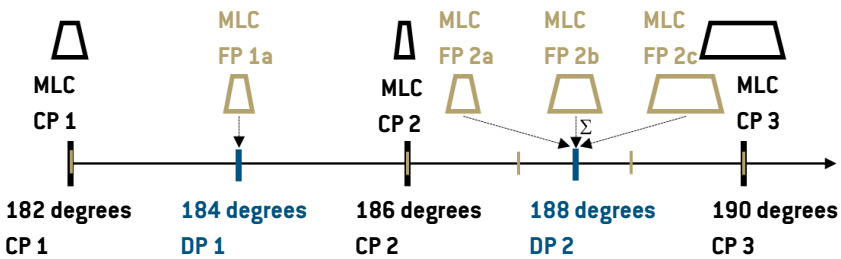

Figure 30. The figure illustrates how the fluence and dose is calculated for an arc beam. The schematic MLC shapes of the first three control points, CP 1, CP 2 and CP 3, (black) of an arc with gantry spacing 4 degrees are shown.

The above figure illustrates how the fluence and dose is calculated for an arc beam. The schematic MLC shapes of the first three control points, CP 1, CP 2 and CP 3, (black) of an arc with gantry spacing 4 degrees are shown.

In the first arc segment between CP 1 and CP 2, the leaf travel for each leaf is less than 1.5 cm and the fluence computation sub-segment is the same as the arc segment (indicated by the golden tick markers). The MLC shape is interpolated to the middle of this sub-segment (FP 1a). The fluence and the CC dose is computed at this angle (DP 1).

In the second arc segment between CP 2 and CP 3, the longest leaf travel is between 3 and 4.5 cm. Three fluence computation sub-segments are created (the regions between the golden tick markers) to obtain a maximum of 1.5 cm leaf travel in each sub-segment. The control point MU is distributed over the sub-segments and the MLC is interpolated to the middle of each sub-segment (FP 2a, FP 2b, FP 2c). A fluence computation is performed for each interpolated MLC shape and summed to the dose computation point (DP 2). The CC dose is based on the summed fluence and computed at the dose computation point (DP 2).

Sliding window VMAT

In RayStation, VMAT plans can be created using sliding window VMAT sequencing, a version of VMAT with alternating leaf motion direction in sub-arc intervals of ~24 degrees.

Dose calculation wise, there is no difference between plans created using sliding window sequencing and ordinary sequencing.

Wave arcs

Wave arcs are one special version of VMAT available in RayStation. During wave arc delivery the couch angle (i.e., ring angle when using a Vero machine) varies during arc delivery. To ensure that sufficient control point spacing is obtained, temporary dose computation control points are added so that the Euclidian norm of the couch and gantry angle does not exceed four degrees (Figure 31). The control points are linearly interpolated from the adjacent control points and equally distributed between them. These temporary control points are used together with the original control points, to obtain a denser control point distribution. The fluence and dose computations are then performed using this new set of control points at the dose computation point in the same way as for a regular VMAT beam (Figure 32). The TERMA is accumulated over 10 degrees of the Euclidian norm of the couch and gantry angles, instead of the gantry angle alone.

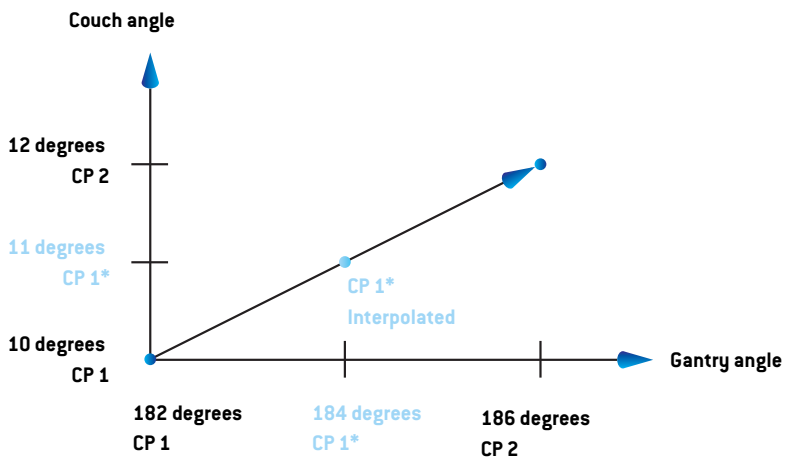

Figure 31. The first control point (CP 1) is at gantry angle 182 degrees and couch angle 10 degrees, the second control (CP 2) is at gantry angle 186 degrees and couch angle 12 degrees. The Euclidean norm of the angle motion in gantry and couch is $(4^2+2^2)^{0.5} = 4.47$ degrees which exceeds 4 degrees spacing. In this case one interpolated control point is enough to achieve at least 4 degrees control point spacing, therefore one temporary interpolated control point (CP1*, light blue) is added in the middle between the two actual control points (black) at gantry angle 184 degrees and couch angle 11 degrees. The MU of CP1 is equally distributed between CP1 and the interpolated control point CP1*. If the couch movement is increased, more interpolated control points are added and equally distributed so that at most 4 degrees spacing is maintained.

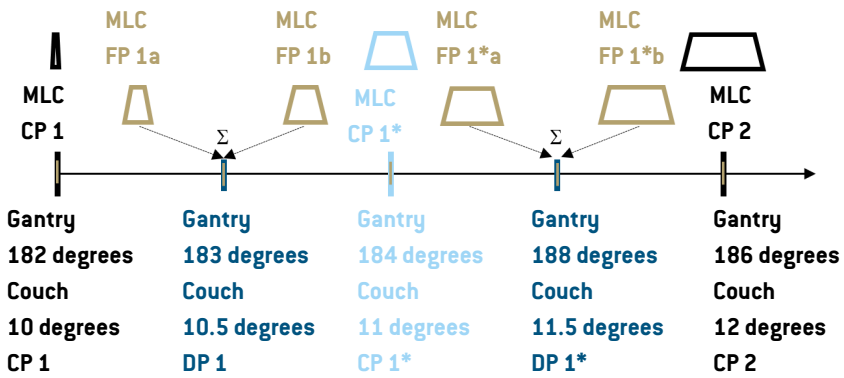

Figure 32. During fluence and dose computation the temporary interpolated control points (CP1*, light blue) are treated as if they were actual control points (CP1 and CP2, black). MLC positions are interpolated (FPs, gold) and summed to ensure at most 1.5 cm leaf travel and dose computation is performed in the middle (DPs, dark blue) between the interpolated and actual control points in the same way as for standard VMAT.

Arc burst mode

Siemens machines are not capable of moving the MLC leaves while the beam is on. For these machines, RayStation has the burst mode option that is another special version of VMAT. The arc burst technique is a rotating step and shoot beam. The gantry rotates continuously, and for every other segment, the beam is on with a fixed MLC opening, and for every other segment the beam is off and the MLC leaves move into position for the next segment shape.

4.5.9 Conformal arc

Conformal arc is a rotational therapy where the arc segments are created using target projections from each gantry angle instead of using intensity modulation. The dose computation in RayStation for Conformal arcs is identical to the dose computation for modulated arcs. For more information, see *section 4.5.8 Modulated arc therapy/VMAT on page 99*.

4.5.10 Static arc

Static arc is a rotational therapy where every segment has an identical aperture. Static arc beams are stored in RayStation with two control points, one start control point and one stop control point. During dose computation, virtual control points are created every second degree gantry angle. Fluence is computed once and the same fluence is assigned to each control point since all segments are identical. TERMA is always computed for each virtual control point for Static arcs. The collapsed cone part of the dose computation for Static arcs is identical to the dose computation for modulated arcs. For more information, see *section 4.5.8 Modulated arc therapy/VMAT on page 99*.

4.5.11 Collapsed arc

In the QA Preparation module in RayStation, it is possible to create verification plans with collapsed arc beams. This option is available for VMAT and Conformal arc plans by selecting to collapse all gantry angles to the same value. During the fluence part of the dose computation, a collapsed arc beam is handled in the same way as a VMAT/Conformal arc beam. During the collapsed cone part of the dose computation, the collapsed arc is handled as a non-rotational, static beam.

4.5.12 DMLC

For DMLC beams, one fluence map is created for the entire beam and then used during the collapsed cone dose computation. RayStation has two different ways of calculating the DMLC fluence map depending on the machine and plan characteristics.

The first fluence computation approach is used when computing DMLC fluence for "sliding window" plans. In RayStation a sliding window type DMLC plan has no jaw motion while the beam is on, and the MLC movement is strictly in one direction. This is the case for Varian style machines (except Varian Halycon), i.e., machines with backup jaw and the jaws positioned closer to the source than the MLC. For sliding window type plans and Varian style machines, the fluence calculation creates an MLC transmission map taking into account how much the different parts of the beam have been exposed or covered by the MLC leaves. The sources are then projected through the MLC transmission map and the jaws.

The other fluence computation is used for Varian Halcyon and Elekta style machines or plans that do not fulfill the sliding window definition. An Elekta style machine is a machine without backup jaw or a machine with backup jaw but with the MLC positioned above both jaws. In this case a static conversion approach is used during fluence computation. The fluence will be computed per control point in the same way as for a static plan, but if any MLC leaf moves more than 3 mm between control points, interpolated control points will be created in-between the original control points. The computed fluence from the different control points, both original and interpolated, will be summed into a beam fluence.

DMLC dose computation is not supported for machines with fixed jaw, except for Varian Halcyon.

4.5.13 TomoHelical

As a standard, the gantry moves 360/51 = 7.06 degrees during a TomoHelical segment. A TomoHelical segment is also called a projection. During fluence computation, each segment is sub-divided into three equally long sub-segments, and fluence is calculated for each sub-segment using jaw positions interpolated as the average between the start and stop jaw positions, assuming that the jaws move linearly between start and stop of the segment. MLC leaf open fractions are calculated for each sub-segment based on the assumption that all leaf open times are centered in the center of the segment. The gantry angle, couch offset and jaw positions listed for a segment in RayStation refer to the start of the segment and all of these properties are assumed to be moving linearly to the end of the segment, which is the same as the start of the next segment.

For a TomoHelical beam, the same gantry angle is repeated in the different helical laps. The dose from a TomoHelical beam is computed as the sum of the doses from groups of segments from different laps that have identical gantry angles. The group dose can be well approximated by a single

collapsed cone superposition convolution of the accumulated TERMA of all segments in the group using the 7.06 degrees segments' middle gantry angle. The point sphere kernels are aligned following divergence from a line source. The TERMA from a segment is computed as the sum of the TERMA of the three sub-segments.

For TomoHelical beams, the dose computation corrects for the lack of kernel-tilt in the algorithm by adjusting the effective beam direction according to the fluence center-of-gravity during the collapsed cone convolution/superposition step. This improves the accuracy of the dose computation for off-axis targets. The inverse square law de-scaling of TERMA and rescaling of dose which is done for other delivery techniques (see *Kernel tilt on page 95*) is not done for TomoHelical dose computation.

4.5.14 TomoDirect

During the fluence computation, each TomoDirect segment, also referred to as a projection, is sub-divided into three equally long sub-segments. Fluence is calculated for each sub-segment using the jaw positions interpolated as the average between the start and stop jaw positions, assuming that the jaws move linearly between start and stop of the segment. MLC leaf open fractions are calculated for each sub-segment based on the assumption that all leaf open times are centered in the segment. The couch movement during a TomoDirect segment is described by the pitch. The gantry angle is fixed within each TomoDirect beam. All TERMA is accumulated and one point sphere kernel tracing is performed per beam, using the divergence from a line source.

For TomoDirect beams, there is no kernel tilt in the sphere point kernel convolution step. Instead each projection is traced using an effective beam direction given by the fluence center-of-gravity of all projections with the same gantry angle. The inverse square law de-scaling of TERMA and rescaling of dose which is done for other delivery techniques (see *Kernel tilt on page 95*) is not done for TomoDirect dose computation.

The difference between the dose computation for a TomoHelical and a TomoDirect beam is that the gantry angles of the TomoHelical sub-segments are interpolated as the average of the start and stop position of the segment, while the gantry angle is kept fixed for all TomoDirect segments. Thus, all segments for a TomoDirect beam can be grouped together, and the TERMA computation only needs to be performed once.

4.5.15 CyberKnife

A CyberKnife segment is defined by an aperture (a circular cone or MLC opening), a node with a source position (x, y, and z coordinates) and three angles (yaw, roll and pitch). For MLC and iris cones, one single beam is used for a CyberKnife treatment plan. For fixed cone plans, one beam is used per cone size. Fluence computation, TERMA computation and point sphere kernel tracing is performed for each segment individually, since the node position and angle directions are specified per segment. Dose from all segments are summed after computation, and dose is reported per beam.

4.5.16 Algorithm weaknesses

The collapsed cone dose computation and the dual source model are designed for accuracy in clinically relevant settings. Pushing the algorithm to its limits – e.g. small source-to-skin distances

(SSD), small or large fields, high energies, off-axis fields, wedges – challenge the accuracy gradually. The clinic should always test the dose computation and beam model for the full clinically interesting range of densities, inhomogeneities, field sizes, field positions and SSDs. In some cases it might be preferable to tune two parameter sets which have high accuracy in different circumstances instead of using one which is a trade-off with slightly lower accuracy.

Below is a list of some approximations and what effect they may have on dose accuracy. The list does not claim to be exhaustive and new research may lead to future revisions.

Resolution

Resolution artifacts can most readily be seen in test fields where one can see details when measuring with film or EPID, which are not fullly resolved in dose computation. For example, the depth of a dose valley in a tongue-and-groove style test or the dose dip between two abutting segments. For IMRT/VMAT style fields such detail is often relatively smeared over the field, and it is the overall increase or decrease from an MLC detail that is more important than the shape. The primary fluence resolution is 1 mm, see *Fluence plane on page 61*, and the dose grid cannot be set smaller than 1 mm.

Collapsed cone with endless water point sphere kernels

The collapsed cone dose computation traces TERMA into dose using point sphere kernels. The kernels were computed in a large homogenous water volume where the first interaction was forced at the center and then all secondary interactions were allowed to occur according to their statistical probability including scattering between voxels in all directions. This means that scattering between rays is computed in an almost endless water geometry. The point sphere kernels are handled as though the dose spread along one kernel direction is independent of the geometry in the other directions. This assumption is only true in situations where there is electron equilibrium. Examples where there is no electron equilibrium are lung, bone and air interfaces [21]. The build up region is a specific such region where the point sphere kernels include scatter from the water that was above the interaction point in the endless water simulation and which is now not there. This leads to the collapsed cone dose computation giving an increased surface dose compared to a Monte Carlo dose computation with the same beam model.

Moreover, point spread kernels are traced using the effective density of the heterogeneous patient. This is a good approximation for the long-range photon part of the kernel which interacts through Compton scattering. The short-range electron propagation is better described using stopping powers and this approximation can lead to errors again in areas where there is a lack of electron equilibrium and the stopping power ratio with respect to water differs from the effective density ratio with respect to water. Examples of affected areas are interfaces between different materials, in particular the lung interface in tangential treatment and tissue adjacent to bone [21]. Surface dose is also affected and, to a lesser extent, field edges.

SSD variation

There are a number of approximations in both the fluence and in the Collapsed Cone dose computation that may reduce accuracy when going towards small SSDs.

Scattered photons are known to be created at several places in the LINAC head. The scatter component has a larger opening angle than the primary photon fluence. At some distance from the LINAC head,

the complex phase space can be relatively well approximated as coming from one single diffuse flattening filter source. However, closer to the LINAC head, the scatter component has a larger relative importance and more detail may be required. The same is true for the electron contamination component.

The position of the sources are used when creating the fluence map at isocenter; however, when tracing into TERMA all photons are transported along rays coming from the primary source. The approximation influences the beam model parameters and some SSD extrapolation uncertainty is introduced.

The point sphere kernel tracing is performed without tilting the kernels, but instead with a phenomenological rescaling procedure. This again influences beam model parameters and leads to extrapolation uncertainties.

For this reason, beam models are often created using a setup which best mimics treatment, with isocenter at depth 10 cm. Most conventional LINACs have SAD = 100 cm, and the dose computation is therefore best tested at source-to-skin distances of 75-95 cm and less tested at <70 cm and >100 cm.

Arc approximations

There are also a number of arc approximations influencing accuracy, one being the discretization into arc segments (intervals between control points).

In dose calculations for VMAT, conformal arc, static arc and TomoHelical plans, any surface dose errors due to control point discretization and TERMA accumulation between control points can be expected to be emphazised at the surface and become more pronounced at small SSDs.

WARNING!

Arc gantry angle spacing for rotational plans for small, off-axis targets. The arc gantry spacing determines the number of directions used during dose computation for rotational plans. Dose overestimation around 3.5% has been found for some plans with a small target that is off-axis with respect to the in-plane direction for arc beams, when using 4 degrees gantry spacing compared to using 2 degrees. The same effect is not seen for small central targets. Use a gantry angle spacing of 2 degrees when creating such arc plans.

(723988)

Build-up region

The build-up region is an inherently difficult region, both for measurement and modeling. A small depth error, or effective point of measurement shift error, for a PDD curve used in commissioning can change the electron beam model parameters, increasing or decreasing dose to the same level as the build-up gradient (which can be 20%/mm).

A RayStation beam model generally contains two diffuse electron sources that give increasing surface dose to larger fields. However, it does not show the full complexity of SSD variation, variation with how much exposed MLC there is, or if there are blocks or wedges.

Off-axis fields

At least two approximations influence off-axis doses. The no-tilt approximation in the point spread kernel tracing from TERMA to dose influences the beam profile correction which becomes higher at larger radii for collapsed cone beam models than for Monte Carlo models. While this is necessary for dose accuracy for large fields when computing dose with the collapsed cone algorithm, it could lead to dose overestimation for smaller off-axis fields. Another approximation is how the scatter component is given a fixed position along the z-axis and a width instead of the complex phase space of linac head scatter. A dose contribution from a flattening filter source which is lower than the primary source will be shifted relative to the primary source contribution due to its different z position. Be aware of this behavior when creating and evaluating the beam model.

For flattening filter free beam qualities there is often a rather large variation in the beam profile correction, this is used only for the primary source. Therefore off-axis fields will be composed by one primary source component that follows the beam profiles correction shape and a flattening filter component that is shifted and relatively higher off-axis than on-axis. Be aware of this behavior when creating and evaluating the beam model.

Collimator gain and curvature can also give unexpectedly large dose increase, or shift at off-axis position. For all these reasons, it is mandatory to include off-axis information when creating a beam model that will be used for multi-target or off-axis treatments.

Elongated fields

Both elongated and off-axis fields challenge the flat-collimator and the output factor correction assumptions and the user should test the applicability of the beam model with a mix of field shapes and positions which are clinically applicable.

Low density regions

Large regions with low density become very sensitive to radiation range, for example 1 mm range difference in water translates to almost 1 m in air. Air dose is seldom important for clinical applications but lung dose is. Low density regions are also almost by definition electron disequilibrium regions and for some cases (such as lung tumor) tumor coverage and lung dose may differ between collapsed cone and Monte Carlo.

Inside bone regions

The dose in bone regions differs between dose reporting conventions as described in *section 4.7 Dose-to-water, dose-to-medium, or dose-to-tissue on page 119*. The Collapsed Cone D_w^w is in-between D_m^m and D_m^w. For treatments where the dose can approach critical levels for bone, it is important to adapt the clinical goals to the dose convention in RayStation.

Out of field dose

There are several factors which limit the dose accuracy outside the field penumbra:

- The lack of kernel tilt leads to underestimation of the out-of-field dose, as described in *section 4.5.5 Point spread kernels on page 90*.
- The calculation mask (described in *section 4.5.7 Dose engine speed-ups on page 96*) cuts the computation region to where the TERMA is 0.5% of maximum. No point spread kernel tracing is performed in directions outside of this region and 5 cm further out the dose is replaced by the TERMA (radiological distance).
- The head scatter component and leakage is tuned to give good dose computation in and around the target and may have errors out-of-field. There is no y-jaw transmission (x-jaw for LINACs with MLC in the y-direction).
- There is also no neutron dose in the photon dose computation. Neutron dose may give a non-negligible contribution to out-of-field dose for beam qualities above 10 MV.

Point sphere kernel trace direction artefacts

The collapsed cone point sphere kernel tracing is done in sixteen directions in ϕ and eight (>4 MV) or twelve (4 MV) directions in θ (see section *Point spread kernel trace directions on page 94*). This number has been selected as a sweet spot that gives fast dose computation without sacrificing accuracy. However, the discretization still leads to low level artefacts. This section describes what this is for the interested reader.

For a square field, the discretization in ϕ (lateral directions) gives rise to a star pattern that can be seen in the low dose region outside the beam edges in the plane perpendicular to the beam, if the color scale is set to low percent levels (see Figure 33). The edges of the high TERMA region leads to edges in the dose distribution when traced in the sixteen different ϕ directions.

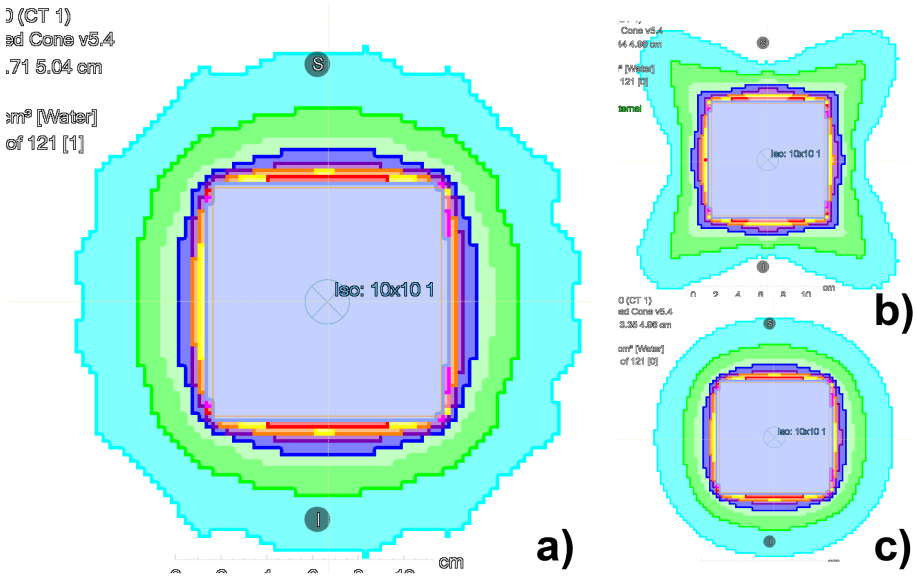

Figure 33. Low dose cloud outside a 10x10 cm^2 field in the isocenter plane perpendicular to the beam direction. The color table ranges from 0 to 10% of D_{max} meaning that the green corresponds to 2% of D_{max}. a) Clinical version with sixteen ϕ directions. b) Non-clinical example with four ϕ directions. c) Non-clinical example with 64 ϕ directions.

The discretization in θ (forward/backward) gives rise to artefacts for large field PDDs echoing the field edge position at the surface. The artefact appears just beyond D_{max} for 40x40 cm^2 fields, at D_{max} for 30x30 cm^2 fields and closer to the surface for smaller fields (see Figure 34).

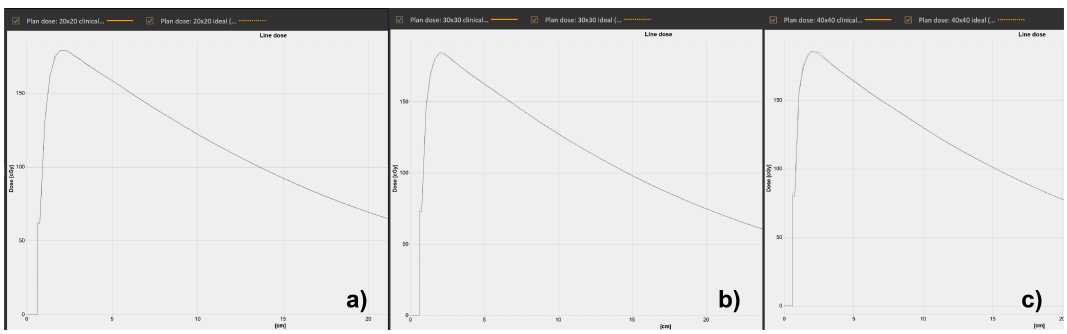

Figure 34. Depth doses for square fields computed with the clinical number of trace directions and an ideal (and slow) CC version with 64 ϕ and 32 θ directions which should be seen as an artefact free dose version in this example. a) 20x20 cm^2, small differences before D_{max}, b) 30x30 cm^2 field, dose overestimation at D_{max}, c) 40x40 cm^2 field, an overestimation just beyond D_{max}.

Physically wedged fields

The wedge fluence computation involves a transmitted component which scales the open fluence along the line of sight from source to fluence pixel in a relatively straight-forward way. The wedge also creates a wedge fluence component which is described in *section 4.9 Wedges on page 129*. The behavior of the wedge scatter component for off-axis fields may not be as expected intuitively.

Therefore, it is important to validate the commissioned wedge model for all type of fields that will be used clinically, in particular off-axis fields in all directions in the jaw coordinate system. It may be that it is preferable to adjust the planning such that the isocenter is central in the field, rather than using off-axis wedged fields.

Output for fields with retracted jaws

The field measure used to select output factor corrections during fluence computation is calculated from the jaw opening for machines where the jaws are closest to the source, for example Varian LINACs (for more information, see *Output factor corrections – used in energy fluence computations on page 70* and *Field measure on page 70*). For standard treatment plans, including modulated IMRT and VMAT plans, the jaws are positioned conformed around the MLC. If the jaws are retracted far from the MLC opening, using the jaw opening to calculate the field measure may not be a good approximation. Therefore, the output of the computed dose may not be correct for fields were the jaws are retracted far from the MLC opening for a machine where the jaws are closest to the source. The effect is however small for standard treatment plans, where the jaws are positioned conformed around the MLC.

Off-axis fields for TomoTherapy

The TomoTherapy dose calculation computes dose without tilting the point sphere kernels and without the kernel tilt corrections described in *section 4.5.6 Superposition/convolution on page 94*.

Commissioning is performed using a wide central beam, where the superposition of un-tilted kernels leads to dose overestimation at the center and dose underestimation at larger radii. This is adjusted for by scaling with the transverse profile.

For a single small off-axis field, the kernels are not individually tilted, but follow the direction of the fluence center-of-gravity of the small field. This may give a good dose shape, but depending on the transverse profile, this can lead to dose overestimation.

For a field consisting of off-axis openings which are separated in the x-direction (IEC beam collimator system) the direction of the fluence center-of-gravity differs from the average beam direction in each opening. This may influence both the output and the shape of the dose distribution.

Ensure that dose accuracy is tested for all clinically relevant fields.

TomoTherapy plans with short leaf open times and short leaf close times

For TomoHelical and TomoDirect plans with a large number of short leaf open times and short leaf close times, the delivered dose may differ significantly from the computed dose [121] [123]. The reason is that for fast leaf movements, the treatment machine will not open/close the leaves in accordance with the model used in the dose computation.

The TomoTherapy optimization algorithm was updated to avoid a large number of leaf openings with the exact same leaf open time to make the dose more robust to local deviations of delivered versus requested leaf open times.

No inclusion of TomoTherapy MLC leakage

MLC leakage is neglected in the TomoTherapy beam model in RayStation, which is the same as how it is generally handled in the Accuray model. This may lead to dose underestimation for plans where the target is covered by the MLC during a large fraction of the time. For MLC leakage of ~0.5% [122] and average opening times of 10% above the target, the dose underestimation could be of the order of 4.5%.

4.6 MONTE CARLO DOSE COMPUTATION

This chapter describes the main features of the Monte Carlo dose engine for photons and its implementation in RayStation. An overview of the applied algorithms is provided with references to forward sections that give further details on each topic.

In this section

This section contains the following sub-sections:

4.6.1	Overview	p. 112
4.6.2	Dose to medium	p. 112
4.6.3	Sampling of particles from fluence	p. 112
4.6.4	Photon transport	p. 112
4.6.5	Electron transport	p. 113
4.6.6	Discrete interactions	p. 114
4.6.7	Condensed history	p. 114
4.6.8	Statistical uncertainty	p. 116
4.6.9	Post-processing	p. 117
4.6.10	Algorithm weaknesses	p. 117

4.6.1 Overview

The Monte Carlo (MC) dose engine uses the same fluence computation as the Collapsed Cone (CC) dose engine. This means that the MC dose engine can be used in the same way as the CC dose engine.

The MC dose engine is developed by RaySearch for use in RayStation and makes no use of any external software packages. The algorithms and implementation are specialized to meet the accuracy requirements of radiotherapy dose calculation for treatment planning. The design goal is to realize an implementation that is optimized for speed while carefully maintaining a sufficiently faithful modeling of the relevant physics processes.

The differences between the CC and the MC dose engine are large enough that it is not possible to use the same beam model parameter values for both dose algorithms, even though they use the same fluence algorithm and implementation. The beam measurement data needed for commissioning the MC dose engine are however the same as is needed for the CC dose engine.

The Monte Carlo code is a Class II algorithm (condensed history) and transports photons, electrons and positrons. For photons, Compton scattering, photoelectric absorption and pair creation events are simulated. For electrons and positrons, Møller scattering, bremsstrahlung and positron annihilation are simulated as discrete events and multiple scattering using the random hinge condensed history method.

4.6.2 Dose to medium

Unlike the other RayStation dose algorithms, the photon MC dose algorithm computes dose to medium with radiation transport in medium, D_m^m. The difference to the dose to water calculated by CC will be small for tissues other than bone and air. Differences may be larger inside phantom or implant materials. See discussion in *section 4.7 Dose-to-water, dose-to-medium, or dose-to-tissue on page 119*.

4.6.3 Sampling of particles from fluence

Fluence is computed as described in *section 4.3 Fluence computation – CyberKnife and C-arm LINACs on page 60* and *section 4.4 Fluence computation - TomoTherapy LINACs on page 76*. The fluence distributions are then converted into tables that can be sampled from by the MC algorithm. The fluence is assumed to be constant over each pixel. A pixel is sampled from the fluence distribution, and then the particle position is sampled uniformly inside this pixel. The energy is sampled from the local spectrum in the pixel, taking off axis softening and wedge thickness into account. As in the TERMA computation (*section 4.5.4 TERMA computation on page 87*) in the CC dose engine, all photons and electrons are given an initial direction pointing from the primary source towards the fluence position.

4.6.4 Photon transport

Photons transfer energy to the medium via three processes: photo-electric absorption dominates for low energies, Compton scattering for medium energies and pair creation for high energies. In addition, they can undergo Rayleigh scattering which change the direction of the photon. For

radiotherapy energies, Compton scattering is the dominant process. Rayleigh scattering is not modelled in the MC dose computation since it has a negligible effect at these energies.

Total energy differential cross sections for the elements are taken from the NIST XCOM database [124] . These are combined into the RayStation core and interpolated materials, and interpolated in energy, according to the NIST XCOM instructions.

Primary photons are transported from the sampled fluence positions to the edge of the dose grid. From there the distance to the next interaction is sampled and the photon is transported there. To avoid traversing each voxel, the fictitious cross section method is used (also known as Woodcock tracking) [143] . The idea is that by setting the total cross section to the same in the entire patient, there is no need to step through each voxel. At the site of the interaction, it is rejected with a probability that depends on the local cross section. In order for this approach to work, the global cross section must be greater than or equal to the greatest cross section in the patient. There is no loss of accuracy by using this method.

Compton scattering

The target electrons are treated as free electrons, i.e. binding effects are ignored. The differential cross section is then given by the Klein-Nishina formula (Equation 2.2.1 and 2.2.2 in the egs manual [11]). The total Compton scattering cross sections are obtained by integration of the Klein-Nishina differential cross section.

Photo-electric absorption

Photo-electric absorption is modelled by killing the initial state photon and creating an electron with a kinetic energy equal to the photon energy, if the energy is above the electron production cutoff. If the energy is lower, it is deposited locally. The direction of the electron is then sampled from the Sauter distribution (Equation 2.3.8 in the egs manual [11]).

Pair creation

Pair creation is the conversion of a photon into an electron-positron pair in the presence of a nucleus or electron. The total cross section for pair creation is taken as the sum of the pair creation in the nuclear field and in the electron field. Triplet production is ignored. In the MC dose computation, the available energy is distributed randomly between the electron and the positron. The angles are then sampled from the leading order term of the angular distribution (see chapter 2.2.1.v and Equation 2.1.18 in the egs manual [11]).

4.6.5 Electron transport

When an electron moves through a medium it undergoes a large number of interactions. Most of these make only a very small difference in direction and/or energy, but some involve large energy losses and changes of direction. In the MC dose computation, the latter are handled in discrete interactions, and the former in so called condensed history steps where the cumulative effect of many interactions are taken into account.

Positrons are transported as electrons in the MC dose computation, with the exception that they can annihilate with another electron.

4.6.6 Discrete interactions

Møller scattering

Electron-electron scattering is defined by the Møller cross section (Equation 2.15 in ICRU 37 [30]) when binding effects are ignored. By only handling interactions where there is an energy loss larger than some threshold energy, the approximation of ignoring binding effects is good, given that the threshold is larger than the binding energies. The threshold is set to 250 keV, which is significantly higher than the binding energies (which are of the order of a couple of keV for Tungsten). At the same time an electron with this energy only has a range in water of ~0.6mm. The sampling of energies and directions follows the method described in chapter 2.4.3.i in the egs manual [11] .

Bremsstrahlung

The total bremsstrahlung cross section is computed as the default bremsstrahlung cross section in chapter 2.4.2.i in the egs manual [11] . The cross section is then scaled by a constant in order to reproduce the radiative stopping power from NIST ESTAR [4] for each material. The sampling of photon energies follows the method described in chapter 2.4.2.ii in the egs manual [11] . As an approximation the direction of the photon in radians is given by:

$$\theta = \frac{m_e}{m_e + T} \qquad \text{[Eq. 49]}$$

where m_e is the electron mass and T is the kinetic energy of the electron. The initial electron only lose energy and does not change direction.

Positron annihilation

The handling of positron annihilation follows the method described in chapter 2.4.5 in the egs manual [11] . A positron can either annihilate in-flight or at rest. The annihilation cross section goes to infinity as T → 0. To remedy this, the cross section is capped to the value at 400keV.

4.6.7 Condensed history

We apply the so-called random hinge method pioneered in MC codes for electron/positron transport see [111] and [54] . A random hinge consists of two straight legs connected by a hinge point where a deflection due to multiple scattering is applied (see Figure 35). A sequence of random hinges, where each hinge leg may extend over multiple voxels, is applied until the electron energy reaches a predefined low energy threshold. The deflection angle is sampled from a probability distribution given by the Goudsmit-Saunderson theory (see *Multiple scattering on page 116*).

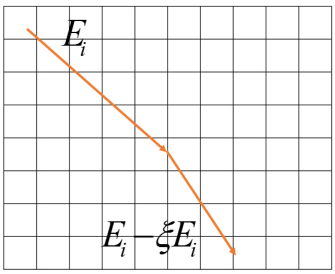

Figure 35. A random hinge step with two legs for an electron with energy E_i at the beginning of the step and losing energy $\Delta E = \xi E_i$ after the step. The deflection due to multiple scattering is applied at the hinge point.

The length of the random hinge (in energy) is the smallest of the following:

- Distance to the next discrete interaction
- 15% of the kinetic energy
- 500keV

Below the electron production threshold of 250 keV, electrons are transported without multiple scattering. At this energy the residual range is ~0.6mm in water.

Collision stopping power and energy loss

The stopping power calculation is the one described in Equation 2.16 in ICRU 37 [30].

$$S_{col} = 2\pi r_e^2 \rho_e mc^2 \frac{1}{\beta^2} \left[\ln(T/I)^2 + \ln(1+\tau/2) + F^-(\tau) - \delta\right] \qquad \text{[Eq. 50]}$$

where

$$F^-(\tau) = (1-\beta^2)[1 + \tau^2/8 - (2\tau+1)\ln 2] \qquad \text{[Eq. 51]}$$

ρ is the mass density, ρ_e the electron density, r_e the classical electron radius, T the kinetic energy and τ the kinetic energy in terms of electron masses (T/m_e).

The density correction term, δ, is computed for all materials as in [125]. In this calculation the default density of the material is used, and all materials are treated as compounds.

One part of the collision stopping power, with energy transfers larger than the threshold, is accounted for in the Møller scattering. The remaining part is the so-called restricted stopping power, L.

The energy loss over a voxel is calculated by integrating the restricted stopping power in the local density and medium. The integration is approximated as:

$$\Delta E \approx \frac{s\left(L\left(E_0\right)+L\left(E_0-sL\left(E_0\right)\right)\right)}{2} \qquad \text{[Eq. 52]}$$

where s is the geometric distance, L the restricted stopping power and E_0 the initial energy of the electron.

Multiple scattering

The angular deflection due to multiple scattering is sampled from an angle probability distribution which is calculated with the Goudsmit-Saunderson theory [104], [105]. The Goudsmit-Saunderson formalism is, with respect to the underlying elastic scattering cross section used, an "exact" theory for any angle multiple scattering without small angle approximations. The Goudsmit-Saunderson theory was originally derived for electron multiple scattering assuming motion in a homogenous medium while neglecting energy loss.

We use the screened Rutherford cross section following the work by Kawrakow and Bielajew in [106] and later refined by Kawrakow in [107]. In each medium we compute two medium composition dependent parameters b_c and X_{cc} of [54]. The multiple scattering angle is sampled for the actual energy of the electron at the local medium of the voxel containing the hinge point. The sampling uses a pre-computed "q2-surface" similarly to how it is described in [107].

4.6.8 Statistical uncertainty

The statistical error of the dose distribution is estimated using an online algorithm with batches as described by Kawrakow and Fippel [151].

First the standard deviation of a voxel ΔD_{ijk} is computed as

$$\Delta D_{ijk}^2 = \frac{(Average(D_{ijk}^2)-Average(D_{ijk})^2)}{(N_{batch}-1)} \qquad \text{[Eq. 53]}$$

Then the overall uncertainty for the whole geometry and all beams in the treatment setup is computed as

$$Overall\ uncertainty = \frac{1}{N_{voxels}} \sum\nolimits_{voxels} \frac{\Delta D_{ijk}}{D_{max}} \qquad \text{[Eq. 54]}$$

where the sum runs over all voxels having a dose above 50% of the maximum treatment setup dose, D_{max}.

If the value exceeds the selected upper uncertainty entered by the user, the algorithm adds more batches. This means that the estimated voxel variance will become both lower and more and more accurate with increased computation time.

The MC calculated dose will be considered clinical if the statistical error is smaller than a user-defined threshold. Otherwise, the dose will be considered approximate. The uncertainty is always computed

for the summed dose over all beams and becomes invalid if there is MU-rescaling or similar. In such cases the dose is relabeled as approximate.

The voxels with dose lower than 50% of D_{max} will not be used to estimate uncertainty. In general, the dose variation in low dose regions is small in absolute measures but larger relative to the low local dose. Uncertainty is also larger in low density regions than in high density regions since the dose is mediated by fewer interactions.

The RayStation Monte Carlo dose computations are deterministic in the sense that the same random number sequence is always used.

4.6.9 Post-processing

When computing dose curves in the beam commissioning module in RayPhysics, an optional post-processing of the Monte Carlo computed dose can be performed to reduce fluctuations in the dose distribution. Post-processing is performed using the adaptive Savitzky-Golay filter algorithm [140] . The size of the filter window is adapted for each voxel, and the algorithm generally gives a good reduction of statistical noise in regions where the dose distribution is homogenous, while preserving steep gradients in other parts of the distribution.

Post-processing can be used to reduce computation time while initially adjusting beam model parameters, as a higher statistical uncertainty threshold can then be used. It is not used in other dose calculations, and curves used to commission a beam model must be computed without post-processing.

4.6.10 Algorithm weaknesses

Since the MC dose engine shares the same fluence calculation as the CC dose engine, many of the fluence related weaknesses also apply to the MC.

SSD variation

See *SSD variation on page 104*. The same holds for the MC dose engine, except the parts about the no-tilt approximation.

Build-up region

See *Build-up region on page 105*. The CC dose engine kernels are simulated with forced interactions at the center of a 90 cm large sphere, which leads to dose overestimation at the surface. This error is not present for Monte Carlo computations. Taking away the approximation does not necessarily lead to better dose agreement in this region, since this error can for the CC dose engine to some extent compensate that the photon fluence starts at 0.5 MeV.

Off-axis fields

See *Off-axis fields on page 106*. The no-kernel tilt approximation in CC is expected to influence the beam profile corrections needed for a good beam model in particular for large fields. The MC does not have the no-kernel tilt approximation. The kernel tilt and the different beam profile corrections are expected to lead to different dose distributions for off-axis fields.

Arc approximations

See *Arc approximations on page 105*. The limitations in control point spacing apply equally for Monte Carlo as for collapsed cone.

Elongated fields

See *Elongated fields on page 106*.

Low density regions

See *Low density regions on page 106*.

Inside bone regions

See *Inside bone regions on page 106*. Note that the MC computes D_m^m and not D_w^w like the CC dose engine. It is important to be aware of the differences and make sure that the clinical goals are adapted.

Out of field dose

See *Out of field dose on page 106*. The comments about head scatter and neutron dose holds for the MC as well as the CC dose engine. However, the no-tilt approximation and the calculation mask only affect the CC dose engine.

Physically wedged fields

See *Physically wedged fields on page 109*.

Output for fields with retracted jaws

See *Output for fields with retracted jaws on page 109*.

Patient material data

Even though this is a Monte Carlo dose algorithm, the accuracy of the dose computation is limited to the accuracy of the assigned densities and materials in the patient. Extra care should be taken for dose computation on MR and Cone Beam CT images where there are larger material uncertainties.

4.7 DOSE-TO-WATER, DOSE-TO-MEDIUM, OR DOSE-TO-TISSUE

In the RayStation collapsed cone dose engine, radiation transport is performed in a patient which is modelled as water with different effective density (dose-to-different density water). The effective density is close to the electron density, with a small energy-dependent correction that is introduced in order to give the best computation of TERMA. This type of dose is denoted D_w^w, i.e., dose to water with radiation transport in water or dose-to-different-density-water.

Monte Carlo methods more naturally lead to D_m^m, dose-to-medium with radiation transport in the medium. The concept dose-to-water for this case is defined as the dose that would be deposited in a specific point if an infinitesimal volume of the tissue is replaced with an infinitesimal volume of water. This would give D_w^m, dose to water with radiation transport in medium. This version of dose-to-water, D_w^m, can be obtained from D_m^m by a multiplication with the ratio of restricted mass collision stopping power of electrons, as recommended by AAPM TG-105 [117].

There has been debate about which dose convention that is desirable for the future [117]. The AAPM TG-105 recommendation for Monte Carlo dose engines is to explicitly indicate the material to which the dose is computed and allow conversion between dose-to-water and dose-to-medium as a user choice [117]. The American organization NRG-IROC recommends D_m^m [115] and this is currently the only option for the RayStation photon Monte Carlo.

It is not obvious how different algorithms and implementations compare in different materials. Ma and Li [113] performed Monte Carlo computations with different-density-water and compared the dose to that from the computations with the actual materials. The simulation geometry in one of their simulations was a layered phantom with 9 cm water, 2 cm compact bone (or water with the same electron density) and 9 cm water. The field was 20 cm x 20 cm, the beam energy 6 MV and SSD = 100 cm. They concluded that for bone, the dose-to-different-density water D_w^w was in-between dose-to-medium D_m^m and dose-to-water D_w^m, but, contrary to what was thought at the time, closer to dose-to-medium D_m^m than to dose-to-water D_w^m. This setup has been recreated in RayStation and dose computed using the RayStation collapsed cone dose engine giving D_w^w, the clinical RayStation photon Monte Carlo dose engine giving D_m^m and a non-clinical version of the same dose engine giving D_w^m using conversion with restricted stopping power ratios. The non-clinical version is not released in RayStation 2024A. Figure 36 shows the depth dose for the case with Bone 1; the statistical uncertainty was 0.5%, the voxel size 2.5 mm and doses are sliding averages over three voxels in the cross-plane and in-plane direction. In Figure 37, the average dose was extracted from a 9 mm cube at depth 10 cm for the different RayStation materials. The base materials, which are used for computations on CT-data, are listed in *section 2.3 CT mapping on page 21*, and the interpolation strategy is described. Note that Figure 37 includes Soft tissue, which is not one of the RayStation base materials.

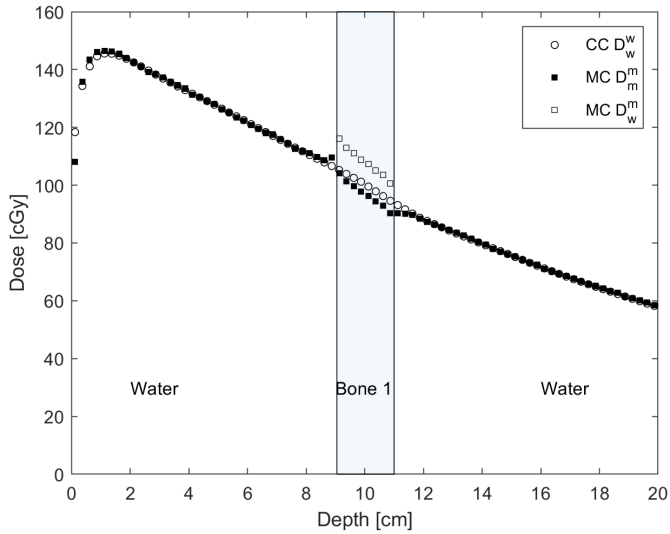

Figure 36. Depth dose through a 2 cm bone slab at depth 10 cm in water, computed using the RayStation collapsed cone dose engine giving D_w^w, the clinical RayStation photon Monte Carlo dose engine giving D_m^m and a non-clinical (non-released) version of the same dose engine giving D_w^m. SSD was 100 cm, field size 20 cm x 20 cm and beam quality 6 MV.

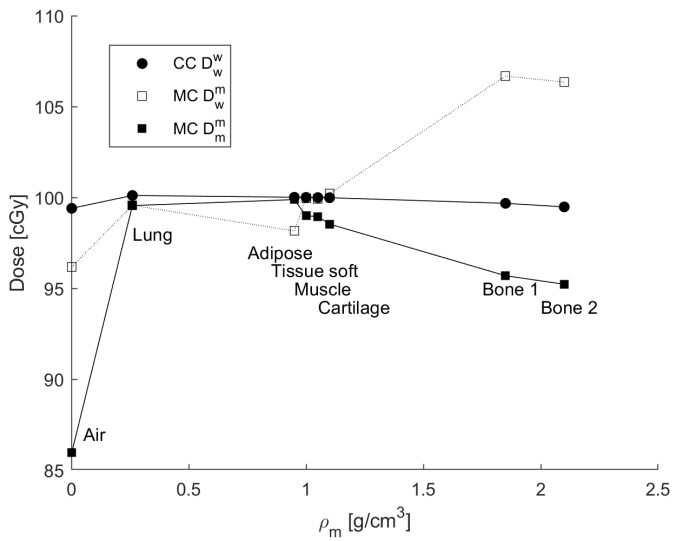

Figure 37. Dose at the center of a 2 cm material slab inside water at depth 10 cm, SSD = 100 cm, field size 20 cm x 20 cm and beam quality 6 MV.

The AAPM TG-329 report [115] recommends using dose-to-tissue for cases where dose-to-medium is not available and lists the dose convention for different commercial algorithms and implementations. The report shows the difference in depth doses obtained for a 10 cm x 10 cm field computed in tissue and different density water; the SSD was 95 cm. The setup has been recreated in RayStation using 6 MV and 10 MV for soft tissue, muscle and the interpolated material obtained for $\rho_m = 1g/cm^3$ for computations on CT-data. Dose was extracted in a region at depth 5 cm. The scaling factor from collapsed cone D_w^w to Monte Carlo D_m^m was for no case further than 0.2% from 0.99, consistent with the results reported by AAPM TG-329. The depth dose curve for soft tissue and 6 MV is shown in Figure 38.

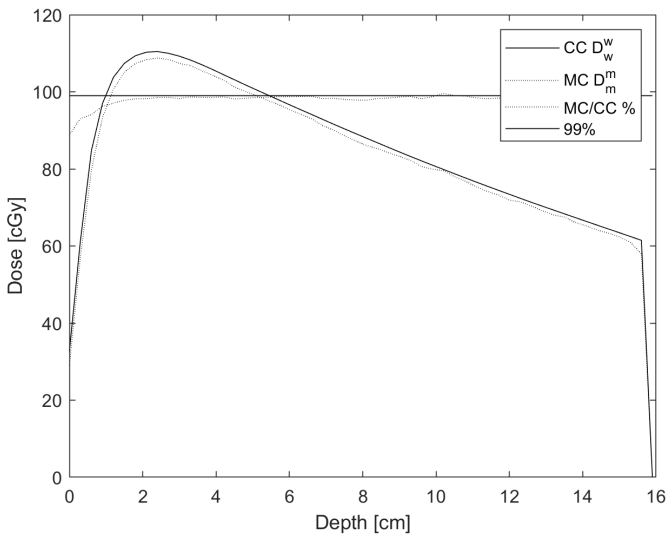

Figure 38. Depth dose in soft tissue for a 6 MV, 10 cm x 10 cm field computed with the RayStation collapsed cone and the RayStation Monte Carlo algorithms. The differences at the surface is not due differences in the dose reporting convention.

The use of scaling factors is valid only for situations where there is electron equilibrium, that is away from interfaces between materials or field edges. For materials other than soft tissue or muscle the corresponding conversion factors differ from 0.99. Figure 39 shows conversion factors from collapsed cone D_w^w to Monte Carlo D_m^m obtained from the slab setup. Note that materials in the range between lung and cartilage all have values that differ less than 2% from unity. The same plot shows also the conversion from Monte Carlo D_m^m to Monte Carlo D_w^m (non-clinical, not included in RayStation 2024A) which can be interesting for users that have experience from Monte Carlo systems with D_w^m reporting.

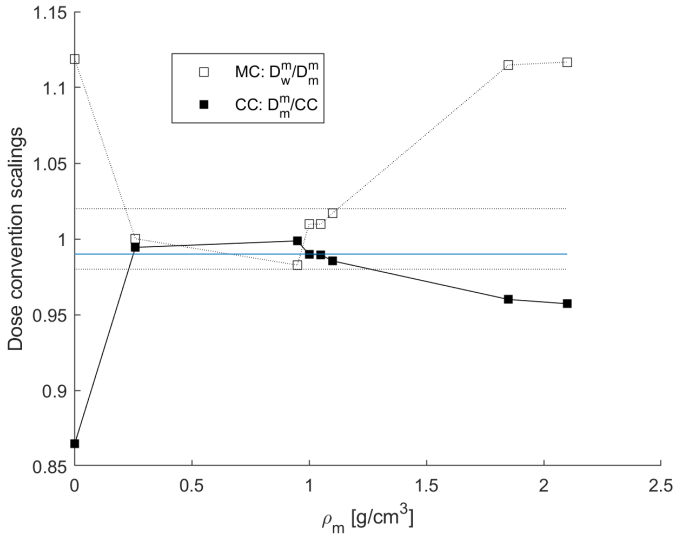

Figure 39. Conversion factors from collapsed cone D_w^w to Monte Carlo D_m^m obtained from doses extracted at the center of a 2 cm material slab in water for a 6 MV, 20 cm x 20 cm, SAD = 100 cm field. Note that materials in the range between lung and cartilage have factors which differ less than 2% from unity (dotted lines). Also shown is the conversion from Monte D_m^m to Monte Carlo D_w^m (non-clinical, not included in RayStation 2024A). Materials corresponding to the data points are listed in Figure 36.

AAPM TG-329 recommends applying the factor 0.99 to the output in the RayStation beam model to obtain dose-to-tissue rather than dose-to-water. If such a scaling is done, it is important to keep this in mind during QA and not convert measurement to dose-to-water but to dose-to-tissue. The scaling must also not be used for the Monte Carlo beam model. In RayStation, the Monte Carlo and the collapsed cone beam models share absolute dose calibration when the same machine is commissioned for both dose engines. For such cases, a scaling can only be done to the dose normalization value of the collapsed cone beam model after finishing the beam modeling. After this scaling, the measured and computed dose curves for collapsed cone will no longer match in output.

When it comes to using clinical goals from literature, it is important to remember that doses from different algorithms and implementations differ also in details other than the dose reporting convention. A DVH can include regions of different materials or regions which are not in electron equilibrium.

4.8 ELECTRON CONTAMINATION

Even for a photon beam, electrons arise due to interactions between the photons of the beam and the machine head and the air. The electrons, in turn, deposit their energy on their way through the LINAC head and the air or through ionization in the upper layers of an irradiated material. The contribution of these contamination electrons to the total dose in a patient or a phantom is a few percent; but due to their different properties compared to photons, the contribution must not be neglected. This is particularly important for dose calculations in the upper layers of the dose grid. The beam model for TomoTherapy LINACs does not include contamination electrons. For CyberKnife LINACs, it is possible to specify an electron source, but usually no electron contamination contribution is needed.

In this section

This section contains the following sub-sections:

4.8.1	Electron energy fluence	p. 124
4.8.2	Electron energy distribution	p. 124
4.8.3	Contamination electron dose	p. 124

4.8.1 Electron energy fluence

The electron energy fluence is modeled as originating in one broad direct source, and one source which has the same width as the flattening filter photon source.

$$\Psi_e = weight \cdot \left[(1-FF)\ \Psi_{directelectron} + FF\ \Psi_{flatteningfilterelectron} \right] \qquad \text{[Eq. 55]}$$

Here $weight$ is the total weight of the electron sources and FF is the relative amount of electrons that come from the flattening filter electron source, FF is between 0 and 1. The direct electron source is a wide Gaussian placed at the primary photon source [28] and the flattening filter electron source has the same width and position as the flattening filter photon source; both are projected through the collimators down to the fluence plane as described for photons in *section 4.3.4 Source projection on page 75*.

The two electron contributions are traced from their respective z-positions to the fluence plane. When computing dose, the electron contributions in the fluence pixels are backtraced from the fluence plane to the patient surface and are assumed to have originated in the primary source $\propto 1/r^2$.

4.8.2 Electron energy distribution

The electron energy spectrum

$$f(E) \propto E^c e^{-E/E_0} \qquad \text{[Eq. 56]}$$

has two parameters: E_0, which determines the exponential fall-off, and c which reduces the number of low-energy electrons. Typical values for 6 MV photon beams are E_0 between zero and one MeV and c between zero and one. The spectrum is the particle fluence versus energy.

4.8.3 Contamination electron dose

When entering a material, the electrons undergo primary interactions immediately with limited secondary transport; the primary interactions are ionizations which occur continuously along the electron path until the electron stops. With a very high number of ionizations, the range for a mono-energetic electron can be defined using the continuous slowing down approximation and a range straggling; electrons with energies in the 100 keV range reach some mm's into the tissue and electrons in the MeV-range lose approximately 2 MeV/cm in water. Examples of depth dose curves in different tissue and at different energies can be found in Ref. [6] and range tables in [4]. When computing dose with the Monte Carlo dose engine, contamination electrons are sampled from the electon fluence as described in *section 4.6.3 Sampling of particles from fluence on page 112*. After transport to the dose grid, they are treated in the same way as electrons that are released by photon interactions. When using the collapsed cone dose engine, the electron contamination dose is computed using electron pencil beam kernels with effective density scaling as described in section *Electron pencil beam on page 125*.

Electron pencil beam

RayStation 2024A uses cylindrical electron kernels $A(E, r, d)$ which have been pre-computed for a set of electron energies, also obtained using the EGSnrc Monte Carlo package (see *EGSnrc on page 90*), but with the user code DOSRZnrc [23]. Details on the simulation parameters are given below.

The electron dose engine uses the generated mono-energetic cylindrical electron kernels (pencil kernels), to produce a composite poly-energetic electron depth dose curve

$$D(d) = 2\pi \int\int w(E) \cdot A(E, r, d) r dr dE \overset{discretization}{\Rightarrow} \sum_{r_i, E_j} \pi \cdot (r_i^2 - (r_i - \Delta r)^2) \cdot w(E_j) \cdot A(E_j, r_i, d) \quad \text{[Eq. 57]}$$

where the summation is performed over the beam energy spectral components for electrons and over discrete radial steps. The factor $w(E_j)$ is the weight for the spectral component E_j. By performing the radial summation (using steps of Δr) of the depth dose curve one single 1D-electron dose profile is obtained, the electron depth dose curve.

The electron dose deposition model relies on the assumption of a semi-infinite slab geometry, which implies that lateral in-homogeneities are not accounted for in the electron contamination dose. Therefore, for beam arrangements which are not perpendicular to the patient's surface, noticeable dose displacement errors can occur at the surface on the sub-cm scale. The same type of error occurs in inhomogeneous regions in the beam entry region. For 6 MV beams, the full electron dose is confined inside a cylinder with 1 cm radius and 3 cm depth and the main part of the dose is within 1 cm depth; it is at this scale that dose displacement errors can occur.

Note: *Both dose measurement and dose modeling in the build-up region suffers from uncertainties even in a case with an ideal geometry.*

The electron pencil beams are simulated as parallel inside the patient. The error due to the assumption of parallel beams is partly corrected at the dose calculation stage by a simple scaling of dose using the inverse square law in distance from the primary source.

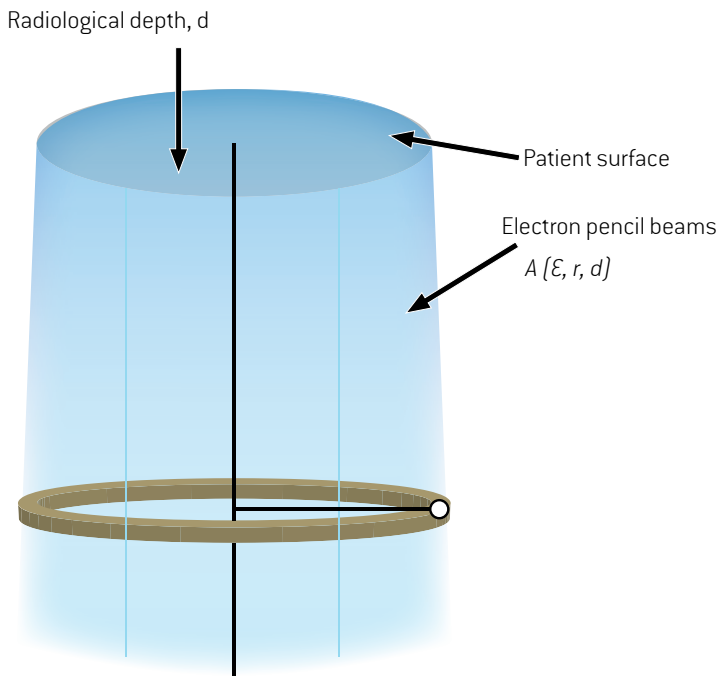

Figure 40. The electron pencil beam.

For the electron kernel Monte Carlo simulations with DOSRZnrc, a homogenous cylinder of the material "H20521ICRU" with a height of 25 cm and a radius of 14.075 cm was used, with the primary electrons incident at the center of the top of the cylinder. Only the scoring of the topmost 20 cm is used in dose computation.

The electron transport cut off energy was set to 521 keV, the photon cut off energy to 1 keV, maximum fractional energy loss to 25%, maximum first elastic scattering moment per step was 0.5, exact boundary crossing with BCA skin depth of 3 MFPs and the electron-step algorithm PRESTA-II was used. Spin effects were enabled; KM Bremsstrahlung angular sampling, BH Bremsstrahlung cross sections, KM pair angular sampling, photoelectron angular sampling, Rayleigh scattering and atomic relaxations were also used for the simulations.

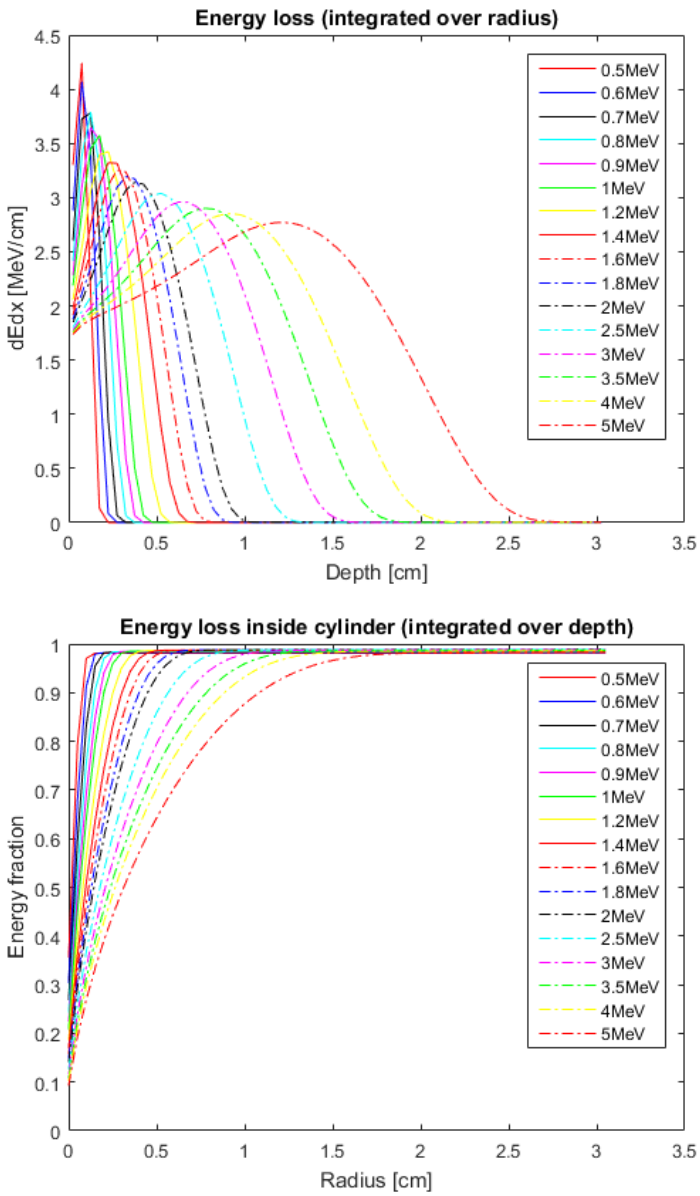

Figure 41. The electron kernel Monte Carlo simulations with DOSRZnrc, 0.5-5 MeV.

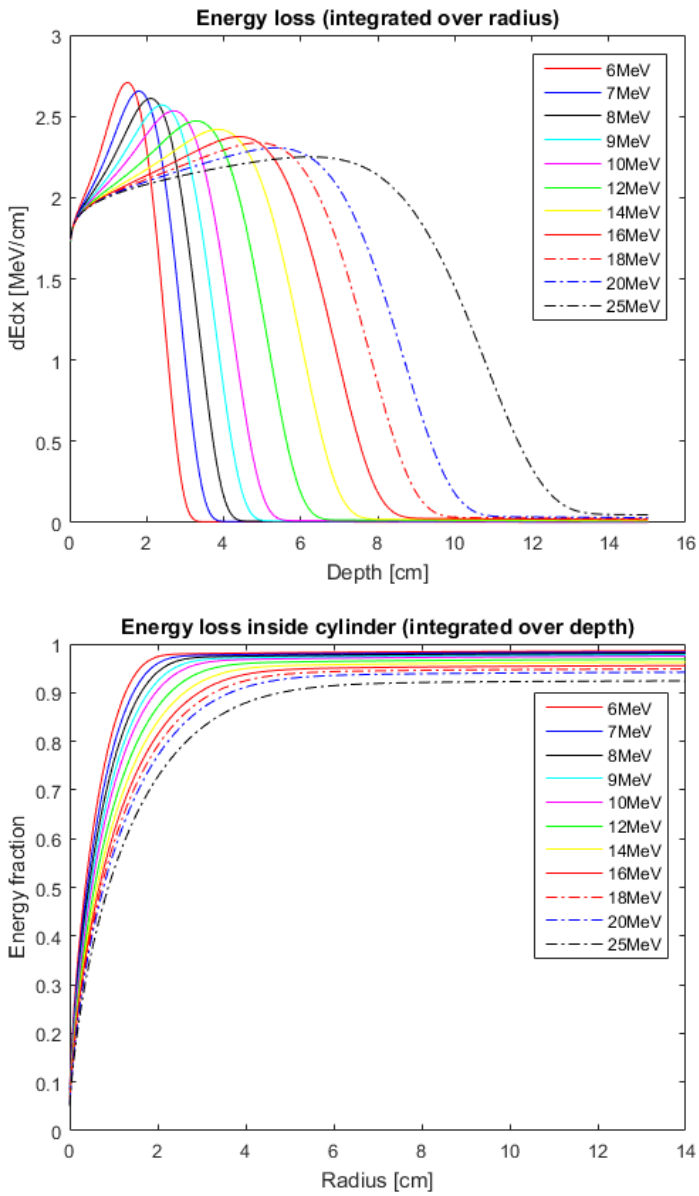

Figure 42. The electron kernel Monte Carlo simulations with DOSRZnrc, 6-25 MeV.

4.9 WEDGES

Wedges are used in 3D-CRT to create inclined isodose lines even though there is only one segment shape. Several wedge types are supported by RayStation 2024A. These include:

- **Standard wedges:** Metal wedges which are inserted into an accessory tray attached to the gantry. One physical wedge corresponds to one wedge angle. (Siemens physical wedge, Varian physical wedge)
- **Motorized wedges:** Physical wedges that are mounted in the treatment machine head. The wedge angle is altered by combining a fully wedged and an open field with the same field shape. (Elekta motorized wedge)
- **Dynamic wedges:** Wedges that are formed by moving one of the y-jaws in order to produce a distribution similar to that of a physical wedge [35]. (Varian Enhanced Dynamic Wedge, Siemens Virtual Wedge)

In this section

This section contains the following sub-sections:

4.9.1	Wedge angle	p. 130
4.9.2	Wedge orientation	p. 131
4.9.3	Wedge factor	p. 131
4.9.4	Maximum field size	p. 132
4.9.5	Physical wedges	p. 132
4.9.6	Dynamic wedges	p. 137

4.9.1 Wedge angle

The wedge angle is the angle between the isodose line (at 10 cm depth, or the 80% isodose line) and the line perpendicular to the source-to-isocenter axis. There are a few more elaborate definitions of the wedge angle, the choice of definition is important when manufacturing physical wedges or determining jaw motion for dynamic wedges. In RayStation, the wedge angle is a label of the beam model (for physical wedges), the fraction between wedged and open fields (for motorized wedges) or the fluence modulation (for dynamic wedges).

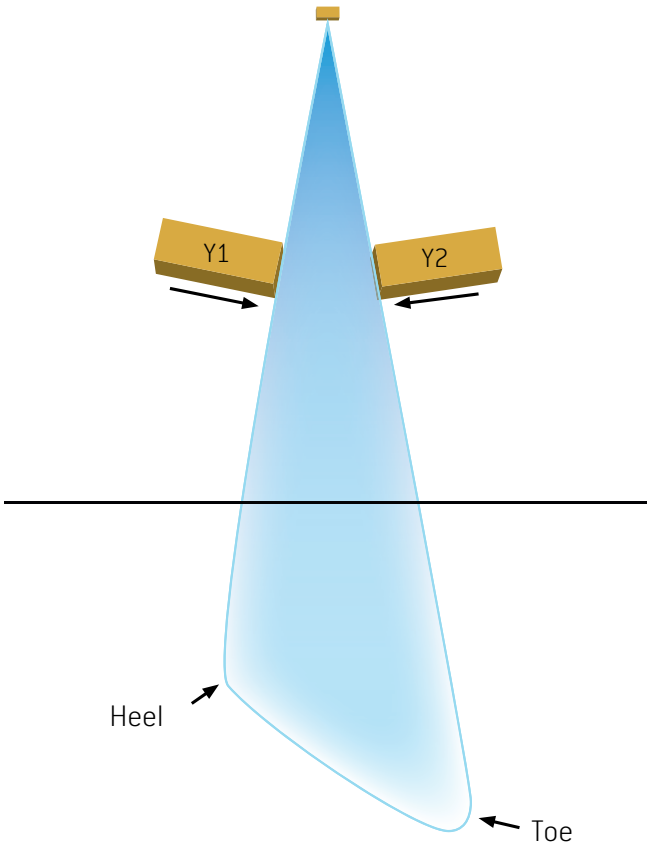

Figure 43. A wedged field created by jaws.

4.9.2 Wedge orientation

The thin side of a metal wedge, and the high transmission side of a jaw-created wedge, is called the wedge toe. The opposite side is called the wedge heel.

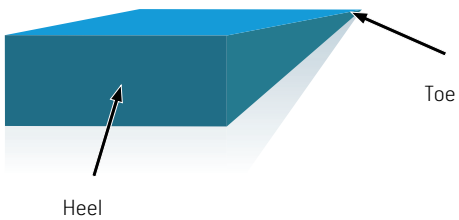

Figure 44. The thin side of a metal wedge is called the wedge toe and the opposite side is called the wedge heel.

The wedge orientation angle is the angle between the wedge filter coordinate system and the beam limiting device coordinate system. Refer to the *RSL-D-RS-2024A-IFU, RayStation 2024A Instructions for Use* for more information about the coordinate systems. In IEC 61217, the toe points towards the gantry when both the collimator and the wedge orientation angles are zero. The wedge angle increases with a counter-clockwise rotation in the beams-eye-view.

Standard wedges can be oriented with angle 0, 90, 180 and 270 degrees.

Elekta motorized wedges have only one insertion direction, which is 0 degrees; wedged fields in other orientations must be created by rotating the collimator angle.

Both the dynamic wedges, Siemens virtual wedge and Varian Enhanced Dynamic wedge, create a wedged field by the moving y-jaw so possible wedge orientations are 0 degrees and 180 degrees.

4.9.3 Wedge factor

For physical wedges (Standard wedge and Elekta Motorized wedge) the wedge factor is the measured dose for a wedged field divided by the measured dose for the open field with the same field size and under the same measurement conditions (collimation, number of MUs, SSD, measurement point). The output is measured in the same point as the output factors for open fields (*Output factors – measured input to the beam model on page 69*). The wedge factor depends not only on wedge angle but also on field size, similarly to the output factors. The wedge factors are only used to set the scale of wedged measurement, they are not part of the dose computation. Instead, the wedge output factor corrections are used to scale the computed wedged fluence. This is done on top of scaling with output factor corrections.

The Siemens Virtual wedge fluence is scaled to give the same fluence as an open field at the central axis. The Varian Enhanced Dynamic wedge gives the same fluence in the wedge toe.

4.9.4 Maximum field size

The maximum field size of a wedge can be set at beam commissioning. Segment feasibility is checked when computing dose for a wedge, both the maximum wedged field size and the maximum and minimum jaw positions must be obeyed.

The maximum field size for an Elekta Motorized wedged field is typically 30 cm in the wedge direction and 40 cm in the non-wedged direction.

4.9.5 Physical wedges

Physical wedges are wedge shaped metal blocks. A similar computation model is used for Standard wedges and Elekta Motorized wedges.

The dose computation for a physical wedge starts with the open field fluence computed with the corresponding open field beam model. This fluence is then scaled to create a wedged fluence. Additionally, wedge scatter is added to the photon fluence (*Wedge scatter on page 135*). Finally the beam hardening through the wedge is taken into account in the TERMA and dose computation (*Wedge beam hardening on page 135*).

Note: *This means that any imperfections in the open model will also be present in the wedge model.*

Wedge shape

The properties of a wedge are primarily determined by its shape, described as the transmission of the wedge projected onto the isocenter plane. It can be adapted during beam commissioning to give a good fit to measured curves. The same shape is used for all physical phenomena, i.e. attenuation, beam hardening and scatter.

Standard wedges

Standard wedges are inserted in an accessory tray attached to the gantry. The wedges are locked into position so that the source-to-isocenter line passes through the same point on the wedge irrespective of segment shape.

Standard wedges are positioned below all collimators, at an effective distance from the source that can be changed during commissioning.

Since each wedge angle is created by a physically different slab of metal, there is one model (set of parameters) for each wedge angle.

Wedge shape for standard wedges

For Standard wedges, the transmission along the y axis is given in coordinates specified by the user. Along the x axis, the user can specify a correction to the transmission along the y axis. For points off-axis, the transmission is extrapolated so that the correction goes to one for infinitely thin wedges (transmission = 1.0) and decreases with the thickness of the wedge.

Elekta Motorized wedge

The Elekta motorized wedge is a physical wedge made from a cast lead and antimony alloy. It has a 60 degree wedge angle and is mounted in the LINAC head with the toe towards the gantry, i.e. with 0 degree angle in the IEC wedge coordinate system. Refer to the *RSL-D-RS-2024A-IFU, RayStation 2024A Instructions for Use* for more information about the coordinate systems. Wedge angles between 0 and 60 degrees are created by combining fully wedged and open fields (*section 4.9.1 Wedge angle on page 130*).

Wedge shape for Elekta Motorized wedges

In RayStation, the transmission of an Elekta motorized wedge is parameterized in x and y

$$\frac{Water\ equivalent\ thickness\ (x,y)}{-\mu_0(E)} = \\ = f(x,y) = (q_3y^3 + q_2y^2 + q_1y + q_0) \cdot tan(p_2x^2 + p_0)$$ [Eq. 58]

Both the x-direction and the y-direction are defined in the wedge coordinate system, projected onto the isocenter plane. The third-degree y-polynomial is in the wedged direction and the tangent x-part is in the direction perpendicular to the wedge. $\mu_0(E)$ is the linear attenuation coefficient and E is the energy.

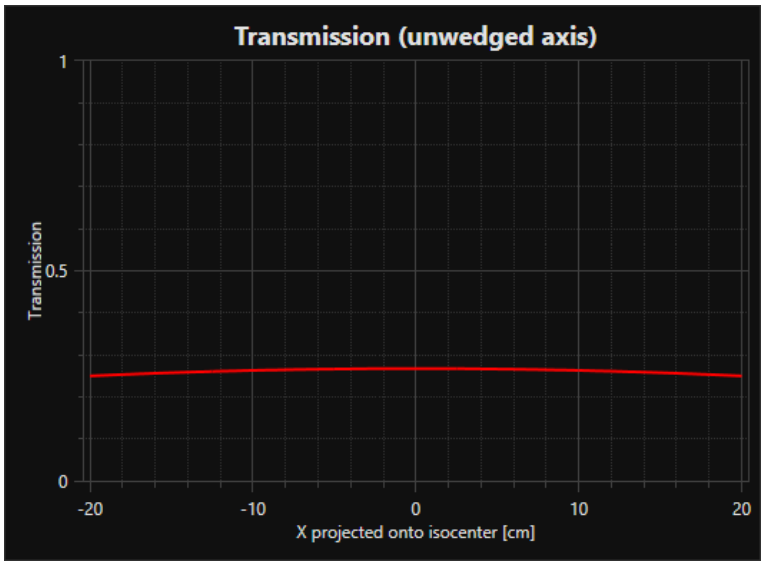

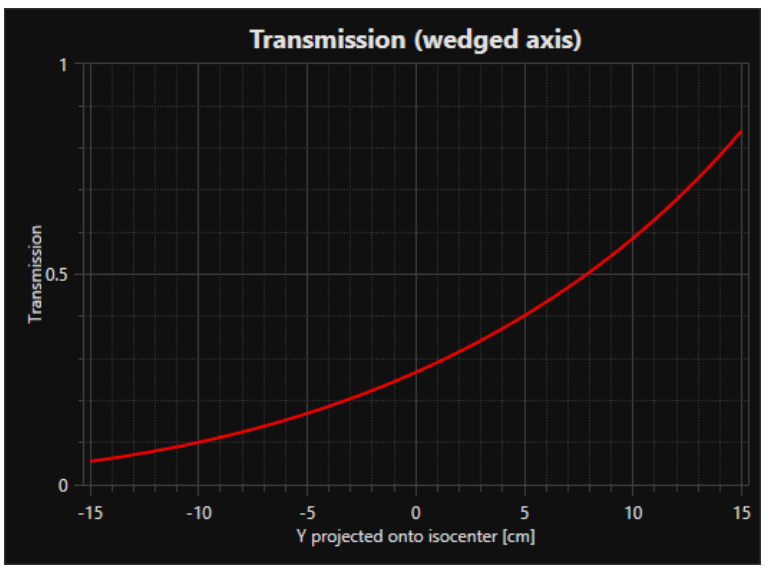

Figure 45. Transmission along x (top) and y (bottom), projected onto the isocenter plane.

The transmission through the wedge is given by

$$Transmission(x, y) = e^{f(x,y)} \qquad \text{[Eq. 59]}$$

where $f(x, y)$ is the expression from Equation 58. The negative attenuation coefficient for the wedge is consequently contained in the parameters p and q.

Wedge beam hardening

Beam hardening through the wedge is computed in the same way as for the flattening filter (*section 4.3.3 Flattening filter on page 74*) for both standard and Elekta Motorized wedges. The water equivalent thickness of the wedge is computed from its local transmission, using the linear attenuation coefficient in water for the mean value of the beam energy spectrum. The hardening effect is highly dependent on the material and the energy of the beam, for example reducing for higher energies. Due to pair production, the spectrum may even be softened for very high energies. These effects are taken into account by scaling the water equivalent thickness with a material factor that can be adjusted during beam commissioning.

Wedge scatter

When a physical wedge is present, an additional photon source is added to the fluence computation. The amount of scatter at a point in the fluence plane is determined by the irradiated part of the effective wedge shape, the angular distribution of the scatter and the weight of the scatter source.

Motorized wedged are situated above the collimators, so the irradiated part is given by the opening angle of the primary collimator and the effective distance to the source. For standard wedges, situated below the collimators, the irradiated part is dependent on the segment shape.

A thicker wedge will create more scatter, but at the same time more photons will be attenuated. It can be shown [38] that the amount of scatter in a wedge with local transmission tr is proportional to

$$Scatter \propto tr \ln(tr) \qquad \text{[Eq. 60]}$$

The maximum is reached for one mean free path, i.e. when the transmission $= e^{-1} \approx 0.368$. This means that the scatter is largest in the heel of low angle wedges and around the center for high angle wedges. The standard deviation of the scattering angle distribution is referred to as the scatter source width. During beam commissioning, the source width can be adjusted in order to match the measured curves.

The scattering angle of a photon is approximately normally distributed and depends on the material and the beam energy. During beam commissioning the width of the scattering angle distribution can be adjusted in order to match the measured curves.

The wedge scatter fluence is computed by back projection through any apertures including blocks (see *section 4.3.4 Source projection on page 75*). In addition to affecting the penumbra and the field size dependency, the wedge scatter will result in asymmetrical fluence as the scatter intensity is dependent on the wedge shape.

Synthesized wedge angle for Elekta Motorized wedges

The Elekta wedge system use 60 degree wedges in combination with open fields to create fields with lower wedge angles. For a specific synthesized wedge angle, the ratio F (in dose) on the central beam axis between the open and the wedged segment is given by

$$F = \frac{tan\ \nu}{tan\ \psi} \qquad \text{[Eq. 61]}$$

$$D_w = D_t \cdot F \qquad \text{[Eq. 62]}$$

$$D_0 = D_t - D_w \qquad \text{[Eq. 63]}$$

where ν is the synthesized wedge angle and ψ is the maximum wedge angle (60°). D_w is the dose received by the wedged segment, D_0 is the dose received by the open segment and D_t is the total dose, all doses at isocenter on the central beam axis for a field size of 10 cm x 10 cm with isocenter at 10 cm depth.

MU ratio for Elekta Motorized wedges

The dose ratio has to be transformed into an MU ratio. The MU ratio, and not the dose ratio, is used in the fluence computation. The MU ratio is calculated in such a way that the dose ratio is fulfilled within a few percent. The MU ratio is also used in DICOM export where the wedged field is exported as two separate segments.

The dose ratio to MU ratio transformation in RayStation depends on the Elekta MW beam model parameters for the machine in question and is performed according to

$$MU_{wedged} = MU_{total} \cdot MU_{ratio} \qquad \text{[Eq. 64]}$$

$$MU_{open} = MU_{total} \cdot (1 - MU_{ratio}) \qquad \text{[Eq. 65]}$$

where

$$MU_{ratio} = \frac{tan\ \nu}{tan\ \psi \cdot t_{cax} + tan\ \nu \cdot (1 - t_{cax})} \qquad \text{[Eq. 66]}$$

where the angles are expressed in radians, and t_{cax} is the beam model wedge transmission in the central beam axis point. The wedge transmission is calculated according to Equation 59. In the central axis point, x and y are both zero, and Equation 59 in combination with Equation 58 reduces to

$$t_{cax} = e^{q_0 \cdot tanp_0} \qquad \text{[Eq. 67]}$$

In Equation 67, the p_0 value collected from the beam model should be used as if it is in radians, i.e., no degrees-to-radians conversion needs to be applied to p_0.

4.9.6 Dynamic wedges

Dynamic wedges are created by motion of one of the y-jaws with the beam on. This creates a segment where the fluence is higher in one part (the toe) and lower in the other (the heel).

For Siemens Virtual wedge, the y-jaw starts at the minimum gap of 1 cm and ends at the jaw position that delimits the segment. For Varian Enhanced Dynamic the motion starts at the jaw position that delimits the segment and ends at the minimum gap of 0.5 cm. Different wedge angles are created using different jaw motion patterns.

Fluence computation with dynamic wedges is implemented as a fluence modulation. The field measure for the wedged segment is computed using the segment maximum jaw positions. The extension of the primary source in the direction of the jaw sweep for virtual and dynamic wedges is also taken into account when the collimator is rotated. The source size in the gantry coordinate system is projected on the collimator y-axis in the beam coordinate system.

Varian Enhanced Dynamic wedge

The Varian Enhanced Dynamic Wedge jaw motion is described by a golden segmented treatment table (GSTT) with MU versus jaw position (sometimes also referred to as dose versus jaw position).

The parameters (a, b, c, d) which describe the motion appear to be the same from LINAC to LINAC and for different x-jaw field sizes and positions and is described by the following equation [37]:

$$Fluence\ scaling(y) = a - b \cdot tan\ \theta[1 - c \cdot y - exp(d \cdot y)] \qquad \text{[Eq. 68]}$$

Here y is the position of the moving jaw; it is negative when the moving jaw is in the heel side and positive when the moving jaw is on the toe side. θ is the wedge angle. The GSTT-parameters are available for 4 MV, 6 MV, 10 MV, 15 MV, 18 MV and 20 MV. The open field fluence is scaled using (Equation 68). The wedged fluence is then normalized to correspond to the open field fluence at the toe side of the wedge.

The y-position is shifted with the empirical parameter $\alpha = 0.6\ cm$ obtained in [37]. Note that a more correct approximation has been presented in [38]. However, the wedge factors predicted by both approximations differ by at most 1% for field sizes between 4 x 4 cm and 20 x 20 cm. With respect to the approximation in [38], the resulting wedge factors in RayStation 2024A are slightly worse for small field sizes and slightly better for large field sizes. For a 10 x 10 cm field, both approximations differ from measured values by less than 1%.

Beam model parameters for jaw calibration (offset, gain, curvature) are taken into account for the wedge calculation which means that a different fluence modulation is obtained for a different set of offset, gain and curvature.

Possible wedge angles are 10, 15, 20, 25, 45 and 60 degrees. Allowed field sizes are 4 to 30 cm in the wedge direction and asymmetric fields are allowed.

Fields wedged with the Enhanced Dynamic Wedge differ from physically wedged fields in that the penumbra is smaller, the maximum dose is higher and the isodoses perpendicular to the jaw direction

are similar to the open field isodoses. Also the depth doses are similar between wedged and open fields – as most of the dose comes from the primary energy fluence.

Siemens Virtual wedge

The Siemens Virtual wedge shape is implemented as a fluence modulation

$$MU_E(y) = MU_{CAX} \cdot e^{-c\mu(E)ytan(\alpha)} \qquad \text{[Eq. 69]}$$

where y is the position of the moving jaw, $MU_E(y)$ is the number of monitor units to be delivered at position y, MU_{CAX} the number of monitor units to be delivered at the central axis, α is the wedge angle at 10.0 cm depth, c is a calibration factor that can be used to calibrate the angle of the virtual wedge and $\mu(E)$ is the mean linear attenuation factor for the selected photon energy E. The parameters *c* and *μ* are entered during beam commissioning and should be taken from the real LINAC. The output of the wedged field will be close to that of the open field on the beam central axis. Possible wedge angles are 15, 30, 45 and 60 degrees.

Beam model parameters for jaw calibration (offset, gain, curvature) are taken into account for the wedge calculation which means that a different fluence modulation is obtained for a different set of offset, gain and curvature.

Field size limits for Siemens Virtual wedge

Due to physical limitations of the treatment machine, the maximum field opening for Siemens Virtual Wedge fields recommended by the LINAC vendor is more restricted in the wedged direction than the maximum field opening without a wedge. It is still possible to deliver a larger field on the treatment machine. Delivering a larger field opening with a virtual wedge will not result in a wedged field shape over the entire field. Instead, a high dose plateau region will be the result at the toe side of the field beyond the recommended field size, see Figure 46.

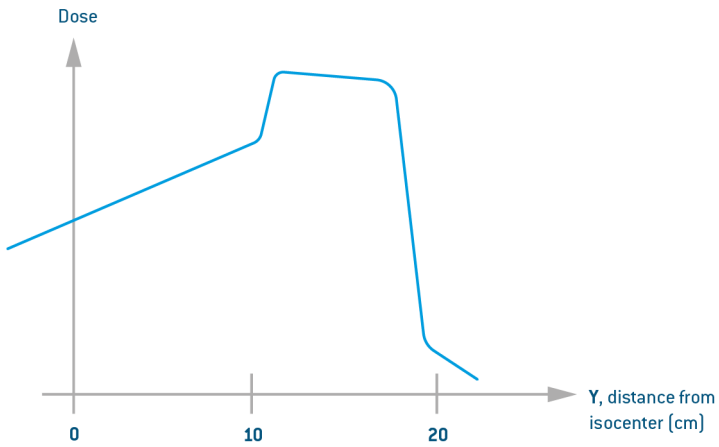

Figure 46. Example of delivered dose shape for a Siemens Virtual Wedge field outside LINAC vendor recommended field size. A high dose plateau region is formed at the toe side of the wedge beyond the recommended field size. This high dose plateau is never included in the RayStation dose calculation.

The RayStation implementation for Siemens Virtual Wedge is based on the assumption that the high dose plateau region should never be included in a treatment plan. Thus, the high dose plateau region is not accounted for in the RayStation dose computation for virtual wedges, irrespective of how the machine model is set up. If such a field would be delivered, this would result in a difference between delivered dose and RayStation computed dose, see Figure 47.

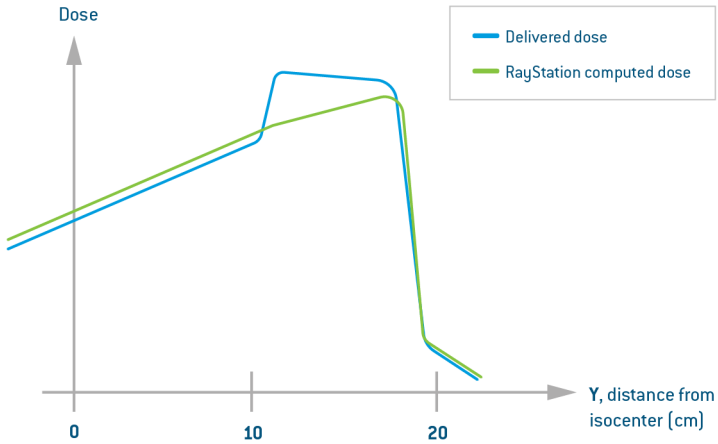

Figure 47. Example of a difference between delivered dose (blue line) and RayStation computed dose (green line) for a Siemens Virtual Wedge field outside the LINAC vendor recommended field size, if the machine model in RayStation has been set up to allow too large Siemens Virtual Wedge fields.

Siemens only specifies field sizes between 6 cm and 20 cm in the wedged direction for virtual wedges. Therefore, RayStation will only allow dose calculation with Siemens Virtual Wedge if the y-jaws in the fully open field are in retracted positions between 3 cm and 10 cm.

4.10 BLOCKS

RayStation 2024A supports dose computation with a shielding block and an aperture block. The modification to the dose due to the block shape is implemented on the fluence level. Only blocks with a specified transmission are supported. All blocks are treated as if they were located at the plane specified by the source to block tray distance, having no physical extension in the z direction.

The fluence resulting from projecting the sources through the collimators are projected through the block contour in the same way as for the collimators. The fluence is scaled with a block factor dependent on the location of the point in relation to the block. The block factor is 1.0 when a point is completely outside of the block and has the value of the block transmission when fully under the block.

The attenuation of the block tray is taken into account by scaling the photon and electron fluence with the block tray factor.

4.11 CIRCULAR CONES FOR C-ARM LINACS

RayStation 2024A supports dose computation with a circular cone for 3D-CRT and Static Arc beams. The cone modification of the beam is implemented on the fluence level only. In the fluence calculation, cones are treated as having no physical extension in the z-direction (same as for jaws and MLC) and are positioned at the plane specified by the physical bottom position in RayPhysics for the selected cone. In the fluence computation, the sources are first projected through MLC and jaws positioned according to the jaw/MLC field size specified in RayPhysics for the selected cone. The resulting fluence is then projected through the cone opening as well. The cone opening is defined by the diameter of the cone, and a transmission map is created where pixels can have transmission factor 1.0 (pixel completely inside the cone opening), transmission factor 0.0 (pixel fully outside the cone opening, the cone is assumed to have no transmission) or a value between 0.0 and 1.0, depending on the level of coverage, for pixels at the edge of the cone aperture.

4.12 CIRCULAR CONES FOR CYBERKNIFE LINACS

CyberKnife LINACs can use two different types of cones, fixed and iris. Fixed cones are fixed at a specific diameter while the iris cone opening can be varied. The iris opening is formed by two stacked hexagonal banks of tungsten. This means that that the iris cone opening is in reality not a perfect circle, but a dodecahedron, a 12-sided aperture. The iris cone opening is however approximated with a circular opening in the fluence computation, where both fixed and iris cones are handled in the same way. Both fixed and iris CyberKnife cones come in the following nominal field sizes: 0.5, 0.75, 1.0, 1.25, 1.5, 2.0, 2.5, 3.0, 3.5, 4.0, 5.0 and 6.0 cm. The smallest iris cone aperture (0.5 cm) can however sometimes be mechanically unstable and is not supported by RayStation 2024A.

The cone opening in the fluence computation can be modified from the nominal opening to an effective one using a diameter correction factor specified per cone in RayPhysics. The nominal cone diameter is multiplied by the the diameter correction factor. In the fluence calculation, CyberKnife cones are treated as having no physical extension in the z-direction and are positioned at the plane specified by the physical bottom position in RayPhysics for the selected cone. The sources are projected through the cone opening defined by the cone diameter, including the diameter correction factor, and a transmission map is created where pixels can have transmission factor 1.0 (pixel completely inside the cone opening), transmission factor 0.0 (pixel fully outside the cone opening, the cone is assumed to have no transmission) or a value between 0.0 and 1.0, depending on the level of coverage, for pixels at the edge of the cone aperture.

For the smallest cone sizes, the energy spectrum may differ from the energy spectrum for larger cone sizes and MLC collimated fields. To account for this, an energy correction factor is introduced per cone in the beam model. Applying the energy correction factor makes the energy spectrum softer or harder, which changes the slope of the computed depth dose curve. The energy correction factor is only available for fixed cones for the collapsed cone dose algorithm but for both fixed and iris cones for the Monte Carlo dose algorithm. Therefore, the collapsed cone dose algorithm can normally only compute an approximate dose for small iris cone sizes and to get clinical dose the Monte Carlo dose algorithm must be used.

The energy spectrum used for collapsed cone is modified bin by bin by multiplying the intensity of each bin by a factor

$$f_i = 1 + 7.7(1-c)(1-e_i/E_{max}) \qquad \text{[Eq. 70]}$$

where e_i is the energy of bin i, E_{max} the highest energy in the spectrum and c the cone energy correction factor. The overall normalization of the spectrum is preserved.

For Monte Carlo, the energy of the sampled photons is multiplied by the energy correction factor.

4.13 BEAM COMMISSIONING

Before clinical dose computation, the different beam model parameters which are described in this document need to be adjusted to the specific LINAC used at the clinic. This is done using the beam commissioning application and the procedure is described in *RSL-D-RS-2024A-RPHY, RayStation 2024A RayPhysics Manual*. Machine geometry is entered manually but things such as source sizes, off-axis softening and beam profile corrections need to be adjusted using measured data: depth dose curves, in-line and cross-line profiles and output factors.

This section contains a detailed description on how the detector sizes are implemented in the dose computation.

In this section

This section contains the following sub-sections:

4.13.1	Measurement conditions	p. 145
4.13.2	Detector width	p. 145
4.13.3	Detector height and depth offset	p. 145

4.13.1 Measurement conditions

When computing curves in beam commissioning a problem is set up where a water phantom is put at the correct source-surface-distance (SSD). The collimators and sources are put at their beam model distance from the source. Jaws and MLC-leaves are positioned to create rectangular fields as described in the beam commissioning manual. Dose is computed using the beam model parameters. In a regular dose computation dose is computed to the center of each dose voxel. For dose curves in beam commissioning, the dose is computed to each data point in all curves, but not to the center of the voxels in the dose grid. The dose grid is however used to discretize all the intermediate steps in the dose computation such as the TERMA-grid.

4.13.2 Detector width

Typically, curves are measured using an ionization detector. Other possibilities are diodes or parallel plate chambers or a mix of the different detector types. Large ionization chambers suffer volume averaging effects over the sensitive volume. This broadens the penumbra, an effect which is particularly pronounced for small fields where the underlying penumbra is sharper.

One method to account for detector resolution is to de-convolve the measurement with the detector convolution kernel. If this method is used, it should be applied to the measured curves before reading them into beam commissioning and no detector size should be entered in RayPhysics.

If this method is not used, the second possibility is to account for the detector resolution effect in the beam commissioning. Instead of de-convolving the measured curves, one should use the inverse method: to convolve the computed dose curve with the detector convolution kernel.

The convolution kernel in RayStation is a rectangular box. For collapsed cone, the box is used to convolve the photon TERMA, if the detector width is larger than the dose grid resolution. Convolving the TERMA instead of the dose is feasible since the TERMA to dose tracing is linear. It is necessary to do this at the TERMA-step since the convolution shall be in three dimensions; TERMA is computed in three dimensions but dose is only computed to the curve data points.

For photon Monte Carlo, the dose is computed for the full grid, and curves are extracted matching the data points using interpolation. Therefore the convolution can be, and must be, performed in dose.

A few examples of convolution kernels for ionization detectors can be found in [27] , [154] , [155] and similar publications.

The x- and y-convolution (detector width) increases penumbra widths in RayPhysics. Since there is no detector convolution in RayStation, the penumbras will be sharper for patient and phantom cases than for the curves in RayPhysics. For small fields where penumbras overlap, the output can be higher in RayStation than in RayPhysics.

4.13.3 Detector height and depth offset

Also depth dose curves are influenced by the detector. A shift for the effective point of measurement can often be applied by the measurement acquisition software before the curves are written to file. The first report from the AAPM Task Group 51 recommended a shift towards the surface by 0.6 times the cavity radius for cylindrical ionization chambers [156] . A later addendum corrected this [157]

. The recommendation is now to use the shift that gives the best shape correspondence between the measured depth dose curve and the true depth dose curve. The ideal shift depends primarily on detector and beam quality and weakly on field size. Examples of lists of effective point of measurement shifts can be found in [158] , [159] , [160] or similar publications.

Using a shift which is too large leads to dose overestimation at the surface, primarily in how the measurements in RayPhysics represent the machine, but also in how RayStation computes dose, since the beam model has been fitted to data. Using a shift which is too small leads to underestimation at the surface. The effect after D_{max} for either case is small.

There is also an option to enter a detector height in RayStation. The height is intended to make the dose curve computation mimic how an unshifted detector measures dose. A non-zero detector height decreases computed dose at the surface for dose curves in RayPhysics. For collapsed cone this is done by a square well convolution of TERMA, which includes zeroes above the surface. The electron contamination part is also convolved, but only inside the part of the detector that overlaps the phantom. For photon Monte Carlo the convolution is performed in dose, with zeroes above the surface for both photon and electron components. Since literature shows that a shifted measured depth dose curve follows the real water depth dose curve closely, a shift is preferrable to a detector height when possible [158] , [159] , [160] .

The detector height is only used for dose curve computation in RayPhysics, and not when computing patient or phantom doses in RayStation. Therefore the surface dose suppression that is obtained from having the detector height in RayPhysics is not present for patient or phantom doses in RayStation. If RayStation overestimated dose at the surface, it is recommended to inspect the depth offset and detector height settings.

4.14 GPU COMPUTATION

In RayStation 2024A, fluence, collapsed cone and Monte Carlo dose may only be computed on a GPU. The relative performance on a GPU, as compared to previously available algorithms computed on a CPU, depends not only on the compared hardware, but also on the type of plan (dose grid resolution, treatment technique, etc.). In general, a collapsed cone dose computation on a GPU should be 3 to 7 times faster than on a CPU.

The GPU algorithm source code implementations are identical for different GPU models. This prevents major differences between doses computed on different GPU models, but minor differences may still be present. Such differences originate in how floating-point numbers are represented on different hardware as well as variation in the precision of certain floating-point operations. These floating-point differences are on the order of 10^{-6} but due to rounding and interpolation, the effects can locally be up to about 0.2% of dose maximum. For Monte Carlo dose computation, the access order of the random numbers might differ between GPU models and this can change the random noise in the resulting dose.

These kinds of minor differences can not only be expected between different GPU models, but also, in some cases, between different operating system versions and GPU driver versions.

4.15 SVD DOSE COMPUTATION

The SVD dose engine is based on the pencil beam convolution technique and can be considered equivalent in terms of accuracy. It uses a more simplified fluence model as compared to the collapsed cone dose engine. The pencil beam kernel is approximated by three components that are separable in depth and lateral directions. This separation eliminates the need for three-dimensional convolutions and increases calculation speed, as was first described for the purpose of dose calculation by Bortfeld et al. [126]. SVD dose computation is used for optimization in RayStation. A photon dose computed with the SVD dose engine is always non-clinical.

Fluence model

Fluence computation is performed by summing the contributions from the primary and scatter photon sources. Electron contamination is not included, reducing dose accuracy in the build-up region. For each pixel center in the fluence plane, the fluence contribution from all open leaf pairs is calculated from x- and y-fluence filters and accumulated. The fluence filters are modeled as the sum of a left and right filter in the x-direction (top and bottom filter in the y-direction) as:

$$Totalfilter(x) = F_{left}(x) + F_{right}(x) = erf\left(\frac{x_{left}-x}{\sqrt{2}\sigma}\right) + erf\left(\frac{x-x_{right}}{\sqrt{2}\sigma}\right), \qquad \text{[Eq. 71]}$$

where x_{left} is the left MLC position and x_{right} is the right MLC position, with collimator calibration offset applied. Jaw collimator calibration, MLC gain and curvature, tongue and groove and MLC leaf tip width are not accounted for. σ is the source size as projected onto the isocenter plane.

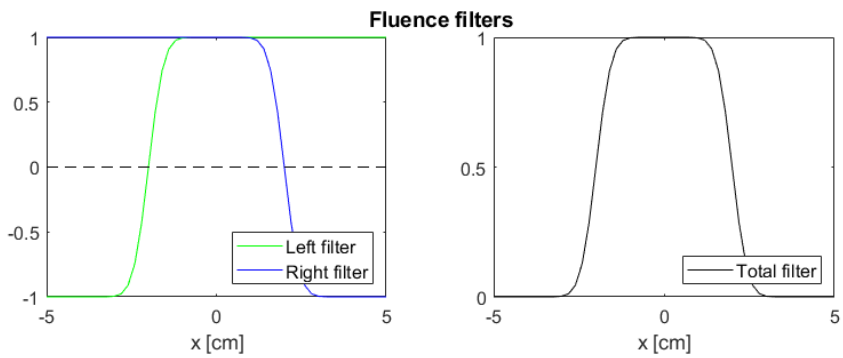

Figure 48. The x fluence filter for an MLC leaf with a 4 cm opening.

Primary and scatter fluence are summed using the flattening filter source weight. Beam profile correction as well as output factor correction are applied.

Fluence is calculated per control point for static, DMLC and arc beams. Tomo fluence calculation uses the jaw and MLC filters as described in *section 4.4.3 Collimators on page 77*.

Dose computation

A cylindrical symmetric pencil beam kernel is computed from mono-energetic kernels simulated in water, using the beam energy spectrum. The kernel is expressed as a matrix $K(z,r)$ (Equation 72) with radial and depth coordinates, where the radial coordinates are resampled to a diverging grid (the fan-line system described in Bortfeld et al. [126]) accounting for beam source-skin and source-axis distance.

$$K(z,r) = \begin{bmatrix} K(z_0,r_0) & K(z_1,r_1) & \dots & K(z_0,r_{N-1}) \\ K(z_1,r_0) & \dots & \dots & \vdots \\ \vdots & \ddots & \ddots & \vdots \\ K(z_{M-1},r_0) & \dots & \dots & K(z_{M-1},r_{N-1}) \end{bmatrix} \qquad \text{[Eq. 72]}$$

The singular value decomposition is used to express the matrix as a series of outer products summed with decreasing weight factors in which only a few terms are necessary for accurate reconstruction (Equation 73). RayStation uses the first three M x 1 vectors $\mathbf{U_i}$ to represent the depth components of the kernel and the first three N x 1 vectors $\mathbf{V_i}$ to represent the radial components.

$$\begin{aligned} &K(z,r) = USV^* = \sum_{i=0}^{N-1} \sigma_i \mathbf{U_i}(z) \otimes \mathbf{V_i}(r) \approx \sum_{i=0}^{2} \sigma_i \mathbf{U_i}(z) \otimes \mathbf{V_i}(r), \\ &U = [\mathbf{U_0}, \mathbf{U_1}, ..., \mathbf{U_i}, ..., ..., \mathbf{U_{M-1}}] \\ &V = [\mathbf{V_0}, \mathbf{V_1}, ..., \mathbf{V_i}, ..., \mathbf{V_{N-1}}] \\ &S = \begin{bmatrix} \sigma_0 & & \\ & \ddots & \\ & & \sigma_{N-1} \end{bmatrix} \end{aligned} \qquad \text{[Eq. 73]}$$

With this representation of the kernel, the radial spread of the kernel is accounted for in dose computation by convolving each included radial component with the energy fluence in the fluence plane. This greatly reduces computation time in comparison to the standard pencil beam convolution algorithm, where convolution is performed once for each depth layer of the dose grid. No correction for lateral tissue inhomogeneity is performed, as is common for pencil beam algorithms. Additionally, there is a lateral dose cut-off relatively close to the border of the fluence field. For treatments with many control points the missing out-of-field dose for each control point can sum up to a significant fraction of the total dose. The effect may result in a variation of dose output of the SVD dose engine as compared to the CC dose engine, depending on the field setup.

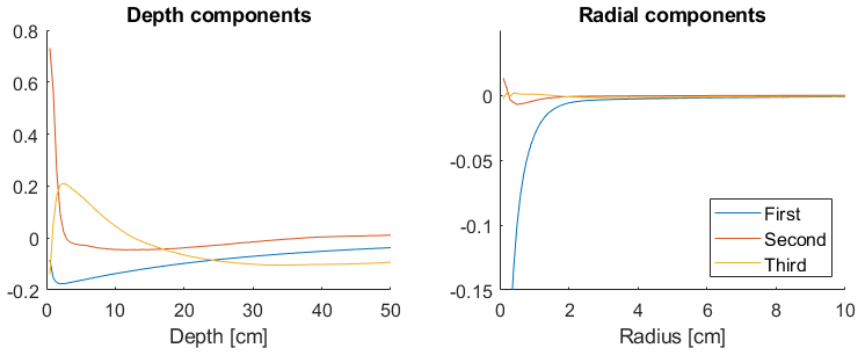

Figure 49. Kernel components for a 10 MV beam with SSD = 60 cm.

To obtain 3D dose, the convolved fluence is projected through the voxels and weighted with the depth contribution of each component. The inverse square law is applied, to account for beam divergence that is not included in the pencil beam kernel. Each voxel is assigned a radiological depth by ray tracing and this depth, rather than the physical depth, is used to find the depth dose contribution. The SVD dose engine thus accounts for tissue inhomogeneities in the depth direction by the so-called path length correction.

In the SVD computation of 3D dose, lateral transport occurs along surfaces of the same radiological depth, i.e., parallel to the skin rather than perpendicular to the beam. This introduces some additional approximation for very inclined beams (e.g., for breast treatments).

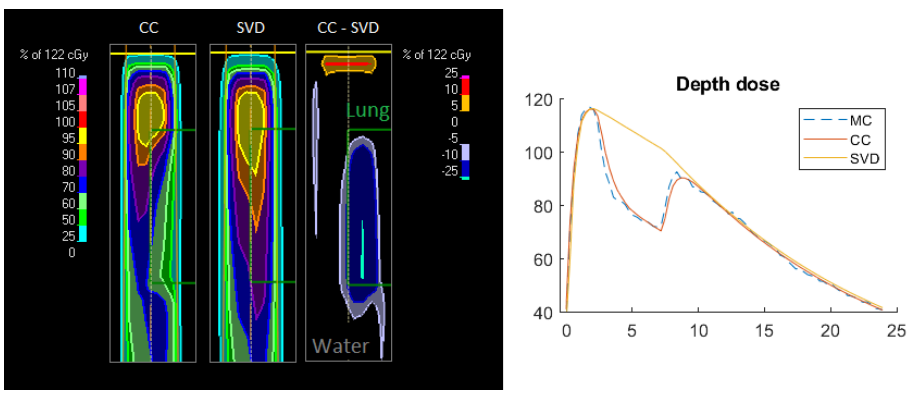

Figure 50. Dose distribution of the CC and SVD dose engine for a 2 x 2 cm^2 field, 10 MV beam through a water phantom with a lung-slab insert (left) and depth doses through the lung insert, offset 0.5 cm from central-axis (right). The SVD dose engine does not account for lateral inhomogeneities, leading to overdosage in the lung region, where there is electron disequilibrium. After the lung insert, where electron equilibrium is stabilized, dose distribution of the SVD dose engine corresponds to that of the CC dose engine, due to the inclusion of path length correction.

5 ELECTRON DOSE CALCULATION

The Electron Beam Design module in RayStation 2024A supports manual planning for standard C-arm linear accelerators equipped with applicators with cutouts. The following are the key capabilities of the Electron Beam Design module:

- Energy range 4 MeV - 25 MeV.
- Supports rectangular and square applicators from all major vendors.
- Accurate electron beam phase space model.
- Dose calculation by the Monte Carlo method.
- Calculation of absolute monitor units for arbitrary cutout shapes and SSD.
- Supports use of bolus.
- User friendly graphical interface to set up beams and create cutouts.
- Cutouts with straight profiles, i.e. cut surface parallel to the beam axis. Only Cerrobend cutouts are supported for RayStation 2024A.

As a basis for discussions in this document, *section 5.1 Accelerator electron beam line design on page 153* reviews the design of current accelerator systems and how clinical electron beams are realized. The electron dose calculation algorithm in RayStation is described in *section 5.2 Electron dose calculation algorithm on page 157*.

In this chapter

This chapter contains the following sections:

5.1	Accelerator electron beam line design	p. 153
5.2	Electron dose calculation algorithm	p. 157
5.3	Statistical uncertainty	p. 170

Beam commissioning of electron beams

For information, see *RSL-D-RS-2024A-RPHY, RayStation 2024A RayPhysics Manual*.

5.1 ACCELERATOR ELECTRON BEAM LINE DESIGN

This section describes the design of the accelerator electron beam line.

In this section

This section contains the following sub-sections:

5.1.1	The accelerator electron beam line design	p. 154
5.1.2	The primary and secondary scattering foils	p. 155
5.1.3	The ion chamber and collimators	p. 155
5.1.4	The applicator and cutout	p. 155

5.1.1 The accelerator electron beam line design

In a modern C-arm medical linear accelerator an electron beam is accelerated along a linear wave guide, passes through a bending magnet for energy selection, and then emerges from the evacuated chamber into air through an exit window. The vast majority of linear accelerators in clinical use today use the so called dual foil technique to form the electron beam (see Figure 51). In the dual foil technique, the beam is scattered by two separate foils before passing through the monitor chamber, the collimators and the applicator/cutout. The elements of a typical beam path are:

1. A linear accelerator that generates a narrow quasi-monoenergetic electron beam.
2. A primary scattering foil that also acts as the vacuum to air interface.
3. A primary collimator with an opening angle of about 14 degrees.
4. A secondary scattering foil.
5. A jaw pair and an MLC.
6. An applicator with two to four scraper layers.
7. A cutout mounted in the lowermost scraper layer.

Different linear accelerator models have variations of this sequence. For instance, the order in which the jaws and MLC are placed may be different and some machines may only have a single backup jaw.

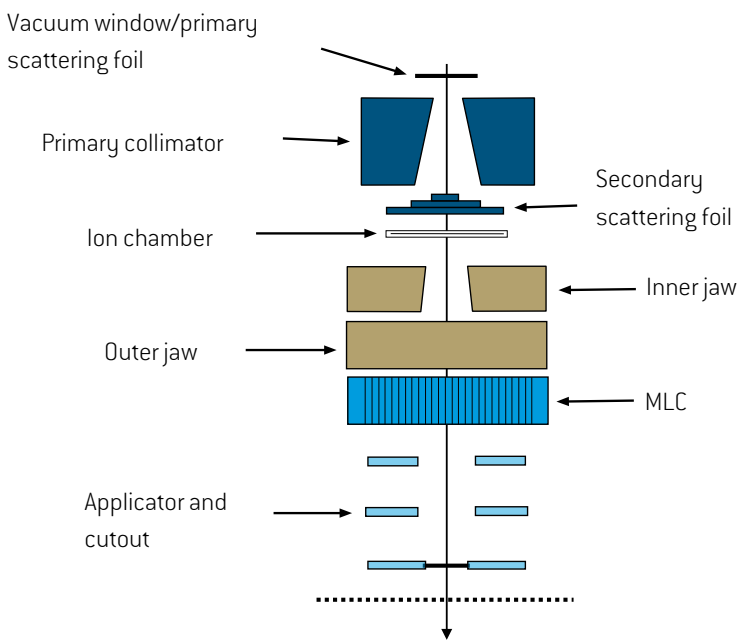

Figure 51. Elements of a dual foil electron beam line.

5.1.2 The primary and secondary scattering foils

The geometry and materials of the primary and secondary scattering foils are optimized per nominal beam energy to yield a flat dose distribution at the iso-plane while producing as little bremsstrahlung as possible. The resulting design is then a thin high-Z primary foil and a low-Z secondary foil with varying thickness [52]. The thickness is at maximum on the beam axis and decreases with increasing distance from the beam axis. A common technique to realize a varying thickness is to stack a set of discs with different radius and thickness on top of each other as is illustrated in Figure 52.

Figure 52. Secondary scattering foils. The outer ring is a mounting support and is not irradiated by the electron beam. The outer diameter is about 8 cm.

5.1.3 The ion chamber and collimators

An ion chamber is located a few centimeters downstream of the secondary scattering foil. The ion chamber foils are made of low-Z materials (e.g., Mylar and Teflon) and cause multiple scattering but very little bremsstrahlung. The electron field is collimated by the jaws, the applicator and the cutout. The MLC is usually fully retracted, but still needs to be considered for the modeling of electron beams. The MLC is considered to be closed outside its extension in the y-direction, with the exception of the HDMLC (Varian TrueBeam) which is smaller than the maximum jaw field size in the y-direction. This MLC is considered to be fully open outside its extension in the y-direction. For machines that only have jaws perpendicular to the MLC (such as Siemens machines and the Elekta Agility) the MLC replaces the non-existing jaw and needs then to be included in the model. For the Elekta Beam Modulator millstone, MLC and the fixed jaws are all included. The treatment head is filled with air and has two additional foils: a mirror and an exit foil. As is the case for the ion chamber, the air and the foils are made of low-Z materials (e.g. Mylar and Teflon) and cause multiple scattering but very little bremsstrahlung.

5.1.4 The applicator and cutout

The applicator has two to four scraper layers of decreasing aperture where the lowermost layer holds the cutout. For a treatment unit with standard fixed applicators with optional patient specific cutouts, the jaws and possible MLC have pre-programmed positions per energy/applicator

combination. Typically the margins (projected to the iso-plane) between the applicator's maximum field size and the jaw positions are a few centimeters (jaws set wider). The cutout has a thickness of one centimeter and is made of an intermediate-Z alloy with low melting point such as Cerrobend. Only Cerrobend cutouts with straight edges, i.e., parallel to the beam axis line, are supported and validated for RayStation 2024A. The applicator may also be used without a cutout which then is replaced by a 'factory frame' which defines the nominal field size of the applicator. An example of an electron applicator is shown in Figure 53.

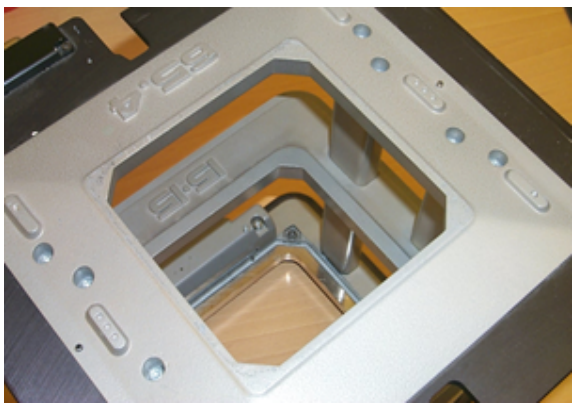

Figure 53. Scraper layers of a Varian Type III electron applicator. The view is in the beam's direction. The cutout is mounted in the most distant scraper layer. In the picture the cutout is replaced by the 'factory frame' defining the nominal field size of the applicator.

The materials available for scraper layers are aluminum, Cerrobend, lead, yellow brass and "Zinc-Aluminum".

Name	Density [g/cm³]	I (eV)	Composition
Aluminum	2.7	166.0	Al (100%)
Cerrobend	9.76	721.1	Bi (50%), Pb (26.7%), Sn (13.3%), Cd (10.0%)
Lead	11.32	823.0	Pb (100%)
Yellow brass	8.47	324.7	Cu (66.0%), Zn (34%)
Zinc-Aluminum	6.3	309.7	Al (8.8%), Cu (1.3%), Zn (89.9%)

For the purpose of modeling the electron beam, the particle fluence can be divided into three major components: electrons that have had a free passage from the secondary foil, electrons that have been out-scattered from collimators and contamination photons from bremsstrahlung in scattering foils. The next section describes how these components are modeled in RayStation.

5.2 ELECTRON DOSE CALCULATION ALGORITHM

This section describes the electron dose calculation algorithm.

In this section

This section contains the following sub-sections:

5.2.1	Background and rationale	p. 158
5.2.2	Modeling the electron beam phase space	p. 160
5.2.3	In-patient energy transport and energy scoring	p. 168
5.2.4	Dose reporting, dose-to-water	p. 168
5.2.5	Electron density weighted depth	p. 168
5.2.6	Algorithm weaknesses	p. 169

5.2.1 Background and rationale

The calculation of a 3D distribution of energy depositions in a model of a patient irradiated by an electron field from a linear accelerator is a demanding task. In such a beam the electrons are the major energy carrier and are accompanied by an order of magnitude lower amplitude of contamination photons. The electrons suffer continuous energy loss and elastic scatterings leading to an entangled and difficult to approximate pattern of energy depositions. For narrow fields or in heterogeneous geometries the radiation transport problem becomes particularly difficult to solve by approximate methods such as the pencil beam infinite slab approximation. Historically, the clinical application of electron beam therapy has been hampered by a combination of poor beam modeling approximations together with the limitations of semi-analytical pencil beam models. For the pencil beam models errors in dose calculation including correction for patient inhomogeneity can be large (up to 40% is possible) and may lead to a "geometric miss" of the target volume. Further, calculation of monitor units for non-standard situations such as extended SSD or arbitrary shaped irregular applicator cutouts, as well as treatments that apply bolus on the patient surface is often too inaccurate or not possible. As a consequence this demands that the medical physicist makes time-consuming measurements of output factors to confirm treatment planning system estimates in the clinic.

The RayStation approach

RayStation uses a hybrid model where the electron beam phase space emitted from the accelerator treatment head is combined with an in-patient Monte Carlo (MC) dose engine. This is implemented as three different steps. First, initial generation of electrons and photons at a phase plane, and then transport of electrons through the collimating elements. As last step, transport and scoring of electrons and photons in the dose grid using the same Monte Carlo dose engine as for photons (see *section 4.6 Monte Carlo dose computation on page 111*).

The electron phase space generation

The electron phase space generation starts at a plane located at the secondary scattering foil by the generation of direct electrons. The electrons are propagated by a MC code to the plane of the cutout. The propagation is done as a sequence of in-air 'randomhinge' condensed history transport steps using the Goudsmit-Saunderson theory [53] together with energy loss using the total stopping power of air. During the propagation it is checked if the electron has a free passage through the collimating elements (jaws, MLC, applicator scrapers, cutout). Electrons that reach the exit of the cutout constitute the direct electrons. If an electron does not have a free passage, the interactions with the collimating element is simulated to determine if it is out-scattered. Out-scattered electrons that reach the exit of the cutout constitute the indirect electrons.

Dose contribution of contamination photons

The photon contamination dose calculation uses a special photon fluence model that accounts for the collimation (i.e., lowermost scraper layer and cutout) and the photon contamination energy fluence. The photon fluence model is then sampled during the dose computation and the photons are transported and scored together with the electrons by the in-patient MC code.

Reference information

The method to generate the electron beam phase space is described in *section 5.2.2 Modeling the electron beam phase space on page 160* and the dose engine is described in *section 5.2.3 In-patient energy transport and energy scoring on page 168*. The dose contribution from contamination photons is calculated as described in *Contamination photons on page 167*.

5.2.2 Modeling the electron beam phase space

Phase space components

The upper part of the treatment head down to and including the secondary scattering foil defines what in the following will be referred to as the source phase space denoted as Φ_S defined in the source phase space plane. The source phase space consists of an energy spectrum $\varphi_E(E)$ and a spatial distribution $\varphi_S(x, y, u, v)$ which are uncorrelated. Thus,

$$\Phi_S = \varphi_E(E) \times \varphi_S(x, y, u, v) \qquad \text{[Eq. 74]}$$

Here E is the electron kinetic energy and (x, y, u, v) represents the electrons position and direction at the source phase space plane. Compared to most other modalities, the electrons are significantly affected by interactions in air between the source phase plane and the patient. To account for this, electron multiple scattering and energy loss are simulated in dry air until the electron reaches a voxel with a density significantly higher than air.

Note that in the beam model, the position of the primary scattering foil is fixed at 0 cm, and the position of the secondary scattering foil is a variable parameter.

Particles that emerge from the treatment head at the plane of the cutout and move towards the patient define the exit phase space. As discussed in *section 5.2.1 Background and rationale on page 158*, the RayStation electron beam model divides the exit phase space into three components:

1. Direct electrons that have had a free passage from the secondary scattering foil (no collimator interactions, only multiple scatter in air and foils). See *Direct electrons on page 160* for more information.
2. Indirect electrons out-scattered from collimators (only first generation out-scatter considered). See *Indirect electrons on page 165* for more information.
3. Contamination photons to account for bremstrahlung in the secondary scattering foil. See *Contamination photons on page 167* for more information.

Direct electrons

Energy spectrum

The energy spectrum $\varphi_E(E)$ describes the energy distribution of the direct electrons at the source phase space plane. The spectrum is treated as uncorrelated to the electron's position and direction at this plane. It is suitable to deduce the spectrum shape from an analysis of a water depth dose measured for an open field (i.e. no applicator mounted) with the photon jaws and MLC leaves maximally retracted. Under these circumstances the dose contribution from indirect electrons is minimized and only contributions from direct electrons and treatment head generated brehmstrahlung photons created in the scattering foils need to be considered.

The energy spectrum is derived through fitting parameters of a calculated depth dose towards the measured depth dose. The contribution of direct electrons to the calculated depth dose is modeled

by superposition of pre-calculated mono-energetic depth dose distributions with energy dependent weights. In the fit, the weights are varied until an optimal agreement between the measured and the calculated depth dose is achieved. Either individual weights per mono-energetic depth dose can be used as free parameters in the fitting or the energy weights can be calculated by a suitably parameterised analytical spectrum function where all or some of the parameters of the spectrum function are subject to fitting. In the current implementation, a spectrum function is used. The analytical spectrum function is composed of a linear tail and two opposed soft threshold functions of the form

$$\frac{1}{1+e^{\frac{E_0-E}{w}}} \qquad \text{[Eq. 75]}$$

which for increasing values of the electron kinetic energy E goes from zero to unity centered around an inflection point E_0 with a steepness determined by w.

The spectrum function is given by

$$\varphi_E(E) = \left(B + KE + \frac{1}{1+e^{\frac{-(E-E_0)}{w_l}}}\right) \times \left(\frac{1}{1+e^{\frac{E-E_0-\Delta}{w_h}}}\right) \quad if \quad E > E_{cut} \qquad \text{[Eq. 76]}$$

$$\varphi_E(E) = 0 \qquad if \quad E < E_{cut} \qquad \text{[Eq. 77]}$$

where B and K define a linear low energy tail and w_l and w_h are the steepness of the rising and declining parts of the energy spectrum peak. The parameter Δ defines a displacement between the inflection points of the rising and declining parts and controls the width of the peak in the energy spectrum. The parameter E_{cut} is a low energy cut-off below which the spectrum weight is zero.

To ensure consistency it is essential that the mono-energetic depth doses are calculated by the same method as used for the in-patient energy transport. Therefore, we calculate the mono-energetic depth doses by using the same transport parameters as used for the in-patient dose calculations. The depth doses are calculated on a coarse energy grid for 16 energies from 1.0 MeV to 60 MeV in logarithmic steps using a plane parallel incident beam with 80 cm of air between the source phase plane and the water surface.

Special attention must be given to the source and scoring geometry applied when calculating the mono-energetic depth doses. The electron's original spatial-angular distribution high up in the treatment head in combination with multiple scattering in air yields diverging electron fluence at the iso-plane with an apparent source location slightly downstream of the primary scattering foil. The beam divergence is accounted for by a applying a $1/r^2$ correction on the depth doses as

$$DD'(z) = \left[\frac{z'}{z'+z}\right]^2 DD^{\infty}(z) \qquad \text{[Eq. 78]}$$

where z' is the distance to the apparent source from the phantom surface and z is the depth in the phantom. For typical conditions the value of z' is about 85 cm.

The procedure has been tested on beam data obtained by a detailed BEAMnrc simulation of a Siemens Primus accelerator [55]. In this work simulated open field depth doses for nominal beam energies from 6 to 21 MeV were used as input to the spectrum analysis. The simulation used electron pencil beam sources with a Gaussian distributed energy distribution with a realistic standard deviation. It was found that the resulting analytical spectra shapes agree well with simulated spectra (see Figure 54). It should be noted that for a real linear accelerator the incident spectra may not be well described by a Gaussian shape. However, this procedure has been found to perform well also for measured data from a large number of real linear accelerators.

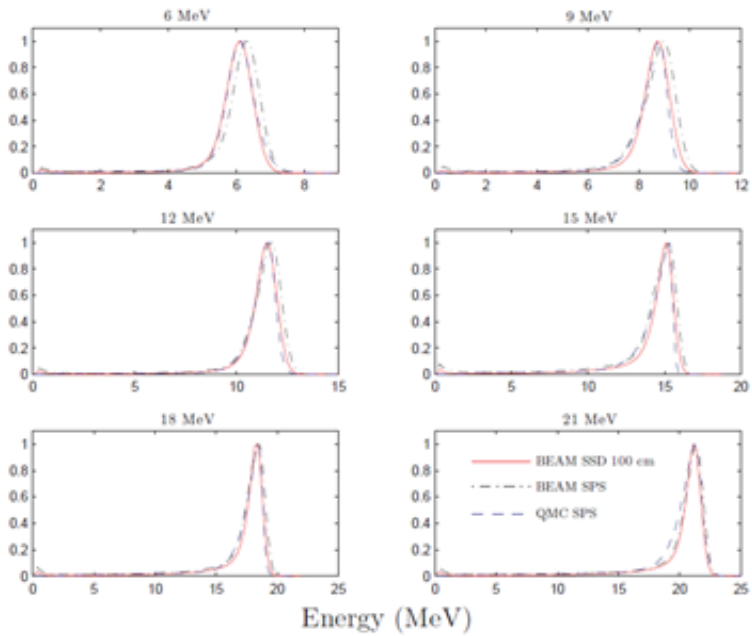

Figure 54. Spectrum analysis of simulated Siemens Primus beams [55]. Solid line: energy spectrum scored at the iso-plane. Dot-dashed line: energy spectrum scored as the source phase space plane. Dashed line: fitted energy spectrum function.

Spatial distribution at the source phase space plane

The spatial part of the source phase space distribution, $\varphi_S(x, y, u, v)$, specifies the direct electron phase space at the plane of the secondary scattering foil. It is modeled by a suitably parameterized analytical function whose functional form and choice of parameters is a tradeoff between phase space reconstruction accuracy versus sampling speed and number of adjustable parameters. The

latter number should be limited such that the parameters can be determined from a manageable set of LINAC specific data during the beam commissioning procedure.

Ideally, each parameter of the spatial distribution function should be chosen such as to yield a strong correlation to the design elements of a dual foil assembly and the process through which a flattened electron field is formed. From the idealized dual foil assembly depicted in Figure 51 it can be argued that the phase space is determined by the geometrical configuration of the upper part of the treatment head according to:

1. The accelerator delivers a narrow quasi-monoenergetic pencil beam on the thin primary scattering foil.
2. The primary foil scatters the electron beam into a nearly Gaussian shaped forward peaked distribution.
3. The beam is laterally confined by the primary collimator's opening cone yielding a distinct fluence cutoff as the beam reaches the secondary scattering foil. The cut-off radius is determined by the cone opening angle and the position of the secondary scattering foil.
4. At the secondary foil the electrons are multiple scattered again. Since the scattering foil thickness is at maximum at the beam axis and decreases away from the beam axis the amount of scatter will depend on the point of incidence on the secondary scattering foil.

The spatial distribution resulting from these determining factors is modeled as a rotationally symmetrical lateral fluence surface combined with a point electron source with Gaussian angular spread added, thus

$$\Phi_R(s,\xi) \propto e^{\frac{-s^2}{2\sigma_s^2}} \times e^{-\frac{\xi^2}{2\sigma_\xi^2(s)}} \qquad S \leq S_{max} \qquad \text{[Eq. 79]}$$

$$\Phi_R(s,\xi) \propto e^{\frac{-s^2}{\sigma_s^2}} \times e^{-\frac{\xi^2}{\sigma_\xi^2(s)}} \qquad S \leq S_{max} \qquad \text{[Eq. 80]}$$

$$\Phi_R(s,\xi) = 0 \qquad S > S_{max} \qquad \text{[Eq. 81]}$$

where $s = \sqrt{x^2 + y^2}$ is the distance from the beam axis. The parameter σ_s is the width of a Gaussian modulation of the lateral fluence and s_{max} denotes the cut-off radius beyond which the fluence is zero. The parameter ξ is the angle between the electron's emission direction and the mean emission angle $\overline{\theta}_s$ versus the beam axis at radius s. The mean angle $\overline{\theta}_s$ at radius s is constructed by assuming an upstream virtual source point on the beam axis, hence

$$\overline{\theta}_s = \tan^{-1} s/z_{eff} \qquad \text{[Eq. 82]}$$

where z_{eff} is the distance between the source phase space plane and the virtual source point.

The angle ξ is Gaussian distributed with a width σ_ξ that is a function of the distance from the beam axis. In the current implementation we adopt the following relationship between the angular spread and the distance from the beam axis:

$$\sigma_\xi(s) = \sigma_\xi(s_{cut}) + (\sigma_\xi(0) - \sigma_\xi(s_{cut}))(1-(s/s_{cut})^\gamma)^{1/\gamma} \qquad \text{[Eq. 83]}$$

where $\sigma_\xi(0)$, $\sigma_\xi(s_{cut})$ and γ are free parameters. In conclusion, for a given location of the source phase space plane and a given primary collimator opening angle, there are in total five free parameters of the source phase space spatial distribution function: σ_s , z_{eff} , $\sigma_\xi(0)$, $\sigma_\xi(s_{cut})$, and γ . The values are derived as part of a beam commissioning process by fitting calculated air fluence profiles towards measured air fluence profiles. This procedure is not described further here.

It should be noted that even if each parameter is by design strongly coupled to a specific design characteristic there exists a correlation to the other parameters. Accordingly, the parameters should be considered as "effective parameters" which thereby also account for additional effects like multiple scatter in air, in the ion chamber and in the exit foil. For example, the influence (mainly multiple scattering) of the ion chamber and air scatter above the source phase space plane is accounted for by the parameters a and b. As an example, Figure 55 shows the linear parameterization of the angular spread compared to a full BEAMnrc simulation. Out to a radius of about 2 cm the linear approximation is in reasonable agreement with the full simulation. Outside of 2 cm the secondary scattering foil of this particular linac model has a thick support frame that is also irradiated. However, this frame is so thick and far away from the beam axis that electrons that hit this part of the surface are few and has a small probability of reaching the exit of the applicator and can be neglected.

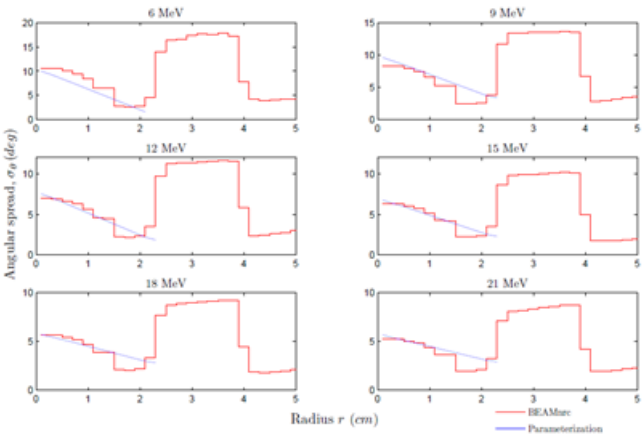

Figure 55. Simulated angular spread at the exit from a Siemens Primus secondary scattering foil as a function of the distance to the beam axis [55]. Red line: BEAMnrc simulation. Blue line: beam model parameterization.

5

Indirect electrons

Direct electrons hitting a collimating element have a certain probability of being scattered back into the field and may deposit dose in the patient. The characteristics of the collimator out-scatter vary with the energy of the incident electron, scattering material and the electron's angle of incidence on the scattering surface. Owing to the latter factor there is a strong dependence on whether the incident electron enters the scattering object though the inner edge surface or the front face surface, see Figure 56. Since the dominating direction of direct electrons is parallel to the beam axis the front face surface is hit at small incident angles in contrast to the inner edge surface for which the incidence angle is near 90 degrees. Owing to the small incidence angle on the front face the out-scatter will be strongly forward peaked with the electrons suffering minor energy losses before being emitted back into the field. Hits on the inner edge result in out-scatter at much larger angles and with an energy distribution ranging from the incident energy to very low energy.

In the current implementation we consider out-scatter from front face and inner edge of the applicator scraper layers and cutout. For the collimators and millstone we only consider out-scatter from the front faces and neglect inner edge out-scatter. The rationale for this is that only the forward peaked out scatter from the front faces will reach the patient with a reasonable probability. For jaws and MLC, it is possible to define the shape of the tip as either focused or rounded with a user-specified radius. The tip shape will affect the front face out-scatter, where a rounded tip will result in a larger proportion of scatter electrons compared to a focused tip.

The out scatter is generated by transporting electrons in a parameterized representation of the geometry of the collimating element that is hit. Each geometry is characterized by its material, thickness and the distances and angles of each face compared to the beam axis. The electron transport is performed with the same condensed history MC code as the in-patient transport with the exception that no dose is scored and generated photons are disregarded.

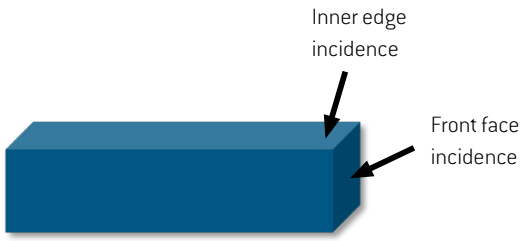

Figure 56. Edge geometry used for the out-scatter simulation showing incidence on the inner edge and front face surfaces.

The method has been validated against simulations with the EGSnrc code [11] for relevant materials, incident angles and energies. The method is substantially faster than a full EGSnrc simulation while still reproducing energy spectrum and spatial distribution with sufficient accuracy. Results for a 12 MeV electron beam incident on a Tungsten surface are shown in Figure 57.

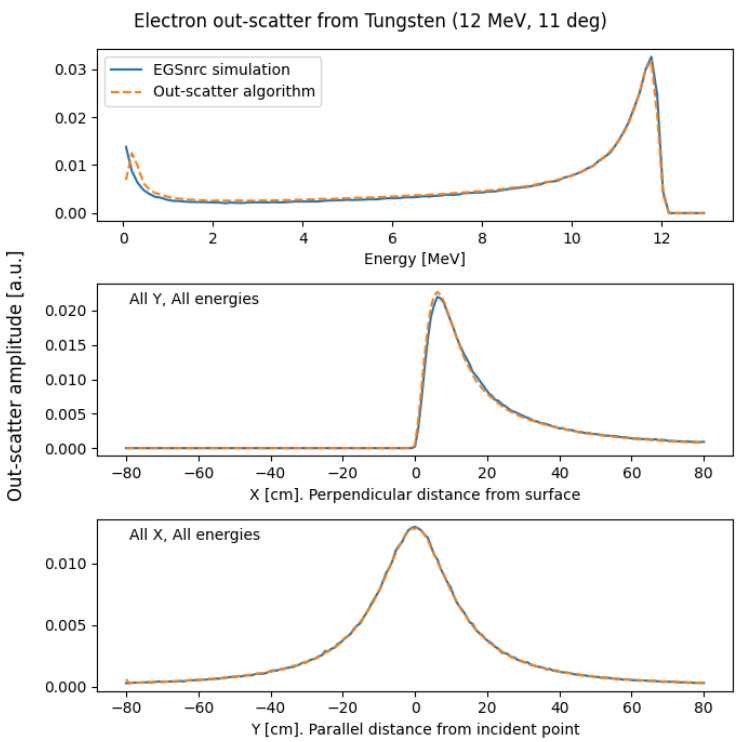

Figure 57. Simulated out-scatter for 12 MeV electrons incident at 11 degrees on a Tungsten surface. Spatial distributions are scored in a plane located 35 cm from the point of incidence.

Contamination photons

The dose distribution from contamination photons is calculated by the same dose engine as the electrons. After the direct and indirect electron particles have been transported to the beam line exit, the contamination photon fluence is sampled at the beam line exit. The photons are added to the set of active particles and are transported in the patient together with the electrons. The empirical energy spectrum of the treatment head generated bremsstrahlung photons is combined with a Gaussian lateral energy fluence modulation.

As input to the spectrum analysis we use a homogeneous water depth dose calculated as [56]

$$D_B(z) \propto [e^{-\mu_p z} - \nu e^{-\mu_e z}] \qquad \text{[Eq. 84]}$$

where z is the depth, E is nominal beam energy in MeV, $\mu_p = 0.08595/E^{0.2537}$, $\mu_e = 8.763/E^{0.7465}$ and $\nu = 428.9 \times (1 - e^{-0.0009928E^2})/E^{1.74}$. This depth dose shape is used to determine the photon energy spectrum.

The width σ_B of the lateral Gaussian is obtained from a lateral profile measured at a depth beyond the electron range. The photon dose under the blocking part of a cutout is attenuated by an empirical factor which can be derived from measurements of semi-blocked fields. The Gaussian fluence distribution is pixelized at the beam line exit plane, and pixels under the blocking part of the last layer in the beam line are reduced by the applicator transmission or cutout transmission if present. The initial photon position is uniformly sampled in a pixel sampled from the fluence distribution at the beam line exit. The photon direction is set so that it points from the primary source position.

Variance reduction

To increase the efficiency of the beam line transport, a number of common Monte Carlo variance reduction techniques are used (for a brief description, see [151]). After each beam line layer, particles that hit the edge top or front face and did not out-scatter are removed and can be replaced by splitting some of the surviving particles. The statistical weight is adjusted so that the total fluence is the same. The split particles are then transported independently.

In addition, Russian roulette is used to reduce the number of secondary low energy electrons in the beam line transport. Depending on a random number they are removed, or the statistical weight is increased to keep the fluence unbiased.

5.2.3 In-patient energy transport and energy scoring

Electron beam dose computation uses the same dose engine as the photon Monte Carlo dose computation for transporting particles and scoring dose in the voxelized patient dose grid. For details, see *section 4.6.4 Photon transport on page 112* to *section 4.6.8 Statistical uncertainty on page 116*. The exception is that the electron dose computation is set to score dose-to-water where photon dose is set to score dose-to-medium, see *section 4.7 Dose-to-water, dose-to-medium, or dose-to-tissue on page 119* and *section 5.2.4 Dose reporting, dose-to-water on page 168*.

A patient/phantom voxel is characterized by a material identifier and a density. The material identifier points to a discrete material with known composition. The modeling of materials is the same as used for the proton dose calculation algorithm, see *section 2.3.2 CT to material properties mapping on page 22*.

5.2.4 Dose reporting, dose-to-water

Monte Carlo methods, including the RayStation electron Monte Carlo, naturally lead to dose-to-medium with radiation transport in the medium, D_m^m. The RayStation electron Monte Carlo dose engine, however, reports dose-to-water, where dose-to-medium is converted into dose-to-water using a multiplication with the ratio of restricted mass collision stopping power of electrons, as recommended by AAPM TG-105 [117]. This gives D_w^m, dose-to-water with radiation transport in medium. Dose-to-water in this case is defined as the dose that would be deposited in a specific point if an infinitesimal volume of the tissue is replaced with an infinitesimal volume of water.

5.2.5 Electron density weighted depth

Electron density weighted depth is reported for the Beam Dose Specification Point after an electron dose calculation or after change of the Beam Dose Specification Point.

This quantity depends only on the patient geometry and is computed by a trace through the dose grid from the source to the specification point, taking patient material inside the External ROI, and Support, Fixation and boli ROIs into account. The path length through each voxel l is multiplied by the ratio of the electron density for the material assigned to the voxel ρ_{mat}^e and the electron density of water ρ_{water}^e. It is also multiplied by the mass density in the voxel ρ divided by the mass density of the assigned material ρ_{mat}. Since $\rho^e = \rho < Z/A >$ where $< Z/A >$ is the weighted mean nuclear Z/A ratio and the weight for each element corresponds to the mass fraction of that element in the material, then:

$$\textit{Electron density weighted depth} = \sum_i l_i \frac{\rho_i}{\rho_{water}} \frac{<Z/A>_{mat,i}}{<Z/A>_{water}} \qquad \text{[Eq. 85]}$$

where i = all traversed voxels. As described in *section 2.3.2 CT to material properties mapping on page 22*, a voxel is described as containing a different density version of a material in the material list. The electron density of the voxel is therefore dependent both on the material properties of the material (ρ_{mat} , ρ_{mat}^e) and the voxel density (ρ_i).

The electron density weighted depth will be DICOM exported as Beam Dose Point Equivalent Depth (300A,0089).

5.2.6 Algorithm weaknesses

Output for small cutout sizes

Limited accuracy in calculated output for small cutout sizes has been reported for the RayStation electron dose calculation for a previous RayStation version [141].

In RayStation 12A, the previously used plug-in for in-patient transport for the electron Monte Carlo dose engine (VMC++) was replaced by a fully integrated electron Monte Carlo dose engine. In the development of the new dose engine, improvements have been made to increase the accuracy for small cutout sizes. However, small cutout sizes are challenging and users of RayStation 12A should still take special care when using small cutout sizes.

The RayStation electron dose calculation does not include output factors for different cutout sizes, and there is no way to correct the output of an electron beam model for different cutout sizes. Therefore, differences in output between measured and computed dose for small cutout sizes cannot be corrected and is a limitation of the RayStation electron dose calculation.

WARNING!

Electron dose calculation for small cutout sizes. Limited accuracy in calculated output for small cutout sizes has been reported for the RayStation electron dose calculation. A difference between measured and computed output of more than 3% has been reported for cutout sizes of 4x4 cm^2, and more than 5 % for cutout sizes of 2x2 cm^2.

The user needs to be aware of this limitation and thoroughly verify the output of the calculated electron dose for small cutout sizes.

(142165)

5.3 STATISTICAL UNCERTAINTY

The statistical uncertainty for an electron dose is computed as described in *section 4.6.8 Statistical uncertainty on page 116*, with one important difference: For electrons, the uncertainty is always computed for each beam dose separately, not for the summed dose.

6 PROTON DOSE CALCULATION

RayStation supports planning for Pencil Beam Scanning (PBS), Line Scanning (LS), Uniform Scanning (US), Single Scattering (SS), Double Scattering (DS), and Wobbling proton beam delivery systems. This chapter gives a detailed description of the PBS and US/SS/DS/Wobbling proton dose calculation engines in RayStation. Since the dose engines are identical for PBS and LS, and these two modes can be referred to as step-and-shoot PBS and Line Scanning PBS, respectively, the term PBS will in this manual refer to both modes, unless explicitly stated.

For PBS beams, RayStation offers two clinical dose engines. One is based on the Pencil Beam algorithm, and the other is a Monte Carlo (MC) dose engine. Normally, a Pencil Beam dose calculation will be faster than that using MC, but is on the other hand less accurate. MC is especially recommended for patients/cases with large inhomogeneities and all beams using a range shifter. For beams that are collimated by a block aperture or an MLC, only MC will generate a clinical dose. Computation of LET is only supported in MC.

For PBS beams, RayStation supports machines that deliver discrete, step-and-shoot pencil beams (spots) organized in a finite number of energy layers. For LS beams, RayStation supports machines that deliver continuous lines within each individual layer. RayStation also has limited support for machines that deliver quasi-discrete spots. Quasi discrete PBS machines are modelled as step-and-shoot PBS, and spill dose is not calculated in RayStation. The energy layers for both PBS and LS are chosen either continuously within specified limits, or from a list of discrete energies defined in the treatment machine. The supported beam limiting devices include the use of fixed thickness range shifters, block apertures and MLC.

The same dose engines are used for LS as for step-and-shoot PBS, but special handling is needed in optimization and in the dose calculation, where the line segments are discretized into spots. This is described in detail in *section 6.11 Optimization and dose calculation for Line Scanning on page 250*.

For US, SS, DS and Wobbling beams, RayStation offers a clinical dose engine based on the Pencil Beam algorithm. Wobbling may be viewed as a hybrid between US and DS, and the algorithms in RayStation are therefore more or less identical to those for US/DS. There are however some differences and these differences are described in *section 6.8 Pencil beam dose computation for Sumitomo Wobbling beams on page 213*.

The Mitsubishi SELECT BEAM NOZZLE in US mode is in some aspects handled differently compared to generic US. The differences are described in *section 6.7 Pencil beam dose calculation for Mitsubishi Electric Corporation US beams on page 209*

In addition to the description of the dose engines, *section 8.2 Automatic proton beam parameters using Treat and Protect on page 325* accounts for how the US/SS/DS/Wobbling plans are determined from the Treat and Protect parameters in the Proton Beam Design Module.

In this chapter

This chapter contains the following sections:

6.1	Beam modeling of proton beams	p. 173
6.2	General algorithms	p. 174
6.3	Beam model parameters	p. 177
6.4	Pencil Beam dose engine	p. 180
6.5	Pencil Beam dose calculation for PBS beams	p. 188
6.6	Pencil Beam dose calculation for US/SS/DS/Wobbling beams	p. 198
6.7	Pencil beam dose calculation for Mitsubishi Electric Corporation US beams	p. 209
6.8	Pencil beam dose computation for Sumitomo Wobbling beams	p. 213
6.9	Monte Carlo Dose calculation	p. 216
6.10	Dose engine accuracy and limitations	p. 229
6.11	Optimization and dose calculation for Line Scanning	p. 250
6.12	Optimization and dose calculation for Mevion Hyperscan	p. 255
6.13	Optimization with spot dose cache	p. 260
6.14	Optimization with LET functions	p. 262

6.1 BEAM MODELING OF PROTON BEAMS

The machine model parameters in RayStation are comprised of geometrical/material properties of the machine (machine parameters), and of beam model parameters that are determined in the beam modeling procedure. The beam modeling procedure refers to the adjustment of different beam model parameters to the specific treatment machine used at the clinic, and needs to be done before clinical dose computation. The machine parameters are described in the RayPhysics manual. Normally, only one beam model is created for each machine (treatment room), but in RayStation it is possible to assign independent beam models for each beam line in a delivery system that has more than one (fixed) beam line in a treatment room. For proton PBS and LS machines, the beam modeling is done by the users in RayPhysics. The Pencil-Beam and MC dose engines share the same beam model. SS/DS/US/Wobbling machines are modeled by RaySearch Laboratories using beam data provided by the customer. For further details contact the RaySearch Laboratories support organization.

6.2 GENERAL ALGORITHMS

The section describes some algorithms that are equally used by both the Pencil-Beam and the Monte Carlo dose engines.

In this section

This section contains the following sub-sections:

6.2.1	Stopping power	p. 175
6.2.2	Linear Energy Transfer (LET)	p. 175
6.2.3	Energy loss straggling	p. 175
6.2.4	Water equivalent depth at beam dose specification point	p. 176
6.2.5	Compensator physical thickness at beam dose specification point	p. 176

6.2.1 Stopping power

The stopping power model in RayStation is used for on-the-fly calculation of radiological (water equivalent) depth, and for absolute energy loss in the Pencil Beam and Monte Carlo dose engines. We use the well-established Bethe-Bloch formula, where we have omitted the shell and density correction terms, which are only of importance for energies well below and above those of interest for therapeutic protons [65]. In the CGS system of units, the Bethe-Bloch stopping for protons in compounds can then be written as:

$$S = \rho \frac{a_1}{\beta^2}\left[a_2 - \ln\left(\frac{1}{\beta^2} - 1\right) - \beta^2\right]$$
$$\beta^2 = 1 - \left(1 + \frac{E}{m_p c^2}\right)^{-2} \qquad \text{[Eq. 86]}$$

with

$$a_1 = \frac{\kappa}{u}\sum_i w_i \frac{Z_i}{A_i}$$
$$a_2 = \ln\frac{2 m_e c^2}{I} \qquad \text{[Eq. 87]}$$
$$\kappa = \frac{4\pi e^4}{m_e c^2}$$

where E is the kinetic energy of the protons, Z_i, w_i, and A_i the elemental composition, in atomic number, weight and mass, respectively, and ρ and I the mass density, and mean ionization energy of the medium. u is the atomic mass unit, c the speed of light, m_e and m_p the electron and proton masses, and e the elementary charge.

6.2.2 Linear Energy Transfer (LET)

The unrestricted linear energy transfer, $LET_{-\infty}$, is the mean energy loss per pathlength due to all electronic collisions. It equals the total electronic collision stopping power.

The computation of linear energy transfer requires a more precise description of the unrestricted stopping power for low energies than the Bethe model. For this purpose, stopping power tables obtained with the FLUKA Monte Carlo code [88], [89] are used.

6.2.3 Energy loss straggling

Energy loss straggling is calculated using the classic Bohr expression, which assumes a Gaussian distribution of the energy loss after traversing a slab of thickness Δz. The standard deviation of the straggling is given by Bohr as:

$$\sigma_B{}^2 = 4\pi e^4 n_e \frac{1-\beta^2/2}{1-\beta^2} \Delta z \qquad \text{[Eq. 88]}$$

where n_e is the target total electron density given by

$$n_e = \frac{\rho}{u} \sum_i w_i \frac{Z_i}{A_i} \qquad \text{[Eq. 89]}$$

Energy straggling is only evaluated in the RayStation Monte Carlo dose engine, but is included here, since it is natural to describe in the same context as the stopping power.

6.2.4 Water equivalent depth at beam dose specification point

Water equivalent depth is the physical path length along a ray from the beam source to the BDSP, scaled with the relative stopping power between the traversed materials and water at 150 MeV/u. Differences in SAD X and Y are included in the calculation to match the dose calculation. Beam line objects are not considered.

Note: *Inaccuracies in the water equivalent depth calculation can occur due to dose grid resolution effects. These inaccuracies are the same as the range inaccuracies for the dose calculation.*

Note: *Inaccuracies in the computation of the water equivalent depth can occur when placing the BDSP in a region with a high density gradient.*

Note: *The user is advised to always use these values in combination with subsequent patient-specific QA.*

6.2.5 Compensator physical thickness at beam dose specification point

Compensator physical thickness is calculated as the thickness of the compensator along a ray from the beam source to the BDSP. Differences in SAD X and Y are included in the calculation to match the dose calculation.

Note: *Inaccuracies in the computation of the compensator physical thickness can occur when placing the BDSP in a region with a high compensator thickness gradient.*

Note: *The user is advised to always use these values in combination with subsequent patient-specific QA.*

6.3 BEAM MODEL PARAMETERS

This section describes the beam model parameters for proton machine models in RayStation, i.e. the parameters in the machine model that are derived from beam data measurements for a specific delivery system. In RayStation a single PBS machine model for a particular delivery system can support both the MC and the pencil beam dose calculations. The beam measurement data needed for commissioning the MC dose engine is thus the same as is needed for the pencil beam dose engine.

In addition to beam model parameters, the machine model also contains machine parameters, which are described in the RayPhysics manual. Examples of machine parameters are geometrical and material properties of range shifters, compensator, block aperture (including the dimensions of available milling tools) and MLC, as well as inner and outer dimensions and extension limits of the snouts included for the machine. The lateral limitations of a scanning field is also included in the machine parameters.

For most PBS machines, one beam model is assigned per machine, but RayStation also supports one beam model per fixed gantry angle.

For US/SS/DS/Wobbling, the beam model parameters are organized in one or several range intervals, referred to in RayStation as Range Options. The Range Options may be viewed as independent sub beam models within the machine model, that may be defined for intervals of prescribed range/nominal beam energy and field size.

6.3.1 Beam model parameters

The beam model parameters, which are the same for PBS, SS, DS, US and Wobbling beams in RayStation, include:

- Effective energy spectrum: *dN/dE*
  - Function of the nominal beam energy
- Spatial-angular distribution moments at the isocenter: $\{\overline{\theta_0^2}, \overline{r\theta_0}, \overline{r_0^2}\}$, referred to as spatial-angular moments
  - In cylindrical coordinates
  - Function of the nominal beam energy
  - Can also be a function of the snout position, e.g., for systems with the vacuum window placed in the extendable part of the nozzle
- Beam meterset calibration: S_{MU}
  - In units of Ions/MU or NP (PBS/US) or Protons/(MU cm^2) (SS, DS, Wobbling, Mitsubishi Electric Corporation SELCT BEAM NOZZLE in US mode)
  - Function of the nominal beam energy
- The virtual source axis distance in X and Y: SAD_{vir}^{Y} and SAD_{vir}^{X} :

- For PBS and US:
  - Provided explicitly as the effective focal points of the scanning magnets: f_X and f_y
  - Constant value over the energy range

- For SS, DS and Wobbling:
  - Provided implicitly by the spatial-angular moments: $\overline{x_0^2}/\overline{x\theta_0}$ and $\overline{y_0^2}/\overline{y\theta_0}$
  - Function of the nominal beam energy

In addition to the parameters above, the effective weights of the range modulation steps of a US/SS/DS/Wobbling SOBP are also included in the beam model parameters. The weights are determined per Range Option and may therefore vary with the range of the field.

6.3.2 Interpolation of beam model parameters

The energy dependent beam model parameters of a machine (i.e. the energy spectrum, the spatial-angular moments, and the dose monitor sensitivity) are stored for a discrete number of nominal beam energies in the RayStation machine model. However, most beam delivery systems allow for a continuous selection of maximum range/nominal beam energy. In RayStation, this is handled by interpolating the model parameters of an arbitrary nominal energy, between parameters with closest matching nominal energies in the machine model. For SS/DS/US/Wobbling, this interpolation is always performed for parameters within each Range Option, which thus allows for discrete jumps in parameter values when going from one Range Option to the next.

The spatial-angular moments and the dose monitor sensitivity are linearly interpolated between the stored nominal energies. For machines with movable snouts, the spatial-angular moments of each nominal beam energy may also be stored for a discrete number of snout positions. In this case the spatial-angular moments are determined for both the specific nominal energy and snout position by linear interpolation.

The energy spectrum for an arbitrary nominal energy E_N, $dN/dE|_{E_N}$, is determined by interpolating between the stored energy spectra with closest lower (E_{N1}) and upper (E_{N2}) nominal energies, $dN/dE|_{EN1}$ and $dN/dE|_{EN2}$, respectively:

$$\frac{dN\,(E)}{dE}\Big|_{E_N} = c_1 \frac{dN\,\left(E - E_{m,E_N} + E_{m,E_{N1}}\right)}{dE}\Big|_{E_{N1}} + c_2 \frac{dN\,(E - E_{m,E_N} + E_{m,E_{N2}})}{dE}\Big|_{E_{N2}} \qquad \text{[Eq. 90]}$$

where E_{m,E_N}, $E_{m,E_{N1}}$ and $E_{m,E_{N2}}$ are the mean beam energies of the interpolated and the two neighboring energy spectra, respectively. E_{m,E_N} is determined by linear interpolation between $E_{m,E_{N1}}$ and $E_{m,E_{N2}}$:

$$E_{m,E_N} = E_{m,E_{N1}} + \frac{(E_{m,E_{N2}} - E_{m,E_{N1}})}{(E_{N2} - E_{N1})}(E_N - E_{N1})$$ [Eq. 91]

The relative weights c_1 and c_2 in Equation 90 are given by:

$$c_1 = (E_{m,E_{N2}} - E_{m,E_N}) / (E_{m,E_{N2}} - E_{m,E_{N1}})$$
$$c_2 = (E_{m,E_N} - E_{m,E_{N1}}) / (E_{m,E_{N2}} - E_{m,E_{N1}})$$ [Eq. 92]

It is straightforward to show that the variance of the interpolated spectrum will vary linearly with the nominal energy between the variance of $dN/dE|_{E_N1}$ and $dN/dE|_{E_N2}$.

For US/SS/DS/Wobbling beams, all parameters in the beam model are derived from measurements (e.g. pristine Bragg peaks) for fields with a certain prescribed maximum range. However, the beam model parameters are stored as a function of nominal beam energy and not prescribed range. To convert the prescribed ranges of the measurements to nominal energies, the same conversion function is used in the beam modeling procedure as that used in the dose computation (*section 6.6.1 Beam model on page 199*). This means that the exact form of the range to energy function is not crucial, and may be viewed as a way to interpolate the parameters at a given prescribed range between those provided in the beam model.

The spatial-angular moments are most often modeled by a single set of distribution moments (single Gaussian model). However, there are delivery systems where this assumption is not valid, and RayStation therefore supports the use of two sets of distribution moments to model the beam (double Gaussian model). The secondary set of moments is coupled with a weight that defines the fraction of the fluence that originates from the primary and secondary spatial-angular moments. The double Gaussian model is only supported in the Monte Carlo dose engine and hence only allowed for PBS beams. If the pencil beam dose engine is used for a machine with a double Gaussian beam model, the secondary set of distribution moments will be discarded and the dose will be labeled as non-clinical (approximate) dose.

6.4 PENCIL BEAM DOSE ENGINE

The analytical proton dose engine in RayStation is a so-called pencil beam dose algorithm, where the proton fluence is decomposed into a large number of closely spaced mini-beams. In this manual we will refer to these algorithmic mini-beams as "pencil-beams", while physical pencil beams delivered by a PBS system will be referred to as "spots". The dose contribution from each of these pencil beams is calculated by performing a factorization of the dose to the lateral proton fluence Φ and the longitudinal, integrated depth dose IDD components:

$$dose(z,r) = \Phi(z,r)IDD(z) \qquad \text{[Eq. 93]}$$

where z is the coordinate along the pencil-beam central axis and r the radial coordinate in the lateral plane.

This factorization is only correct within the so-called infinite slab approximation, which stipulates that the patient model consists of semi-infinite layers, extended transversally to the central beam axes. The pencil beams thus get a radial symmetry, and therefore a pencil like shape, giving its name to the algorithm.

In the dose computation a set of phase space parameters are initialized and transported along the central axis of each pencil beam through the patient according to *section 6.4.1 Initialization and tracing of phase space parameters on page 181*, under the influence of stopping power, Multiple Coulomb Scattering, and non elastic Nuclear Scattering. The lateral fluence function (Φ) of Equation 93 is given directly from the phase space parameters, while the integrated depth dose is obtained by the stopping power scaling of a reference integrated depth dose (IDD) curve. The unscaled IDD is valid for the dose deposition in water. The algorithm therefore generically provides absorbed dose as dose-to-water. The pencil beam algorithm has been extensively used in various proton dose algorithms [68], [58], [63], [73], [67], [77], [72], [57].

The decomposition of the total proton fluence into a number of discrete pencil beams is different for a PBS and a US/SS/DS/Wobbling beam in RayStation. For PBS, each spot is discretized to a number of pencil beams (sub-spots), which are not reused, nor shared with other spots. For a US/SS/DS/Wobbling beam, which has a uniform intensity in each energy layer, the fluence plane is discretized using an orthogonal grid, with a pencil beam originating from each pixel and energy layer. This section describes the features of the RayStation pencil beam dose engine that are shared between PBS and US/SS/DS/Wobbling, while the parts that differ are given in *section 6.5 Pencil Beam dose calculation for PBS beams on page 188*, *section 6.5 Pencil Beam dose calculation for PBS beams on page 188* and *section 6.8 Pencil beam dose computation for Sumitomo Wobbling beams on page 213*, respectively.

In this section

This section contains the following sub-sections:

6.4.1	Initialization and tracing of phase space parameters	p. 181
6.4.2	Energy loss and radiological depth	p. 182
6.4.3	Multiple Coulomb Scattering	p. 182
6.4.4	Nuclear scattering	p. 184
6.4.5	Calculation of the integrated depth dose in water	p. 186
6.4.6	Scoring of dose	p. 187

6.4.1 Initialization and tracing of phase space parameters

The dose computation of a pencil beam starts at the entrance of the patient outline, or the most upstream device of aperture (block or MLC) and range compensator if present. The initial phase space parameters needed for each pencil beam are defined as:

- Mean direction, $e = \{e_x, e_y, e_z\}$,
- Mean beam energy, E_m
- Spatial-angular moments, $\{\overline{\theta^2}, \overline{r\theta}, \overline{r^2}\}$
- Integrated depth dose in water, IDD^w

The values of these parameters are determined by the beam model, as described in *section 6.5.1 Beam model on page 189* and *section 6.6.1 Beam model on page 199*, where the mean direction **e** is calculated from the virtual source axis distance along the X- and Y-axes, respectively:

$$e_x = \frac{x}{SAD^x_{vir}}/k$$
$$e_y = \frac{y}{SAD^y_{vir}}/k \qquad \text{[Eq. 94]}$$
$$e_z = 1/k$$

Where k is a normalization factor to ensure |**e**|=1.

Starting at the center of each pencil beam, a ray trace with direction **e** is performed going through the compensator and the air gap (if present), and then through the voxelized patient geometry.

The tracing grid in the patient coincides with the dose grid, where the Hounsfield value of a voxel is the average of all Hounsfield values within that voxel as determined from the original CT data, which often is obtained at a higher resolution than the tracing/dose grid. The entrance point of the patient is taken as the entrance point of the first voxel along the trace path that is (partially) intersected by

the patient outline. (For the handling of the density of the surface voxels, see *section 2.7.1 Dose grid effect on the External ROI on page 35*.)

The material properties of each voxel are either reconstructed from the Hounsfield values (*section 2.3.2 CT to material properties mapping on page 22*), or are given explicitly when tracing trough an ROI associated with a material override. As the tracing progresses, the mean beam energy, the spatial-angular moments, and the radiological depth, z^w, are calculated and stored at the crossing points of each voxel surface. The tracing continues until the mean beam energy has fallen below the stopping threshold value (1 MeV), or the tracing exits the grid.

The handling of range shifter and aperture for PBS is described in *section 6.5.3 Modeling of a range shifter on page 195* and *section 6.5.4 Modeling of an aperture on page 196* and the details of the tracing procedure through a compensator and block and MLC for US/SS/DS/Wobbling are given in *section 6.6.2 Transport through aperture and compensator on page 202*.

6.4.2 Energy loss and radiological depth

The mean energy loss over distances up to 1 cm is computed using the 4-point Runge-Kutta (RK4) method [69]. For greater thicknesses, e.g. in the calculation of the mean energy loss through a range shifter, the total thickness is divided into slabs of thickness ≤ 1 cm.

The radiological, or water-equivalent, depth, z_w, is a measure that is widely used in treatment planning. In the pencil beam dose engine, z_w is for example used to determine the deposited dose at a certain depth from a reference depth dose curve in water. For photon radiation, z_w is usually determined as the integral of the path length, weighted by the medium to water electronic density ratio. This approximation does not hold so well for protons, since the proton stopping power not only depends on the electronic density, but also on material composition. Instead, we determine z_w as the integral of the path length, weighted by the medium to water stopping-power ratio.

$$z^w(z) = \int_0^z \frac{S(z')}{S^w(z')}\, dz' \qquad \text{[Eq. 95]}$$

With this definition, z^w is the depth in water where a beam has lost the same amount of energy via electronic stopping, as it has at depth z in the patient.

6.4.3 Multiple Coulomb Scattering

The lateral spread caused by multiple coulomb scattering (MCS) is treated in the framework of Fermi and Eyges [59]. There are two main limitations to this theory:

1. it only handles Gaussian distributions, and therefore omits the non-Gaussian tails, which are also created by MCS [60].
2. it does not take lateral inhomogeneities into account.

Fermi-Eyges transport

Using the small angle approximation, Fermi and Eyges solved the transport equation considering a lateral, diffusive scattering power T along a transport step z, and showed that an initial Gaussian distribution remains Gaussian after the step and is characterized by:

$$\overline{\theta^2}(z) = \overline{\theta^2}(0) + \int_0^z T dz'$$

$$\overline{r\,\theta}(z) = \overline{r\,\theta}(0) + \overline{\theta^2}(0)\ z + \int_0^z (z - z')\ T dz' \qquad \text{[Eq. 96]}$$

$$\overline{r^2}\,(z) = \overline{r^2}\,(0) + 2\overline{r\theta}\,(0)\ \ z + \overline{\theta^2}\,(0)\ \ z^2 + \int_0^z (z - z')^2\ T dz'$$

where $\overline{\theta^2}$ is the angular variance, $\overline{r\theta}$ the spatial-angular covariance (beam divergence), and $\overline{r^2}$ the spatial variance of the Gaussian distribution. The set of spatial angular distribution moments, i.e. $\left\{\ \overline{\theta^2}, \overline{r\theta}, \overline{r^2}\ \right\}$, is referred to as the spatial-angular moments in the beam model. It should be noted that we refer to cylindrical coordinates in our use of the spatial-angular moments. This also reflects on the definition of the scattering power, see *Scattering Power on page 183*.

Scattering Power

For scattering power, we use the expression of Rossi [62]:

$$T = \left(\frac{E_s}{p\beta c}\right)^2 \frac{1}{X_0} \qquad \text{[Eq. 97]}$$

where p is the proton momentum and X_0 is the radiation length, for which we use the expressions suggested by Tsai [74]. For compound materials, the radiation length is calculated according to Bragg's rule [61]:

$$X_0{}^{-1} = \sum_i w_i\, X_{0i}^{-1} \qquad \text{[Eq. 98]}$$

E_s in Equation 97 is a constant given by Rossi as E_s=21 MeV. However, a study of published measurements of lateral spread in water [67], [71], [63] and [75], revealed that a value E_s=18 MeV gave the overall best fit. Interestingly enough, this value falls right between the suggested values in two similar studies: E_s=17.0 MeV [73] and E_s=18.7 MeV [67].

Note: *The quoted values for E_s refer to radial, and not projected, scattering power.*

There are more sophisticated scattering power models than that of Rossi, but it has been shown that the difference for low Z materials in the therapeutic energy range is small [70], [61].

6.4.4 Nuclear scattering

The lateral scattering of a proton beam can be considered to be composed of a central, small-angle part that generates a more-or-less Gaussian distribution around the central axis, and a large-angle component that generates a wide, low-intensity distribution around the Gaussian distribution, sometimes referred to as the nuclear halo. The former is typically associated with MCS, and the latter with nonelastic nuclear scattering (NS). This is a somewhat oversimplified picture, since MCS also contributes to the non-Gaussian tail of the lateral distribution [60]. Since the non-Gaussian tails of the lateral distribution is a large-volume, low-dose phenomenon, the reproduction of the detailed shape of the nuclear halo is not critical. Despite of this, the inclusion of the halo in itself is important since it removes up to 18% of the dose from the central Gaussian region [73].

As opposed to the Gaussian part of the MCS, there is no simple, computationally efficient solution to the transport equation for the nuclear halo. Instead, more ad hoc methods have to be used. In 2005, two studies where published, suggesting the use of a second, NS Gaussian in the lateral fluence function [67], [73]. In these works, the width, σ^{NS}, and relative weight, w^{NS}, of the NS Gaussian are given as a function of the initial beam energy and the radiological depth, z_w. Recently, a third experimental study was also published giving an alternative parameterization of the NS Gaussian [57]. The major drawback of this method is that it does not handle transport in inhomogeneous systems. This is especially a problem when thick compensators or range shifters are used in combination with relatively large air gaps. For these setups, the lateral spread of the nuclear halo is underestimated, which may lead to an overestimation of the dose level, especially at shallower depths and for small- and medium-sized fields.

In the RayStation proton Pencil Beam dose engine, the results from Soukup et al [73] who provided compact look-up formulas for the NS Gaussian parameters of an initially infinitely thin proton beam are used:

$$\frac{\sigma_0^{NS}}{\sqrt{2}} = 0.285 + 0.0014R^B \ln(10z^w + 3) + 0.06z^w$$

$$-7.4 \times 10^{-4}(z^w)^2 - 0.0022\,\frac{R^B}{(z^w - R^B - 0.5)^2}$$

$$w^{NS} = 0.052 \ln\left(1.13 + \frac{z^w}{1.12 - 0.023R^B}\right)$$

$$+0.035\frac{R^B\,\left(0.017R^B - 1\right)}{(R^B + 0.3)^2 - (z^w)^2} - 1.61 \times 10^{-6} z^w \left(R^B + 0.3\right)^2$$

[Eq. 99]

where R^B is range of the proton beam in water. R^B and z^w should here be given in units of cm. Under the assumption that the MCS is correctly handled by the dose engine, it is mainly the treatment of the fluence in the nuclear halo that decides how well the dose engine will handle the absolute output for small field sizes. A field size study performed at RaySearch in collaboration with IBA, demonstrated that the expression above did not accurately predict the output for field sizes between

4x4 cm^{2}and 12x12 cm^2, in the energy range between 120 MeV and 226 MeV. For this reason, a correction to the σ^{NS} of Soukup has been developed:

$$\sigma_{0,corr}^{NS} = (1 + c_0 e_0)\sigma_0^{NS} \qquad \text{[Eq. 100]}$$

Where $c_0 = c_0(z_w/R_B)$ and $e_0 = e_0(E_{RB})$ are piece-wise linear functions as depicted in Figure 58, and E_{RB} is the energy corresponding to a mono energetic proton field with range R_B in water.

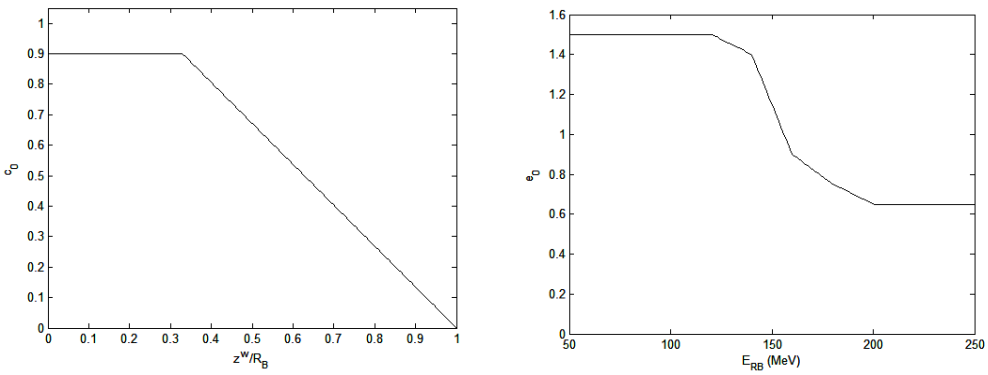

Figure 58. The functions c_0 (left) and e_0 (right) used in the corrected expression for the nuclear halo size.

σ_0^{NS}, $\sigma_{0,corr}^{NS}$ and w^{NS} of Equation 99 are depicted in Figure 59 as functions of z^w for a number of beam energy between 50 MeV and 250 MeV.

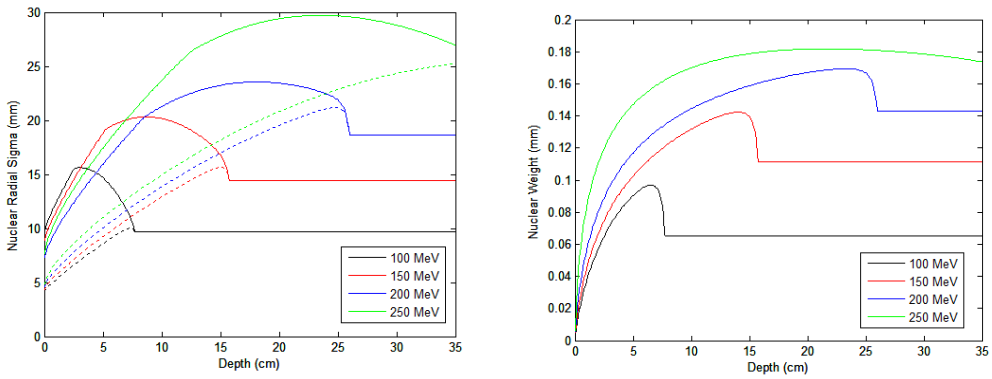

Figure 59. Standard deviation (left) and relative weight (right) of the NS Gaussian as a function of depth for initial proton energies of 50 to 250 MeV. The standard deviation graph shows both the original expression of Soukup et al. Equation 99 (broken lines) and the modified version used in RayStation, Equation 100 (solid lines).

One may speculate on why this, sometimes relatively large, correction had to be included. Soukup et al. extracted their σ_0^{NS} by fitting two Gaussians (MCS + NS) to the lateral profiles of single spot doses, obtained from Monte-Carlo (MC) simulations. Setting any possible inaccuracy of the MC dose engine aside, one important point is that a Gaussian function does not describe the shape of the nuclear halo profile very accurately, as pointed out by e.g. Pedroni et al. [67]. This means that the Gaussian that gives the best possible fit to the nuclear halo of a single spot may not be the one that gives the most accurate result in a field size study. In this context it is interesting to note, that the modified σ_0^{NS} as compared to the original expression, has a closer resemblance to the corresponding nuclear sigma as determined in the experimental study of Pedroni et al. [67]. Another possible contribution to the correction could be the contribution from a non-Gaussian tail in the spot fluences of the proton delivery system used for the field size study. Such tails were not seen in the measured spot profiles, but could exist below the noise level of those measurements. In that case, the corrected NS sigma may not be entirely general, but will, at least partly, include a machine specific component and may have to be revised when experience from more systems has been gained.

In the pencil beam dose calculation, the width of the nuclear scattering is determined by modulating the nuclear scattering Gaussian described in this section with the width of the MCS part [73]:

$$\sigma^{NS} = \sqrt{(\sigma_{0,corr}^{NS})^2 + (\sigma^{MCS})^2} \qquad \text{[Eq. 101]}$$

6.4.5 Calculation of the integrated depth dose in water

The integrated depth dose in water and the proton energy spectrum are to a large extent interchangeable entities. In RayStation, the beam model first provides the energy spectrum

$dN/dE|_{E_N}$ for a certain energy. The integrated depth dose, IDD^w, is then determined from $dN/dE|_{E_N}$, by superposition of Monte-Carlo pre-calculated, mono-energetic IDDs:

$$IDD^w(z, E_N) = \sum_i \frac{dN(E_i)}{dE}|_{E_N} \; idd_i(z)\Delta E_i \qquad \text{[Eq. 102]}$$

where idd_i is the pre-calculated integrated depth profile in water with an energy of E_i, in units of cGy cm^2/proton. The energy spacings $\Delta E_i = (E_{i+1} - E_{i-1})/2$ are chosen to give a corresponding spacing of the *IDD* bragg peaks of 0.2 mm, and the depth resolution of the *IDD*s is likewise set to 0.2 mm. The energy spectrum of Equation 102 is normalized to unity.

The *IDD*s are determined by lateral integration of mono-energetic, single-spot dose calculations using the RayStation Monte Carlo dose engine (see *section 6.9 Monte Carlo Dose calculation on page 216*). This means that the depth dose of a simple field in water (no range shifter or other beam modifier used) calculated with the RayStation Pencil-Beam algorithm should always match that of the RayStation Monte Carlo dose engine, as long as they have been calculated from the same energy spectrum. This statement is actually only true for a certain field size, since the field-size dependence is different for the two dose engines. The field-size effect will saturate for smaller field sizes using the pencil beam dose engine as compared to the Monte Carlo algorithm, which is the more accurate of the two. This means that a choice has to be made in the calculation of the mono-energetic *IDD*s. Namely at which field size the exact match is to be achieved. If the *IDD*s are determined by radially integrating the Monte Carlo calculated single spot doses to infinity, one could expect that the depth doses in water of the PB and MC dose engines will agree at very large field sizes, >20x20 cm^2. However, for more commonly used field sizes around 10x10 cm^2, the PB dose engine would yield too high a dose, especially at higher energies. To achieve the best match between PB and MC doses for a field size around 10x10 cm^2, the mono-energetic IDDs used in Equation 102 are instead calculated as:

$$idd_i(z) = idd_i^{\varnothing 11cm}(z)/f_i^{\varnothing 11cm}(z) \qquad \text{[Eq. 103]}$$

Where $idd_i^{\varnothing 11cm}(z)$ is the Monte Carlo calculated spot dose at energy E_i integrated to a diameter of 11 cm, and $f_i^{\varnothing 11cm}(z)$ is the corresponding fraction of dose within that circle as given by the pencil-beam dose engine (Equation 116).

6.4.6 Scoring of dose

The scoring and summation of dose from the individual pencil beams is described in *section 6.5.2 Scoring of dose in the patient (PBS) on page 193* for PBS and *section 6.6.3 Scoring of dose in patient on page 206* for US/SS/DS beams. The dose is calculated at the center of each voxel, and this dose will represent the dose in the entire voxel. The dose in RayStation is given as dose-to-water.

6.5 PENCIL BEAM DOSE CALCULATION FOR PBS BEAMS

A PBS plan consists of a number of energy layers, each with a matrix of spot positions and corresponding meter-set weights. This section gives a detailed description on how the RayStation pencil beam dose engine calculates the dose for a PBS plan. However, it only provides details that are specific to PBS beams, while the algorithms that are valid for all pencil beam dose calculations in RayStation are given in *section 6.4 Pencil Beam dose engine on page 180*. The reader is advised to be well acquainted with the content of *section 6.4 Pencil Beam dose engine on page 180*, before reading this section.

In this section

This section contains the following sub-sections:

6.5.1	Beam model	p. 189
6.5.2	Scoring of dose in the patient (PBS)	p. 193
6.5.3	Modeling of a range shifter	p. 195
6.5.4	Modeling of an aperture	p. 196
6.5.5	Modeling of an energy selector	p. 197

6.5.1 Beam model

The phase space of a single spot in RayStation is given by:

- Mean direction of the protons: **e**
- Energy spectrum: dN/dE
- Spatial-angular distribution moments: $\{\overline{\theta^2}, \overline{r\theta}, \overline{r^2}\}$
- Absolute spot weight: w^a (in units of number of protons)

For a given spot position, nominal beam energy, and meter-set weight (as given by the plan), these parameters are obtained more or less directly from the phase space parameters of the machine model defined in section beam model parameters.

The mean direction **e** is calculated as described in *section 6.4.1 Initialization and tracing of phase space parameters on page 181*, with SAD_X^{vir} and SAD_Y^{vir} determined by the effective scanning magnet focal lengths, f_x and f_y, respectively (See *section 6.3.1 Beam model parameters on page 177*).

The spatial-angular moments obtained from the phase space parameters in the machine model are transported from the isocenter plane to the entry point of the patient, see *Fermi-Eyges transport on page 183*. This, typically upstream transport step, is performed in vacuum, since the spatial-angular moments of the beam model have been extracted from measured spots assuming vacuum.

The absolute weight of the spot is given as the product of the meterset weight from the plan (in units of MU) and the energy dependent dose monitor sensitivity as provided by the phase space parameters in the machine model.

Discretization of the spot fluence

By studying the phase space parameters of a spot and the parameters needed to calculate dose for a single pencil-beam (*section 6.4.1 Initialization and tracing of phase space parameters on page 181*), it becomes obvious that it is possible to represent a spot by just a single pencil-beam tracing, referred to as single tracing below. However, considering that a pencil-beam sees the patient as a stack of semi-infinite layers, lateral inhomogeneities within the area of the spot fluence will not be accurately accounted for [77]. One way to improve on, albeit not completely solve, this problem is to discretize the spot into a number of sub-spots. There have been two approaches:

1. Scahffner et al. [77] discretized the fluence plane using a regular grid and performed a pencil-beam computation for each pixel. The weight of this pixel-dose in the total dose was then decided by the fluence contribution to that pixel from all spots in the energy layer. This method has computational advantages, but does not consider the fact that the mean direction of protons at a point in the plane is not the same for different spots. Instead, **e** for a certain point will be solely determined by SAD_{vir}, and the angular phase space of the spot is therefore lost. It is easy to understand the problem with this algorithm considering a system where the spots are not divergent, but focused towards the isocenter.
2. Soukup et al. had another approach to the problem [73]. They also created a discretized fluence grid, but did so for each spot separately. In this way, the phase space of the original

spot was not lost. The number of pixels used for each spot was configurable in the series 1, 9, 25, 49, 81,...

The sub-spot division in RayStation handles each spot separately, but unlike Soukup et al. we do not use a regular grid but set up the sub-spots in concentric circles. Below follows a detailed account for the sub-spot (multi tracing) algorithm in RayStation.

Start by considering a spot characterized by the spatial-angular moments $\{\overline{\theta^2}, \overline{r\theta}, \overline{r^2}\}$ at some depth z (referred to below as the original spot). The spatial fluence of the original spot can then be expressed as:

$$\Phi_{spot} = G(x, y, 0, 0, \sqrt{\overline{r^2}}) \qquad \text{[Eq. 104]}$$

where G is the Gaussian distribution centered at the coordinates $\{x_0, y_0\}$:

$$G(x, y, x_0, y_0, \sigma_{1/e}) = \frac{1}{\pi\sigma_{1/e}^2} \exp\left[-\frac{(x-x_0)^2 + (y-y_0)^2}{\sigma_{1/e}^2}\right] \qquad \text{[Eq. 105]}$$

where $\sigma_{1/e}^2$ is the variance of G in cylindrical coordinates (i.e. $\sigma_{(1/e)}^2 = 2 \times \sigma_{proj}^2$, where σ_{proj}^2 is the variance projected on one of the coordinate axes). We will now try to recreate the spatial fluence of Φ_{spot} by a superposition of the fluence from 19 sub-spots, one at the center, and 6 and 12 positioned at two concentric circles around the center spot. The multi tracing spatial fluence becomes:

$$\begin{aligned}\Phi_{MT} &= w' G(x, y, 0, 0, \sqrt{\overline{r^2}'}) + w'' \sum_{i=2:7} G(x, y, x_i, y_i, \sqrt{\overline{r^2}''}) \\ &+ w''' \sum_{i=8:19} G(x, y, x_i, y_i, \sqrt{\overline{r^2}'''})\end{aligned} \qquad \text{[Eq. 106]}$$

where $\{x_i, y_i\}_{i=2:7}$ are evenly distributed on a circle with a radius r'', and $\{x_i, y_i\}_{i=8:19}$ are evenly distributed on a circle with a radius r'''. To determine the relative weights (w', w'', w'''), positions (r'', r'''), and sizes ($\overline{r^2}'$, $\overline{r^2}''$, $\overline{r^2}'''$) of the sub-spots in Equation 106, an optimization is performed where the fit of Φ_{MT} to a single Gaussian (Φ_{spot}), as well as the amount of overlapping of the sub-spots are considered. The weighting between these conflicting goals are set such that the The fluence error, $\Delta\Phi = \Phi_{MT} - \Phi$ spot shall not exceed 1% of the maximum spot fluence, at any point in the fluence map. The solution to the optimization yields the following parameters:

$$w' = 0.0747$$
$$w'' = 0.1009$$
$$w''' = (1-w'-6w'')/12$$

[Eq. 107]

$$r'' = 0.5878\sqrt{\overline{r^2}}$$
$$r''' = 1.2118\sqrt{\overline{r^2}}$$

[Eq. 108]

$$\overline{r^2}' = 0.2050\overline{r^2}$$
$$\overline{r^2}'' = 0.2865\overline{r^2}$$
$$\overline{r^2}''' = 0.3385\overline{r^2}$$

[Eq. 109]

The placement and size (FWHM) of the sub-spots are depicted in Figure 60. The fluence error of Equation 106 is shown in Figure 61, which confirms the premise that $|\Delta\Phi| < 1$.

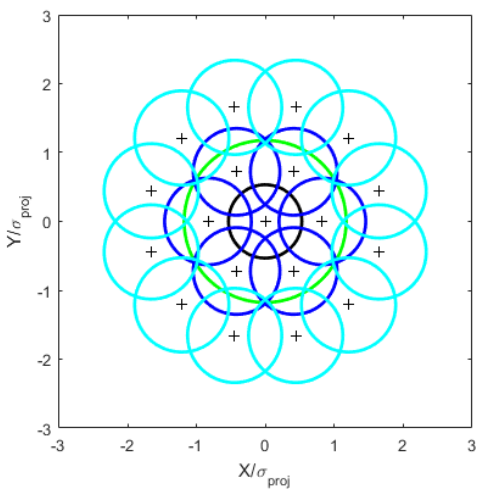

Figure 60. Distribution of the 19 sub-spots where the diameter of the circles represents the FWHM of the sub-spots (black, blue and cyan) and of the original spot (green) in relation to the projected σ of the original spot size.

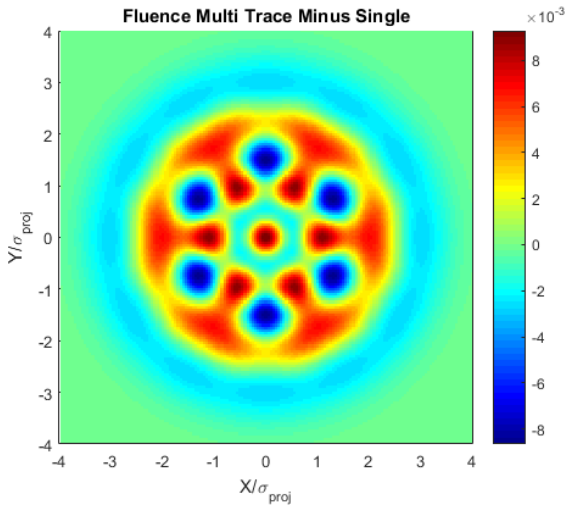

Figure 61. The difference between the multi traced (Equation 106) and the original spot fluences, in relation to the maximum fluence of the original spot.

After the spatial distribution of the sub-spots has been established, the angular distribution has to be considered. The mean direction of the sub-spots (below described by the polar angle θ relative the original spot) is taken as the most probable direction for the protons in the original spot [66], at positions corresponding to the centers of the sub-spots:

$$\overline{\theta}_1 = 0$$

$$\overline{\theta}_{2:7} = r'' \frac{\overline{r\theta}}{\overline{r^2}} \qquad \text{[Eq. 110]}$$

$$\overline{\theta}_{8:19} = r''' \frac{\overline{r\theta}}{\overline{r^2}}$$

The divergence of each sub-spot, $\overline{r\theta}_i$, is less straight forward to deduce. After testing a variety of expressions, the final conclusion was simply to set the sub-spot divergence to 0:

$$\overline{r\theta}_i = 0 \qquad \text{[Eq. 111]}$$

The angular spread of a sub-spot i can be obtained if we stipulate that the angular spread at any given point of any of the sub-spots shall be equal to the angular spread at any point of the original spot:

$$\overline{\theta_{Ci}^2} = \overline{\theta_C^2} \qquad \text{[Eq. 112]}$$

where $\overline{\theta_C^2}$ is the local angular spread at some spatial point of a spot. We can now use the fact that the local angular spread for a spatial-angular Gaussian distribution is constant for all points in the plane, and is given by [66]:

$$\overline{\theta_C^2} = \overline{\theta^2} - \frac{\overline{r\theta}^2}{\overline{r^2}} \qquad \text{[Eq. 113]}$$

With Equation 111, Equation 112 and Equation 113, we now finally get the (total) angular spread of each sub-spot as:

$$\overline{\theta^2}_i = \overline{\theta^2} - \frac{\overline{r\theta}^2}{\overline{r^2}} \qquad \text{[Eq. 114]}$$

Sub-spot algorithm limitations

With the sub spot arrangement of Equation 106 and Equation 107, the distance between neighbouring sub-spots is roughly equal at $0.6\sigma_{1/e} \approx 0.85\sigma_{proj}$. The question is if this distance is sufficiently small for all situations. For a 5 mm (σ_{proj}) spot, the sub-spot distance thus becomes ~4 mm, but for very large spots, the distance between the sub-spots may become larger than some geometrical variations of the patient. This could for example be the case when a range shifter with a large air gap is used in combination with low beam energies. This effect would decrease if more sub-spots were used, but the choice of 19 sub-spots is a compromise between the sufficiently dense sampling of the patient geometry for typical spot sizes, and the calculation speed.

6

6.5.2 Scoring of dose in the patient (PBS)

The scoring of the dose from a PBS plan is performed in receiving mode, where the total dose to point (x, y, z) in the patient is determined as the sum of the contributions from the spots j of each energy layer e:

$$dose\ (x, y, z) = \sum_e \sum_j S_e w_{ej}^{MU} d_{ej}(x, y, z) \qquad \text{[Eq. 115]}$$

where S_e is the energy dependent dose monitor sensitivity in units of protons/MU, w_{ej}^{MU} the meterset weight of spot j in energy layer e, and d_{ej} the dose contribution to the point (x, y, z) from spot ej in units of cGy per proton. S_e is obtained from the machine model while w_{ej}^{MU} is a plan parameter. d_{ej} is the sum of the dose contributions from all sub-spots and from the nuclear halo:

$$d_{ej}(x,y,z) = \sum_{k=1:19} (w_k \Phi_{ejk}^{MCS} IDD_{ejk}) + \Phi_{ej}^{NS} IDD_{ej} \qquad \text{[Eq. 116]}$$

where w_k is the relative weight of sub-spot *k* according to Equation 107. The fluence function for the sub-spots only includes the contribution from MCS, while the NS dose is represented by a single pencil-beam trace. The use of single tracing for the NS part is motivated by the fact that the NS contribution to the total dose is rather small compared to that of the MCS. The fluence contribution from sub-spot k is:

$$\Phi_{ejk}^{MCS}(x,y,z) = \left(1 - w_{ejk}^{NS}\right) \left[G\left(\Delta\, x_{ejk}, \Delta\, y_{ejk}, 0, 0, \sigma_{ejk}^{MCS}\right) + \delta_{ejk}^{MCS}\right] \qquad \text{[Eq. 117]}$$

where Δx_{ejk} and Δy_{ejk} are the coordinates of point {x, y, z} in the sub-spot coordinate system. (The z-axis of the sub-spot coordinate system coincides with the sub-spot central axis, and the origin is set to the starting point of the pencil beam ray trace.) w_{ejk}^{NS} is the nuclear halo weight and σ_{ejk}^{MCS} the MCS sub-spot width (equal to the square root of the spatial variance of the sub spots as given by Equation 109), both at the depth z_{ejk}, which is the depth of the sub-spot trace to the point where the distance between the sub-spot z-axis and the point {x, y, z} is shortest. G is given by Equation 105.

The fluence function for the NS dose contribution is given by:

$$\Phi_{ej}^{NS}(x,y,z) = w_{ej}^{NS} \left[G\left(\Delta\, x_{ej}, \Delta\, y_{ej}, 0, 0, \sigma_{ej}^{NS}\right) + \delta_{ej}^{NS}\right] \qquad \text{[Eq. 118]}$$

where σ_{ej}^{NS} is the nuclear spread at depth z_{ej} (*section 6.4.4 Nuclear scattering on page 184*), and the omission of sub script k for Δx, Δy, and z indicates that the they have been evaluated for a ray trace going through the center of the original spot.

δ_{ejk}^{MCS} and δ_{ej}^{NS} in Equation 117 and Equation 118 are rest contributions to account for the fact that we only score the dose up to a radial distance from the central trace axis of r_{cut}^{MCS} and r_{cut}^{NS} for the MCS and NS fluence contributions, respectively. By integrating the dose deposited outside these distances, and averaging over the dose scoring area, δ becomes:

$$\begin{aligned} \delta_{ejk}^{MCS} &= \frac{1}{\pi \left(r_{cut,ejk}^{MCS}\right)^2} \exp\left[-\left(\frac{r_{cut,ejk}^{MCS}}{\sigma_{ejk}^{MCS}}\right)^2\right] \\ \delta_{ej}^{NS} &= \frac{1}{\pi \left(r_{cut,ej}^{NS}\right)^2} \exp\left[-\left(\frac{r_{cut,ej}^{NS}}{\sigma_{ej}^{NS}}\right)^2\right] \end{aligned} \qquad \text{[Eq. 119]}$$

The cut-off radii are set to $r_{cut,ejk}^{MCS} = 2.628\sigma_{ejk}^{MCS}$, and $r_{cut,ej}^{NS} = 2.145\sigma_{ej}^{NS}$, corresponding to a radius within which, respectively, 99.9% and 99 % of the MCS and NS fluence contributions originate.

Finally, the value for the integrated depth dose in Equation 116 is simply given by:

$$IDD_{ejk} = IDD_e^w(z_{ejk}^w) \qquad \text{[Eq. 120]}$$

where IDD_e^w is the water reference integrated dose profile for energy layer e in units of cGy cm²/proton, as provided by the beam model (Equation 102), and z_{ejk}^w the water equivalent depth at z_{ejk} (*section 6.4.2 Energy loss and radiological depth on page 182*).

For optimization of PBS plans, the user has the possibility to calculate the spot doses with a fast dose engine. In this case, the single tracing mode is employed and no division into sub-spots is performed. The optimization dose calculated with the pencil beam dose engine is always labeled as Approximate, and a Final dose calculation with a clinical dose engine (Pencil beam or Monte Carlo) has to be performed to be able to approve the plan.

6.5.3 Modeling of a range shifter

For shallow targets, the lowest available energy of the delivery system may not be sufficiently low to guarantee target coverage and it may be necessary to use a range shifter, sometimes referred to as an energy absorber.

In the RayStation pencil beam dose engine, the effect of a range shifter is accounted for by introducing offsets in the mean beam energy and water equivalent depth at the start of the dose calculation. Furthermore, the spatial-angular moments at the isocenter are replaced to reflect the lateral spread caused by the range shifter. These parameters are determined by tracing the phase space for each spot, starting at the range shifter upstream surface, through the range shifter, and then to the isocenter plane, where the transport from the range shifter exit point to the isocenter is performed in vacuum. The dose computation then progresses as if the range shifter is not in place, with the difference that the initialization, tracing and subsequent scoring of the sub-spots will take the updated spatial-angular moments and the offsets in mean beam energy (used in Equation 95 and Equation 97) and water equivalent depth (used in Equation 99 and Equation 120) into account.

The range shifter material properties, physical thickness, and position along the beam line are obtained from the machine model. Since the range shifter is incorporated in the dose calculation in RayStation, no additional beam modeling data is required.

In the RayStation PBS dose engine validation it was noted that the error in dose at especially shallow internal depths for some PBS fields using a range shifter with a sizable air gap was larger than the defined acceptance threshold. This is likely an effect of the secondary protons/nuclear halo algorithm, which does not handle inhomogeneities in a formal way (see *section 6.4.4 Nuclear scattering on page 184* for details). Since the nuclear halo is a second order effect, it is typically not a problem for the inhomogeneities seen within a patient (see e.g. reference [73]). The set-up with a range shifter/airgap/phantom is, on the other hand, a geometry with a very large inhomogeneity. The lack of formal handling of the nuclear halo/secondary protons created in the range shifter, that are

transported over the air gap and into the phantom, should be a larger problem for secondary protons with low kinetic energy, than those with higher energy, since the lower energy protons can be expected to have interacted more and therefore have a greater angular spread. This would explain why the error is larger at shallow depths.

6.5.4 Modeling of an aperture

RayStation supports PBS planning with a collimating device for improved lateral penumbra. A collimating device, referred to as aperture, can be either a block aperture or an MLC. In the pencil beam dose engine the aperture is accounted for by masking the sub-spots of each spot. Any sub-spot whose center falls outside of the aperture contour will be excluded from the dose calculation, and the dose contribution from the nuclear halo component will be down-scaled accordingly. In the presence of an aperture, Equation 116 will thus read:

$$d_{ej}(x,y,z) = \sum_{k=1:19} (H_{jk} w_k \Phi_{ejk}^{MCS} IDD_{ejk}) + f_j \Phi_{ej}^{NS} IDD_{ej} \qquad \text{[Eq. 121]}$$

with

$$f_j = \sum_{k=1:19} H_{jk} w_k \qquad \text{[Eq. 122]}$$

and where H_{jk} is a step function equal to 1 if the center of sub-spot k of spot j falls inside the aperture contour, and equal to 0 if it is outside. In addition to this, the spatial variance of the sub-spots belonging to a spot that is partially covered by the aperture will be down-scaled as they pass the downstream edge of the aperture according to:

$$\overline{r_{jk}^2}^{ap+} = f_j^{1.2} \overline{r_{jk}^2}^{ap-} \qquad \text{[Eq. 123]}$$

where $\overline{r_{jk}^2}^{ap+}$ and $\overline{r_{jk}^2}^{ap-}$ represents the sub-spot spatial variance just down- and upstream of the aperture edge, respectively. The form of Equation 123 is strictly empirical and has been determined to give the best possible fit to a range of measured lateral dose curves of PBS plans including a aperture.

When an aperture is used in combination with a range shifter, the creation and tracing of the sub-spots are done differently depending on which side of the aperture the range shifter is mounted. For systems where the range shifter is upstream of the aperture, the sub-spots are created at the patient surface as usual and the masking is done by projecting these sub-spots to the downstream plane of the aperture. However, if the range shifter is mounted downstream of the aperture, the sub-spots corresponding to spots that are partially covered by the aperture contour will be created and masked at the downstream plane of the aperture and are then transported through the range shifter, over the air gap and into the patient. For these spots/sub-spots, the range shifter is thus treated as an extension of the patient. It should be noted that this is only done for spots that are intercepted by

the aperture edge. Spots well within the aperture contour are unaffected by the aperture, and the corresponding sub-spots are created at the patient surface.

When an aperture is inserted into a proton beam, some of the protons close to the aperture edge will enter the aperture, but then scatter out of it again. This effect is referred to as the edge scatter effect and may add characteristic ears to the lateral dose profiles close to the surface, but may also add dose more centrally and deeper into the target, especially for smaller fields. The edge scatter effect is not included in the Pencil-Beam dose engine. For this reason, the dose calculated with the pencil beam dose engine will be labeled as Approximate for PBS beams with apertures. A Final dose calculation using the Monte Carlo dose engine has to be performed to obtained a Clinical dose. If the difference between the Pencil-Beam and Monte Carlo calculated doses is significant, it is recommended to use Monte Carlo also for optimization of the plan.

6.5.5 Modeling of an energy selector

For treatment delivery techniques where the energy modulation takes place close to the patient, RayStation models the nominal (open beam) energy of the machine and to handle the energy modulation as a part of the dose calculation.

An energy selector (binary range shifter) is modeled as a series of range shifters. Each energy selector plate is considered a range shifter with corresponding introduced offset in mean beam energy and water equivalent depth.

The spatial-angular moments will be replaced similarly to the modeling of a single range shifter, to reflect the lateral spreading in the energy selector. The spots will be traced, starting at the upstream surface of the first energy selector plate, through the stack of energy selector plates and then to the isocenter plane. The gaps between energy selector plates and between the most downstream surface and the isocenter plane are also included in the transport and treated as vacuum. The individual material properties of each plate is taken into account in the energy loss calculation and tracing. A machine with an energy selector may also have a nozzle exit window attached as the most downstream part of the treatment snout. This object is also modeled as a range shifter in the dose calculation. Sub-spot creation will be performed as described in *section 6.5.4 Modeling of an aperture on page 196*.

Using the pencil beam dose engine in RayStation in combination with an energy selector introduces a number of range shifters and potentially large air gaps. In the RayStation PBS pencil beam dose engine validation it has been noted that dose accuracy is limited under such circumstances, especially for shallow depths. The pencil beam dose engine will therefore never produce clinical dose in the presence of an energy selector, and shall mainly be viewed as an option for fast optimization and range evaluation. No clinically relevant evaluations should be performed based on approximate dose.

6.6 PENCIL BEAM DOSE CALCULATION FOR US/SS/DS/WOBBLING BEAMS

This section gives a detailed description on how RayStation calculates the dose for a US/SS/DS/Wobbling plan. However, it only provides details that are specific to US/SS/DS/Wobbling beams, while the algorithms that are valid for all proton dose calculations in RayStation are given in *section 6.4 Pencil Beam dose engine on page 180*. The reader is advised to be well acquainted with the content of *section 6.4 Pencil Beam dose engine on page 180*, before reading this section.

In this section

This section contains the following sub-sections:

6.6.1	Beam model	p. 199
6.6.2	Transport through aperture and compensator	p. 202
6.6.3	Scoring of dose in patient	p. 206
6.6.4	Absolute dosimetry	p. 208

6.6.1 Beam model

The responsibility of the beam model is to first identify the energy layers (e) of the US/SS/DS/Wobbling beam, and then to determine the parameters that are needed by the dose engine for each of these layers. These parameters are:

- Mean direction of the protons at any given point in the fluence plane: **e**
- Mean beam energy at the patient surface (without compensator), $E_{m,e}$
- Integrated depth dose curve in water (without compensator), IDD_e^w
- Local angular variance at the position of the compensator entrance plane, $\overline{\theta_{C,e}^2}$
- Relative weight of the energy layer, w_e
- (Optional) Radial fluence correction

RayStation assumes that the fluence is laterally homogeneous for all supported techniques, unless a radial fluence correction is explicitly defined.

This section describes how the energy layers are selected and how the phase space parameters for these layers are calculated from the machine and beam model parameters. The beam models for the Mitsubishi Electric Co and Sumitomo Wobbling systems are somewhat different, and are therefore separately covered in *section 6.7 Pencil beam dose calculation for Mitsubishi Electric Corporation US beams on page 209* and 5.8.

6

In this section

This section contains the following sub-sections:

6.6.1.1	Energy layer selection	p. 200
6.6.1.2	Continuous R and M machines	p. 200
6.6.1.3	IDDs and mean beam energies	p. 201
6.6.1.4	Spatial-angular distribution	p. 201

Energy layer selection

The energy layers of a certain beam are defined by the nominal beam energy of the deepest energy layer at the nozzle entrance (E_N), and, for each layer, the nozzle water equivalent thickness (NET_e), and relative weight (w_e). The NET_e is often equal, or related to to the thickness of the range modulator steps. The selection method of these values depends on the type of beam delivery system.

Continuous R and M machines

The proton beam model in RayStation 2024A supports beam delivery systems capable of generating SOBPs with continuously variable maximum range (R) and modulation width (M), and where it is the prescribed SOBP R and M that are communicated to the treatment control system rather than the detailed nozzle settings. Examples of such systems include the IBA Universal nozzle for DS and US and the Mevion S250 DS beam delivery systems. For these machines, the entire achievable interval of Rs is divided into a number of intervals, referred to as "Range Options", equivalent to IBAs and Mevions concept of "Options" and "Configurations". For each of these Range Options, the NETs of the energy layers are fixed. To achieve flat SOBPs for all ranges within a Range Option, a Range Option interval may further be divided into "Sub Options", in which the weights of the energy layers are kept constant. This possibility to define different energy layer weights for sub intervals within a Range Option is compatible with, for example, the IBA Double Scattering/Uniform Scanning systems where different Beam Current Modulation Curves/Weight Files are used for different Sub Options within an Option.

When determining the energy layer data for a given R and M, the correct Range (i) and Sub Options (j) are first established according to:

$$Range\ Option\ (i)_{lo\lim} < R \leq Range\ Option\ (i)_{hi\lim} \qquad \text{[Eq. 124]}$$

$$Sub\ Option\ (j)_{lo\lim} < R \leq Sub\ Option\ (j)_{hi\lim} \qquad \text{[Eq. 125]}$$

The nominal beam is determined as the energy which gives the total range at the nozzle entrance:

$$R_0 = R + NET_0 \qquad \text{[Eq. 126]}$$

where NET_0 is the water equivalent thickness of the nozzle for the deepest energy layer. To convert range to energy, a Range-to-energy conversion function is used (see *section 6.3 Beam model parameters on page 177*). The continuous modulation of the SOBP is achieved by varying the weight of the last energy layer in the SOBP from 0 to the value when the layer is completely included in a SOBP. The number of full energy layers and the weight of the last layer are determined by an interpolation procedure from look up tables that are specific for each Sub Option.

IDDs and mean beam energies

The integrated depth dose in water for each energy layer e is determined by subtracting the nozzle equivalent thickness from the integrated depth dose at nominal beam energy, IDD_N^w, as obtained by the beam model (*section 6.4.5 Calculation of the integrated depth dose in water on page 186*):

$$IDD_e^w(z) = IDD_N^w(z - NET_e)H(z - NET_e) \quad \text{[Eq. 127]}$$

where H is the Heaviside step function. The mean energies for each energy layer are given as:

$$E_{m,e} = E_{m,E_N} - \Delta E(NET_e) \quad \text{[Eq. 128]}$$

where $E_{m,EN}$ is the mean energy given by the energy spectrum $dN/dE|_{EN}$, and $\Delta E(NET_e)$ is the energy loss through a slab of water with a thickness of NET_e, calculated as outlined in *section 6.4.2 Energy loss and radiological depth on page 182*.

Spatial-angular distribution

The phase space of the reference fluence plane, which is positioned at the entrance point of the compensator, is characterized by a distribution of uniformly spaced point sources. The distribution of their intensities is uniform unless a radial fluence correction is explicitly defined. The point sources are defined by the angular variance, $\overline{\theta_{C,e}^2}$, around the most probable direction of the protons $\mathbf{e}_e(x,y)$, as given by $SAD_{vir,e}^{X,Y}$. The initial spatial-angular moments in the pencil-beam calculation for each pixel in the fluence plane is thus $\{\overline{\theta_{C,e}^2}, 0, 0\}$.The calculation of $\overline{\theta_{C,e}^2}$ and $SAD_{vir,e}^{X,Y}$ from the beam model parameters are slightly different for Single Scattering, Double Scattering and Uniform Scanning in RayStation, although it mainly is a matter of bookkeeping.

Uniform Scanning

For Uniform Scanning nozzles, $SAD_{vir,e}^X$ and $SAD_{vir,e}^Y$ are set to the effective scanning magnet positions f_X and f_Y, respectively. In RayStation, f_X and f_Y are fixed beam model parameters, i.e., independent on the nominal beam energy. The angular variance of the point sources is directly given by the angular variance of the spatial-angular moments at the nominal energy:

$$\overline{\theta_{C,e}{}^2} = \overline{\theta_0^2}|_{E_N} \quad \text{[Eq. 129]}$$

Single Scattering/Double Scattering

For single and double scattering systems, the virtual source axis distance and the angular variance are computed from the spatial-angular moments as if the moments described the scattering beam as a whole [66]:

$$SAD^{X}_{vir,e} = SAD^{Y}_{vir,e} = \frac{\overline{r_0^2}}{\overline{r\theta_0}}\Big|_{E_N} \qquad \text{[Eq. 130]}$$

and

$$\overline{\theta_{C,e}{}^2} = \overline{\theta_0^2} - \frac{(\overline{r\theta_0})^2}{\overline{r_0^2}}\Big|_{E_N} \qquad \text{[Eq. 131]}$$

We note here that this different treatment of US, SS and DS is mainly a question of book keeping, since it is possible to get a set of spatial-angular moments to give exactly the same $\overline{\theta_{C,e}^2}$ and $SAD^{X,Y}_{vir,e}$ as for uniform scanning. However, the above treatment for SS and DS does give the possibility to let $SAD^{X,Y}_{vir,e}$ depend on the nominal beam energy, while it is fixed for US.

The calculations above do not distinguish between the different energy layers, and the same values are used for all layers of the beam. This can be motivated by the fact that the lateral dose distribution of a field is typically dominated by the deepest energy layers, which deliver a majority of the dose, and by the fact that most modern range modulators are designed to give a constant amount of (lateral) scattering for all layers.

6.6.2 Transport through aperture and compensator

This section describes how the beam limiting devices block, MLC and range compensator are handled in the pencil beam dose engine.

Modeling of the aperture

RayStation supports proton US/SS/DS planning with either a block aperture or an MLC as collimating device, referred to as aperture. The effect of the aperture is included by calculating the transparence, a_j, of each fluence pixel j. a_j is determined by how large fraction of the pixel surface is inside the collimating contour. Pixels that are completely inside the contour gets a transparency value of $a_j = 1$. This treatment is equivalent to treating the density of the aperture to be infinitely high. In RayStation, only non-divergent edges of the aperture is supported. The contour at both the downstream and upstream plane of the aperture are taken into account (the upstream contour may affect the fluence for off axis targets). If a pixel surface is inside the contour in both planes, the minimum value of a_j is chosen. This choice will lead to a slight underestimation of the dose, but will ensure target coverage during planning. The effect of aperture edge scatter, which introduces characteristic “ears” at the field edges in dose profiles at relatively shallow depth, but also may affect the dose at the center of the field for smaller targets, is not included in the dose calculation.

Leakage between MLC leaves for protons

In the RayStation proton dose engines, a collimating MLC is regarded as an aperture block with a jagged contour, meaning that actual leakage between adjascent leaves or closed leaf tips are not handled by the dose engines. The dose difference between the computed plan and the delivered

plan needs to be assessed by the user in the commissioning of RayStation as well as during patient specific QA.

Apertures downstream of the compensator

In some systems, the block aperture is mounted downstream of the range compensator. Examples include the Sumitomo HI Wobbling, and the Mitsubishi Electric Co Uniform Scanning delivery systems. This setup is a rather challenging problem for a pencil beam based dose engine. The tracing of the algorithmic pencil beams starts at the entrance of the compensator and does therefore have a finite width as they pass the block aperture. For pencil beams that pass close to the aperture edge, a substantial part of the protons, as represented by the pencil beam, will extend into the aperture and should be blocked (or scattered) by the aperture edge. However, this effect of the aperture edge can not be accurately accounted for by a pencil beam dose engine due to the infinite slab approximation; the radial symmetry of the Pencil Beam has to be maintained. Extensive comparisons to measured dose profiles show that if the aperture edge is ignored (i.e., if the aperture is treated in the same way as for delivery systems were the block is mounted upstream of the compensator) the lateral penumbra (20-80%) of the calculated field will be overestimated by as much as 4-5 mm for typical clinical setups. In RayStation, we have introduced an algorithm that will improve the lateral penumbra for delivery systems where the aperture is mounted downstream of the compensator. In this algorithm, the spatial-angular moments of the pencil beams are modified as the tracing passes the downstream plane of the block aperture. By comparing calculated to measured lateral profiles for several hundred beam configurations, the following simple down-scaling of the spatial-angular moments has proven to give penumbra widths better than 1 mm for most situations:

$$\overline{\theta^2}(z^+) = 0.50 \cdot \overline{\theta^2}(z^-)$$

$$\overline{r\,\theta}(z^+) = 0.50 \cdot \overline{r\,\theta}(z^-) \qquad \text{[Eq. 132]}$$

$$\overline{r^2}(z^+) = 0.50 \cdot \overline{r^2}(z^-)$$

where z^- and z^+ represent the position just before and after the downstream block plane along the pencil beam longitudinal axis, respectively. This scaling of the spatial-angular moments is performed for all Pencil Beams over the lateral fluence plane. It may be tempting to suggest a model where the degree of scaling would depend on the distance to the aperture edge. Unfortunately, this leads to large numerical artifacts since the sum of the contribution from each fluence pixel no longer adds up to a uniform fluence for a uniform field (flat compensator).

Since the down-scaling of the spatial-angular moments is performed uniformly over the fluence plane, it means that the scattering from the compensator at some distance away from the edge will be underestimated. The question is how much of an effect this is. One may argue that the thickness of most range compensators is considerably smaller in the center as compared to the thickness around the edges, and that the underestimation of the scattering in the central part of the compensator therefore should not be a significant problem. To test this assumption, the dose for a number of typical clinical cases has been compared with and without the down-scaling in Equation 132. Figure 62 shows the comparison for one of the fields in a two-field prostate Wobbling

plan in RayStation. Only the penumbra region of the doses are notably affected by the down-scaling of the spatial-angular moments.

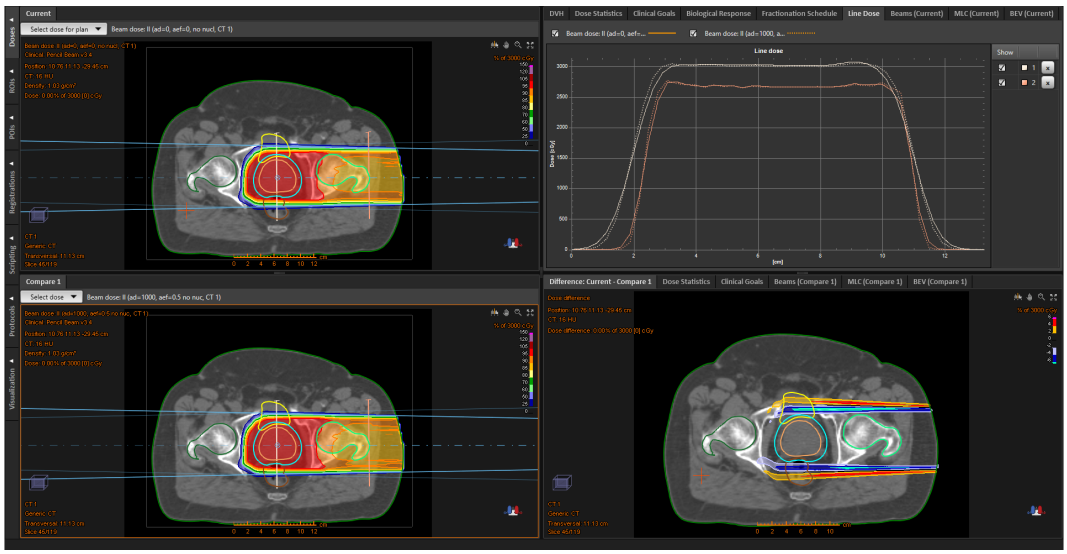

Figure 62. The graphs to the left show the transversal dose distributions through the isocenter for dose calculations, without (top) and with the aperture algorithm of Equation 132 (bottom), for one of the fields in a prostate Wobbling plan. The top right graph shows the lateral profiles of the doses through the isocenter (beige) and entrance region (orange) of the top left (solid lines) and bottom left (dotted lines) graphs. The bottom right graph shows the difference between the top and bottom left graphs.

A similar comparison was also made for a smaller brain tumor case, with more or less the same result as for the prostate case. However, the down-scaling of the spatial-radial moments should be more important for cases that require compensators with larger gradients towards the center. One such case is the Head and Neck case shown in Figure 63 where the PTV surrounds the brain stem. To obtain as high gradients as possible, this compensator was created without any smearing or gradient filter. For this case it is clear that the aperture algorithm affects the dose also in the center of the field (away from the aperture edge) and that the observed difference in dose in this region shall be viewed as an incorrect artifact introduced by the aperture algorithm.

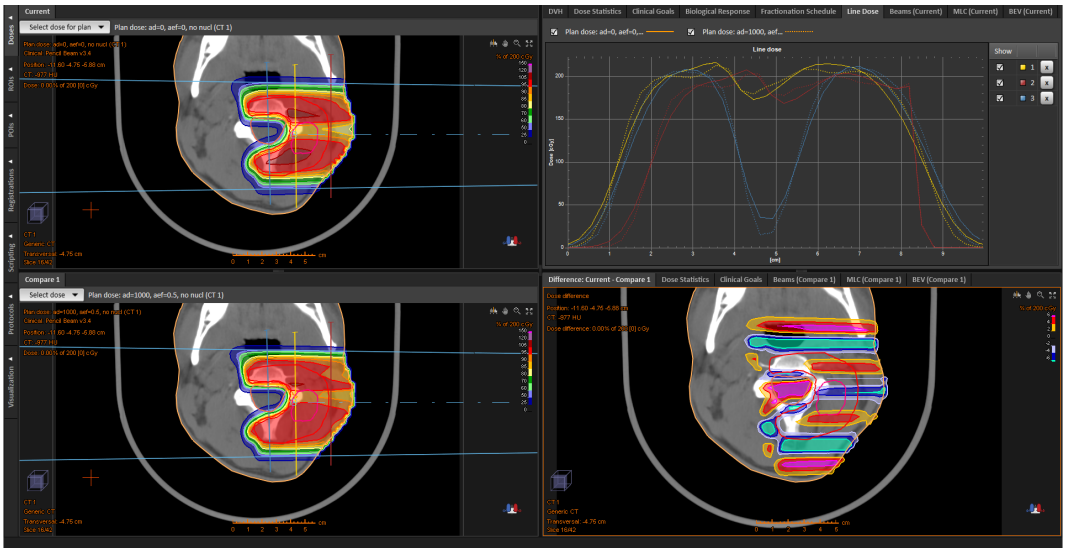

Figure 63. The graphs to the left show the transversal dose distributions through the isocenter for dose calculations, without (top) and with the aperture algorithm of Equation 132 (bottom), for one of the fields in a Head and Neck Wobbling plan where no smearing or gradient filtering have been applied to the compensator. The top right graph shows the lateral profiles of the doses through the isocenter (beige), entrance (orange), and distal dose regions (blue) of the top left (solid lines) and bottom left (dotted lines) graphs. The bottom right graph shows the difference between the top and bottom left graphs.

The plan shown in Figure 63 was created without any smearing and gradient filtering done to the compensator, and might therefore not be seen as a fully relevant case. A second plan was made for the same case, but now with a smearing of 0.5 cm. For this plan, the dose difference in the central region was considerably smaller than those seen in Figure 63.

Tracing of the compensator

All compensators in RayStation are assumed to be mounted with the milled out side facing the source (it is noted that DICOM does not specify how the milled out side is directed). The phase space parameters are transported to the upstream plane of the compensator. This transport step is performed in air (here treated as vacuum), which means that only the spatial-angular moments are affected. At this plane all compensator pixels with a center within one compensator milling tool radius from the intersection point are selected and the smallest physical thickness value of these compensator pixels, t_{min}, is determined. The compensator entrance point for the current trace is then calculated as the intersection point between the trace line and a plane, offset upstream of the compensator downstream plane by a distance of t_{min}. The tracing is then performed through the compensator, which now is treated as a semi-infinite slab with a thickness of t_{min}. This treatment naturally incorporates the "smearing" effect of the compensator milling tool. The transport through the compensator is performed using the material properties as specified by the machine model.

After exiting the compensator, the tracing continues to the external surface of the patient, as described in *section 6.4.1 Initialization and tracing of phase space parameters on page 181*.

6.6.3 Scoring of dose in patient

Final dose engine

The scoring of the dose from a US/SS/DS/Wobbling beam is performed in receiving mode, where the total dose to a point (x, y, z) in the patient is determined as the sum of the contributions from energy layers e and fluence pixels j:

$$dose(x,y,z) = MU \sum_j a_j \sum_e I_e \, d_{ej} \qquad \text{[Eq. 133]}$$

where MU is the meterset weight of the beam, a_j the collimator transparency number for pixel j , I_e the number of protons per MU originating from layer e and pixel j , and d_{ej} the corresponding dose contribution per proton to (x, y, z). For a US field, I_e is determined as

$$I_e = w_e S_N A \, / A_{SF} \qquad \text{[Eq. 134]}$$

while it for an SS or DS field becomes:

$$I_e = w_e S_N A \qquad \text{[Eq. 135]}$$

where w_e is the relative weight of the energy layer, S_N the dose monitor sensitivity at the nominal beam energy, A is the area of a fluence pixel, and A_{SF} the area of the scanned field at the isocenter plane.

Note: *The dimension of S_N is protons/MU for US and protons/(MU cm^2) for SS and DS.*

d_{ej} is the product of the integrated depth dose and the lateral fluence function, which in turn is composed of contributions from MCS and NS:

$$d_{ej}(x,y,z) = (\Phi_{ej}^{MCS} + \Phi_{ej}^{NS}) IDD_{ej} \qquad \text{[Eq. 136]}$$

The values of the fluence contribution Φ_{ej} and integrated depth dose IDD_{ej} are determined by first finding the perpendicular projection of center of the voxel onto the pixel ray trace line, z_j, and the corresponding closest distance $\{\Delta\, x_{ij}, \Delta\, y_{ij}\}$. The fluence from MCS and NS can now be written as:

$$\Phi_{ej}^{MCS}(x,y,z) = \left(1 - w_{ej}^{NS}\right) \left[g\left(\Delta\, x_j, \Delta\, y_j, L_j^x, L_j^y, \sigma_{ej}^{MCS}\right) + \delta_{ej}^{MCS}\right] \qquad \text{[Eq. 137]}$$

and

$$\Phi_{ej}^{NS} = w_{ej}^{NS} \left[g\left(\Delta\, x_j, \Delta\, y_j, L_j^x, L_j^y, \sigma_{ej}^{NS}\right) + \delta_{ej}^{NS} \right] \qquad \text{[Eq. 138]}$$

where σ_{ej}^{MCS} is equal to the square root of the $\overline{r^2}$ at z_j, and L_j^x, and L_j^y are the dimensions of the fluence pixel j, projected to a plane, perpendicular to the trace line, positioned at z_j. g is the fluence function obtained when integrating Gaussians, evenly distributed over a rectangular area $\{L_x, L_y\}$ and is given by [58]:

$$g\left(x, y, L_x, L_y, \sigma_{1/e}\right) = \frac{1}{4L_xL_y}\left[erf\left(\frac{L_x/2-x}{\sigma_{1/e}}\right) - erf\left(\frac{-L_x/2-x}{\sigma_{1/e}}\right)\right]\left[erf\left(\frac{L_y/2-y}{\sigma_{1/e}}\right) - erf\left(\frac{-L_y/2-y}{\sigma_{1/e}}\right)\right] \qquad \text{[Eq. 139]}$$

δ in Equation 137 and Equation 138 are rest contributions to account for the fact that we only score the dose up to a radial distance from the central trace axis of r_{cut}^{MCS} and r_{cut}^{NS} for the MCS and NS fluence contributions, respectively. The expressions for δ_{ej}^{MCS} and δ_{ej}^{NS} given in *section 6.5.2 Scoring of dose in the patient (PBS) on page 193* by Equation 119, are valid also for US/SS/DS/Wobbling, with the difference that the term $\sqrt{L_j^{x2} + L_j^{y2}}/2$ have been added to r_{cut}^{MCS} and r_{cut}^{NS} to account for the size of the pixel.

The term of the integrated depth dose in Equation 133 is simply given by

$$IDD_{ej} = IDD_e^w\left(z_{ej}^w\right) \qquad \text{[Eq. 140]}$$

where IDD_e^w is the integrated depth dose in water for energy layer e in units of cGycm^2/proton, as provided by the beam model, and z_{ej}^w the water equivalent depth at z_{ej}.

Fast dose engine

For US/SS/DS/Wobbling plans where a substantial amount of manual editing may be required, the changes need to be confirmed by a dose computation after each edit. In such cases, it is important that the dose calculation is as fast as possible. In RayStation there is therefore a possibility to launch a Fast dose calculation, which will result in an approximate dose. Once the editing is completed and the dose is satisfactorily, clinical dose can be computed as described above, see *Final dose engine on page 206*. The fast dose calculation simply replaces the IDD of the highest energy layer with the total SOBP and tracing is only performed for that energy layer. This removes the energy dependencies in Equation 133 to Equation 138 and Equation 140, and thus reduces the computation time substantially. The resulting dose distribution is normally very close to the dose from the clinical dose engine with just small deviations in cases with large patient heterogeneities.

Exclusion of nuclear scattering

In the RayStation SS/DS/US/Wobbling dose calculation it is possible to exclude scoring of the nuclear halo dose and transfer that part of the fluence to the MCS Gaussian (Equation 136). This possibility

has been introduced to artificially sharpen the edges of the lateral profiles and thereby compensate for the fact that aperture edge scatter is not taken into account in the dose calculation. The effect of the aperture edge scatter is to add "ears" to, and sharpen the lateral dose profiles in the entrance region of the field. With this omission of the nuclear halo, the calculated lateral dose profiles has proven to give a better fit to the measured profiles of some broad beam systems, despite the fact that the nuclear halo effect has no relation to the edge scatter effect that is the cause of the poor agreement. The price to pay for the omission of the nuclear halo in the dose calculation is a slightly lesser agreement to the low dose tail of the lateral profiles. The choice to exclude the nuclear halo from the dose calculation is controlled by a parameter in the beam model and cannot be altered once the beam model has been commissioned in RayStation.

6.6.4 Absolute dosimetry

The proton beam model and dose engine calculations described above is not expected to provide accurate absolute dose in terms of output with respect to the beam meterset. There are two main reasons for this: (1) the above relation between the energy layer weights, the beam meterset number, and the dose in the patient, is only correct if the primary dose monitor is positioned upstream of the range modulating devices. However, the dose monitor is often positioned downstream of the range modulator. (2) The magnitude of the lateral spread of large angle scattered protons, generated in the compensator and transported over the air gap, will be underestimated, since the nuclear halo model does not consider the effect of inhomogeneities. This may lead to an overestimation of the dose at the central axis by several percent.

The beam meterset number in RayStation should therefore only be regarded as a way to control the dose level of the computed dose. As a consequence, the DICOM tag Beam Meterset (300A,0086) in the RT Fraction Scheme Module, is not included in the DICOM RT ION plan export for US/SS/DS/Wobbling.

6.7 PENCIL BEAM DOSE CALCULATION FOR MITSUBISHI ELECTRIC CORPORATION US BEAMS

RayStation 2024A supports planning for the Mitsubishi Electric Corporation Uniform Scanning proton delivery system (Mitsubishi Electric Co SELECT BEAM NOZZLE in US mode), which has some significant differences compared to other broad beam techniques supported in RayStation. This sections outlines the features of the RayStation that are specific to Mitsubishi Electric Co SELECT BEAM NOZZLE in US mode.

In this section

This section contains the following sub-sections:

6.7.1	Introduction	p. 210
6.7.2	RayStation dose engine	p. 210

6.7.1 Introduction

With Mitsubishi Electric Co SELECT BEAM NOZZLE in US mode, the coarse range of the protons is determined by a small number of nominal beam energies, while the fine tuning of the field is adjusted by a binary range shifter mounted in the nozzle. The number of available beam energies is typically 4-5, which means that the range shifter will be set to up to ~60 mm water equivalent thickness (WET). For longitudinal modulation of the field, the Mitsubishi Electric Co SELECT BEAM NOZZLE in US mode uses several discrete range modulators/ridge filters, similar to the Sumitomo Wobbling system.

Additional nozzle settings for the Mitsubishi Electric Co SELECT BEAM NOZZLE in US mode include the thickness of a scattering foil, and the scan pattern of the US field expressed in the number of spots, spot spacing and field edge spot weight enhancement factor. These nozzle settings are organized in a relatively large number of so-called "beam data sets" (typically ~140). Each beam data set has a unique combination of:

- Nominal beam energy
- Range shifter thickness limits
- Maximum field size
- Ridge filter ID

The scatterer thickness and spot pattern is defined for each beam data. In RayStation, the Mitsubishi Electric Corporation concept of beam data sets has been mapped, with a one-to-one relationship, to the RayStation "Range Option" concept, which will be the term used from here on.

6.7.2 RayStation dose engine

The features of the Mitsubishi Electric Co SELECT BEAM NOZZLE in US mode described in the previous section places new demands on, and opens new possibilities for the RayStation dose engine.

For our other broad beam techniques, the RayStation beam model provides the energy spectrum of the deepest energy layer of the SOBP from which the pristine Bragg peak is calculated (Equation 90 and Equation 102). The Bragg peaks for the remaining energy layers are determined by subtracting the WET of the range modulator/ridge filter steps from the pristine Bragg peak curve. The weights of each energy layer are given by the beam model, and have been determined by fitting the energy layer Bragg peaks to measured SOBP depth dose curve (see *section 6.4 Pencil Beam dose engine on page 180* for details).

For Mitsubishi Electric Co SELECT BEAM NOZZLE in US mode, the process of determining the IDDs and relative weights of the energy layers is more-or-less reversed. The beam model first provides the energy spectrum for the entire SOBP (Figure 64). One energy spectrum is stored for each Range Option and is valid for the lower range shifter thickness limit of the Range Option. The SOBP energy spectrum is then divided into several sub energy spectra (energy layer spectra), where the intervals are chosen to correspond to a fixed range interval in water (Figure 64). The energy layers of the dose calculation are then formed from these energy intervals, and the energy layer IDDs and relative weights are reconstructed from the energy layer spectra (Figure 65), where the net range shifter WET is subtracted from the IDDs. The net range shifter WET in this case is defined as the difference

between the range shifter WET of the beam, and that of the minimum range shifter thickness of the chosen Range Option. This is done since the minimum range shifter thickness has already been accounted for in the Range Option energy spectrum. The choice of the fixed range interval is a compromise between dose computation accuracy and computational efficiency. In RayStation, a value of 10 mm has proven to be small enough not to affect the calculated dose for a wide range of cases. However, in plans with wedges a smaller value of 4 mm is used instead.

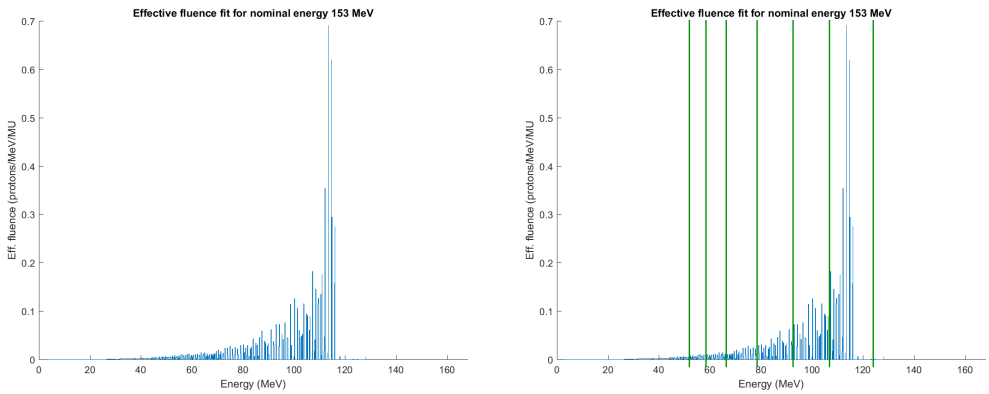

Figure 64. (Left) Energy spectrum fitted to a measured central axis depth dose curve of a field with a SOBP range and modulation of 15, and 12 cm, respectively (black circles in Figure 65). (Right) The energy spectrum is divided into a number of sub intervals, defined by a fixed WET, that will form the energy layers in the dose calculation.

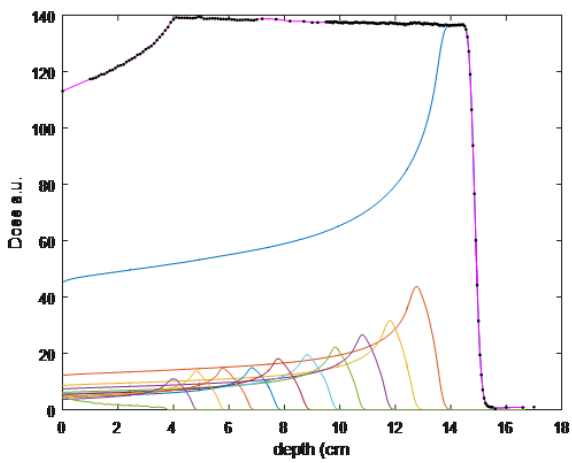

Figure 65. IDDs with relative weights extracted from the total energy spectrum (Figure 64) with an energy layer WET of 10 mm. The black circles represent the measured SOBP, to which the total energy spectrum was fitted. The sum of the IDDs are included as the magenta colored line.

The modeling of the spatial-angular phase space of the SOBP energy layers has also been updated for the Mitsubishi Electric Co SELECT BEAM NOZZLE in US mode. For the broad beam techniques in RayStation, the angular phase space is expressed as the local angular variance ($\overline{\theta_C^2}$) in the plane where the pencil beam ray tracing starts. This plane coincides with the upstream plane of the range compensator. For previous supported systems, the value of $\overline{\theta_C^2}$ is a function of nominal beam energy only, and therefore does not consider the range modulator steps or the Snout Position. For the Mitsubishi Electric Co SELECT BEAM NOZZLE in US mode, this simple model does not hold, not in the least due to the range shifter, which has proven to have a significant impact on the lateral penumbra, especially at large airgaps. In addition to considering the range shifter and the Snout Position/airgap, the effect of the individual range modulator/ridge filter steps on $\overline{\theta_C^2}$ is also taken into account. So, for the Mitsubishi Electric Corporation US beam model in RayStation, one set of angular spatial distribution moments (see *Spatial-angular distribution on page 201*), defined at the isocenter is stored for each Range Option. In the dose calculation, the distribution moments are first (reversely) transported (Equation 96) from the isocenter to the ridge filter mounting plane assuming vacuum. The moments are then transported through the ridge filter, range shifter, and down to the pencil beam ray-tracing start plane, where $\overline{\theta_C^2}$ is determined from the distribution moments according to Equation 113. $\overline{\theta_C^2}$ is calculated for each energy layer separately, where the thickness of the ridge filter for each layer is given by the range intervals of the energy spectrum division (above), where the WET of the layers are converted to physical thickness by scaling with the relative stopping power of the ridge filter material. In this algorithm, the ridge filter thickness of the deepest energy layer is 0. This implies that the beam model distribution moments at isocenter shall include the effect of any base thickness of the ridge filter, as well as of the scattering foil. On the other hand, the beam model distribution moments shall not include any range shifter thickness, even though the minimum range shifter thickness of the Range Option may be non-zero.

The different handling of Mitsubishi Electric SELECT BEAM NOZZLE in US mode and other broad beam techniques in the RayStation dose engine does thus only apply to the calculation of the phase space parameters of the SOBP, see *section 6.6.1 Beam model on page 199*. The transport of the pencil beams and the subsequent scoring of dose in the patient is identical to that of the other system (described in *section 6.6.2 Transport through aperture and compensator on page 202* and *section 6.6.3 Scoring of dose in patient on page 206*.)

6.8 PENCIL BEAM DOSE COMPUTATION FOR SUMITOMO WOBBLING BEAMS

RayStation supports the Wobbling proton delivery technique as adopted by the Multipurpose nozzle of the Sumitomo HI proton delivery system. This section accounts for the adjustments that have been made to the RayStation dose engine to support Sumitomo Wobbling.

In this section

This section contains the following sub-sections:

6.8.1	About Sumitomo Wobbling	p. 214
6.8.2	Dose engine adjustments	p. 214

6.8.1 About Sumitomo Wobbling

Wobbling is a proton delivery technique utilized by the Multipurpose nozzle of the Sumitomo HI proton delivery system, which can produce energies at nozzle entrance from 70 MeV to 230 MeV. The Sumitomo Wobbling technique is very close to other proton broad beam techniques such as Double Scattering (DS) and Uniform Scanning (US). The common denominator for all of these techniques is the delivery of a laterally uniform so-called Spread Out Bragg Peak (SOBP) in combination with a field-specific collimating device (block or MLC) and range compensator.

In the Sumitomo Wobbling delivery system, lateral spread of the narrow proton beam is achieved by a combination of passive scattering and electromagnetic scanning of the beam, and the delivery system may therefore be seen as a hybrid of Single/Double Scattering and Uniform Scanning. The scanning pattern (relative the scan size) is the same for all scan sizes, while the spot size is a function of scan size and is determined by a Scatterer system of binary tungsten scattering foils. The Sumitomo Wobbling delivery system is typically tuned to deliver three fixed field sizes. For each fixed field size, the total thickness of the scattering foils is a unique function of the chosen beam energy and is determined by look-up tables in the Treatment Planning System (TPS). The beam energy and Scatterer setting (thickness) are plan parameters (i.e., exported in DICOM RT ION BEAM) that in the TPS are determined from the desired maximum distal range and the maximum field size. The latter is determined by the dimension of the aperture, as projected on the isocentric plane.

Longitudinal modulation of the field (SOBP width) is performed by a system of discrete Ridge filters. Ridge filters are available for modulations from 1 cm to 18 cm. The same Ridge filter may be used for all ranges/nominal energies, which implies that the SOBPs will not be fully flat for all ranges.

6.8.2 Dose engine adjustments

The RayStation dose calculation algorithms for US, SS and DS beams with a collimating device (block aperture or MLC) and range compensator is described in *section 6.3 Beam model parameters on page 177* and *section 6.6 Pencil Beam dose calculation for US/SS/DS/Wobbling beams on page 198*. This section describes the differences in the dose calculation algorithm that have been introduced for the support of Sumitomo Wobbling. The user is recommended to be well acquainted with all the contents in these sections before continuing with this section.

While the design of the Sumitomo Wobbling delivery system is rather different compared to other broad beam techniques already supported in RayStation, the implications of these differences on the dose calculation are rather limited.

Machine model parameters

For the SS, DS and US delivery systems in RayStation, the beam energies and weights of the energy layers within one Range Option are determined using a single Range Modulator. How many of the Range Modulator energy layers that are included for a given field (including the fraction of the last layer) is determined by the desired modulation width (M). For the Sumitomo Wobbling technique, on the other hand, any number of Range Modulators may be defined, since the Sumitomo Wobbling delivery system uses fixed Range Modulators (Ridge filters).

Energy Layer Selection

The Nominal Energy E_N and Scatter thickness t_{SC} of a Wobbling plan is determined from the expected range in patient R by look-up tables stored in the beam model. These look-up tables are given for each supported maximum field size (typically three for the Sumitomo Wobbling delivery system), which in RayStation translates to three Range Options. The relation between E_N and t_{SC} is provided by the clinic while the range of a field for a certain combination of E_N and t_{SC} is given by measured depth doses provided in the beam modeling procedure. The process to determine E_N and t_{SC} from R is strictly speaking not part of the dose calculation, and is done automatically once RayStation has suggested an R for a plan (via the Treat and Protect functionality) or if the user has entered R manually. The choice of a suitable Ridge filter is either done by the Treat and Protect functionality or alternatively manually selected by the user.

The energy spectrum used to calculate the Integrated Depth Dose (IDD) of the deepest energy layer for the Sumitomo Wobbling delivery system, is defined downstream of the Scatterer. This is possible since the energy after the Scatterer is a unique function of the nominal beam energy for each Range Option. This means that the Scatterer in the Sumitomo Wobbling delivery system is never explicitly included in the dose calculation (i.e., it is not included in R_0 of Equation 126), and that the difference between the nominal beam energy (the energy of the protons at nozzle entrance) and the mean energy of the energy spectrum can be substantial.

The calculation of the IDDs and mean energies for each energy of a field is identical to that for SS/DS/US fields as descried in *section 6.6 Pencil Beam dose calculation for US/SS/DS/Wobbling beams on page 198*.

Spatial-angular distribution

The calculation of $SAD^X_{vir,e}$, $SAD^Y_{vir,e}$, and $\overline{\theta^2_{C,e}}$ is the same as that described for SS and DS delivery systems in *Spatial-angular distribution on page 201* with the difference that $SAD^X_{vir,e}$ and $SAD^Y_{vir,e}$ may have different values for Sumitomo Wobbling.

Scoring of dose in patient

It is possible to exclude scoring of the nuclear halo dose and transfer that part of the fluence to the MCS Gaussian. This possibility has, as described in *section 6.6.3 Scoring of dose in patient on page 206* , been introduced to artificially sharpen the edges of the lateral profiles and thereby compensate for the fact that aperture edge scatter is not taken into account in the dose calculation. The omission of the nuclear halo has proven to be important for Wobbling to give a better fit to the measured profiles.

6.9 MONTE CARLO DOSE CALCULATION

This chapter describes the main features of the Monte Carlo dose engine for proton PBS beams and its implementation in RayStation. An overview of the applied algorithms is provided with references to forward sections that give further details on each topic.

The Monte Carlo and Pencil Beam dose engines share many concepts and models but there are also fundamental differences. The chapter reviews the shared concepts with references to previous sections of the manual and introduces the new concepts and models unique for the Monte Carlo dose engine.

In this section

This section contains the following sub-sections:

6.9.1	Overview	p. 217
6.9.2	Statistical uncertainty	p. 218
6.9.3	Sampling of source protons	p. 218
6.9.4	Transport mechanics	p. 220
6.9.5	Stopping power and energy loss integration	p. 221
6.9.6	Energy loss straggling	p. 222
6.9.7	Multiple scattering	p. 223
6.9.8	Nuclear reactions	p. 223
6.9.9	Handling of range shifters	p. 226
6.9.10	Handling of energy selector	p. 226
6.9.11	Handling of apertures	p. 226
6.9.12	Scoring of dose-averaged LET	p. 227

6.9.1 Overview

The Monte Carlo (MC) dose engine supports dose calculation for proton PBS beams and can be used in the same way as the proton Pencil Beam (PB) dose engine. Thus, it is possible to compute spot dose distributions as input for optimization as well as to compute the dose for an existing proton PBS plan. Dose can be computed for beams holding beam modifiers such as an MLC, a range shifter and a patient specific aperture block with arbitrary air gaps in between. As with the Pencil Beam dose engine, the aperture (block or MLC) can be included also during the optimization.

The MC dose engine is developed by RaySearch for use in RayStation and makes no use of any external software packages. The algorithms and their implementation are specialized to meet the accuracy requirements of radiotherapy dose calculation for treatment planning. The design goal is to realize an implementation that is optimized for speed while carefully maintaining a sufficiently faithful modeling of the relevant physics processes.

In RayStation a single PBS machine model for a particular delivery system can support both the MC and the PB dose calculations. The beam measurement data needed for commissioning the MC dose engine is thus the same as is needed for the PB dose engine.

The Monte Carlo code transports primary protons and secondary ions (protons, deuterons and alphas). A Class II transport method is applied for all ions. Nuclear absorption is neglected for the secondary deuterons and alphas. Neutral reaction products (neutrons and gammas) are not transported, but their given fractions of the absorbed energy are included in the energy balance and considered to leak out. Delta electron production is not considered. This is justified by the fact that released electrons have on average a very short range and therefore have a small effect on the calculation of physical dose in voxels of size 0.5 mm or larger. For example, for a 200 MeV proton the highest delta electron energy is around 500 keV which corresponds to a range of approximately 2 mm in water. With a cross section that is strongly peaked towards lower energies the net effect becomes negligible (see discussion in ICRU Report 55 [103] and references therein). The MC dose engine reports physical dose as dose to a small water cavity embedded in the local medium, i.e., as dose-to-water in agreement with the PB dose engine.

The transport simulation is performed in geometries represented by rectilinear voxel grids where a voxel is characterized by its mass density, elemental composition, and mean ionization energy. For a patient the transport grid coincides with the dose grid. Beam modifiers are represented by rectilinear grids where the grid dimensions are chosen such as to best represent each beam modifier. See *section 6.9.9 Handling of range shifters on page 226* and *section 6.9.11 Handling of apertures on page 226* for descriptions of how a range shifter and an aperture are modeled, respectively. For the beam modifiers one of the cardinal directions of the transport grid is aligned with the beam's central axis during the transport simulation. The gaps between transport grids (e.g., the air gap between a range shifter and the patient) are treated as vacuum. The transport simulation in beam modifiers is carried out using the same transport mechanics and same physics models as is applied for patients except that energy depositions are only scored while in the patient transport grid.

The Monte Carlo transport starts by generating primary protons in a plane upstream of the patient (or phantom) transport grid or upstream of the most upstream beam modifier, if present. The protons are then propagated through the transport grids until they either stop or escape out of the geometry. The MC dose engine and the PB dose engines use the same parametrization of the incident phase

space per spot (see *section 6.5.1 Beam model on page 189*). The sampling of primary protons from the spot phase space is described in *section 6.9.3 Sampling of source protons on page 218*.

The calculation of proton stopping power uses the same models for ionization energy loss (see *section 6.2.1 Stopping power on page 175*) and material modelling (see *section 6.9.6 Energy loss straggling on page 222*) as is used for the PB dose engine. This is further discussed in *section 6.9.5 Stopping power and energy loss integration on page 221*. Energy loss straggling is done in the Bohr approximation (see *section 6.9.6 Energy loss straggling on page 222*). Modeling of multiple scattering is handled by the theory of Goudsmit-Saunderson (see *section 6.9.7 Multiple scattering on page 223*).

The transport mechanics, i.e., the method of propagating ions through the scoring grids and the incorporation of the electromagnetic processes mentioned in the previous paragraph (ionization energy loss, energy loss straggling and multiple scattering), are deeply intertwined. Thus, the transport mechanics uses the so called random hinge method pioneered in MC codes for electron/positron transport. In the current implementation a sequence of random hinges, where each hinge may extend over multiple voxels, is applied until the ion energy reaches an energy threshold. While energy loss must be computed for every voxel traversal, multiple scattering and energy straggling are only computed once per random hinge. The transport mechanics is further detailed in *section 6.9.4 Transport mechanics on page 220*.

The modeling of non-elastic nuclear reactions is data driven and based on a cross section data library derived from published ICRU63 data [110]. No models are used. Elastic scattering of protons on hydrogen and on nuclei are included through parametrized models of the absorption probabilities and differential cross-sections. The handling of nuclear absorption is further discussed in *section 6.9.8 Nuclear reactions on page 223*.

6.9.2 Statistical uncertainty

For Final dose calculation of a PBS treatment plan, the statistical error is estimated using the method of independent batches. The statistical error per voxel is estimated as the dose variance of the dose per voxel over all batches in an online algorithm that adds more and more batches the longer it computes. A single statistical error estimate is reported per beam as the mean one standard deviation error over all voxels having a dose above 50% of the maximum dose per beam. The MC calculated Final dose will be considered Clinical if the statistical error is smaller than a user-defined threshold. Otherwise, the dose will be considered Approximate. The statistical error is not calculated when the MC dose engine is used to drive the optimization. As a consequence, the dose after optimization will always be considered Approximate when the MC is chosen as the optimization dose engine. The calculation is deterministic i.e., repeated calculations yield the same numerical result. However, in case beams are renumbered the result will not be numerically identical between the original and altered beam ordering.

6.9.3 Sampling of source protons

The source protons are sampled from an energy spectrum and the Fermi-Eyges spot parameters as described in *section 6.5.1 Beam model on page 189*. The parameter values are determined per PBS energy layer as given by the beam model.

The spot source phase space is defined in a reference plane typically located perpendicular to the beam line at the gantry rotation point for a gantry equipped system, i.e., the isocenter plane. The spot parameters are summarized here:

- Energy spectrum dN/dE defined by the mean beam energy E_m
- Virtual source axis distances SAD_X^{vir} and SAD_Y^{vir}
- Spatial-angular distribution moments $\{\overline{\theta^2}, \overline{r\theta}, \overline{r^2}\}_x$ and $\{\overline{\theta^2}, \overline{r\theta}, \overline{r^2}\}_y$
- Absolute spot weight (number of protons)

Note: *The spatial-angular distribution moments can be a total of two sets, a primary and a secondary with respective weights to specify their contribution. A model without secondary spatial-angular moments is equivalent to having secondary weight zero.*

First a kinetic energy is sampled from the energy spectrum. The mean direction of the spot **e** $= \{e_x, e_y, e_z\}$ is defined according to Equation 94. The direction with respect to the mean direction **e** is determined in two orthogonal planes by sampling as described below. Finally the resulting direction vector is rotated into the beam coordinate system.

The sampling of position and direction is separable in the x and y planes (note: we assume the spot radius and emission angles within a spot are small).

In the x direction the sampling proceeds as follows ($N(0, \sigma)$ is a normal distributed random number with mean zero and standard deviation σ):

1. The proton spot center position x_c is given by the treatment plan
2. The proton direction at the spot center x_c is given by the mean direction **e**
3. Sample position relative to the spot center

   $$\Delta x = N\left(0, \sqrt{\langle r_x^2 \rangle}\right)$$

4. Calculate the proton position as $x = x_c + \Delta x$
5. Determine whether to use primary or secondary spatial-angular distribution by random choice based on respective weights.
6. Determine the angular rms spread at $x_c + \Delta x$, using the chosen distribution, as $\langle \theta_x^2 \rangle = \overline{\theta_x^2} - \frac{\overline{r\theta_x}^2}{\overline{r_x^2}}$
7. Sample the emission angle as $\theta_x = N\left(0, \sqrt{\langle \theta_x^2 \rangle}\right) + \Delta x \times \frac{\overline{r\theta_x}}{\overline{r^2}_x}$
8. Rotate (in small angle approximation) into the beam coordinate system relative to the spot's mean direction **e**.

The same is repeated for the y plane. Finally the proton is translated (assuming vacuum) upstream to a plane located above the most upstream located transport grid.

6.9.4 Transport mechanics

The method of propagating protons through a transport grid is herein referred to as transport mechanics. The transport mechanics must fulfill the following two criteria simultaneously:

- The physics processes shall be modeled so that the achieved accuracy is adequate with respect to the problem domain.
- The modeling methods shall be possible to implement in computer code in such a way that reasonable computation times for the treatment planning workflow are achieved.

As will be discussed here, this trade-off concerns mainly the way multiple scattering and energy loss straggling is incorporated. Our solution represents a well-balanced trade-off between accuracy and computation efficiency and is the result of careful analysis and trial and error during code development.

Below the transport mechanics is discussed for a primary proton that enters the patient density grid with incident kinetic energy E. Transport of secondary protons and transport in the other types of grids (range shifter, block and MLC) are handled in the same manner and need not be described separately.

To avoid evaluating the nuclear cross sections for each voxel, the fictitious cross section method, also known as Woodcock tracking [143], is used. The distance to the next nuclear interaction is sampled from the minimum mean free path. At the site of the interaction, it is rejected with a probaility that depends on the local cross section. There is no loss of accuracy by using this method.

We apply the so called random hinge method pioneered in MC codes for electron/positron transport see [111] and [54]. A random hinge consists of two straight legs connected by a hinge point where a deflection due to multiple scattering is applied (see Figure 66). A sequence of random hinges, where each hinge leg may extend over multiple voxels, is applied until the ion energy reach a predefined low energy threshold. The deflection angle is sampled from a probability distribution given by the Goudsmit-Saunderson theory discussed in *section 6.9.7 Multiple scattering on page 223*.

While energy loss needs to be computed for every voxel traversal, the multiple scattering and energy straggling is only computed once per random hinge leading to an efficient calculation scheme.

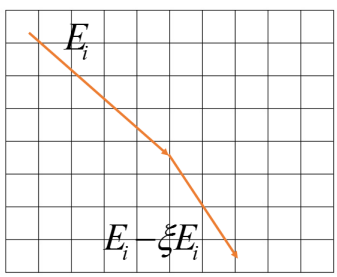

Figure 66. A random hinge step with two legs for an ion with energy E_i at the beginning of the step and losing energy $\Delta E = \xi E_i$ after the step. The deflection due to multiple scattering is applied at the hinge point.

The random hinge steps propagate the proton from its incident energy E down to and below a threshold energy of $E_{cut}^{RH} = 30.7\ \mathrm{MeV}$ which corresponds to a residual range in unit density water of about 9 mm. Below this energy the proton is transported without considering multiple scattering and energy loss straggling. This threshold is 5 MeV (corresponding to a range of about 0.4 mm) for primary protons in range shifters and energy selectors to accurately model the fluence exiting the beam line object.

The summed lengths of the two hinge legs are determined in the energy domain per random hinge prior to propagation and is calculated from the fractional energy loss parameter $\xi = 0.1$ as

$$\Delta E_i = \xi E_i \qquad \text{[Eq. 141]}$$

where E_i is the proton kinetic energy before the step and i denotes RH index. Thus, at the start of the next RH step the energy of the proton is $E_{i-1} = E_1 - \Delta E_i$. The hinge point is defined by sampling an efficient energy E_{RH}^{eff} uniformly distributed between E_i and E_{i-1}. (see also discussion in *section 6.9.7 Multiple scattering on page 223*). The choice of $\xi = 0.1$ is based on investigations of numerical stability and performance. Using a much smaller value ($\xi = 0.01$) as base line it was verified, by comparisons with water phantom data and patient data with and without range shifters and apertures, that this value represents a conservative working point.

This RH stepping proceeds until the proton exits an RH step with an energy below the threshold E_{cut}^{RH} , or exits the current beam limiting device geometry (i.e., range shifter, block aperture or MLC). Below this energy the proton is propagated through the residual range without considering multiple scattering and energy loss straggling $E_{cut}^{Transport} = 1\ \mathrm{MeV}$.

Ionization energy loss integration and nuclear absorption are evaluated for every voxel traversal. To ensure accurate results in these evaluations we restrict the maximum step length to 4 mm in unit density water. This means that in some situations an ion is actually moved only a fraction of the actual path length between entrance and exit of a voxel. This is for example the case for a range shifter which is represented by a grid with a single voxel.

6.9.5 Stopping power and energy loss integration

The ionization energy loss per voxel traversal is calculated by integrating the stopping power in the local density and medium. As for the Pencil Beam dose engine, the stopping power calculation is based on direct evaluation of the Bethe-Bloch formula and uses the same approximation of disregarding shell and density correction terms (see discussion in *section 6.2.1 Stopping power on page 175*).

However, to gain calculation efficiency, and in contrast to the pencil beam dose engine, energy loss integration is done by a two-point method making use of the observation that the stopping power is a strict monotonically decreasing function for increasing energies over the energy range of relevance here (note that the cut off threshold for transport is 1 MeV/u kinetic energy).

The Monte Carlo dose engine reports physical dose as dose-to-water (as does also the Pencil Beam dose engine). This is achieved by a scaling of the deposited ionization energy per voxel traversal

by the water to local medium energy dependent mass stopping power ratio evaluated at run-time. The small amount of energy originating from local deposition of non-elastic interactions (*Non-elastic nuclear reactions on page 224*) and from the recoil energy of elastic p-nucleus scattering (*Elastic proton - nucleus scattering on page 225*) is not included in the dose-to-water scaling.

6.9.6 Energy loss straggling

Range straggling refers to the spread in ion ranges even in a mono-energetic beam because energy loss is a statistical process that occurs in discrete steps. In a condensed history Monte Carlo dose engine the corresponding energy loss fluctuations must somehow be accounted for explicitly as part of the transport. Note that this is in contrast to a Pencil Beam dose engine where the effects of range straggling are embedded in the integrated depth dose curves.

We model the range (or energy loss) straggling in the Bohr approximation where, for a thick absorber or sufficiently long step, the spread can be characterized by a Gaussian distribution (see *section 6.2.3 Energy loss straggling on page 175*). The range straggling is nearly proportional to the range, as is shown in Figure 67, with only a weak dependence on the ion kinetic energy. Further, the dependence on the material composition is also weak and in particular so for tissue like media dominated by low Z elements. This nearly material-independent behavior means we can assume the Bragg peak shapes (scaled to water equivalent depth coordinates) to be similar to a reference material such as e.g., water even if some stopping occurred in media of other compositions.

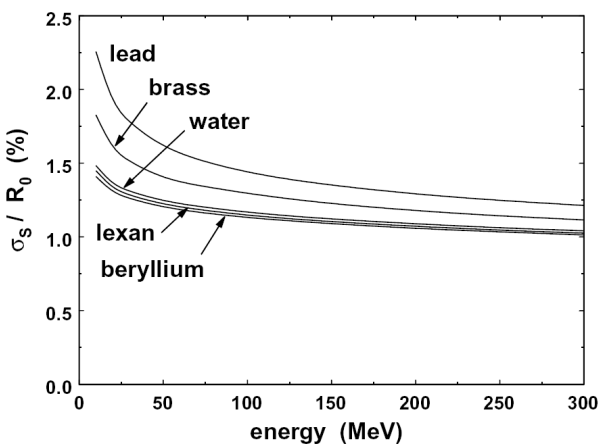

Figure 67. Relative proton range straggling for energies of relevance for radiation therapy [112].

The effect of straggling is incorporated in the transport mechanics by applying a single straggling correction per random hinge step. We define the reference medium to be unit density water during the entire RH step. From the energy loss over the RH step, ΔE_i ,we calculate an effective thickness to be used in the Bohr expression as

$$\Delta S_i = \frac{\Delta E_i}{\frac{dE_{Water}}{ds}} \quad (E = E_{ES}^{eff}) \qquad \text{[Eq. 142]}$$

where E_{ES}^{eff} is the effective energy per step and $\frac{dE_{Water}}{ds}$ is the stopping power in unit density water. Note that the effective energy used for straggling, E_{ES}^{eff}, is selected in the same way, but is independent from the effective energy used for the multiple scattering hinge point, E_{RH}^{eff}. Finally, the corresponding rms energy straggling width σ_{ES} for the effective step is calculated by Equation 88. This calculation is performed prior to executing the RH step. The energy loss straggling is incorporated in the transport through a stopping power correction given by

$$c_i^{SP} = 1 + \frac{N(0, \sigma_{ES})}{\Delta E_i} \qquad \text{[Eq. 143]}$$

where $N(0, \sigma_{ES})$ is a normal distributed random number with mean zero and rms spread σ_{ES}. The correction factor c_i^{SP} multiplies all stopping power evaluations within this random hinge step.

6.9.7 Multiple scattering

The angular deflection due to multiple scattering is sampled from an angle probability distribution which is calculated with the Goudsmit-Saunderson theory [104], [105]. The Goudsmit-Saunderson formalism is, with respect to the underlying elastic scattering cross section used, an "exact" theory for any angle multiple scattering without small angle approximations. The Goudsmit-Saunderson theory was originally derived for electron multiple scattering assuming motion in a homogenous medium while neglecting energy loss. The Goudsmit-Saunderson theory has since been applied for electron/positron transport in various Monte Carlo codes such as egsnrc [11] and VMC++ [54] and is now applied also to protons.

We use the screened Rutherford cross section following the work by Kawrakow and Bielajew in [106] and later refined by Kawrakow in [107]. In each medium we compute two medium composition dependent parameters (equivalent to the b_c and X_{cc} of [54]). The multiple scattering angle is sampled at the efficient energy E_{RH}^{eff} introduced in *section 6.9.4 Transport mechanics on page 220* in the local medium of the voxel containing the hinge point. The sampling uses a pre-computed "q2-surface" similarly to how it is described in [107].

To obtain an optimal adaptation to experimental data the resulting multiple scattering angles are down scaled by a factor 0.93 independent on energy and medium. Input to this fine tuning was mainly block aperture collimated water lateral profile penumbras for which the penumbra shape is maximally sensitive to multiple scattering.

6.9.8 Nuclear reactions

Nuclear interactions lead to absorption of primary protons and generation of a halo of secondary ions that are emitted at large angles relative to the direction of the incident proton. It is essential to model this in sufficient detail as the absorption decreases the amount of protons that reach the

Bragg peak. It is also essential for correctly reproducing field size variation effects (e.g., output factors) as the halo carries non-negligible amounts of energy away from the track of the incident proton.

The RayStation Monte Carlo dose engine considers three nuclear interaction processes:

1. Non-elastic nuclear reactions leading to production of secondary protons, deuterons and alpha
2. Elastic proton – proton scattering
3. Elastic proton – nucleus scattering

The non-elastic reactions and the elastic proton – proton scattering events are treated as catastrophic events i.e., the incident proton is absorbed and is replaced by one or several secondary ions. The probability for absorption through these catastrophic channels are evaluated from macroscopic cross section which are discussed in the following subsections.

The probability for elastic proton – nucleus scattering at large angles is relatively low. As this process is governed partly by the Coulomb force it is treated as a non-catastrophic event embedded in the handling of multiple scattering as described below.

Non-elastic nuclear reactions

Non-elastic nuclear reactions involve a substantial rearrangement of the nucleons in the nuclei. This results in a high dimensional space of final states which is costly and difficult to model. We therefore chose to base the inclusion of non-elastic reactions by use of a data library of pre-stored tables of the needed quantities. The data library is compiled from data provided in the ICRU 63 report [110] for a sequence of elements in the periodic table. The following quantities per element from the ICRU 63 report are used:

- Total non-elastic cross section
- Production cross section for proton, deuterons and alphas
- Fraction of incident energy leading to protons, deuterons, alpha, neutrals (neutrons and gammas) and heavy recoils (A>4)
- Double differential emission spectra for production of protons, deuterons and alphas

The data is tabulated from a few MeV up to 250 MeV kinetic incident proton energy for the isotopes ^{12}C, ^{14}N, ^{16}O, ^{27}Al, ^{28}Si, ^{31}P, ^{40}Ca, ^{56}Fe, ^{63}Cu, ^{184}W and ^{208}Pb. Note that the ICRU 63 tables only provides data for a subset of the elements in the periodic table. Missing elements are redistributed to the nearest neighbors of the ICRU 63 isotopes with weights according to the relative distance to the respective neighbor in terms of their geometrical cross sections, here calculated as $A^{2/3}$.

From the ICRU 63 data we construct, prior to each dose calculation, macroscopic cross section data for all materials of the transport calculations. These materials include the interpolated patient materials used for the CT to voxel material mapping (see *section 6.9.6 Energy loss straggling on page 222*), materials of any material override, as well as the materials of any beam limiting devices such as a range shifter, block and MLC.

In a proton transport step, first the distance to the next interaction is sampled from the minimum mean free path. At the interaction point it is sampled if an interaction should occur depending on the density and cross section of the voxel. Second, based on the relative cross section between the tabulated nuclei and the elemental composition of the material in the voxel, a reaction channel is sampled. The incident proton is absorbed and replaced by secondary ions sampled from the double differential cross sections. The fraction of the incident energy that goes to heavier secondary ions (A>4) is considered by the creation of a carbon ion with the same direction as the incident proton. The secondary ions are queued on the transport stack for subsequent transport.

Similarly to the multiple scattering tuning, an energy dependent fine tuning of the nonelastic nuclear absorption cross section to achieve an optimal match with measurements (the multiplicities of the reaction channels were left intact) was performed. The driving input to this was a large set of measured IDD curves in water. In particular the higher energies were found to be sensitive to the absorption tuning. As we are limited to IDD data in water this tuning was done only for the oxygen total absorption cross section leaving other nuclei unchanged.

Elastic proton - proton scattering

This process is modeled as a catastrophic event. The incident proton is absorbed and replaced by two secondary protons which are queued on the transport stack for subsequent transport.

The macroscopic cross section $\sum_{pp}(E_p)$ of proton – proton collisions of a material with index m is calculated from the microscopic cross section $\sigma_{pp}(E_p)$ as

$$\sum_{pp}(E_p) = \rho N_A \frac{w_{H,m}}{A_H} \sigma_{pp}\left(E_p\right) \qquad \text{[Eq. 144]}$$

where E_p is the proton kinetic energy, N_A is the Avogadro constant, $w_{H,m}$ is the weight proportion of hydrogen in the material and A_H is the atomic weight of hydrogen.

For the microscopic cross section we use the parametrization of [108] where

$$\sigma_{pp}(E_p) = 4,71 \times 10^{-24}\left[E_p^{-1,126} + 12 \times 10^{-6} E_p\right] \qquad \text{[Eq. 145]}$$

with the kinetic energy E_p in MeV. We treat the angular distribution as isotropic in the center-of-momentum system which is a good approximation in the energy interval of relevance here (see e.g., data in [109]).

Elastic proton - nucleus scattering

The elastic proton – nucleus scattering is treated as a non-catastrophic event and is embedded it in the handling of multiple scattering (see *section 6.9.7 Multiple scattering on page 223*).

In the current implementation the cross section is derived from the simplified method proposed in [108] where it is assumed that the scattering is on oxygen embedded in water scaled with the local mass density but independent of the local material composition.

The macroscopic cross section $\sum_{p0}(E_p)$ of proton – oxygen collisions is given by the microscopic cross section $\sigma_{p0}(E_p)$ as

$$\sum_{p0}(E_p) = \rho N_A \frac{w_0}{A_0} \sigma_{p0}(E_p) \qquad \text{[Eq. 146]}$$

where w_0 is the weight proportion of oxygen in water and A_0 is the atomic weight of oxygen. As for the case of proton – proton scattering, for the microscopic cross section we use the parametrization of [108] where

$$\sigma_{p0}(E_p) = 2,9916 \times 10^{-23} \left[\frac{1.88}{E_p} + 4 \times 10^{-5} E_p - 0,01475 \right] cm^2 \qquad \text{[Eq. 147]}$$

with the kinetic energy E_p in MeV.

The angular distribution is derived from a fit to proton - oxygen data tabulated in ICRU 63. For the details of the fit and the procedure for sampling see [108].

6.9.9 Handling of range shifters

A range shifter is modeled as a grid with a single voxel filled with a material of a mass density and composition as selected by the user during the commissioning process. The voxel size in the beam direction equals the thickness of the range shifter. The lateral extension of the grid corresponds to the actual physical size of the range shifter plate (if this is known). The lateral extension of circular range shifters are handled through a special procedure during the transport. To ensure accurate results, the multiple scattering threshold is lowered to 5 MeV for primary protons and the maximum step length is restricted by the method discussed in *section 6.9.4 Transport mechanics on page 220*.

6.9.10 Handling of energy selector

If an energy selector (binary range shifter) is used in the nozzle (e.g., for Mevion Hyperscan), it is modeled as a voxelized geometry consisting of a stack of thin voxels in the beam direction. The density of the voxels is determined by the plate setting of a particular nominal energy. In the presence of an energy selector, the Monte Carlo geometry "seen" by a proton is therefore dependent on the nominal energy. The voxel size in the beam direction is less than 1mm. The lateral extension is considered to be very large (and not limiting for transport). Downstream of the energy selector there can also be a nozzle exit window, which is modeled as a thin range shifter that is always a part of the geometry, irrespective of the nominal energy.

6.9.11 Handling of apertures

An aperture (block or MLC) can be inserted in the beam line and used as beam collimator. The aperture is included in the dose calculation both during optimization and when computing dose for existing PBS plans. This section describes briefly how the aperture is handled by the Monte Carlo dose engine.

For static apertures (not Mevion adaptive apertures), the aperture shape is discretized by a separate transport grid with a lateral voxel size dependent on the aperture area normal to the beam direction. The lateral voxel size is proportional to the square root of the area, with a minimum and maximum cap such that it is 0.5 mm for apertures larger than 100 cm^2 and 0.2 mm for apertures smaller than 10 cm^2. Along the beam direction the length of voxels equal the thickness of the aperture. The grid voxels are either void voxels (vacuum) representing the open part of the aperture or given a mass density and composition corresponding to the actual aperture material (typically brass). Voxels that have a center point inside the aperture contour are set to vacuum. Currently it is assumed the aperture inner faces are straight (i.e., not focused).

The transport simulation treats the aperture grid in the same way as the patient grid. A proton may enter the grid either in the open part in which case it is traced along a straight line until it exists through the open part of the distal surface or enters into the aperture material. In the latter case the proton is propagated using the same physics models discussed previously in this chapter. More specifically this means that a primary proton that enters the aperture material may be scattered out into the open part of the aperture. Similarly, the proton may generate secondary ions that may reach the outer part. These out-scattered ions are propagated further and may reach the patient or phantom surface and deposit dose. This is the main source of the dose "ears" that can be observed at shallow depths. As for the range shifter, is the maximum step length restricted by the method discussed in *section 6.9.4 Transport mechanics on page 220*.

In the final dose calculation, the Mevion adaptive aperture is modeled with voxels corresponding to the leaf widths and positions. The Mevion adaptive aperture is modeled differently when using the Monte Carlo dose engine for optimization and final dose computation, see *section 6.12 Optimization and dose calculation for Mevion Hyperscan on page 255* for details.

6.9.12 Scoring of dose-averaged LET

The RayStation Monte Carlo dose engine computes dose-averaged LET (LET_d) in water normalized to unit density [152] . LET from primary and secondary protons are included but LET from heavier fragments are not. The dose-averaged LET in a voxel i from a single beam b is in RayStation computed as:

$$LETd_{b,i} = \frac{\sum_{s,h} (d * let)_i}{D^p_{b,i}} \qquad \text{[Eq. 148]}$$

$$D^p_{b,i} = \sum_{s,h} d_i \qquad \text{[Eq. 149]}$$

where $D^p_{b,i}$ is the total beam dose deposited from primary and secondary protons, d_i the dose deposited in voxel i from the MC simulated proton h in spot s. $(d * let)_i$ is the corresponding integral of LET with respect to deposited energy along the proton track Γ_i across the voxel:

$$(d * let)_i = \frac{1}{\rho V} \int_{\Gamma_i} LET_\infty dE \qquad \text{[Eq. 150]}$$

where ρ and V is the mass density and volume of the voxel, respectively, and LET_∞ the unrestricted linear energy transfer in water (see *section 6.2.2 Linear Energy Transfer (LET) on page 175*). E in Equation 150 is the energy of the proton only considering energy loss to the electrons along Γ_i. For protons that stop within the voxel, the integral is evaluated down to an energy of 1 keV. It should be noted that $D^p_{b,i}$ will differ slightly from the total beam dose in the plan, $D_{b,i}$, since contributions from heavier fragments are not included in $D^p_{b,i}$. To compute to total LET_d from all beams, the beam LET_d values are thus averaged using the proton only beam doses:

$$LETd_i = \frac{\sum_b D^p_{b,i} * LETd_{b,i}}{\sum_b D^p_{b,i}} \qquad \text{[Eq. 151]}$$

At optimization, LET_d is computed in a slightly different way, meaning that it does not exactly agree with LET_d computed at final dose.

WARNING!

Always evaluate the dose distribution when using LET evaluation. The LET distribution of a plan is an auxiliary quantity, meant to provide additional information to the primary quantity of RBE-weighted dose. The definition of averaged LET is chosen to conform to how LET is generally reported in the literature, and how it is used when estimating the biological effect using RBE models, rather than producing a directly measurable quantity.

The correlation between LET and biological effect in patients is an evolving field of science. The user must always review the literature and base the usage of LET evaluation on the current state of knowledge in the field and clinic-specific treatment techniques and modalities.

(408388)

6.10 DOSE ENGINE ACCURACY AND LIMITATIONS

This section summarizes the acceptance criteria and identified limitations of the RayStation proton pencil beam dose engine for PBS, US, SS and DS plans and the Monte Carlo dose engine for PBS plans. It is important that the user is familiar with, and understands these limitations.

In this section

This section contains the following sub-sections:

6.10.1	PBS Pencil beam and Monte Carlo dose engine acceptance criteria	p. 230
6.10.2	PBS Pencil beam dose calculation limitations	p. 231
6.10.3	PBS Monte Carlo dose calculation limitations	p. 235
6.10.4	US/SS/DS/Wobbling Pencil beam dose calculation acceptance criteria	p. 237
6.10.5	US/SS/DS/Wobbling Pencil beam dose calculation limitations	p. 239

6.10.1 PBS Pencil beam and Monte Carlo dose engine acceptance criteria

Relative dose heterogeneous patient

The following accuracy requirements shall apply to the relative dose distribution in a heterogeneous patient:

- 95% of the computed dose values shall pass gamma(5%, 5mm)<1
- 90% of the computed dose values shall pass gamma(3%, 3mm)<1

Relative dose homogenous patient

The following accuracy requirements shall apply to the relative dose distribution in a homogenous patient:

- 98% of the computed dose values shall pass gamma(5%, 5mm)<1
- 95% of the computed dose values shall pass gamma(3%, 3mm)<1

The distal range of a central axis relative depth dose curve shall be within 2 mm in a homogenous patient.

Absolute dose heterogeneous patient

The following accuracy requirements shall apply to the absolute dose distribution in a heterogeneous patient:

- 95% of the computed dose values shall pass gamma(7%, 5 mm)< 1
- 90% of the computed dose values shall pass gamma(5%, 3 mm)< 1

Absolute dose homogeneous patient

The following accuracy requirements shall apply to the absolute dose distribution in a homogeneous patient:

- 95% of the computed dose values shall pass gamma(5%, 5mm)<1
- 90% of the computed dose values shall pass gamma(3%, 3mm)<1

The field size factor errors shall be within ±3% for plans without range shifter in a homogeneous patient.

The field size factor errors shall be within ±5% for plans using a range shifter in a homogeneous patient.

Absolute dose-averaged LET compared to simulations

The following accuracy requirements shall apply to the dose-averaged LET computation for comparison to a calculated reference dose-averaged LET (for 3D distributions):

- 90% of the computed dose-averaged LET values shall be within 3% of the reference level or 2 mm (global gamma). Only voxels with a physical dose value above 10% of the max physical dose are considered.
- 95% of the computed dose-averaged LET values shall be within 5% of the reference level or 2 mm (global gamma). Only voxels with a physical dose value above 10% of the max physical dose are considered.
- 98% of the computed dose-averaged LET values shall be within 8% of the reference level or 2 mm (global gamma). Only voxels with a physical dose value above 10% of the max physical dose are considered.

The reference LET level is 100 MeV/cm.

6.10.2 PBS Pencil beam dose calculation limitations

WARNING!

The effect of the infinite slab approximation in the PB dose engine on proton PBS/Line Scanning. The proton PBS/Line Scanning Pencil Beam dose engine is based on the so-called infinite slab approximation. This approximation disregards lateral inhomogeneities for individual ray traces, which will see the patient as a stack of semi-infinite layers. The effect of this approximation is more severe for patients with large lateral inhomogeneities, especially closer to the target area. This situation is common for many lung cases, but other treatment sites may also be affected. For lung cases with range shifters, dose to tumors in lung tissue has been shown to be overestimated by up to 10% in the PTV center, with significant loss of target coverage even after dose rescaling.

Be aware that the dose computation may not be accurate for patients with large lateral inhomogeneities relative the beam direction. It is strongly recommended to use the RayStation Monte Carlo dose engine for computation of final dose for any patient where the beam will see large lateral inhomogeneities. (369533)

WARNING!

Sub-spot limitations for Proton PBS PB dose engine. In the RayStation PBS pencil beam dose calculation, the Gaussian spot fluence is discretized into 19 sub-spots. This is done to minimize the errors introduced by the inherent infinite slab approximation of the pencil beam algorithm. The choice of 19 is a compromise between the accurate representation of the initial Gaussian fluence and the sufficiently course sampling of the patient geometry for typical spot sizes on the one hand, and the calculation speed on the other.

The distance between the sub-spots in the proton Pencil Beam PBS dose engine is dependent on the spot size. The sub-spot distance is around 85% of the spot size (spot sigma), which for a 5 mm spot results in a sub-spot distance of around 4 mm. When the spot size gets very large, the distance between the sub-spots may be larger than the geometrical variations of the patient, which then will not be taken into account by the Pencil Beam dose engine. For spots that are glancing the patient surface (for example from tangential beams) only the sub-spots that intersect the patient geometry (External ROI) will be taken into account. As a consequence, there is a potential loss of dose in the surface region. Large spot sizes are for example common when a range shifter with a large air gap is used in combination with low beam energies.

Refer to *RSL-D-RS-2024A-REF, RayStation 2024A Reference Manual* for more details.

The user shall be aware of this limitation in the PBS dose calculation and it is strongly recommended to use the RayStation Monte-Carlo dose engine for computation of final dose for any beam including a range shifter. (369528)

WARNING!

Accuracy of Pencil Beam dose engine for proton PBS and Line Scanning beams with range shifters. In the RayStation PBS Pencil Beam dose engine validation, a few deviations from the dose accuracy requirements were noted for doses in water, especially at shallow depth, when a range shifter with a relatively large air gap was used. These deviations have been linked to the handling of secondary proton transport over the air gap, resulting mainly in an overestimation of the dose in the surface region, but the spot to sub-spot discretization may also contribute to the dose error when spots at the patient surface become very large.

The user shall be aware of these limitations in the pencil beam dose engine. It is strongly recommended to use the RayStation Monte-Carlo dose engine for computation of final dose for any beam including a range shifter. (369527)

WARNING!

Quasi-discrete spill dose is not computed in RayStation. A quasi-discrete PBS plan is computed as a step-and-shoot PBS plan and the spill dose between spots will not be considered. The dose difference between the computed plan and the delivered plan needs to be assessed by the user in the commissioning of RayStation as well as during patient specific QA. (123711)

WARNING!

Closed MLC leaves may be positioned along the central axis. When automatically or manually positioning MLC leaves, the positions of closed leaf pairs are automatically set. In some cases it is not possible to place the closed leaves at the default closed leaves position defined in the machine due to other MLC leaf position restrictions. In such cases, the closed leaves might be aligned with the central axis. This might result in leakage of dose in the area where the closed leaf pair meets, which is not taken into account in the RayStation ion dose computation. It is the user's responsibility to ensure that the leaves are not closed along the central axis, or that the possible leakage is acceptable. (370014)

WARNING!

Leakage between MLC leaves for protons. In the RayStation proton dose engines, a collimating MLC is regarded as an aperture block with a jagged contour, meaning that actual leakage between adjacent leaves or closed leaf tips are not handled by the dose engines. The dose difference between the computed plan and the delivered plan needs to be assessed by the user in the commissioning of RayStation as well as during patient specific QA. (371451)

WARNING!

Effect of non-collimating MLC leaves in dose computation for protons. In RayStation, the MLC leafs are only taken into account by the proton dose engines if the MLC is regarded as collimating. The MLC leaves are regarded as non-collimating if the MLC leaves are in their most retracted position (outside the snout inner dimension) or if the MLC leaves are positioned outside a block opening. Any effect on the dose distribution from such MLC setups are not reflected in the dose computation. The dose difference between the computed plan and the delivered plan needs to be assessed by the user in the commissioning of RayStation as well as during patient specific QA. (371452)

Energy selector

Using the pencil beam dose engine in RayStation in combination with an energy selector introduces a number of range shifters and (sometimes) large air gaps. In the internal RayStation PBS pencil beam dose engine validation it was noted that the pencil beam dose algorithm is insufficient under such circumstances, especially for shallow depths. Energy selector in combination with the pencil beam dose engine therefore never leads to clinical dose and shall mainly be viewed as an option for fast optimization and range evaluation. No clinically relevant evaluations should be performed based on this dose.

WARNING!

Scanned field size limitations for Proton PBS PB dose engine. The PBS Pencil Beam dose engine validation of RayStation only covers scanned field sizes down to 4 x 4 cm^2. Be extra careful when creating PBS and Line Scanning plans with scanned field sizes smaller than 4 x 4 cm^2. (369529)

6.10.3 PBS Monte Carlo dose calculation limitations

WARNING!

Field size limitations for Proton PBS MC dose engine. The Monte Carlo PBS dose engine validation of RayStation only covers the following setups related to field size:

- Scanned field sizes down to 4 x 4 cm^2
- MLC aperture openings down to 2 x 2 cm^2
- Block aperture openings down to 4 x 4 cm^2
- Block aperture openings with diameters between 8 and 15 mm for shallow fields with ranges between 5 and 30 mm

Be extra careful when creating PBS and Line Scanning plans with scanned field sizes or aperture openings smaller than the setups covered in the dose engine validation.

(369532)

WARNING!

Dose accuracy for the proton MC dose engine used for small shallow fields. The Monte Carlo PBS dose engine validation of RayStation shows some deviations from the dose accuracy requirements when compared with measurements for small shallow fields. The validation includes fields with depth ranging from 5 to 30 mm, using aperture openings with diameters of 8 and 15 mm. The treatment nozzle used in the test setup has a range shifter that is placed 72 cm upstream of the aperture. For these setups, the accuracy requirements are a gamma (3%,0.3mm) pass rate above 90% and a gamma (5%,0.5mm) pass rate above 95%. For the test cases using an 8 mm aperture diameter, the RayStation Monte Carlo PBS dose engine tends to overestimate the dose relative to measurements, and in one case the validation fails the gamma (3%,0.3mm) accuracy requirement, with a fail rate of about 14%. Test cases for an equivalent setup but with a 15 mm aperture diameter pass all accuracy requirements, and all test cases for small shallow fields pass the gamma (5%,0.5mm) requirement.

The user is advised to be extra careful when creating plans with aperture openings smaller than 15 mm.

(824407)

WARNING!

Quasi-discrete spill dose is not computed in RayStation. A quasi-discrete PBS plan is computed as a step-and-shoot PBS plan and the spill dose between spots will not be considered. The dose difference between the computed plan and the delivered plan needs to be assessed by the user in the commissioning of RayStation as well as during patient specific QA. (123711)

WARNING!

Closed MLC leaves may be positioned along the central axis. When automatically or manually positioning MLC leaves, the positions of closed leaf pairs are automatically set. In some cases it is not possible to place the closed leaves at the default closed leaves position defined in the machine due to other MLC leaf position restrictions. In such cases, the closed leaves might be aligned with the central axis. This might result in leakage of dose in the area where the closed leaf pair meets, which is not taken into account in the RayStation ion dose computation. It is the user's responsibility to ensure that the leaves are not closed along the central axis, or that the possible leakage is acceptable. (370014)

WARNING!

Leakage between MLC leaves for protons. In the RayStation proton dose engines, a collimating MLC is regarded as an aperture block with a jagged contour, meaning that actual leakage between adjacent leaves or closed leaf tips are not handled by the dose engines. The dose difference between the computed plan and the delivered plan needs to be assessed by the user in the commissioning of RayStation as well as during patient specific QA. (371451)

WARNING!

Effect of non-collimating MLC leaves in dose computation for protons. In RayStation, the MLC leafs are only taken into account by the proton dose engines if the MLC is regarded as collimating. The MLC leaves are regarded as non-collimating if the MLC leaves are in their most retracted position (outside the snout inner dimension) or if the MLC leaves are positioned outside a block opening. Any effect on the dose distribution from such MLC setups are not reflected in the dose computation. The dose difference between the computed plan and the delivered plan needs to be assessed by the user in the commissioning of RayStation as well as during patient specific QA. (371452)

6.10.4 US/SS/DS/Wobbling Pencil beam dose calculation acceptance criteria

Relative total dose heterogeneous patient

The following accuracy requirements shall apply to the total dose distribution in a heterogeneous patient:

- 95% of the computed dose values shall pass gamma(5%, 5mm)<1
- 90% of the computed dose values shall pass gamma(3%, 3mm)<1

Relative dose homogeneous patient

The following accuracy requirements shall apply to the dose distribution in a homogeneous patient:

- The SOBP range (90%) of the central axis depth dose curve shall be within 2 mm
- The SOBP distal fall off (80-20%) of the central axis depth dose curve shall be within 2 mm
- 95% of the computed depth dose values shall pass gamma(3%, 3mm)<1
- 98% of the computed depth dose values shall pass gamma(5%, 5mm)<1
- 95% of the computed lateral profile dose values shall pass gamma(3%, 3mm)<1 1-2
- 98% of the computed lateral profile dose values shall pass gamma(5%, 5mm)<1
- The FWHM of a lateral dose profile shall be within 2 mm
- The left and right penumbra (20-80%) of a lateral dose profile shall be within 2 mm

The following accuracy requirements shall apply to the dose distribution in a homogeneous patient using a range compensator:

- The SOBP range (90%) of the central axis depth dose curve shall be within 2 mm
- The SOBP distal fall off (80-20%) of the central axis depth dose curve shall be within 2 mm
- 95% of the computed depth dose values shall pass gamma(3%, 3mm)<1

- 98% of the computed depth dose values shall pass gamma(5%, 5mm)<1
- 95% of the computed lateral profile dose values shall pass gamma(3%, 3mm)<1
- 98% of the computed lateral profile dose values shall pass gamma(5%, 5mm)<1
- The FWHM of a lateral dose profile shall be within 2 mm
- The left and right penumbra (20-80%) of a lateral dose profile shall be within 2 mm

The following accuracy requirements shall apply to the dose distributions in a homogeneous patient for delivery systems dedicated for small field sizes (< 4 cm) and intermediate depths (< 15 cm):

- The SOBP range (90%) of the central axis depth dose curve shall be within 1 mm
- The SOBP distal fall off (80-20%) of the central axis depth dose curve shall be within 1mm
- 95% of the computed depth dose values shall pass gamma(3%, 2mm)<1
- 95% of the computed lateral profile dose values shall pass gamma(3%, 2mm)<1
- The FWHM of a lateral dose profile shall be within 1 mm
- The left and right penumbra (20-80%) of a lateral dose profile shall be within 1 mm

The following accuracy requirements shall apply to the dose distribution in a homogeneous patient for an ocular treatment:

- The SOBP range (90%) of the central axis depth dose curve shall be within 0.4 mm. Only applied to fields without lateral modulation.
- The SOBP distal fall off (80-20%) of the central axis depth dose curve shall be within 0.3 mm
- 95% of the computed depth dose values shall pass gamma(3%, 0.3 mm)<1
- 98% of the computed depth dose values shall pass Gamma(5%, 0.5 mm)<1
- The FWHM of a lateral dose profile shall be within 0.4 mm. Only applied to fields without lateral modulation.
- The left and right penumbra (20-80%) of a lateral dose profile shall be within 0.3 mm

6.10.5 US/SS/DS/Wobbling Pencil beam dose calculation limitations

Precautions

WARNING!

The effect of the infinite slab approximation on proton US/SS/DS/Wobbling. The US/SS/DS/Wobbling Pencil Beam dose engine is based on the so-called infinite slab approximation. This approximation disregards lateral inhomogeneities for individual ray traces, which will see the patient as a stack of semi-infinite layers. The effect of this approximation is more severe for patients with large lateral inhomogeneities, especially closer to the target area. This situation is common for many lung cases with the effect of significant loss of target coverage. It should be noted that also other treatment sites may be affected.

Be aware that the dose computation may not be accurate for patients with large lateral inhomogeneities relative the beam direction. (370003)

WARNING!

Apertures mounted downstream of the compensator for US/SS/DS/Wobbling. In the RayStation proton dose engine for delivery systems where the aperture is mounted downstream of the range compensator, there is an algorithm intended for reproducing the sharpening effect of the lateral dose penumbra that this setup provides. An artifact of this algorithm is that the scattering caused by the range compensator in the central parts of the field (away from the aperture edge) is underestimated. This artifact can give significant errors in the computed dose for compensator geometries that host large gradients in the interior of the compensator. A more detailed description of this artifact is given in the *RSL-D-RS-2024A-REF, RayStation 2024A Reference Manual*.

Be aware of this limitation in the dose calculation and be extra careful in the patient specific QA process for delivery systems where the aperture is mounted downstream of the range compensator. (150310)

WARNING!

Flat fluence for US/SS/DS/Wobbling. The RayStation US/SS/DS/Wobbling pencil beam proton dose calculation algorithm assumes a flat fluence unless a radial fluence correction is explicitly defined. It is the user's responsibility to decide whether the flat fluence assumption is acceptable for their delivery system or if radial fluence correction curves for the beam model should be provided.

(372132)

WARNING!

Lateral penumbra at large air gap for US/SS/DS/Wobbling. The lateral penumbra is sometimes significantly underestimated at shallow depths and in a few cases overestimated at the end of the SOBP range for beams with a large air gap between the aperture and the patient. This effect has primarily been observed for beams with a thick range shifter and/or a range modulator with a high-Z material.

The user shall be aware of this limitation in the pencil beam dose algorithm and is recommended to always minimize the air gap for US/SS/DS/Wobbling beams. (372143)

WARNING!

Surface dose overestimation for Wobbling. A systematic overestimation of the computed dose in the surface region has been found for a few beam configurations of the Sumitomo Wobbling delivery system. The error may become significant for beam configurations that combine a high beam energy with a large modulation ridge filter and a thick compensator. The error becomes more pronounced for large field sizes, although the effect is also present for smaller field sizes.

Be aware of this limitation in the dose calculation and be extra careful in the patient specific QA process for fields that involve a combination of high beam energy, large modulation ridge filter and a thick compensator. (261665)

WARNING!

Overestimation of entrance dose for Mitsubishi Electric Co SELECT BEAM NOZZLE in US mode. A systematic overestimation of the computed dose in the entrance region has been found in the dose engine validation for a significant fraction of US beam delivered by the Mitsubishi Electric Co SELECT BEAM NOZZLE in US mode. The error becomes significant for beams employing a range shifter thickness that is significantly larger than the minimum range shifter thickness defined for the present Range Option (Beam Data). The error becomes larger if a range compensator is added to the beam. The error caused by the range shifter is only weakly dependent on the snout position, while the surface dose error caused by the range shifter increases with increasing air gap between compensator and patient.

This error in dose is linked to the handling of secondary proton transport over the air gap, resulting mainly in an overestimation of the dose in the surface region.

The user shall be aware of these limitations in the pencil beam dose engine, and has the responsibility to ensure that a sufficient number of Range Options (Beam datas) with offset range shifter thicknesses are included in the system/beam model. (382252)

WARNING!

Accuracy of Pencil Beam dose engine for proton US/SS/DS/Wobbling beams with thick beam line components. In the RayStation US/SS/DS/Wobbling pencil beam dose engine validation, a few deviations from the dose accuracy requirements were noted for doses in water, especially at shallow depths, for setups where the protons pass through a thick beam-line component (e.g. range shifter, range modulator, or compensator). These deviations have been linked to the handling of secondary proton transport over the air gap, resulting mainly in an overestimation of the dose in the surface region. The effect increases with thickness of the component. When a compensator is used, the effect is larger for increasing air gaps. For components mounted in the non-moveable part of the nozzle, the effect is not primarily dependent on the air gap.

The user shall be aware of these limitations in the pencil beam dose engine, and is recommended to minimize the air gap when a compensator is used. (370009)

WARNING!

Lateral penumbra for beams using block aperture in combination with compensator for Mitsubishi Electric Co SELECT BEAM NOZZLE in US mode. In the dose engine validation of RayStation 2024A, a systematic deviation has been found in the computed lateral dose for beams delivered with the Mitsubishi SELECT BEAM NOZZLE in US mode (Mitsubishi US) using a block aperture in combination with a range compensator. The studied fields used an 8x8 cm^2 squared block aperture opening in combination with a 3 cm or 6 cm homogenously thick range compensator, and were delivered to a water phantom. The measured lateral profiles exhibit more rounded shoulders (high dose field edges) than observed in the calculated profiles, while the low dose part of the calculated profiles (dose levels<50%) is in excellent agreement with the measurements. Consequently, the calculated profiles can be significantly broader than the measured profiles at for example the D95% level, and the difference in 20-80% lateral penumbra has been observed to exceed 2 mm in several cases. The fail rate in Gamma (3 mm, 3%) analysis of the profiles, has also been seen to exceed 5% relatively frequently.

These deviations were not found for Mitsubishi US fields employing the MLC as primary collimator or for fields that used a block aperture without a range compensator.

Refer to *RSL-D-RS-2024A-REF, RayStation 2024A Reference Manual* for more details.

Be aware of this limitation in the pencil beam dose engine and be extra careful in examining this behavior in the commissioning of RayStation and in the subsequent patient-specific QA.

(165?)

WARNING!

Anisotropic lateral beam spread for US/SS/DS/Wobbling. RayStation does not consider anisotropic lateral scattering in the dose calculation of Uniform Scanning, Single Scattering, Double Scattering or Wobbling beams. In the dose engine validation of the Sumitomo Wobbling delivery system, it was found that the error in lateral penumbra is significant (> 2 mm for 80%-20% penumbra width) for fields using the largest fixed field size setting of the treatment machine and an aperture with a physical opening of 15 cm in combination with a large air gap (25 cm).

Be aware of this limitation in the dose calculation and be extra careful in the patient specific QA process for fields that employ a combination of large field sizes and large air gaps. (261663)

WARNING!

Aperture edge scatter effect for SS/DS/US/Wobbling. Scatter from the edges of the MLC and block aperture is not included in the RayStation US/SS/DS/Wobbling proton dose calculation algorithm.

The effect of the edge scatter is to add characteristic "ears" to the edges of the lateral dose profiles. These "ears" are most pronounced in the surface region but may also affect the dose deeper into the patient as well as the shape of a central axis depth dose curve. The shape and magnitude of the edge scatter "ears" depend on factors such as:

- The depth of the measured profiles. The "ears" are sharper at shallow depths and get more diffused at greater depths, to eventually disappear at some distal depth.
- The air gap. The "ears" get more diffused for larger air gaps.
- The field size. More edge scatter is expected for larger fields, since more of the inner aperture edge is exposed to the beam.

The effect of the omission of the edge scatter in the dose calculation can lead to discrepancies between delivered and computed dose, especially in the surface region, and sometimes deeper into the patient.

Be aware of this limitation in the dose calculation and be extra careful in the patient specific QA process to be able to determine if the omission of the edge scatter in the dose calculation is acceptable or not for each individual patient case.

(261664)

WARNING!

Patient-specific calibration of meterset rate for US/SS/DS/Wobbling. The setup used in the patient-specific calibration of beam meterset rate for US/SS/DS/Wobbling beams should be as close as possible to the treatment plan setup. (522820)

WARNING!

US/SS/DS/Wobbling beam monitor units. The beam monitor units value in RayStation is not expected to be dosimetrically correct and shall only be used as a means to control the dose level displayed in RayStation. (370010)

WARNING!

Range compensator effect in proton US/SS/DS/Wobbling Pencil Beam dose calculation. The proton US/SS/DS/Wobbling Pencil Beam dose engine treats any range compensator device as an extension of the patient and the pencil beam tracing will start at the entrance of the range compensator. This means that the broadening of each pencil beam ray trace may have become significant when reaching the patient surface and the dose error caused by the infinite slab approximation in the presence of any lateral inhomogeneity may be large. It is important to point out that the patient outline here becomes a large lateral inhomogeneity when it is angled to the ray traces. This error will thus increase with:

- Magnitude of air gap
- Angle between beam and surface normal
- Shallowness of target
- Internal lateral inhomogeneities

The user shall be aware of this limitation in the pencil beam dose engine. (383008)

WARNING!

Closed MLC leaves may be positioned along the central axis. When automatically or manually positioning MLC leaves, the positions of closed leaf pairs are automatically set. In some cases it is not possible to place the closed leaves at the default closed leaves position defined in the machine due to other MLC leaf position restrictions. In such cases, the closed leaves might be aligned with the central axis. This might result in leakage of dose in the area where the closed leaf pair meets, which is not taken into account in the RayStation ion dose computation. It is the user's responsibility to ensure that the leaves are not closed along the central axis, or that the possible leakage is acceptable. (370014)

WARNING!

Leakage between MLC leaves for protons. In the RayStation proton dose engines, a collimating MLC is regarded as an aperture block with a jagged contour, meaning that actual leakage between adjacent leaves or closed leaf tips are not handled by the dose engines. The dose difference between the computed plan and the delivered plan needs to be assessed by the user in the commissioning of RayStation as well as during patient specific QA. (371451)

WARNING!

Effect of non-collimating MLC leaves in dose computation for protons. In RayStation, the MLC leafs are only taken into account by the proton dose engines if the MLC is regarded as collimating. The MLC leaves are regarded as non-collimating if the MLC leaves are in their most retracted position (outside the snout inner dimension) or if the MLC leaves are positioned outside a block opening. Any effect on the dose distribution from such MLC setups are not reflected in the dose computation. The dose difference between the computed plan and the delivered plan needs to be assessed by the user in the commissioning of RayStation as well as during patient specific QA. (371452)

WARNING!

Dose accuracy for the Optivus double scattering system. In the RaySearch dose engine validation it was discovered that the shoulders of lateral dose profiles are not always accurately reproduced in RayStation. This results in the failure of the dose accuracy requirement: Gamma (3%, 3 mm) passing rate > 95%. For these fails, the computed curves exhibit rounder shoulders than the measured profiles, which results in for example an underestimation of the width of the field at D95%. The effect is most pronounced for shallow and mid depths of large fields (>10 cm) at the higher energies.

Be aware of this limitation in the dose calculation and be extra careful in the patient specific QA process to be able to determine if this deficiency is acceptable or not for each individual patient case.

(410850)

WARNING!

Dose deviation at depths <10 mm for small, shallow proton SS/DS/US/Wobbling beams. In the RaySearch analytical SS/DS/US/Wobbling dose engine validation of ocular proton therapy treatment fields, it was discovered that the shoulders of the lateral dose profiles are not always accurately reproduced at depths <10 mm. This deviation was traced to the generation of low energy protons that are created by a range-verifying system in the treatment nozzle of the delivery system used for validation. These protons are unevenly spread across the aperture opening, which is not supported in the analytical RayStation dose engine. The dose engine assumes that the protons in a field have a lateral fluence independent of energy.

The user shall be aware that the dose at shallow depth may be affected by a range-verifier.

(581160)

Range compensator effect

The proton SS/DS/US/Wobbling pencil-beam dose engine treats any range compensator device as an extension of the patient and the pencil beam tracing will start at the entrance of the range compensator. This means that the broadening of each pencil beam ray trace may have become significant when reaching the patient surface and the dose error caused by the infinite slab approximation in the presence of any lateral inhomogeneity may be large. It is important to point out that the patient outline here becomes a large lateral inhomogeneity when it is angled to the ray traces. This error will thus increase with:

- The magnitude of the air gap
- The angle between the beam and the surface normal
- The shallowness of the target
- Internal lateral inhomogeneities

The user shall be aware of this limitation in the pencil beam dose engine. It is good practice to always minimize the air gap between the range compensator and the patient.

Large air gap/ large modulation

Large-angle, nuclear scattering is treated by an ad hoc method that uses a look-up method based on the radiological depth at a certain physical depth (see *section 6.4.4 Nuclear scattering on page 184*). This lack of proper transport can lead to errors in dose calculation for systems with large variations in density. An example of such a system is a set up with the combination of large SOBP modulation, a thick compensator, and a large air gap. For this case one may anticipate that the dose in the near surface region will be overestimated in the dose calculations, since the thick range modulator and compensator will have generated a sizable fraction of large-angle scattered protons, and those protons will have spread over a larger area after the air gap, than predicted by the model

based on radiological depth. Figure 68 shows the measured and calculated depth dose curves of a field from an IBA Universal nozzle with R=27 cm, M= 15 cm, compensator thickness=10.1 cm (PMMA), and an air gap of 25 cm. As can be seen from the figure, the calculated dose in the near surface region is overestimated in the calculated profile, as could be anticipated from the arguments given above. Figure 68 also gives the measured and calculated profiles for a field with R=27 cm, M=10, cm, no compensator, and an air gap of 10.8 cm. For this field, no such discrepancy between measured and calculated doses is observed.

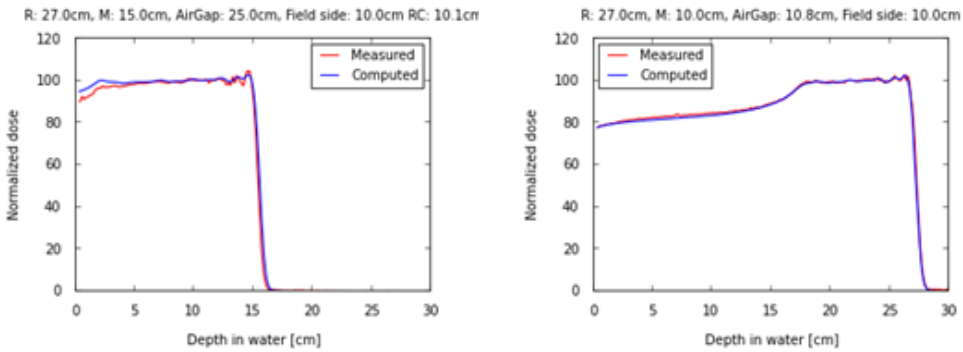

Figure 68. Measured and calculated center-of-field depth dose curves of a field from an IBA Universal nozzle with R=27 cm, M= 15 cm, compensator thickness=10.1 cm (PMMA), and an air gap of 25 cm (left) and for a field with R=27 cm, M=10, cm, no compensator, and an air gap of 10.8 cm (right). The size of the block aperture was 10x10 cm^2 in both cases.

Another example where this overestimation of surface dose for broad beam techniques is the Mitsubishi US system, which employs a system of range shifters of up to 6 cm thickness to fine tune the range between a small number of nominal beam energies. These range shifters are mounted far upstream in the nozzle, resulting in a large distance to the patient. As a consequence, the calculated surface dose of fields delivered with the Mitsubishi US system has proven to be overestimated when range shifters are employed.

Aperture model

Scatter from the inner edges of the aperture is not included in the RayStation dose calculation. The effect of aperture edge scatter is to introduce characteristic "ears" at the field edges in dose profiles at relatively shallow depths. The clinics should evaluate if this omission of edge scatter in the pencil beam dose engine is on a level of clinical relevance.

Absolute dosimetry

RayStation does not provide a model for accurate prediction of dose levels with respect to the meter set weight of the beam. The Monitor Units value in RayStation shall therefore only be viewed as a handle for controlling the dose level, and is consequently not exported in DICOM (DICOM tag Beam Meterset (300A,0086) in the RT Fraction Scheme Module).

Overestimation of the entrance dose for Mitsubishi Electric Co SELECT BEAM NOZZLE in US mode

The dose of the entrance region of a field has been found to be overestimated in RayStation for fields that employ a sizable net range shifter thickness (defined above). The effect becomes enhanced when a thick compensator is included. If a compensator is used, the effect becomes greater for larger air gaps. There is no significant air gap dependence when no compensator is used. An example of the effect is displayed in Figure 69. This effect is related to the transport of secondary protons generated in the range shifter and compensator. The lateral spread of these low energy secondaries are not accurately accounted for in the analytical dose engine, which leads to an overestimation in dose at shallow depth. A solution to this problem in RayStation 2024A would be to include more Range Options in the beam model, measured with offset range shifter thicknesses.

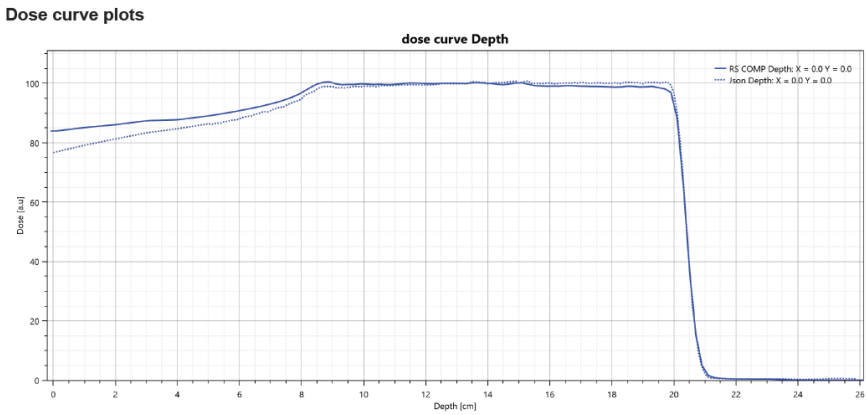

Figure 69. Measured depth dose curve (broken line) of a 210 MeV field with a range shifter thickness of 6 cm, Ridge Filter modulation of 12 cm, and with the MLC leafs in the maximum retracted setting. The minimum range shifter thickness for this Range Option is 0, which means that the net range shifter thickness equals 6 cm. The corresponding RayStation depth dose curve is depicted as a full line.

Lateral penumbra deviations using block aperture and compensator for Mitsubishi Electric Co SELECT BEAM NOZZLE in US mode

A systematic deviation has been found for fields using a block aperture in combination with a range compensator. The measured lateral profiles exhibit more rounded shoulders (high dose field edges) than observed in the calculated profiles, while the low dose part of the calculated profiles (dose levels<50%) is in excellent agreement with the measurements (an example is given in Figure 70). Consequently, the calculated profiles can be significantly broader than the measured profiles at e.g. the D95% level, and the difference in 20-80% lateral penumbra has been observed to exceed 2 mm in several cases. The fail rate in Gamma(3 mm, 3%) analysis of the profiles, has also been seen to exceed 5% relatively frequently. It is currently not clear what causes this deviation.

These deviations were not found for Mitsubishi US fields employing the MLC as primary collimator or for fields that used a block aperture without a range compensator.

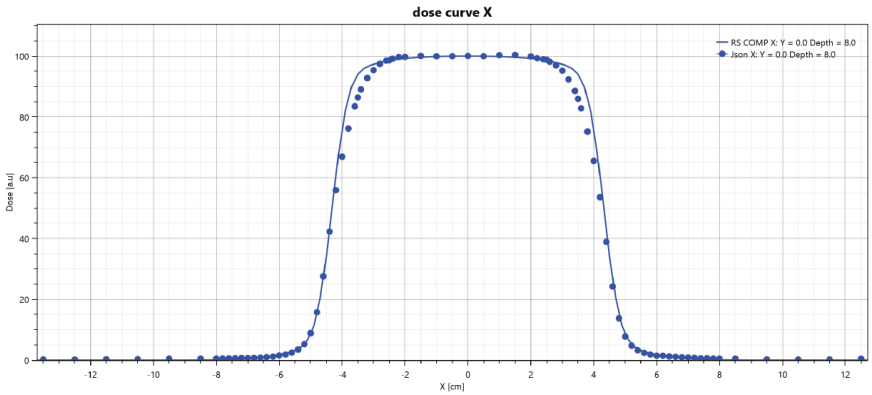

Figure 70. Measured lateral profile (circles) of a 183 MeV field with a range shifter thickness of 3 cm, ridge filter modulation of 12 cm, range compensator with a homogenous thickness of 3 cm, and a block aperture opening of 8x8 cm^2. The profile has been measured at the center of the SOBP. The corresponding RayStation profile is depicted as a full line.

Edge scatter ears in lateral profiles for Mitsubishi Electric Co SELECT BEAM NOZZLE in US mode

This effect is the same as described for the other broad beam techniques, see *section 6.10.5 US/SS/DS/Wobbling Pencil beam dose calculation limitations on page 239*.

Lateral penumbra deviations at large air gap for Mitsubishi Electric Co SELECT BEAM NOZZLE in US mode

The lateral penumbra is sometimes significantly underestimated at shallow depth and in a few cases overestimated at the distal end of an SOBP. This problem has mainly been observed for large air gaps in combination with a thick range shifter and or a brass ridge filter (modulation >= 11 cm). The underestimation of lateral penumbra at shallow depth is likely due to the lack of proper handling of secondary protons generated in the ridge filter and range shifter. The overestimation at greater depth (relatively rare) could be due to insufficient accuracy of the Multiple Coulomb Scattering in the ridge filter. The beam model will typically ensure that the penumbra is correct at mid SOBP. The user shall be aware of this limitation and always strive at minimizing the gap between then snout tip and the patient.

6.11 OPTIMIZATION AND DOSE CALCULATION FOR LINE SCANNING

In Line Scanning, the beam is scanned continuously within an energy layer without turning off the beam. The dose rate is constant within a layer and the fluence modulation is achieved by adjusting the scanning speed of the beam between the line segment end points.

6.11.1 Optimization of a Line Scanning plan

When optimizing a Line Scanning plan, the optimizer needs to ensure that the dose rate and scan speeds are within machine limits. RayStation exports line scan positions and line segment weights (in private tags (300B, 1094) and (300B, 1096)), and it is the responsibility of the treatment control system to make the transition into dose rates and scan speeds. However, to ensure that the line segments will be deliverable, the dose rate of each energy layer needs to be calculated also in RayStation. The choice of dose rate and enforcement of line segment weight limits is done during optimization after the optimization has reached a user definable number of iteration steps. At this iteration, RayStation will (1) choose the dose rate for each energy layer, (2) remove low weighted line segments in the beginning and at the end of each line of an energy layer, and (3) apply lower and upper bounds for the line segment weights in subsequent iterations of the optimization. The details of how these values are calculated are outlined below.

The internal dose rate of a layer, $I_{e,\text{internal}}$, is chosen from the maximum MU per cm, $\max(w_{ej})$, of all line segments j in that layer e and the minimum available speed for that energy, $v_{\min,e}$:

$$I_{e,\text{internal}} = 1.2 \cdot \max_{j \in e}(w_{ej}) \cdot v_{\min,e} \qquad \text{[Eq. 152]}$$

where the factor 1.2 is applied to allow the maximum line weights to increase slightly in the iterations following the selection of the internal dose rate. If the calculation yields an internal dose rate that is higher or lower than the dose rate limits of the machine, it is adjusted to the machine maximum or minimum dose rate value, respectively.

The line segment weight limits, $w_{\min,ej}$ and $w_{\max,ej}$, are then calculated from the internal dose rate and the energy dependent beam scanning speeds limits, $v_{\min,e}$ and $v_{\max,e}$, as:

$$\begin{aligned} w_{\min,ej} &= I_{e,\text{internal}}/v_{\max,e} \\ w_{\max,ej} &= I_{e,\text{internal}}/v_{\min,e} \end{aligned} \qquad \text{[Eq. 153]}$$

In addition to the spot weight limits set by the delivery system, the user can also define an absolute minimum line segment weight (in MU/fx/cm), which will be applied in the removal of line segments in the beginning and at the end of each line. This function has been introduced since a Line Scanning system can deliver energy layers with very low weights that may have little effect for the plan quality, but will elongate the delivery time. This absolute minimum spot weight limit only affects the removal of line segments (and potentially whole energy layers) and is not used for calculation of the line segment weight limits in the subsequent optimization.

6.11.2 Repainting for Line Scanning beams

In RayStation it is possible to define a fixed number of layer repaintings for a beam (refer to *RSL-D-RS-2024A-USM, RayStation 2024A User Manual*). This will affect the choice of the internal dose rate in RayStation such that the combined minimum and maximum line segment weights of the plan is not affected by the number of rescanning layers:

$$I_{e,\text{internal}} = 1.2 \cdot \max(w_{ej}/n_e) \cdot v_{\min,e} \qquad \text{[Eq. 154]}$$

$$w_{\min,ej} = n_e \cdot I_{e,\text{internal}}/v_{\max,e}$$
$$w_{\max,ej} = n_e \cdot I_{e,\text{internal}}/v_{\min,e} \qquad \text{[Eq. 155]}$$

where n_e is the number of repaintings for the energy layer *e*, and the line segment weights and their limits refer to the combined weights of all repainting layers. For a sufficiently large number of repaintings, the minimum dose rate limit of the machine may be reached with the effect that the minimum/maximum line segment weights for the plan increases.

The user defined absolute minimum line segment weights (see *section 6.11.1 Optimization of a Line Scanning plan on page 250*) are applied per repainting layer, which means that the corresponding absolute minimum weight for the combined plan increases with the number of repainting layers. On the other hand, the user defined minimum energy layer meterset operates on the combined meterset of all segment weight in all repainting layers and is therefore not directly affected by the number of rescans.

If repainting is applied prior to optimization, the MU rounding algorithm will be applied for each individual painting. (Note that if the number of paintings for each segment instead is changed through scripting after dose computation, there might be a slight mismatch between the planned and delivered dose. The reason for this is that the dose is not invalidated and the MU rounding algorithm is not applied.)

6.11.3 Dose calculation for Line Scanning beams

In the dose calculation of Line Scanning beams, each line segment is discretized into a number of discrete spot positions. In this way the same dose calculation algorithms can be utilized for Line Scanning beams as for step-and-shoot PBS beams. For the dose calculation during optimization, discretization spots are only placed at the end points of each line segment. In the final dose calculation, internal spots are distributed uniformly along the line segment in addition to the spots placed at the end points. The number of internal spots for each line segment, $N_{\text{internal},j}$, is dependent on the line segment length, l_j, and the beam sigma in air at isocenter, σ, and is given by

$$N_{\text{internal},j} = \lceil l_j/f\sigma \rceil - 1 \qquad \text{[Eq. 156]}$$

where f is set to 0.35 in order to produce a uniform line segment fluence at isocenter with a maximum relative error less than 0.5% for single lines of length 1 cm. The distance between the discretization spots along the line segment is given by

$$\Delta x = \frac{l_j}{N_{\text{internal},j} + 1} = \frac{l_j}{\lceil l_j / f\sigma \rceil} \leq f\sigma \qquad \text{[Eq. 157]}$$

The relative weight of a line segment, w_j, is distributed evenly between the internal spots, whereas the spots at the end points of the line segment each get half of the weight of the auxiliary spots:

$$w_{\text{aux},j} = \frac{w_j}{N_{\text{aux},j} + 1}$$
$$w_{\text{ends},j} = \frac{w_{\text{aux},j}}{2} \qquad \text{[Eq. 158]}$$

6.11.4 Clinical and Approximate dose for Line Scanning

A Line Scanning dose is set to Clinical by the RayStation dose calculation if the distance between the discretization spots is smaller or equal to $f\sigma$. Otherwise the dose will be marked as Approximate. This means that the dose from a Final dose computation will always be clinical, while the dose from an optimization will be approximate.

The dose will also be set to Approximate, after changing MU (achieved by scale to primary prescription, beam weighting or changing MU in the beam list). The reason for this is that the dose after MU scaling could be different from the actual delivered dose for plans not created in RayStation, due to the Sumitomo MU rounding algorithm (see *section 6.11.5 Sumitomo MU rounding algorithm on page 252*).

6.11.5 Sumitomo MU rounding algorithm

When a DICOM plan is transferred through the Sumitomo HI treatment control system, the line scan positions and line segment weights are translated to dose rates for each energy layer, and scan speeds for each line segment according to the following algorithm:

1. **Selection of the dose rate.** The dose rate for the delivery of an energy layer e is chosen from the segment with smallest weight in the layer and the maximum scan speed:

   $$I_e = \min_{j \in e}(w_{ej}) \cdot v_{\max} \qquad \text{[Eq. 159]}$$

   If I_e exceeds the maximum dose rate, the dose rate is set to the maximum dose rate. If I_e is smaller than the minimum dose rate, the corresponding line segment weight is set to zero and the dose rate is instead determined from the remaining non-zero weights. This process is repeated until I_e reaches or exceeds the minimum value.

2. **Calculation of the scan time for each line segment.** The scan time for each line segment is calculated from the line segment weight and the dose rate:

$$T_{ej} = \frac{w_{ej} \cdot l_{ej}}{I_e} \qquad \text{[Eq. 160]}$$

The scan time is then rounded off by the time resolution of the delivery system, ΔT_{res}, to yield a rounded scan time, $T_{ej,\text{round}}$.

3. **Calculation of the scan speed for each line segment.** The scan speed is calculated from the line segment length and the rounded scan time: $v_{ej} = l_{ej}/T_{ej,\text{round}}$. If $v_{ej} > v_{\max}$, then $T_{ej,\text{round}} = \lceil l_{ej}/v_{\max}\Delta T_{\text{res}} \rceil \cdot \Delta T_{\text{res}}$ and the scan speed is recalculated.

4. **Adjustment of the relative weight of each line segment.** The relative weight of each line segment, w_{ej}, will now be based on the rounded scan time and the layer dose rate:

$$\widehat{w_{ej}} = \frac{I_e \cdot T_{ej,\text{round}}}{l_{ej}} \qquad \text{[Eq. 161]}$$

To ensure that the planned and delivered dose is equivalent for all plans, the algorithm has been implemented in the dose computation in RayStation. Furthermore, the algorithm is applied at the end of each optimization. In combination with the restrictions on the line segment pattern (*section 6.11.6 Limitations on line segment lengths on page 253*), this ensures that the subsequent application of the algorithm in final dose computation will not alter the relative line segment weights, and that the planned and delivered MU numbers are equivalent for all plans created through optimization.

6.11.6 Limitations on line segment lengths

The user can control the spot pattern by changing the energy layer spacing and the line spacing (see *RSL-D-RS-2024A-USM, RayStation 2024A User Manual* for more details.) The line spacing will affect both the line segment lengths and the distance between Line Scanning rows. The distance between the Line Scanning rows is determined by the specified line spacing, and will also be adjusted to fulfill the following limitations on line segment length:

1. The line segment length has an upper limit equivalent to the distance obtained from the Automatic line spacing mode with a factor of 1. If the Automatic line spacing mode is used, it is thus possible to decrease, but not increase, the line segment length by changing the line spacing factor.

2. There is a minimum and maximum line segment length of 0.1 mm and 1.5 cm respectively.

3. The line segment length, and also the line spacing, is enforced to be a multiple, k, of the time resolution times the maximum scanning speed (with a small number, ϵ, deducted):

$$l_{ej} = k\Delta T_{\text{res}} v_{\max,e} - \epsilon \qquad \text{[Eq. 162]}$$

The upper limits described in items (1) and (2) have been introduced to enforce a maximum line segment length, which is needed since there are no auxiliary spots used during optimization. In this way, the resulting dose from optimization will not differ to a large extent from the dose from final dose computation.

An effect of the Sumitomo MU rounding algorithm is that the planned and delivered MU may not always exactly match. The random rounding up and down of the segment weights will for the most part even out in terms of total beam MU, but this may not be the case for energy layers where many spots end up at the lower segment weight limit. In fact, this effect has been shown to give a significant difference between planned and delivered MU for some cases. Since the rounding algorithm also is run prior to dose calculation, the calculated and delivered dose will still match, but it is impractical to have significant differences between planned and delivered MU, e.g. when the MU is used as a means to monitor the delivery in real time. With the line segment length determined according to Equation 162, this effect is partly mitigated. From Equation 159, Equation 160 and Equation 162, it can be seen that the scan time for the line segment with the smallest MU per cm will be a multiple of the time resolution:

$$T_{ej,\min} = \frac{w_{ej,\min} \cdot l_{ej}}{I_e} = \frac{w_{ej,\min} \cdot l_{ej}}{w_{ej,\min} \cdot v_{\max,e}} \approx k \cdot \Delta T_{\text{res}} = T_{ej,\text{round, min}} \qquad \text{[Eq. 163]}$$

This means that the adjusted relative weight in Equation 161 for these line segments will be identical to the original relative weight (within the epsilon of Equation 162). One may argue that the planned and delivered MU should always match since the discrete nature of the delivered segment weights have been considered at the end of an optimization (see *section 6.11.5 Sumitomo MU rounding algorithm on page 252*). However, this will not be the case for a plan where the MU has been altered after an optimization, e.g., by the often used function **Auto scale to primary prescription** (refer to *RSL-D-RS-2024A-USM, RayStation 2024A User Manual*). The choice of the line segment length according to Equation 162 will further minimize a potential dose jump after optimization caused by the MU rounding. The line segment length is reduced by the small number ϵ, to ensure that numerical imprecision do not result in different rounding in the Sumitomo HI treatment control system and in RayStation. Numerical imprecision could e.g. occur in the transfer of DICOM plans between the two systems. Please also note that, for the same reason, it is not allowed to commission a machine, if the absolute dose measurements are taken with a line spacing which is a multiple of the time resolution.

6.12 OPTIMIZATION AND DOSE CALCULATION FOR MEVION HYPERSCAN

For a Mevion S250i treatment machine with the HYPERSCAN nozzle (Mevion Hyperscan), treatment delivery optionally uses an adaptive aperture (MLC) to collimate the field on a spot by spot basis. In RayStation, Hyperscan plans are created using aperture contours, which are used as a basis for the actual adaptive aperture collimation. Both a single aperture per beam, or one aperture per energy layer, i.e. multi-layer aperture (MLA), are supported. In RayStation, this is handled by assigning a block to the Hyperscan beam. The block can either be *Static*, corresponding to the single aperture, or *Dynamic*, corresponding to MLA.

When using the pencil beam dose engine, the aperture contours polygons are used directly in the dose computations. Thus the actual MLC positions are not taken into account.

When using the Monte Carlo dose engine during optimization the initial spot pattern is used to generate MLC positions for each individual spot. The difference of the initial and final spot patterns may result in a difference between the optimized and the final dose.

6.12.1 Computation of aperture contours

Single aperture

The computation of the single aperture per beam is performed in the same way as a physical block contour. A geometric projection of all treat ROIs (represented by a mesh) is performed and a single contour is computed on the isocentric plane. Note that if multiple targets are used, only the largest separate aperture will be kept, and inner contours are not allowed. An expansion of the contour, based on the specified margins, is applied using a rolling ball algorithm. Finally, the contour is modified using the specified milling tool diameter, effectively expanding all narrow features in the aperture.

Multi-layer aperture

The computation of MLA contours is based on the radiological depths of each energy layer. The union of all target ROIs (as defined by all ROIs having a minimum dose optimization function) is represented in the voxelized dose grid. An expansion, perpendicular to the beam direction, is applied by a distance of one average sigma in the Bragg peaks at the distal edge. The expansion distance can be scaled using a user-defined factor, or set to a fixed value in cm. Note that the expansion is performed on the dose grid resolution, and the actual expansion will often be to the nearest voxel size above the intended distance.

In the next step, Bragg peak positions are computed on a high resolution grid for all available energy layers, and it is noted if the Bragg peak falls within the expanded target union. This creates a pixel map with areas which falls either inside of or outside of the target union, and contour polygons are created from this map. Contours which fall entirely inside another contour are not allowed. If multiple separate contours are created, they will result in a duplication of the energy layer, since only a single contour per energy layer is allowed. Finally, a "milling", based on the selected milling tool diameter, is applied to each contour. The reason for this is to get a smoother and more deliverable contour, e.g. avoiding narrow features in the aperture.

Note that the final contours may be jagged and have complicated shapes. The main reason for this is that the intersection of the target union and radiological depth surface of an energy may be

complicated and non-intuitive. The jaggedness is also an effect of the discretization on the target union and the ray trace grid, but since the contour is the basis for the actual MLC positions, which is considered in the final dose computation, it should not affect the plan quality.

If any target optimization function is defined as robust, the aperture contours will automatically be expanded according to the robustness uncertainty parameters in range, position and image. Note that this differs from the single aperture case, in which case the uncertainty margin must manually be added to the aperture margin.

6.12.2 Optimization of a Hyperscan plan

When optimizing a Hyperscan plan, special consideration is required for the following:

- Adding energy layers manually might affect plan delivery time. Hyperscan plan optimization with automatic settings for energy layer separation will result in energy layers that use combinations of range shifter plates optimized for short delivery time. Adding additional energy layers manually, or using different separation criteria, might affect the fine-tuning settings between layers and add extra delivery overhead.
- The aperture contours are based on the geometric or radiological projection of the target union, and will not change during the optimization. If the optimized plan e.g. has a problem with target coverage, it may be necessary to increase the lateral margin and reoptimize the plan.
- No spots will be placed outside the aperture contour in the automatic spot selection. If a spot has been manually added outside the contour, it is also not possible to proceed with optimization or dose calculation.
- The number of repaints does not affect plan optimization. This parameter should be set before final dose calculation. The requested number of repaints will be exported in DICOM and handled by the Mevion control system. Note that the value is required to be the same for all energy layers for a given beam, and that changing it in RayStation will set the new value on every layer. The actual number of repaints that will be performed for a particular spot is determined in the Spot Map Converter (see details below).

6.12.3 Dose calculation for Hyperscan beams

When computing dose for a Hyperscan beam using the Monte Carlo dose engine, the spots and the aperture contour(s) are reinterpreted to correctly represent the treatment delivery through the Mevion adaptive aperture. The conversion is performed by passing the relevant parameters in RayStation internally through a Spot Map Converter (SMC), provided by Mevion Medical Systems, Inc. The SMC has two main functions:

- **Determining number of spot paintings and spot ordering.** Spots with high MU are split into multiple pulses, all with the same coordinates and the same corresponding Hyperscan plate settings and with an accumulated MU equal to that of the input spot. Spots might also be reordered. This is done to comply with how the pulses will be delivered from the machine, which also determines collimator movement.

By specifying a value greater than 1 for the **Number of repaints** parameter in RayStation, the SMC will attempt to split the spots even further to be delivered in separate repainted layers.

- **Determining Adaptive Aperture collimation per spot.** Every resulting pulse (after division as described above) is assigned a corresponding set of MLC leaf settings which fully specifies how the aperture will be positioned during delivery. The MLC leaf settings are based on the aperture contour that is given as input to the SMC and these settings should ensure that the collimation is performed accordingly.

The output from the SMC is used in the Monte Carlo dose engine with individual collimator geometries per resulting spot, ensuring a dose computation with the adaptive aperture correctly represented for each pulse delivered by a Hyperscan machine.

When using the Monte Carlo dose engine in optimization, the SMC does not consider spot meterset limits dictated by the delivery system. Neither does it reorder spots and energy layers to match the order of delivery. Furthermore, if a significant number of spots is filtered during optimization the MLC positions used in optimization will no longer be the same as for final dose which may result in a noticeable dose difference between the optimized and final doses. Thus the MLC positions used during optimization are approximate.

When an SMC conversion is performed during final dose calculation, a checksum will be computed on the SMC output. This checksum will be exported by RayStation as part of a DICOM plan export and is used for external verification by the delivery system. Note that even if no block has been added to the beam, a spot map conversion will be performed in order to determine the spot paintings and to generate a checksum. The adaptive aperture will however not be included in calculations for this case. It is assumed that the leaves are placed sufficiently retracted from the field to not have any impact on treatment delivery.

6.12.4 Clinical and approximate dose for Hyperscan

It is possible to compute dose for a Hyperscan beam using the pencil beam dose engine. However, spot map conversion will not be performed. Also, the handling of multiple range shifters with air gap is not modeled with sufficient accuracy for the dose to be considered clinical. The dose will be set to approximate.

The Monte Carlo dose engine will give a clinical dose, provided that the dose grid is fine enough and that the statistical error is smaller than the limit defined in the Clinic Settings application. If the plan is changed after a clinical dose has been computed, the dose is either set to approximate (for example when scaling the MU of a beam) or be invalidated depending on the change. The following rules are Hyperscan-specific:

- If a beam MU is modified on a clinical dose, for example by scaling, the dose will be set to approximate.
- If, for a clinical dose, the **Number of repaints** parameter is changed for all layers of a beam, the dose will be set to approximate.

6.12.5 Validation of a Mevion Hyperscan system

WARNING!

Dose accuracy for the proton MC dose engine used with Mevion Hyperscan. The Monte Carlo PBS dose engine validation for Mevion Hyperscan shows deviations from the dose accuracy requirements when comparing to measurements for the following cases:

- Absolute dose for small targets

  The dose engine validation for Mevion Hyperscan shows a significant deviation (above 3%) in absolute dose for cube targets of size 3 x 3 x 3 cm^3 at different depths, and for single-energy scanned fields with lateral size 4 x 4 cm^2. The deviation becomes larger for larger air gaps.

- Absolute dose at edge-of-field when using apertures

  The dose engine validation for Mevion Hyperscan shows that RayStation significantly overestimates the dose at the field edges. The difference is most pronounced near the surface and when using an aperture.

Be extra careful when creating PBS plans for Mevion Hyperscan in cases where one of the above identified deviations can be clinically significant. (384587)

WARNING!

Dose validation off-axis for Mevion Hyperscan. The dose validation for Mevion Hyperscan shows significant discrepancies for plans with spots at a distance to the isocenter larger than 7 cm in X or Y. These discrepancies are believed to be effects from irregularities in the treatment delivery across the field, where the delivered spot meterset is higher than what is intended in the plan. This effect increases gradually towards the maximum distance to isocenter of 10 cm in X and Y, reaching a maximum of about 3% in the difference between planned and delivered spot metersets. If the peripheral spots have a relatively higher meterset, the corresponding deviation in dose may be even larger. This effect has been confirmed by Mevion Medical Systems.

This issue has been addressed by Mevion Medical Systems and a lateral spot meterset correction is available for Hyperscan machines. Users must implement this correction or take extra care when setting up off-axis fields.

(300)

WARNING!

Mevion Hyperscan machine commissioning. When commissioning a Mevion S250i ("Hyperscan") machine, the beam model only uses input data for the highest deliverable energy of the system. Nevertheless, the dose calculation must be validated for the whole relevant range of clinical treatment fields before clinical use. It is especially important to verify the ranges, and the absolute output for different field sizes and snout positions, for a number of energies covering all the range shifters of the Mevion energy selector.

It is also important to validate the dose computation for beams with apertures (both static and dynamic). In RayStation, such beams are planned with a block. The Mevion Adaptive Aperture will then try to adapt its position and leaves to reproduce the desired aperture contour. This validation shall comprise fields of different sizes, including fields with non-straight edges (complex target shapes). (369009)

6.12.6 Mevion Spot Map Converter version

For dose computation with Mevion Hyperscan, the Spot Map Converter (SMC) from Mevion Medical Systems is used (see *section 6.12.3 Dose calculation for Hyperscan beams on page 256*). When using a RayStation installation with Mevion Hyperscan functionality, the complete software version is defined by the RayStation version and the version of the Mevion Spot Map Converter library that are displayed in the About box.

6.13 OPTIMIZATION WITH SPOT DOSE CACHE

When running a new PBS optimization in RayStation, the first step before the actual optimization starts is to select the energy layers and the spot positions in each layer, and to create a starting guess for the corresponding spot weights. After the spots have been selected, the dose of each spot is computed, after which the spot weight optimization can commence. When using the "Continue" optimization function, energy layers and spot positions are given by the current plan and only the spot doses are determined before the optimization starts.

To speed up subsequent or iterative PBS optimizations, the energy layers and spot selection, as well as the spot doses, are stored (cached) for all beams. This cached data can then be used in repeated optimizations with the same dose engine, provided that the patient geometry, the plan data, or the optimization problem have not been modified in a way that would affect the spot selection or the spot dose calculation. It should be noted that this applies to both new optimizations ("Reset" followed by "Start", as is the recommended workflow), and to "Continue" optimization. The obtained result does not involve any approximations, and will be identical to an actual full recalculation.

The spot dose cache is invalidated automatically by patient or plan modifications that affect the spot selection or the spot dose calculation. For example, when changing the gantry angle of one beam its spot dose cache will be invalidated completely, while the cached energy layers and spot doses for the other fields are still used. Another example that will invalidate the spot dose cache is the addition of a Minimum or Uniform dose optimization objective to an ROI that previously was not associated with a target objective, or modification of robustness settings, since this will lead to a different spot selection. If a plan is modified in a way that invalidates the spot cache, it may be resumed again by undoing the modifying action using the RayStation Undo function. The spot dose cache is not saved to the data base and is completely cleared when the patient is closed.

The following is a non-comprehensive list of allowed actions that will not invalidate the cached spot dose data:

- Modifying/adding/deleting OAR objective/constraint functions (robustness settings cannot be modified)
- Modifying/adding/deleting target objective/constraint functions, while not modifying the effective target (robustness settings cannot be modified)
- Changing beam MU, including manual dose scaling, auto-scale or beam reweighting
- Adding or removing a beam (invalidates the cache for the affected beam)
- Adding/removing energy layers (invalidates the cache for the affected energy layer)
- Adding/removing/moving/changing the weights of spots (moving spots invalidates the cache for the affected spot)
- Changing Optimization settings
- Computing final dose
- Setting or modifying a prescription
- Setting or modifying a clinical goal

- Changing pure annotation data, such as beam name or dose color table

It should be noted that the spot dose cache can only be used for optimization, and not for final dose.

6.13.1 Memory consumption of the Spot dose cache

The size of the spot cache per RayStation instance is controlled by a maximum spot cache size limit. When the spot cache approaches this limit during an optimization, spot doses will be automatically evicted from the cache. Old spot doses that are no longer needed for the current optimization will be evicted first, but spots in the current plan may also be evicted if the plan is large enough in relation to the available memory. The spot cache limit depends dynamically on the amount of installed memory and the amount of free memory of the computer, which ,e.g., will depend on how many other RayStation proton optimizations are executed in parallel on the same server. The spot cache limit for a server is controlled by a number of spot cache limit settings, which have been tuned for a typical RayStation server environment. If you would like to change the behavior of the spot cache limit, e.g., to allow a single RayStation instance to consume more of the total installed memory, contact the RaySearch Laboratories support organization.

6.14 OPTIMIZATION WITH LET FUNCTIONS

6.14.1 Dose threshold for the Max LET_d function

The Max LET_d optimization function penalizes LET_d values above the specified LET_d level, and there is no penalty below that level. In proton therapy, voxels that receive low doses tend to exhibit high LET_d values due to radiation physics. Penalizing these voxels can result in unpredictable effects on the resulting dose and LET_d distributions.

The penalty in the Max LET_d function is weighted by a dose-dependent factor between zero and one, given by the sigmoidal error function shown in Figure 71, where $D_{threshold}$ is a user-specified dose threshold. The threshold refers to the RBE-weighted dose of the beam set (or of the beam in the case of a beam-specific function). Only voxels with doses greater than about 95% of the dose threshold have a non-negligible impact on the penalty. This feature allows users to disregard voxels with doses where the clinical impact of high LET_d is not a concern. To avoid unpredictable effects from low-dose regions, it is strongly advised to always use a dose threshold that is significantly larger than zero.

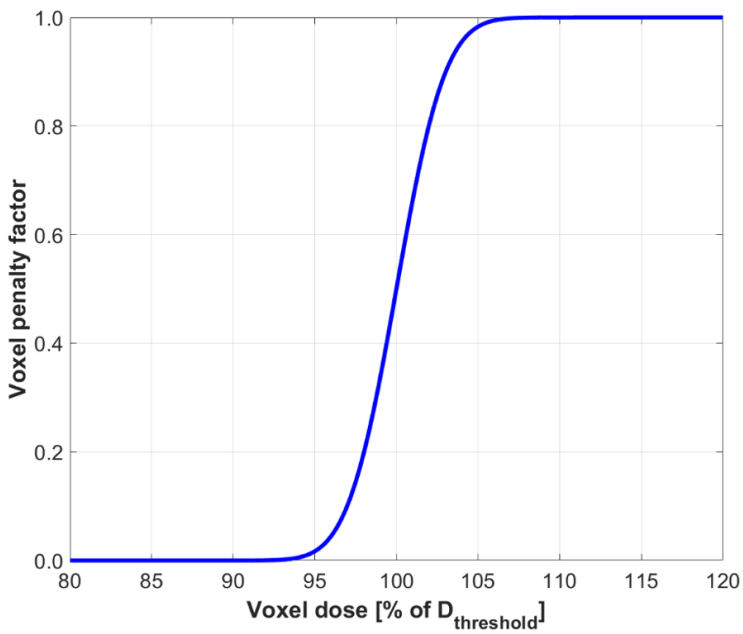

Figure 71. The sigmoidal voxel penalty factor as a function of the voxel RBE dose in percentage (%) of the dose threshold $D_{threshold}$ used in the Max LET_d function. Note that the x-axis only shows values between 80% to 120% of the $D_{threshold}$. For voxel doses below 80% of the $D_{threshold}$ the factor is equal to zero and for voxel doses above 120% of the $D_{threshold}$ it is equal to one.

WARNING!

Evaluate the LET_d distribution after optimization. If LET functions have been used during the optimization, the plan shall be carefully reviewed both with respect to dose and LET_d. Combined dose and LET_d functions may result in conflicting optimization goals, and LET_d is only a predictor of biological effect if analyzed together with the dose.

(722444)

WARNING!

Evaluate the LET_d distribution after robust optimization. After performing a robust optimization with LET functions, the user is strongly advised to evaluate the LET_d distribution using Plan evaluation or the scripting functionality in RayStation to verify that the plan is robust with regards to all relevant uncertainties during delivery.

(722447)

7 LIGHT ION DOSE CALCULATION

RayStation supports planning for Pencil Beam Scanning (PBS) light ion (carbon and helium) beam delivery systems that deliver discrete (step-and-shoot) pencil beams (spots) organized in a finite number of energy layers. The energy layers are chosen either continuously within specified limits, or from a list of discrete energies defined in the treatment machine. The supported beam limiting devices are fixed thickness range shifters, mounted on a fixed or movable snout along the beam line, as well as fixed ripple filters positioned upstream of the treatment nozzle.

RayStation also supports synchrotron based facilities which use so called quasi-discrete spot scanning delivery, where the beam is left on while moving between spot positions, as long as the distance between spots is below a certain threshold. Discrete and quasi-discrete spot scanning yield very similar doses as long as certain machine and plan parameters are within reasonable limits. Spill dose is not explicitly computed in RayStation, but may be taken into account in the minimum spot weight.

This chapter gives a detailed description of the light ion dose and RBE-weighted dose calculation algorithms in RayStation.

Modeling of light ion beams

Before clinical dose computation, the different beam model parameters, which are described in this document, need to be adjusted to the specific treatment machine used at the clinic. A treatment machine may contain multiple beam models, e.g., corresponding to different beam lines in the same treatment room. For light ion treatment machines, the beam modeling process is performed by RaySearch Laboratories and the machine models are provided to the customer. For further details, contact the RaySearch Laboratories support organization.

In this chapter

This chapter contains the following sections:

7.1	General models and algorithms	p. 267
7.2	Light ion dose calculation input data	p. 276
7.3	Dose and RBE-weighted dose calculation for PBS beams	p. 286
7.4	Dose engine accuracy and limitations	p. 291
7.5	Initial RBE computation in the Local Effect Model	p. 295
7.6	Import of initial RBE tables for the user-defined Local Effect Model	p. 300
7.7	The (modified) Microdosimetric Kinetic Model	p. 302
7.8	Import of tables for the user-defined MKM	p. 304
7.9	MKM dose computation	p. 306
7.10	RBE-weighted dose algorithms for LEM	p. 308
7.11	RBE Model limitations	p. 312
7.12	Optimization with LET functions	p. 321

7.1 GENERAL MODELS AND ALGORITHMS

This section describes the physics models and low-level algorithms that are used in the physical and RBE-weighted dose calculations.

7.1.1 Stopping power

The electronic stopping-power model in RayStation is used for on-the-fly calculation of radiological (water equivalent) depth and absolute energy loss in the carbon pencil beam (CPB) dose engine, used for carbon and helium.

For light ions, the well-established Bethe-Bloch formula [84] is used, omitting the shell and density correction terms which are only important well below and above the energies of therapeutic interest [85]. The stopping power in a compound material can then be written as:

$$S = a_1 \frac{\rho Z^2}{\beta^2}\left[a_2 - \ln\left(\frac{1}{\beta^2} - 1\right) - \beta^2\right]$$
$$\beta^2 = 1 - \left(1 + \frac{E}{Mc^2}\right)^{-2} \qquad \text{[Eq. 164]}$$

where E is the kinetic energy of the light ions with atomic number Z and mass M. The material-dependent quantities are given by

$$a_1 = \frac{\kappa}{u}\sum_i w_i \frac{Z_i}{A_i}\text{, and}$$
$$a_2 = \ln\frac{2m_e c^2}{I}\text{, with} \qquad \text{[Eq. 165]}$$
$$\kappa = \frac{4\pi e^4}{m_e c^2}\ .$$

The elemental composition of the target medium is described by its constituent atomic numbers, Z_i, relative weights, w_i, and mass numbers, A_i. The target material also has an average mass density, ρ, and mean excitation energy (potential), I. In these equations, u denotes the atomic mass unit, c the speed of light in vacuum and m_e the electron mass.

7.1.2 Linear Energy Transfer (LET)

The unrestricted linear energy transfer, LET_∞, is the mean energy loss per path length due to all electronic collisions. It equals the total electronic collision stopping power.

The computation of dose-averaged LET, and the evaluation of biological effects when using a track structure RBE model (e.g., the Microdosimetric Kinetic Model (MKM) and the Local Effect Model (LEM)), require a more precise description of the absolute unrestricted LET in the low-energy regime,

below the validity range of the Bethe model. For this purpose, parametrized LET tables obtained with the FLUKA Monte Carlo code [86], [87], [161] are used.

7.1.3 Energy loss and radiological depth

The mean energy loss over distances up to 1 cm is computed using the 4-point Runge-Kutta (RK4) method [69]. For greater thicknesses, e.g., in the calculation of the mean energy loss through the nozzle, the total thickness is divided into slabs of thickness ≤ 1 cm.

The radiological depth, z_{eq}, is a measure that is widely used in treatment planning. In the CPB dose engine, z_{eq} is used to determine the deposited dose at a certain depth from a reference depth dose curve in water. For photon radiation, z_{eq} is usually determined as the integral of the path length, weighted by the medium to water electron density ratio. This approximation does not hold for electrically charged particles, since the stopping power not only depends on the density, but also on the material composition. In this case we determine z_{eq} as the integrated path length, weighted by the ratio of the stopping power in the medium over water.

$$z_{eq}(z) = \int_0^z \frac{S(E(z'))}{S_w(E(z'))}\, dz' \qquad \text{[Eq. 166]}$$

With this definition, z_{eq} is the equivalent depth in water at which a beam has lost the same amount of energy via electronic stopping as it has at the physical depth z in the patient.

7.1.4 Water equivalent depth at beam dose specification point

Water equivalent depth is the physical path length along a ray from the beam source to the BDSP, scaled with the relative stopping power between the traversed materials and water at 150 MeV/u. Differences in SAD X and Y are included in the calculation to match the dose calculation. Beam line objects are not considered.

Note: *Inaccuracies in the water equivalent depth calculation can occur due to dose grid resolution effects. These inaccuracies are the same as the range inaccuracies for the dose calculation.*

Note: *Inaccuracies in the computation of the water equivalent depth can occur when placing the BDSP in a region with a high density gradient.*

Note: *The user is advised to always use these values in combination with subsequent patient-specific QA.*

7.1.5 Multiple Coulomb Scattering

The lateral spread of one pencil beam caused by multiple coulomb scattering (MCS) is treated in the framework of Fermi and Eyges [59]. There are two main limitations to this theory:

1. It only handles Gaussian distributions, and therefore omits the non-Gaussian tails, which are also created by MCS [60].

2. It does not take lateral inhomogeneities into account.

Fermi-Eyges transport

In the small-angle approximation, the transport equation is solved considering a lateral, diffusive, scattering power T along transport step z. An initial Gaussian distribution remains Gaussian after each step. At depth z it is characterized by:

$$\overline{\theta^2}(z) = \overline{\theta^2}(0) + \int_0^z T dz'$$

$$\overline{r\,\theta}(z) = \overline{r\,\theta}(0) + \overline{\theta^2}(0)\, z + \int_0^z (z - z')\, T dz' \qquad \text{[Eq. 167]}$$

$$\overline{r^2}\,(z) = \overline{r^2}\,(0) + 2\overline{r\theta}\,(0)\;\; z + \overline{\theta^2}\,(0)\;\; z^2 + \int_0^z (z - z')^2\, T dz'$$

where $\overline{\theta^2}$ is the angular variance, $\overline{r\theta}$ the spatial-angular covariance (beam divergence), and $\overline{r^2}$ the spatial variance of the Gaussian distribution. The set of distribution moments $\left\{ \overline{\theta^2}, \overline{r\theta}, \overline{r^2} \right\}$ are referred to as the spatial-angular moments. It should be noted that cylindrical coordinates are used for the spatial-angular moments. This also reflects on the definition of the scattering power.

Scattering Power

The scattering power entering in the transport equations is computed using the Rossi formula [62]

$$T = \left(\frac{E_s}{p\beta c} \right)^2 \frac{Z^2}{X_0} \qquad \text{[Eq. 168]}$$

where p is the light ion momentum and X_0 is the radiation length, for which we use the expressions suggested by Tsai [74]. For compound materials, the radiation length is calculated according to Bragg's rule [61]:

$$X_0{}^{-1} = \sum_i w_i\, X_{0i}^{-1} \qquad \text{[Eq. 169]}$$

E_s in Equation 168 is a constant given by Rossi as E_s=21 MeV. However, a study of published measurements of lateral spread in water [67], [71], [63] and [75], revealed that a value E_s=18 MeV gave the overall best fit. Interestingly enough, this value falls right between the suggested values in two similar studies: E_s=17.0 MeV [73] and E_s=18.7 MeV [67].

Note: *The quoted values for E_s refer to radial, and not projected scattering power.*

There are more sophisticated scattering power models than that of Rossi, but it has been shown that the difference for low-Z materials in the therapeutic energy range is negligible [70], [61].

7.1.6 Nuclear scattering

The lateral scattering of a light ion beam leads to a central, small-angle part with a nearly Gaussian distribution around the central axis, and a large-angle component that generates a wider, low-intensity distribution. This is sometimes referred to as the nuclear halo. While the former is typically associated with MCS, the latter is mainly associated with scattering and production of nuclear fragments in inelastic nuclear reactions (NS). However, this is a somewhat oversimplified picture, since MCS also contributes to the non-Gaussian tail of the lateral distribution [60]. Since the non-Gaussian tails of the lateral distribution is a large-volume, low-dose phenomenon, the reproduction of the detailed lateral shape of the nuclear halo is not critical. In spite of this, the inclusion of the halo in itself is important as it removes a significant fraction of dose from the central Gaussian region.

As opposed to the Gaussian part of the MCS, there is no simple, computationally efficient solution to the transport equation for the nuclear halo. Instead, more *ad hoc* methods have to be used to model this effect. A popular method is to introduce a second, much wider, Gaussian in addition to the Gaussian distribution describing MCS (see [92], [73] and also *section 6.4.4 Nuclear scattering on page 184*). A single Gaussian is however a rather coarse approximation of the actual halo shape. Studies have found that dual Gaussians [89], as well as other more complex functions [90], [91] yield more accurate approximations.

The volume of the dose distribution due to the nuclear halo around a scanning spot is much larger than the dose distribution due to MCS. This greatly degrades the computational performance due to the increase of the number of spots that needs to be considered in the dose computation in each voxel. However, it has been found that the Gaussian widths in a dual Gaussian nuclear halo model were well described as constant for all radiological depths [89]. This approximation is adopted in RayStation with the minor modification that the halo widths are allowed to scale according to the beam divergence. This enables a model were the effect of spot superposition on the nuclear halo dose distribution can be handled in a 2D fluence-like domain, which means that the cut-off radius commonly applied to the halo in other models can be relaxed, yielding a more correct field size dependence also for larger fields.

Note that this model only intends to describe the low dose envelope around the primary Gaussian dose distribution as created by nuclear interactions and non-Gaussian MCS in the patient and range shifter. It specifically is *not* intended to describe the dose due to the low fluence envelope that may be present around the pristine spot fluence upstream of the patient or range shifter.

7.1.7 Machine model parameters

The machine model parameters in RayStation are comprised of geometrical/physical properties of the treatment machine (machine parameters), and of beam model parameters that are determined in the beam modeling procedure.

Machine parameters

The machine parameters for a PBS beam in RayStation mainly consists of the geometrical and physical properties of the range shifters and the inner and outer dimensions and extension limits

of the snouts. In addition the lateral limitations of the scanning field are viewed as a machine parameter.

The machine may also include a ripple filter, used for modulating the Bragg peak width. The ripple filter in RayStation is modeled as a static range modulator, with properties that define its range modulation steps (in water equivalent thickness) and corresponding relative weights. A ripple filter may be commissioned for each beam line in the machine, and its dimensions are constant over the entire energy range.

Beam model parameters

The beam model parameters include:

- Effective primary energy spectrum: dN/dE
  - Function of the nominal beam energy
- Spatial-angular distribution moments at the isocenter (measured in air): $\{\overline{\theta_0^2}, \overline{r\theta_0}, \overline{r_0^2}\}$
  - Given in cylindrical coordinates
  - Function of the nominal beam energy, as well as the snout position for movable snouts (if parameters at different snout positions are included in the beam modeling)

    Note: *The spatial-angular distribution moments can be a total of two sets, a primary and a secondary with respective weights to specify their contribution. A model without secondary spatial-angular moments is equivalent to having secondary weight zero.*
- Dose monitor detector sensitivity: S
  - In units of ions/NP (ions per primary particle), alternatively ions/MU (machine unit)
  - Function of the nominal beam energy
- The effective focal points of the scanning magnets: f_X and f_Y
  - f_X f_Y Constant values over the full energy range

The energy dependent beam model parameters of a machine (i.e., the energy spectrum, the spatial-angular moments, and the dose monitor sensitivity) are stored for a discrete number of nominal beam energies in the RayStation machine model. For beam delivery systems that allow for a continuous selection of maximum range/nominal beam energy. The model parameters can be interpolated to an arbitrary nominal energy between the limits set in the machine model.

The spatial-angular moments and the dose monitor sensitivity are linearly interpolated between the stored nominal energies. For machines with movable snouts, the spatial-angular moments for each nominal beam energy can also be stored for a discrete number of snout positions. In this case the moments are interpolated in both the nominal energy and the snout position.

The energy spectrum for an arbitrary nominal energy E_N, $dN/dE|_{E_N}$, is determined by interpolating between the stored energy spectrum with closest lower (E_{N_1}), and upper (E_{N_2}) nominal energies, $dN/dE|_{E_{N_1}}$ and $dN/dE|_{E_{N_2}}$.

7.1.8 Light ion pencil beam dose algorithm

The light ion dose and RBE-weighted dose calculation in RayStation is based on a so called pencil beam dose algorithm, and each pencil beam is associated with a physical pencil beam (also referred to as a scanning spot) delivered by the PBS system. The dose contribution from each of these pencil beams is calculated by performing a factorization of the dose to the lateral dose profile Φ and the longitudinal, integrated depth dose IDD components:

$$dose(z,r) = \Phi(z,r)IDD(z) \qquad \text{[Eq. 170]}$$

where z is the radiological depth of the dose voxel and r is the radial distance from the dose voxel computed by high resolution ray tracing from the beam source point (see below) to the pencil beam center line in the light ion pencil beam dose computation. Note that this differs from many pencil beam implementations, including the RayStation proton pencil beam computation, where z is the radiological depth computed along the pencil beam central axis.

This factorization is only correct within the so-called infinite slab approximation, which stipulates that, for each pencil beam, the patient geometry consists of semi-infinite layers, extended transversely to the central beam axes. The pencil beams thus get a radial symmetry, and therefore a pencil like shape, giving its name to the algorithm. During dose computation the phase space parameters are transported along the central axis of each pencil beam through the patient. The integrated depth dose is obtained by scaling a reference integrated depth dose curve, which unscaled is valid for the longitudinal dose deposition in water. The algorithm therefore generically provides absorbed dose as dose-to-water. The pencil beam algorithm has been extensively used in several carbon and helium dose algorithms [92], [88], [90].

While the scaling of the integrated depth dose captures the effect of longitudinal heterogeneities encountered in 1D ray-tracing through the patient, lateral heterogeneities also have to be taken into account in the dose calculation. For protons, a common approach is to decompose the spot fluence into a large number of sub-pencil beams, see *Discretization of the spot fluence on page 189* and also [73]. This approach greatly degrades performance but has the advantage that the effect of heterogeneities are taken into account both in the longitudinal scaling of the integrated depth dose and also in the Fermi-Eyges transport. Note that the infinite slab approximation is still applicable for each sub-spot and cannot be avoided with the pencil beam algorithm. Since helium and carbon ions are heavier, they experience a smaller amount of scattering compared to protons, and thus this effect is less important for these light ions. Thus, only a single pencil beam per spot is used in the RayStation light ion dose calculation. The effect of lateral heterogeneities is instead captured by using the radiological depth of each voxel when sampling quantities that depend on the radiological depth, such as the integrated depth dose.

Calculation of the integrated depth dose and particle energy spectra in water

The light ion integrated depth dose profiles and particle energy spectra in water can be calculated from either input data pre-generated by RaySearch or from input data provided by the clinic. In the former case the pre-generated input data is weighted with the effective energy spectrum dN/dE from the beam model, while clinic specific input data is used directly in the latter case.

Using input data pre-generated by RaySearch, the integrated depth dose is determined from the effective energy spectra $dN/dE|_{E_N}$, by superposition of pre-calculated mono-energetic IDDs:

$$IDD^w(z, E_N) = \sum_i \frac{dN(E_i)}{dE}|_{E_N} idd_i(z)\Delta E_i \qquad \text{[Eq. 171]}$$

where idd_i is the pre-calculated integrated depth dose profile in water for primary energy E_i, in units of cGy cm^2/ion, and ΔE_i is the bin width.

The pre-generated data is described in *section 7.2 Light ion dose calculation input data on page 276*. Clinic-specific integrated depth doses can be used directly in the dose computation, without performing the weighting procedure described above. In this case, $IDD^w(z, E_N)$ as provided by the clinic is used in the dose computation.

In the same way, primary particle and fragment energy spectra for each depth can be provided by the clinic and used in the RBE-weighted dose computation. If clinic-specific particle spectra does not exist for the required nominal energy, interpolation from existing clinic specific data is performed.

Calculation of Bragg peak widening from ripple filter

The ripple filter is used to widen the Bragg peaks, effectively reducing the number of energy layers needed to achieve target coverage. This is done by introducing a fixed (i.e., not time dependent) range modulating object in the beam line, consisting of a structure with different thicknesses. The ripple filter will thus smear the Bragg peak when ions traverse varying thickness of ripple filter material.

A ripple filter in RayStation is modeled using two sets of parameters: steps of different water equivalent thicknesses and their relative weights. The relative weight of a step corresponds to the fluence fraction traversing that thickness.

The modulation of the final depth dose (widening of the Bragg peak), IDD^T, is determined from the thicknesses and relative weights of the ripple filter model according to:

$$IDD^T(z, E_N) = \Sigma_i \left(w_i * IDD^w(z - wet_i, E_N)\right) \qquad \text{[Eq. 172]}$$

where IDD^w is the energy spectrum weighted depth dose, see Equation 171.

The ripple filter also needs to be considered for the particle energy spectra. This is important since it will change the beam spectral composition in the patient as there will be a significant build-up of secondary particles before reaching the patient surface.

The particle energy spectrum filtering is done in a similar fashion as for the depth doses, i.e., by weighting the spectra for different ripple filter thicknesses.

The user should be aware that this modeling approach assumes that the build-up takes place in water and that the actual material properties of the ripple filter will be disregarded.

Calculation of voxel radiological depths

Calculation of physical dose and RBE-weighted dose in each voxel requires the voxel radiological depth. For physical dose calculation the radiological depth is used when sampling the integrated depth dose and when sampling the spot MCS widths. For RBE-weighted dose calculation it is used for sampling the primary ion and fragment spectra when using the LEM with the "Classic" algorithm [94] and for sampling radiological depth dependent quantities pre-computed from spectral data when using the LEM low dose approximation and MKM (see equations 127 - 128 in [93] or Equation 200 in *section 7.9 MKM dose computation on page 306*).

For each beam direction, the radiological depth in all voxels is computed according to *section 7.1.3 Energy loss and radiological depth on page 268* using regularly spaced ray traces starting upstream of the patient or range shifter with ray directions computed according to the beam model dual focus points. The maximum beam energy is used as the initial energy. The radiological depth in each voxel is computed by averaging over all rays intersecting the voxel. A ray density such that all voxels are hit by at least four rays is used.

Calculation of spot MCS widths as function of radiological depth

Spot MCS widths as function of radiological depth are computed by ray tracing along the spot axes and concurrent transport of the spots Fermi-Eyges parameters according to *section 7.1.5 Multiple Coulomb Scattering on page 268*. For each voxel crossing, the voxel material is taken into account in the energy loss computation and in the scattering power computation used in Equation 167. Only a single ray trace is used for each spot. The ray tracing starts at the proximal surface of the patient or range shifter, if present.

Since the weight of the secondary Gaussian is typically either zero or substantially smaller than that of the primary Gaussian, the corresponding width is calculated with a simplified procedure. The width at the proximal surface of the patient is calculated by using Fermi-Eyges transport (including transport through the range shifter, if present, as described in section 6.3.1 Beam model), and then projected onto a fluence grid. The dose distribution of the secondary Gaussian can then be handled in a 2D fluence-like domain, similarly to the nuclear halo (discussed in *section 7.1.6 Nuclear scattering on page 270*).

Modeling of spot halo widening

To accurately describe the dose of a pencil beam spot, dose deposition resulting from fragments and large angle scattering carbon ions are modeled with additional Gaussians. The parameters of these Gaussians are determined from Monte Carlo simulations for varying energies, range shifter thicknesses and the distance between the range shifter distal surface and the patient, referred to as the airgap.

During the dose computation, a trilinear interpolation in energy, range shifter thickness and airgap is done to determine the halo parameters for all spots in the beam. For each beam direction, the

airgap across the patient surface is determined with a regularly spaced ray trace such that every pixel on the fluence plane is hit once.

The MCS Gaussian in each Bragg peak is convolved with the NS model Gaussians to establish the actual Gaussian halo widths in the Bragg peak. This convolution provides a correction to the halo-widening effect due to the widening of the MCS spot through the range shifter, airgap and patient.

7.2 LIGHT ION DOSE CALCULATION INPUT DATA

The input data needed for light ion dose calculation consist of:

- integrated depth dose profiles
- differential distributions of primary ions and fragments (particle energy spectra)
- nuclear scattering (halo) model parameters

As described in *section 7.1.8 Light ion pencil beam dose algorithm on page 272*, the integrated depth dose profiles and fragment spectra can be obtained by either performing a weighting of RaySearch pre-generated data for mono-energetic light ions with the effective energy spectrum dN/dE given by the beam model (see *section 7.1.7 Machine model parameters on page 270*), or by directly using input data provided by the clinic.

In this section, the pre-generated input data for carbon ions is discussed, as well as nuclear scattering (halo) parameters for helium. This pre-generated input data has been obtained using the FLUKA Monte Carlo transport code [86], [87]. For all FLUKA simulations referred to in this section, an ionization potential of 75 eV was adopted for water as recommended by ICRU [96].

For helium ions, there are no pre-generated clinical integrated depth doses or particle energy spectra. Instead, this data must be provided by the clinic.

7.2.1 Integrated Depth Doses (*idds*)

The one-dimensional laterally integrated depth doses ($idds$) for primary mono-energetic carbon ions are used to determine the integrated dose to be deposited by the pencil beam dose calculation for a certain nominal energy and depth as described in *section 7.1.8 Light ion pencil beam dose algorithm on page 272*.

The *idds* were simulated in water for 1097 energies. The initial carbon energies were chosen so that the distance between the Bragg peak depths of two consecutive energies is shorter than 0.5 mm. The energy of the primary carbon ion in each simulation was sampled from a small rectangular energy distribution to ensure a continuous coverage of all energies between the lowest and the highest supported energy (50 MeV/u to 500 Mev/u). This also results in a slightly widened Bragg peak more suitable for modeling an actual treatment beam. The number of primary particles was set to produce adequate counting statistics.

The FLUKA built-in scoring algorithm *USRBIN* was used to score laterally integrated energy deposition in 0.01 cm thin discs in a cylindrical water volume.

7.2.2 Particle energy spectra

Particle energy spectra refers to the distribution of primary ions and produced fragments differential in energy.

The particle energy spectra are used to characterize the mixed radiation field at a certain depth x in a light ion beam, and are essential in the RBE-weighted dose computation (as described in *section 7.9 MKM dose computation on page 306* and *section 7.10 RBE-weighted dose algorithms for LEM on page 308*). The differential spectra $dN(E_k, T; x)/dE_k$ describe the distribution of kinetic

energy E_k of primary ions and secondary charged particles of type T, characterized by charge Z_T, as a function of depth in water x for a set of beam energies. The spectra are expressed in terms of *particles per primary per energy per area* ($T^{-1}(MeV/u)^{-1}cm^{-2}$).

The spectra for primary carbon ions were generated using FLUKA [86], [87]. Simulations were run for every 20th energy of the idd simulations and with equal initial energy spread, resulting in a libary containing spectra for 55 initial carbon ion energies.The number of primary particles was set to produce adequate counting statistics.

An adjusted version of the user routine *mgdraw* was used to output a collision file, containing the relevant phase space of each energy loss event of each particle transported in the simulation. The collision files were used to score the track lengths within each cylindrical slab of material, which was used to compute the track-weighted particle fluence as a function of depth. The resulting differential spectra are stored in uniform depth bins with size 0.1 cm.

The spectra of primary carbon ions (i.e., Z=6, since no isotopic discrimination) is stored using linear energy binning with bin edges ranging from 0 - 550 MeV/u and bin size 1 MeV/u.

The spectra of fragments (Z < 6) and target recoils (Z = 7, 8) are stored using logarithmic energy binning with bin edges ranging from 0.1 - 999 MeV/u spread over 133 bins.

Examples of the resulting particle energy spectra at different depths are shown in Figure 72. Figure 73 shows an example of the evolution of the total fragment yield with depth.

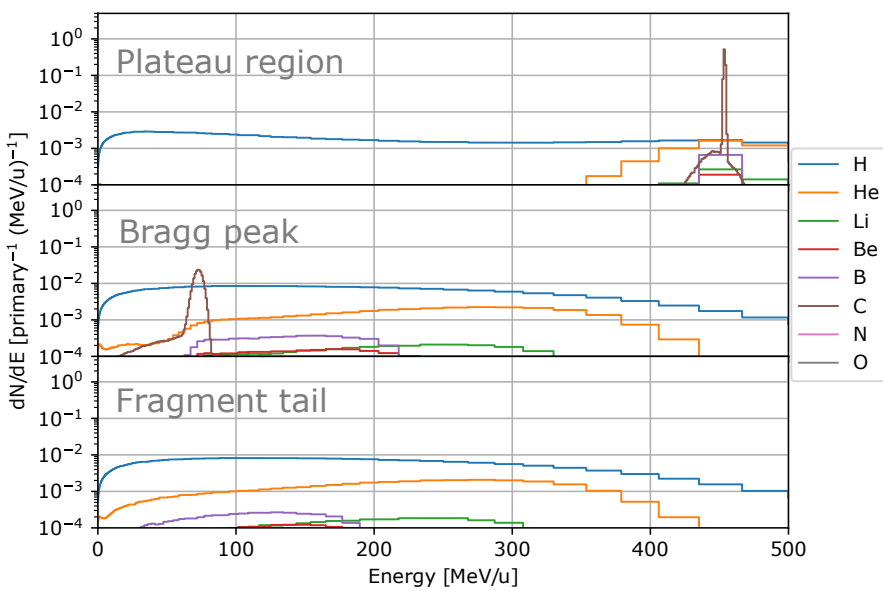

Figure 72. Differential energy spectra of the 500 MeV/u carbon beam - the highest beam energy simulated in the base data.

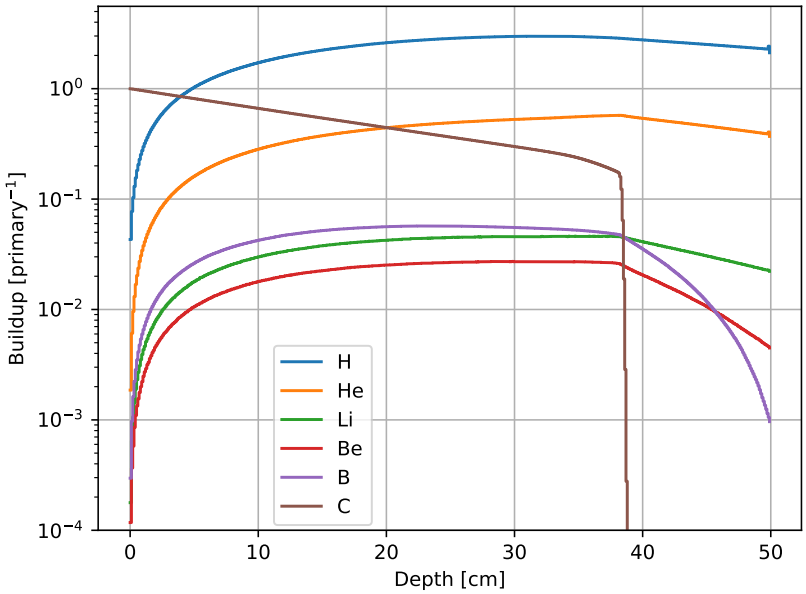

Figure 73. Fragment build-up (total number of particles per primary beam particle) for a 500MeV/u carbon ion beam. Note that the nitrogen and oxygen yield is lower than 10^{-4} and hence not visible in this figure.

7.2.3 Nuclear scattering (halo) parameters

Similar to [95] the RayStation NS model is based on fits to FLUKA [86], [87] Monte Carlo data for single spot simulations for both carbon and helium in water at several different energies, range shifter thicknesses and airgaps. The range shifter material used in the simulation is polymethyl methacrylate (PMMA). The NS model contains two halos including a total of four Gaussians: an inner halo described by a single Gaussian and an outer halo described by three Gaussians with fixed relative weights determined at the Bragg peak depth. Phenomenologically, the inner halo can be associated with heavier fragments and the outer halo with lighter fragments [88], at least for carbon ions. The evolution of each of the two halos is further described by a radiological depth dependent weight (see Figure 74, Figure 75, Figure 76), as well as by four (fixed) Gaussian widths at Bragg peak depth (see Figure 77).

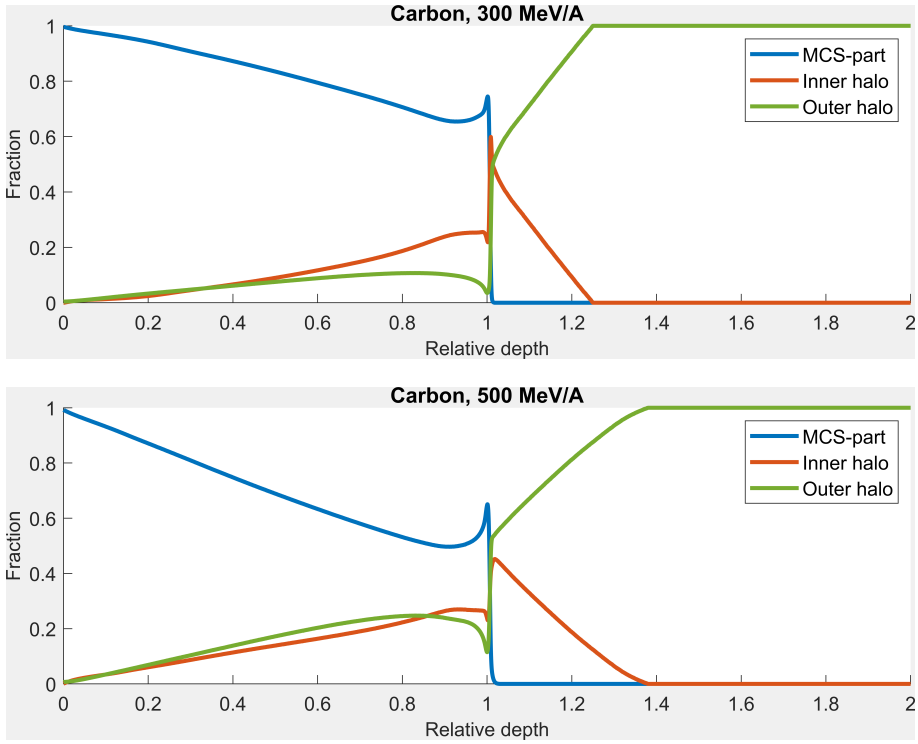

Figure 74. Fraction of dose from the different constituents of the NS model for carbon ions at two different initial energies. All depths are relative to the Bragg peak depths for the corresponding modalities and energies.

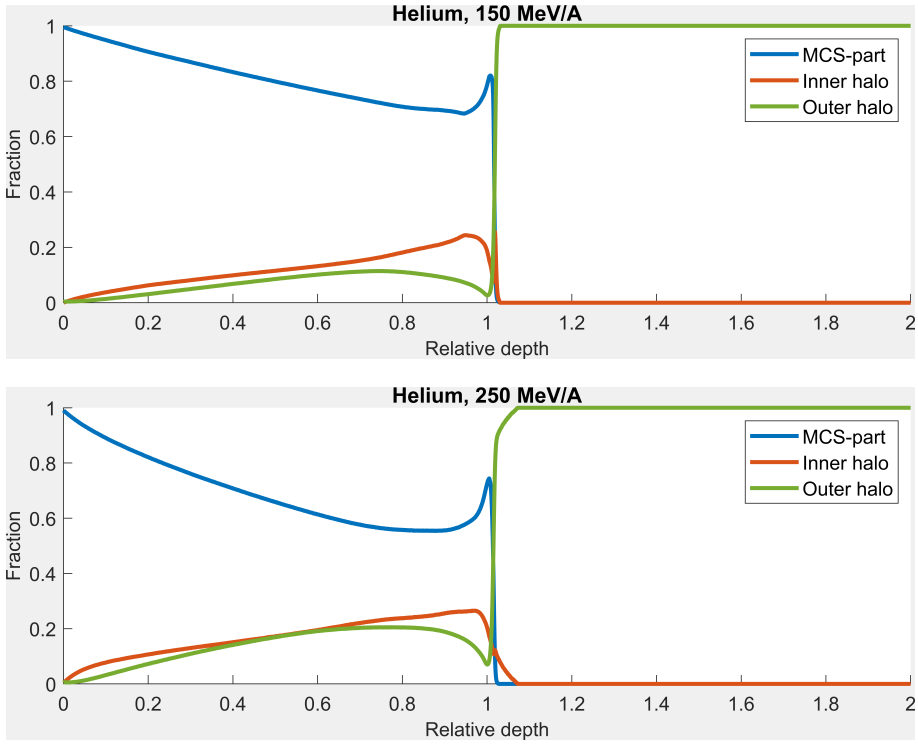

Figure 75. Fraction of dose from the different constituents of the NS model for carbon ions at two different initial energies. All depths are relative to the Bragg peak depths for the corresponding modalities and energies.

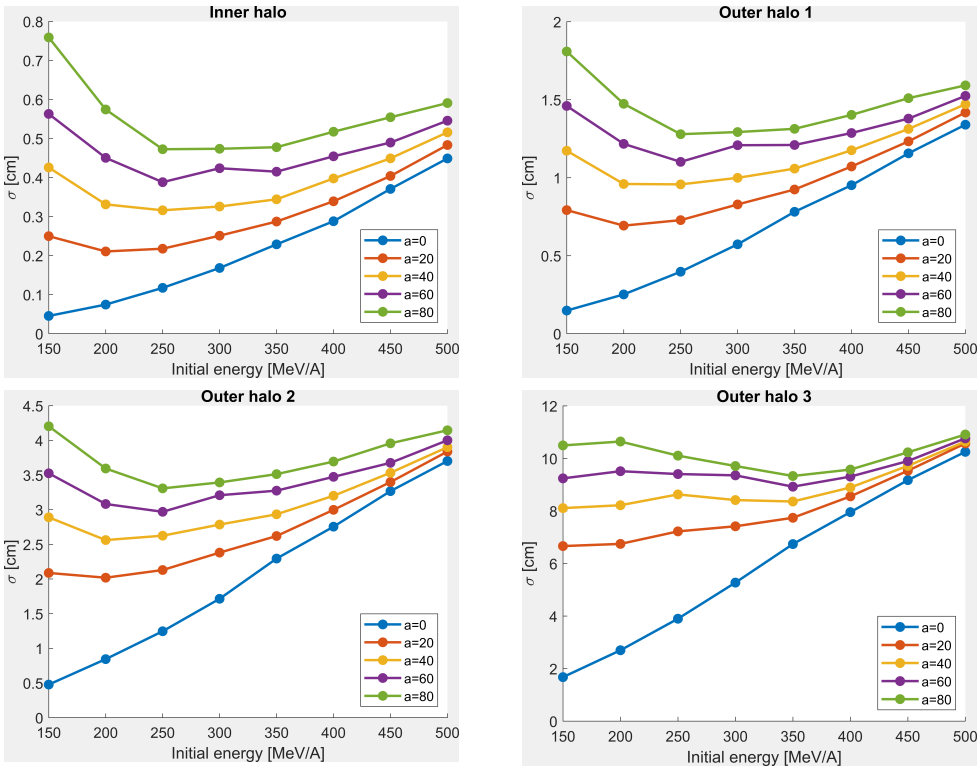

Figure 76. Carbon Gaussian widths $\sigma(\text{Gaussian dose} \propto e^{-r^2/\sigma^2})$ for all parametrized initial energies and airgaps between 0 and 80 cm with a 3 cm PMMA range shifter.

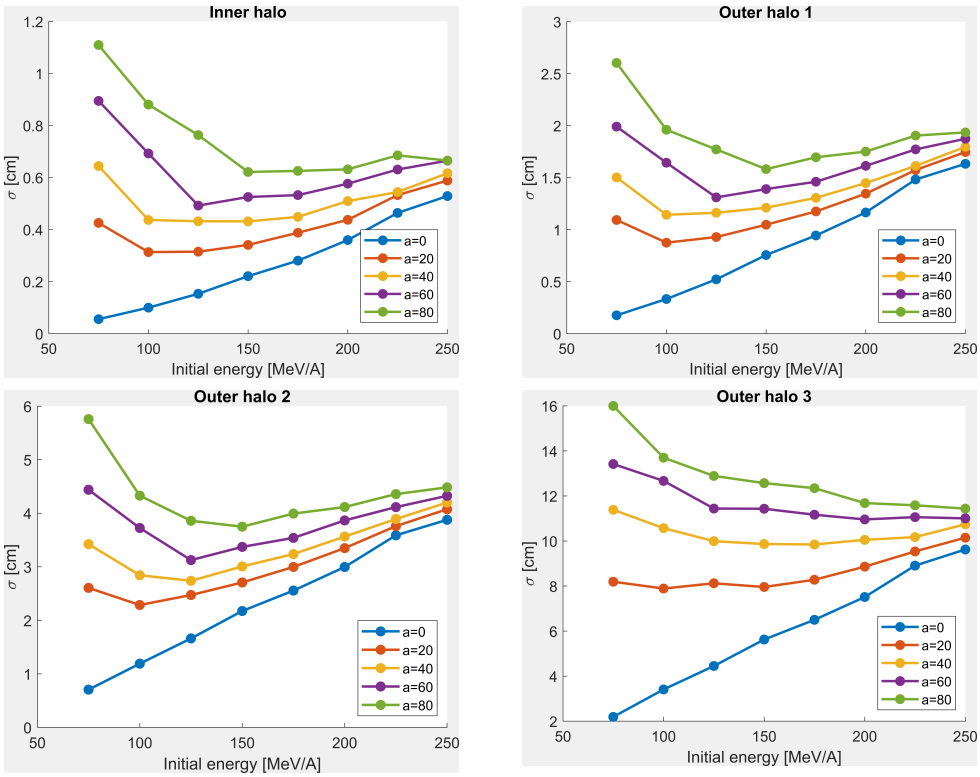

Figure 77. Helium Gaussian widths $\sigma(\text{Gaussian dose} \propto e^{-r^2/\sigma^2})$ for all parametrized initial energies and airgaps between 0 and 80 cm with a 3 cm PMMA range shifter.

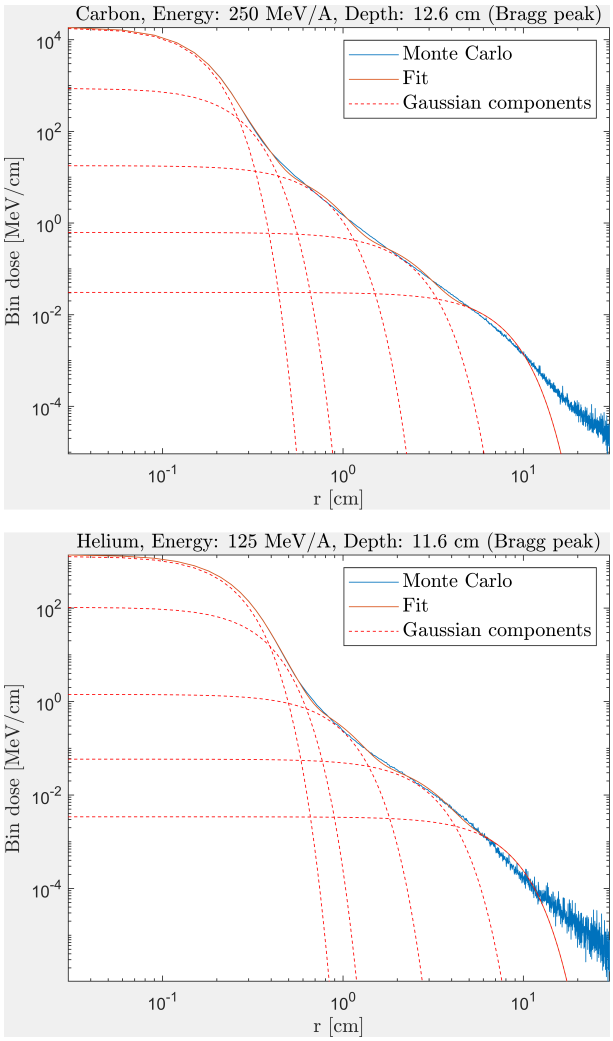

Figure 78. Dose along the radial axis at the Bragg peak for the halo model and the FLUKA simulation it is fitted against. The dashed curves show the MCS component, the inner halo component, and the three outer halo components.

Nuclear interaction correction (NIC)

A limitation of obtaining the halo parameters as fits to data in water and the fact that halo weights only depend on radiological depth is that the halos might not be accurate for materials largely different to water. This is because the probability of undergoing inelastic nuclear interactions is dependent on the properties of the medium. This is loosely accounted for with the dependence of the halo weights on radiological depth which is correlated to the probability of inelastic nuclear interactions [137]. However, using a more advanced model that directly uses the probability for

inelastic nuclear interactions in the medium will yield a more accurate dose computation in materials different to water.

The nuclear interaction correction (NIC) algorithm, originally proposed by Inaniwa et al. [138], calculates a correction factor that depends on the inelastic nuclear interaction probability of an ion projectile traversing a medium. This correction factor is then used to modulate the weight of the halos, using the phenomenological association of the halos with the different fragments.

The probability of inelastic nuclear interactions due to an ion traversing a medium is proportional to the cross section of such interactions multiplied by the number density of the nuclei in the medium.

$$P(interaction) \propto \sum_i \sigma_{Ni} N_i \propto \rho \sum_i w_i \frac{\sigma_{Ni}}{A_i} \qquad \text{[Eq. 173]}$$

where i enumerates the different nuclei in the medium, σ_{Ni} is the cross section for inelastic nuclear interactions of the ion projectile with the nuclei i, N_i is the number density of the nuclei i, ρ is the mass density of the medium, w_i is the mass fraction of nuclei i, and A_i is the mass number of nuclei. The cross sections σ_{Ni} are obtained from the analytical cross section model from Sihver et al. [139], while ρ, w_i and A_i are input data obtained from the CT to material interpretation (see *section 2.3.2 CT to material properties mapping on page 22*) or the material override (see *section 2.5 Material override on page 30*).

In a similar way to the radiological depth from energy losses (see *section 7.1.3 Energy loss and radiological depth on page 268*), a water equivalent depth for inelastic nuclear interactions can be defined as the path length integral weighted by the ratio of the nuclear reaction probability in the medium over water.

$$z_{NIC}(z) = \int_0^z \frac{P(interaction)}{P(interaction)_w} dz' \qquad \text{[Eq. 174]}$$

Assuming that the ion projectiles are attenuated exponentially as they traverse the medium, the NIC correction factor F_{NIC} is obtained as the quotient of the attenuation at the water equivalent depth for nuclear reactions over the attenuation at the radiological depth:

$$F_{NIC}(z) = \frac{exp(-\frac{z_{NIC}}{\lambda})}{exp(-\frac{z_{eq}}{\lambda})} = exp\left(\frac{z_{eq}(z) - z_{NIC}(z)}{\lambda}\right) \qquad \text{[Eq. 175]}$$

where λ is an ion projectile dependent mean free path, with a value of 62.54 cm and 25.60 cm for helium and carbon respectively [138].

The contribution to the dose from primary ions at a given depth z is proportional to the number of primary ions at that depth, which depends on their attenuation as they pass through the medium and undergo inelastic nuclear interactions. Therefore, the weight of the MCS Gaussian at the depth z is multiplied by the correction factor $F_{NIC}(z)$ (see Equation 177). Conversely, since attenuation

of primaries also causes creation of nuclear fragments, the number of produced fragments is inversely proportional to $F_{NIC}(z)$. To account for this, the weight of the outer halo is divided by the correction factor $F_{NIC}(z)$ (see Equation 181). For more details, refer to the original article from Inaniwa et al. [137].

WARNING!

Limitations of the nuclear interaction correction (NIC). The inelastic nuclear interaction cross section model used in the NIC algorithm is valid for all projectiles and targets with atomic number less than or equal to 26. Be extra careful when planning a light ion beam traversing materials that contain a significant mass fraction of atoms with atomic number greater than 26.

(719383)

7.3 DOSE AND RBE-WEIGHTED DOSE CALCULATION FOR PBS BEAMS

A PBS plan consists of a number of energy layers, each with a matrix of spot positions and corresponding meter-set weights. This section gives a detailed description on how RayStation calculates the dose for a PBS plan. The user is advised to be well acquainted with *section 7.1 General models and algorithms on page 267*, before reading this section.

7.3.1 Beam model

The phase space of a single light ion spot in RayStation is given by:

- Mean direction of the light ions: **e**
- Energy spectrum: dN/dE
- Spatial-angular distribution moments: $\{\overline{\theta^2}, \overline{r\theta}, \overline{r^2}\}$
- Absolute spot weight: w^a (number of primary ions)

For a given spot position, nominal beam energy, and meter-set weight (as given by the plan), these parameters are obtained more or less directly from the phase space parameters of the machine model.

The mean direction **e** is calculated as described in *section 6.4.1 Initialization and tracing of phase space parameters on page 181*, with SAD_X^{vir} and SAD_Y^{vir} determined by the effective scanning magnet focal lengths, f_x and f_y, respectively (See *Beam model parameters on page 271*).

The spatial-angular moments obtained from the machine model are transported (*Fermi-Eyges transport on page 269*) from the isocenter plane to the entry point of the patient (or range shifter if used). This, typically upstream, transport step is performed in vacuum, since the spatial-angular moments of the beam model have been extracted from measured spot profiles assuming vacuum transport. Note that if the External ROI has a density that is much lower than that of water, the spatial-angular moments may not be accurate near the surface, especially when a range shifter is used.

The absolute weight of the spot is given by the product of the meterset weight from the plan (in number of primaries, NP, or machine units, MU) and the energy dependent dose monitor sensitivity as provided by the machine model.

Modeling of a range shifter

For beams that include the use of a range shifter, the pencil-beam dose calculation will start at the upstream surface of the range shifter. The range shifter, and the air gap between range shifter and patient outline, will thus be treated as if they are a part of the patient geometry in the pencil-beam tracing. The phase space transport in the range shifter is performed in steps of $\leq$ 0.1 cm, and the transport over the air gap is performed in vacuum. The range shifter material properties, physical thickness, and position along the beam line are obtained from the machine model. Since the range shifter is treated as an extension of the patient geometry in RayStation, no additional beam modeling data is required.

7.3.2 Scoring of dose and RBE-weighted dose in the patient

The scoring of dose from a PBS plan is performed in receiving mode, where the total dose to a point $\overline{p}$ in the patient is determined as the sum of the contributions from the spots of each energy layer e in all beams

$$dose(\overline{p}) = \sum_{e} S_e \left(d_e^{MCS}(\overline{p}, \overline{w}_e^{NP}) + d_e^{NS}(\overline{p}, \overline{w}_e^{NP})\right) \quad \text{[Eq. 176]}$$

where S_e is the energy dependent dose monitor sensitivity in units of ions/NP and $\overline{w}_e^{NP} = \{w_e^{NP}\}$, the meterset weights of all spots j in energy layer e. S_e is obtained from the machine model while the meterset weights are plan parameters. $d_e^{MCS}(\overline{p}, \overline{w}_e^{NP})$ is the dose contribution from the primary light ions (in units cGy/ion) from all spots in energy layer e. $d_e^{NS}(\overline{p}, \overline{w}_e^{NP})$ is the corresponding dose contribution from the nuclear halo and the secondary Gaussian component of the spot fluence.

The primary light ion dose contribution is further decomposed as

$$d_e^{MCS}(\overline{p}, \overline{w}_e^{NP}) = IDD_e(z_{eq}) \sum_{j} F_{NIC,e,j}\, w_{e,j}^{NP}\, \Phi_{e,j}^{MCS}(\overline{p}) \quad \text{[Eq. 177]}$$

where j enumerates all spots in energy layer e, z_{eq} is the radiological depth at point $\overline{p}$, $F_{NIC,e,j}$ is the NIC correction factor (see *section 7.2.3 Nuclear scattering (halo) parameters on page 278*) of spot j in energy layer e, and

$$\Phi_{e,j}^{MCS}(\overline{p}) = (1 - W_e^{IH}(z_{eq}) - W_e^{OH}(z_{eq}))\,(1 - W_s)\, G^{99.9\%}(r, \sigma_{e,j}^{MCS}(z_{eq})) \quad \text{[Eq. 178]}$$

where W_e^{IH} and W_e^{OH} are the radiological depth dependent fractions of the dose in the inner and outer halos, respectively, W_s is the weight of the secondary Gaussian contribution (which can be zero), and r the perpendicular distance from $\overline{p}$ to the axis of spot e, j. $G^{99.9\%}(r, \sigma)$ is a Gaussian function with width σ evaluated at cylindrical radius r. The function is subject to a radial cut-off at the radius where 99.9% of the dose is inside the cut-off. The cut-off dose is compensated for by a scaling factor to normalize the function. $\sigma_{e,j}^{MCS}(z_{eq})$ is the MCS width of spot e, j at the radiological depth of point $\overline{p}$.

The dose contribution from secondary Gaussian and the nuclear halo is

$$d_e^{NS}(\overline{p}, \overline{w}_e^{NP}) = IDD_e(z_{eq}) \Big(W_s (1 - W_e^{IH(z_{eq})} - W_e^{OH(z_{eq})}) \Phi_e^{sec}(\overline{p}_{proj}, \overline{w}_e^{NP}) + W_e^{IH}(z_{eq}) \Phi_e^{NS,IH}(\overline{p}_{proj}, \overline{w}_e^{NP}) + W_e^{OH}(z_{eq}) \sum_{h=1}^{3} c_{e,h} \Phi_{e,h}^{NS,OH}(\overline{p}_{proj}, \overline{w}_e^{NP}) \Big) \quad \text{[Eq. 179]}$$

where $\overline{p}_{proj}$ is the point $\overline{p}$ projected onto the fluence plane according to the beam divergence and $c_{e,h}$ are the normalized (fixed) relative weights of the three outer halo components. $\Phi_e^{NS,IH}$ is a planar fluence-like quantity:

$$\Phi_e^{NS,IH}(\overline{x}, \overline{w}_e^{NP}) = \sum_j w_{e,j}^{NP} G(||\overline{x} - \overline{x}_{e,j}||, \sigma_{e,j}^{IH}) \quad \text{[Eq. 180]}$$

where $\overline{x}_{e,j}$ is the position of spot e, j in the fluence plane and $\sigma_{e,j}^{IH}$ is the inner halo Gaussian width in the Bragg peak projected onto the fluence plane. $G(r, \sigma)$ is a Gaussian function in cylindrical coordinates with a width σ (without any radial cut-off). The three planar fluence-like quantities associated with the outer halo, $\Phi_{e,h}^{NS,OH}$, are computed analogously, except they are also multiplied by the inverse of the NIC correction factor (see *section 7.2.3 Nuclear scattering (halo) parameters on page 278*):

$$\Phi_{e,h}^{NS,OH}(\overline{x}, \overline{w}_e^{NP}) = \sum_j \frac{1}{F_{NIC,e,j}} \; w_{e,j}^{NP} G(||\overline{x} - \overline{x}_{e,j}||, \sigma_{e,j,h}^{OH}) \quad \text{[Eq. 181]}$$

$\Phi_e^{sec}(\overline{p}_{proj})$ is also computed analagousy, with the width, $\sigma_{e,j}^{sec}$, being the secondary Gaussian width at the patient surface projected onto the fluence plane.

For each point $\overline{p}$ the airgap is determined and used to interpolate the W^{IH} and W^{OH} fractions. In effect, all spots that contribute to the fluence at point $\overline{p}$ will have fraction values interpolated from the airgap at point $\overline{p}$. A heterogeneous patient surface resulting in a varying airgap across the field can therefore introduce inaccuracies in the assigned fractions of spots that are off-center from the point $\overline{p}$. However, since the fluence contribution of spots decreases as $x - x^{ej}$ increases, this error is small.

The scoring of RBE-weighted dose from a PBS plan is performed similar to the scoring of voxel physical dose as described above. For more information, see *section 7.9 MKM dose computation on page 306* and *section 7.10 RBE-weighted dose algorithms for LEM on page 308*.

7.3.3 The trichrome approximation

To account for the lateral variation of the particle constituents in the computation of RBE-weighted dose and LET, a trichrome approximation is utilized, adapted from [164]. The approximation consists in associating the particles in the spectra with one of the three lateral fluence components (LFCs): the MCS (see *section 7.1.5 Multiple Coulomb Scattering on page 268*) and the two nuclear scattering halos (see *section 7.2.3 Nuclear scattering (halo) parameters on page 278*). The MCS is mainly associated with primary ions, while the inner halo is mainly associated with heavier fragments and the outer halo is mainly associated with lighter fragments. The exact proportion of particle species per LFC is based on results of FLUKA simulations, and adjusted on a voxel-by-voxel and spot-by-spot basis during dose computation to ensure the total physical dose remains unchanged.

The numerator of dose averaged quantities (such as dose-averaged LET, see Equation 182), as well as the fluence of individual particle species (required for the LEM "Classic" computation), can be obtained by computing one term per LFC (using only the particles assigned to that LFC) and then summing over these terms weighted by the dose contribution of the corresponding LFC.

7.3.4 Scoring of dose-averaged LET

The RayStation light ion dose engine computes dose-averaged LET in water normalized to unit density. Primary particles, fragments and target recoils up to oxygen (Z = 8) are included. The fluences and energy spectra of all particles are given as a function of water equivalent depth by pre-simulated particle energy spectra (see *section 7.2.2 Particle energy spectra on page 276*). Note that there is no lateral dependence in the pre-simulated particle energy spectra.

To account for the lateral variation of the particle constituents in the computation of the spot dose-averaged LET, a trichrome approximation is utilized (see *section 7.3.3 The trichrome approximation on page 288*).

The dose-averaged LET for spot j and lateral fluence component n is computed as follows:

$$LETd_{nj} = \frac{\sum_{h_{nj}} \Phi_{h_{nj}} \cdot LET^2_{\infty,h_{nj}}}{\sum_{h_{nj}} \Phi_{h_{nj}} \cdot LET_{\infty,h_{nj}}} = \frac{\sum_{h_n} d_{h_{nj}} \cdot LET_{\infty,h_{nj}}}{\sum_{h_{nj}} d_{h_{nj}}} \qquad \text{[Eq. 182]}$$

where the sums are over all particles h_{nj} that are associated with the lateral fluence component n in spot j, $d_{h_{nj}}$ is the dose from a particle, $LET_{\infty,h_{nj}}$ is the unrestricted LET in water and $\Phi_{h_{nj}}$ is the fluence. The parametrized stopping power tables from FLUKA are used to evaluate $LET_{\infty,h_{nj}}$ (see *section 7.1.2 Linear Energy Transfer (LET) on page 267* for more details).

The dose-averaged LET for spot j is computed by dose averaging over all lateral fluence components n:

$$LETd_j = \frac{\sum_n d_{nj} \cdot LETd_{nj}}{\sum_n d_{nj}} \qquad \text{[Eq. 183]}$$

where d_{nj} is the dose contribution due to each lateral fluence component n (see Equation 177 and Equation 179).

Finally, the dose-averaged LET in a mixed radiation field with multiple spots j is computed by dose averaging over all spots:

$$LETd = \frac{\sum_j d_j \cdot LETd_j}{\sum_j d_j} \qquad \text{[Eq. 184]}$$

where d_j is the dose contribution from each spot j.

WARNING!

Always evaluate the dose distribution when using LET evaluation. The LET distribution of a plan is an auxiliary quantity, meant to provide additional information to the primary quantity of RBE-weighted dose. The definition of averaged LET is chosen to conform to how LET is generally reported in the literature, and how it is used when estimating the biological effect using RBE models, rather than producing a directly measurable quantity.

The correlation between LET and biological effect in patients is an evolving field of science. The user must always review the literature and base the usage of LET evaluation on the current state of knowledge in the field and clinic-specific treatment techniques and modalities.

(408388)

7.4 DOSE ENGINE ACCURACY AND LIMITATIONS

This section summarizes the acceptance criteria and the algorithm limitations of the RayStation light ion pencil beam dose calculation and validation status. It is important that the user is familiar with, and understands, these limitations.

7.4.1 Dose engine acceptance criteria

This section summarizes the acceptance criteria on physical and RBE-weighted dose and RBE factors that are required by the RayStation dose validation. The reference doses referred to below are of two types:

- Dose from measurements
- Dose computed externally by an independent software, considered to be state-of-the-art in the field.

Physical dose

The following accuracy requirements apply to the computed physical dose when comparing to a reference dose.

For the total dose distribution:

- 95% of the computed dose values shall be within 3% or 3 mm (global gamma). Only dose values above 10% of the max dose are considered.
- 98% of the computed dose values shall be within 5% or 5 mm (global gamma). Only dose values above 10% of the max dose are considered.

The following accuracy requirements apply to a computed depth dose profile when compared to a reference curve:

- The distal range difference shall be smaller than 2 mm.
- 95% of the computed dose values shall be within 3% or 3 mm (1D gamma).
- 98% of the computed dose values shall be within 5% or 5 mm (1D gamma).

The following accuracy requirements apply for comparison of absolute dose to 3D detector block measurements (containing 12 or 24 ion chambers):

- Only points with a dose level exceeding 10% of the maximum reference dose are considered. At least 4 points above this threshold are required.
- At most one point from a block shall fail a 3D gamma(3%, 3 mm)<1 criterion.
- No point from a block shall fail a 3D gamma(5%, 5 mm)<1 criterion.

The following accuracy requirements shall apply to the dose-averaged LET computation for comparison to a calculated reference dose-averaged LET (for 3D distributions):

- 90% of the computed dose-averaged LET values shall be within 3% of the reference level or of 2 mm (global gamma). Only voxels with a physical dose value above 10% of the max physical dose are considered
- 95% of the computed dose-averaged LET values shall be within 5% of the reference level or 2 mm (global gamma). Only voxels with a physical dose value above 10% of the max physical dose are considered
- 98% of the computed dose-averaged LET values shall be within 8% of the reference level or 2 mm (global gamma). Only voxels with a physical dose value above 10% of the max physical dose are considered

The reference dose-averaged LET level is 1500 MeV/cm for carbon ions and 500 MeV/cm for helium ions.

RBE dose

The following accuracy requirements applies to the computed RBE factors compared with 1D RBE factor curves. This applies to the LEM "classic" computation:

- The average relative deviation shall not exceed 2% before the fragment tail.
- The average relative deviation shall not exceed 10% in the fragment tail.

The following accuracy requirements apply to the computed RBE factors when comparing to a 3D reference calculation:

- 95% of the computed RBE factors shall be within 3% or 3 mm (global gamma). Only values where the corresponding dose is above 10% of the max RBE dose is considered
- 98% of the computed RBE factors shall be within 5% or 5 mm (global gamma). Only values where the corresponding dose is above 10% of the max RBE dose is considered.

The following accuracy requirements apply to the RBE-weighted dose computation for comparison to a calculated reference dose. For the total RBE-weighted dose distribution:

- 95% of the computed dose values shall be within 3% or 3 mm (global gamma). Only dose values above 10% of the max dose are considered.
- 98% of the computed dose values shall be within 5% or 5 mm (global gamma). Only dose values above 10% of the max dose are considered.

7.4.2 Algorithm limitations

Infinite slab approximation

The light ion dose calculation in RayStation is based on a pencil beam dose algorithm. The major limitation for this type of dose calculation is that lateral inhomogeneities for each of the ray traces are not accounted for, since each ray trace sees the patient as a stack of semi-infinite layers. An approximate correction for this imprecision is included in the RayStation light ion dose calculation.

However, the user shall be aware of the fact that the dose computations may not be fully accurate for patients with large lateral inhomogeneities relative to the beam direction.

WARNING!

Field size limitations for carbon ion PBS. The dose engine validation of RayStation covers field sizes between 3 x 3 cm^2 and 20 x 20 cm^2. Be extra careful when creating fields with field sizes that are smaller or larger than these field size limits.

(6483)

WARNING!

Field size limitations for helium ion PBS. The dose engine validation of RayStation covers field sizes between 3 x 3 cm^2 and 20 x 20 cm^2. Be extra careful when creating fields with field sizes that are smaller or larger than these field size limits.

(219201)

Particle energy spectra limitations

The particle energy spectra used in RayStation was generated from Monte Carlo simulations of light ions transported through a water phantom, see *section 7.2.2 Particle energy spectra on page 276*. Hence, there is no account taken to patient inhomogeneities or different fragment production cross sections in different materials. This also applies to beam limiting devices such as ripple filters and range shifters. The user should be aware of this limitation and its potential effect on RBE-weighted dose in heterogeneous regions, and primarily in materials largely different to water.

WARNING!

Limitations in RBE-weighted dose and dose-averaged LET computation. The primary and secondary particle energy spectra used in RBE-weighted dose and dose-averaged LET calculation were simulated in water. The user should be aware of this limitation and its potential effect on RBE-weighted dose and dose-averaged LET in heterogeneous regions, and primarily in materials that differ significantly from water.

(5133)

Range shifter air gaps

Carbon plans with range shifters and large airgaps have been successfully validated. For helium, discrepancies have been observed in plans with airgaps larger than 40 cm. This can lead to an underestimation of the lateral dose spread.

WARNING!

Absolute dose accuracy for helium ion PBS with range shifters. There are limitations to the modeling of the beam spread in the region between a range shifter and the patient, also called the air gap, in the analytical dose engine used for helium ion dose calculation in RayStation. The dose engine has been successfully validated for air gaps up to 40 cm, while for larger air gaps discrepancies have been observed, especially for small fields and/or thick range shifters. The user is therefore encouraged to be extra careful when using air gaps larger than 40 cm.

(219202)

7.5 INITIAL RBE COMPUTATION IN THE LOCAL EFFECT MODEL

This section describes the computation of the initial Relative Biological Effectiveness (RBE) values which is implemented according to the Local Effect Model (LEM) version 1 by Scholz et al. [81]. The initial RBE values are stored in 'RBE tables' that are pre-computed for each particle type and energy, and are used in the calculation of RBE-weighted dose (*section 7.10 RBE-weighted dose algorithms for LEM on page 308*).

Initial RBE

The initial RBE value for an ion of a given charge and energy is defined as:

$$RBE_{initial} = \frac{\alpha_Z}{\alpha_X} \qquad \text{[Eq. 185]}$$

where α_Z and α_X are the initial slopes of the cell survival curves as described by the linear-quadratic model for ion and photon irradiation, respectively, as described below. In RayStation, tables of initial RBE values are calculated for ions with charge Z=1 to 8, and energies in the range 0.1 to 1000 MeV/u using the Local Effect Model.

Because the linear energy transfer (LET) as a function of MeV/u is identical for all isotopes of an ion, the initial RBE need only be computed per ion (i.e., charge Z) and not isotope (mass number A).

7.5.1 Local Effect Model

The implementation of the Local Effect Model follows the definition in [81]. The underlying assumption is that the local biological effect of the deposited dose in a small subvolume of the cell nucleus is independent of the primary radiation type depositing that dose. The biological effect in an ion beam may thus be computed from cell survival data for photons together with track structure data (i.e., dose around the ion track or local dose).

General formulation

The general formulation of LEM is briefly outlined here following Scholz and Kraft, 2004 [82].

The particle trajectories resulting in lethal events after photon irradiation are randomly distributed among the individual cells of a population, and the lethal event distribution can therefore be described by a Poisson distribution with the average number of lethal events N_X. If the cell survival probability S_X is determined as the fraction of cells undergoing no lethal event, it can be calculated from N_X as:

$$S_X = e^{-\overline{N_x}}$$
$$\overline{N_X} = -\log S_X \qquad \text{[Eq. 186]}$$

where the subscript x denotes photon radiation.

Introducing a dose-dependent lethal event density, $\nu_x(d)$, gives:

$$\nu_X(d) = \frac{\overline{N_X}}{V_{nucleus}} = \frac{-\log S_X(d)}{V_{nucleus}} \qquad \text{[Eq. 187]}$$

where $V_{nucleus}$ is the cell nucleus volume.

Assuming that the spatial distribution of local dose (i.e., the expectation value of the energy deposited at a given point in the nucleus) is homogeneous for photon irradiation even down to nanometer volumes, the biological effect induced by ion irradiation in a subvolume (of the nucleus) can be derived from photon cell survival data obtained at macroscopic absorbed doses. Furthermore, assuming that the effect is independent of the radiation type for a given local dose, the biological effect induced by ion irradiation can be calculated by integrating the event density for the local ion dose distribution, $\nu_X[d(x,y,z)]$, over the cell nucleus volume, $V_{nucleus}$:

$$\overline{N_{ion}} = \int \nu_X[d(x,y,z)]dV \qquad \text{[Eq. 188]}$$

The biological effect (number of lethal events) $-\log S_{ion}$ in the cell nucleus induced by the local dose d is thus

$$-\log S_{ion} = \int \frac{-\log S_X[d(x,y,z)]}{V_{nucleus}} dV \qquad \text{[Eq. 189]}$$

Equation 189 is the most general formulation of LEM, i.e., that the biological effect is described by the photon cell survival and the distribution of (local) ion dose inside the cell nucleus. In order to apply this expression, the following must be described:

- photon cell survival
- local dose distribution
- volume of the cell nucleus

The cell nucleus volume is obtained from the nucleus radius, r_n, which in RayStation is defined by the user in the RBE Model Administration module in RayBiology.

Cell survival curve

The cell survival curve, describing the cell survival as a function of dose, is expressed in LEM by the linear-quadratic model with the assumption of a exponentially decreasing survival for local fraction doses greater than a threshold dose, D_t. The cell survival is related to the local fraction dose d as

$$-\log S_X(d) = \begin{cases} \alpha d + \beta d^2, & d < D_t \\ \alpha D_t + \beta D_t^2 + s_{max}(d - D_t), & d \geq D_t \end{cases} \qquad \text{[Eq. 190]}$$

where $s_{max} = \alpha + 2\beta D_t$ is the maximum slope of the cell survival curve.

Equation 190 can be used to describe the cell survival for both photon and ion irradiation, however with different parameter values for α and β.

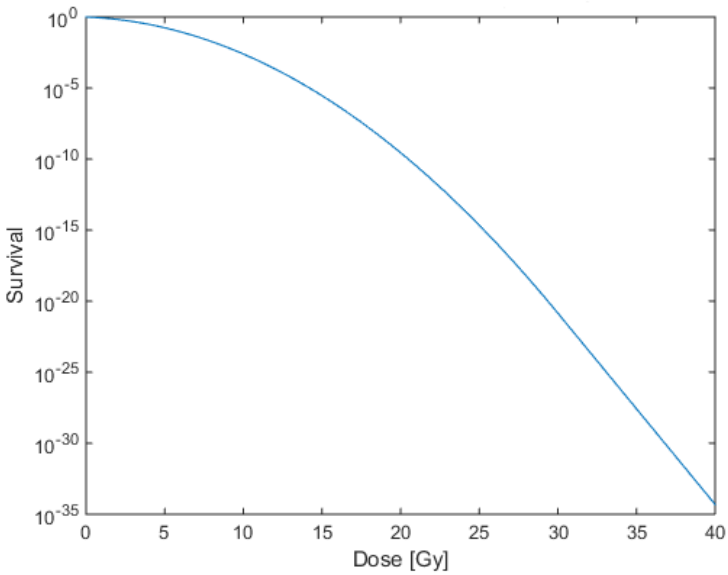

Figure 79. The photon cell survival curve with photon parameters $\alpha_X = 0.1\,\mathrm{Gy}^{-1}, \beta_X = 0.05\,\mathrm{Gy}^{-2}, \mathrm{D_t} = 30.0\,\mathrm{Gy}$.

The input parameters used in the calculation of photon cell survival curves are defined by the user in the RBE Model Administration module in RayBiology. These are:

Parameter name	Unit	Description
α_X	Gy^{-1}	Alpha value for photons.
β_X	Gy^{-2}	Beta value for photons.
D_t	Gy	Dose transition, the dose where the survival curve becomes exponential.

Local dose distribution

The dose around an ion track is approximated as constant up to the track core radius, r_c. At distances greater than r_c, the dose decreases proportionally to $1/r^2$ up to the maximum distance r_{max} after which the dose is assumed to be zero. The local dose at radial distance r from the particle track is

$$d(r) = \begin{cases} \dfrac{\lambda \cdot C \cdot LET}{r_c^2}, & r < r_c \\ \dfrac{\lambda \cdot C \cdot LET}{r^2}, & r_c \leq r \leq r_{max} \\ 0, & r > r_{max} \end{cases}$$ [Eq. 191]

where LET is the linear energy transfer given in keV/µm and C is a unit conversion factor. The normalization constant λ assures that the radial integral reproduces the (unrestricted) LET for a medium with unit density and is equal to:

$$\lambda = \frac{1}{2\pi \cdot (\ln \frac{r_{max}}{r_c} + \frac{1}{2})}$$ [Eq. 192]

The value of r_{max} depends on the particle energy, E (given in MeV/u), and is determined as $r_{max} = \gamma \cdot E^{\delta}$.

For energies below 2 MeV/u, in order to match experimental data better, the Kiefer low energy approximation [83] is applied:

$$r_{max} = 2 \cdot \frac{\gamma \cdot E^{\delta}}{E}$$ [Eq. 193]

An example of the energy dependence of r_{max} is illustrated in Figure 80.

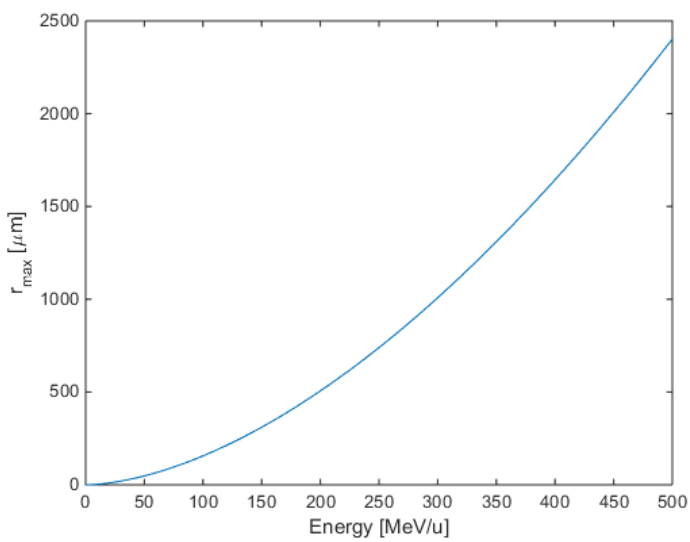

Figure 80. Maximal track radius r_{max} as a function of energy.

The input parameters used in the calculation of local dose around an ion track can be found in the RBE Model Administration module in RayBiology. These so called track dose parameters are:

Parameter name	Unit	Description
r_c	µm	Radius of the core of the ion track (minimum radius).
γ	$\mu\mathrm{m} \cdot \left(\frac{\mathrm{MeV}}{\mathrm{u}}\right)^{-\delta}$	A constant (prefactor) that is used to obtain the maximum radius of the track. Note that the unit of the prefactor is different when the Kiefer low-energy approximation is used (see below).
δ	-	A constant (exponent) that is used to obtain the maximum radius of the track.

7.5.2 Calculation of the initial slope of the cell survival curve

The cell survival after ion irradiation depends on the distance from the cell nucleus to the ion track (the impact parameter), and an integration of S_{ion} over all relevant impact parameters gives the expected cell survival. However, it has been shown to be sufficient to calculate the effect for a single ion traversal through the centre of the cell nucleus, i.e., for zero impact parameter [81]. By carrying out the integration in Equation 189 for this case, the biological effect induced by one ion traversal in the cell nucleus is obtained. The integration is performed up to r_{max} in order to take into account lethal events produced by the entire track, assuming that there are cell nuclei everywhere. Assuming further that all lethal events are produced inside the nucleus, dividing the number of lethal events with the nucleus volume gives the biological effect per cell nucleus and ion traversal. Now, the initial slope of the cell survival curve for ion irradiation, α_Z, is determined as the biological effect divided by the average dose deposited by a single ion traversal in the nucleus, $\overline{D}$:

$$\alpha_Z = \frac{-\log S_{ion}}{\overline{D}} \qquad \text{[Eq. 194]}$$

$\overline{D}$ is calculated from the linear energy transfer of the ion and is thus approximated from the energy deposition over the entire track. This is consistent with the integration in Equation 189 over the transversal profile of the entire track. From α_Z the initial RBE can then be calculated for each ion species and kinetic energy with Equation 185.

7.6 IMPORT OF INITIAL RBE TABLES FOR THE USER-DEFINED LOCAL EFFECT MODEL

As an alternative to the LEM-I calculation in RayStation (described in *section 7.5 Initial RBE computation in the Local Effect Model on page 295*), initial RBE tables can also be imported directly from external data files. This is also referred to as user-defined LEM model, and enables later versions of the LEM to be used for RBE dose computation. The tables can, for example, be based on the LEM-4 model [142].

The data format used for the input tables is given by the following example:

```
CellType Chordoma

Parameter Alpha_x 0.2
Parameter Beta_x 0.1
Parameter DoseTransition 30
Parameter NucleusRadius 5

Fragment H
0.10000000 30.95990558
0.10637648 30.95980750
0.11315957 30.95968249
0.12037517 30.95952474
0.12805087 30.95934004
... ...

Fragment He
0.10000000 30.96646613
0.10637648 30.96653803
0.11315957 30.96660292
0.12037517 30.96666144
0.12805087 30.96671208
0.13621602 30.96675484
0.14490181 30.96678846
0.15414146 30.96681551
0.16397026 30.96683339
0.17442580 30.96684315
... ...
```

Each file can only contain tables for one cell type. The parameters specified in this example are mandatory, and correspond to the LEM cell type parameters $\alpha_x(Gy^{-1}), \beta_x(Gy^{-2}), D_t(Gy)$ and $r_n(\mu m)$.

The fragments are specified by their chemical symbols (H, He, Li, Be, B, C, N, O), followed by the actual table data for that fragment. The first column specifies the fragment energy (MeV/u) and the second column the initial RBE (α_z/α_x).

To be used in the calculation of RBE-weighted dose, the RBE tables must satisfy basic technical requirements:

- One table should be given for each fragment present in the particle energy spectra. All fragments with Z below the primary particle must be included.
- The table must cover the full range of ion energy from 0.1 MeV/u to 1000 MeV/u, with strictly increasing values.
- The number of data points must be at least 150 per fragment, and the initial RBE for each point must be positive.

Note: *Only fragments present in the particle energy spectra will be included in the RBE dose computation, i.e., the set of imported RBE tables does not determine which fragments are included.*

In addition, it is recommended that the maximum error from linear interpolation between two near-lying points does not exceed 1.0%.

When RBE cell type parameters and initial RBE tables are imported to a user-defined LEM model, the user has the full responsibility to ensure the validity and clinical applicability of this data before the RBE model is commissioned. There is no validation of the imported data performed in RayStation.

7.7 THE (MODIFIED) MICRODOSIMETRIC KINETIC MODEL

RayStation supports RBE dose computation using the modified Microdosimetric Kinetic Model. The MKM was originally developed by Hawkins [127], [128], and is based on the theory of dual radiation action (TDRA) [129]. Its main assumption is that the cell survival fraction in sub-cellular volumes, referred to as domains, follows the linear-quadratic model when exposed to an energy deposition with specific energy z. It has since been modified w.r.t. the saturation of RBE due to overkill effects in high LET (or specific energy) areas [130], [131], thereby adding the "modified" prefix to MKM. Additionally, similar to the LEM, amorphous track structure models can be used to compute the biological effects for ion beams. In the case of the modified MKM, the Kiefer-Chatterjee track structure model [132], [133] is used for computing the radial ion dose distribution.

According to the modified MKM [131], the biological effect (number of lethal events) can be computed as

$$-\ln S = (\alpha_0 + \beta z_{1D}^*)D + \beta D^2 \qquad \text{[Eq. 195]}$$

where α_0 represents the initial slope of the survival curve at LET = 0, D is the absorbed dose and β is a constant independent of radiation type. z_{1D}^* represents the saturation-corrected, dose-weighted mean specific energy of the domain, delivered in a single event, as is given by

$$z_{1D}^* = \frac{\int_0^\infty z_{sat} z f_1(z) dz}{\int_0^\infty z f_1(z) dz} \qquad \text{[Eq. 196]}$$

where $f_1(z)$ is the probability density of z deposited by a single energy deposition event in the domain. z_{sat} represents the saturation-corrected specific energy

$$z_{sat} = \frac{z_0^2}{z}\left(1 - exp\left(-\frac{z^2}{z_0^2}\right)\right) \qquad \text{[Eq. 197]}$$

with the saturation coefficient

$$z_0 = \frac{(r_n/r_d)^2}{\sqrt{\beta\left(1 + (r_n/r_d)^2\right)}} \qquad \text{[Eq. 198]}$$

r_n and r_d are radii of the cell nucleus and the domain. Together with α_0 and β, they are parameters that must be specified per cell type in the RayStation MKM.

The saturation-corrected specific energy is given as a function of energy per particle species. Note that z^*_{1D} needs to be computed externally and imported into RayStation, see section *section 7.8 Import of tables for the user-defined MKM on page 304*.

7.8 IMPORT OF TABLES FOR THE USER-DEFINED MKM

In order to use the modified Microdosimetric Kinetic Model for RBE dose computation in RayStation, the saturation corrected, dose-weighted mean specific energy of the domain z_{1D}^{*} tables per particle species must be imported to a user-defined MKM model.

The data format used for the input tables is given by the following example:

```
CellType HSG

Parameter Alpha_0 0.172
Parameter Beta 0.0615
Parameter DomainRadius 0.32
Parameter NucleusRadius 3.9

Fragment H
1.00000E-01 2.97270E+01
1.03128E-01 2.96381E+01
1.06354E-01 2.95464E+01
1.09682E-01 2.94518E+01
1.13113E-01 2.93451E+01
... ...

Fragment He
1.00000E-01 2.20691E+01
1.03128E-01 2.20974E+01
1.06354E-01 2.21266E+01
1.09682E-01 2.21568E+01
1.13113E-01 2.21880E+01
1.16651E-01 2.22203E+01
... ...
```

Each file can only contain tables for one cell type. The parameters specified in this example are mandatory, and correspond to the MKM cell type parameters $\alpha_0(Gy^{-1})$, $\beta(Gy^{-2})$, $r_d(\mu m)$ and $r_n(\mu m)$.

The fragments are specified by their chemical symbols (H, He, Li, Be, B, C, N, O), followed by the actual table data for that fragment. The first column specifies the fragment energy (MeV/u) and the second column the z_{1D}^{*} values.

To be used in the calculation of RBE-weighted dose, the RBE tables must satisfy basic technical requirements:

- One table should be given for each fragment present in the particle energy spectra. All fragments with Z below the primary particle must be included.

Note: *Only fragments present in the particle energy spectra will be included in the RBE dose computation, i.e., the set of imported RBE tables does not determine which fragments are included.*

- The table must cover the full range of ion energy from 0.1 MeV/u to 1000 MeV/u, with strictly increasing values.
- The number of data points must be at least 150 per fragment, and the initial RBE for each point must be positive.

In addition, it is recommended that the maximum error from linear interpolation between two near-lying points does not exceed 1.0%.

When RBE cell type parameters and initial RBE tables are imported to a user-defined MKM model, the user has the full responsibility to ensure the validity and clinical applicability of this data before the RBE model is commissioned. There is no validation of the imported data performed in RayStation.

7.9 MKM DOSE COMPUTATION

This section describes the computation of RBE-weighted dose when using a modified Microdosimetric Kinetic Model, as formulated by Inaniwa et al. in [134].

In order to compute the biological effect of ions, $-\ln S$, the following is required:

- $\frac{dF(E_{beam},x,T,E)}{dE}$, the differential spectra of particles of type T and energy E at water equivalent depth x for incoming primary light ions of nominal beam energy E_{beam}
- $z^*_{1D}(T,E)$ given by the RBE model (see *section 7.7 The (modified) Microdosimetric Kinetic Model on page 302*)
- Reference radiation parameters α_r and β_r
- Reference survival fraction S_r (optional)
- Clinical RBE scaling factor F_{clin}

According to Equation 195, the biological effect is computed from the linear-quadratic model, where we have identified the linear term with:

$$\alpha_{MKM} = \alpha_0 + \beta z^*_{1D} \qquad \text{[Eq. 199]}$$

Similar to the LEM low dose approximation, dose-averages of α_{MKM} are computed in order to account for the contributions from both primary particles and fragments:

$$\overline{\alpha_{MKM}} = \frac{\Sigma_{T,E}\alpha_{MKM}(T,E)D(T,E)}{\Sigma_{T,E}D(T,E)} \qquad \text{[Eq. 200]}$$

where $D(T,E)$ is the dose contribution in the voxel from particle of type T and energy E. Note that this is equivalent to using the dose-average of z^*_{1D} (see eq. 8 in [134]), since α_0 and β are constants. The trichrome approximation (see *section 7.3.3 The trichrome approximation on page 288*) is used to account for the lateral variation of particle species (primary and fragments).

The biological effect, $-\ln S$, in the mixed field is computed from $\overline{\alpha_{MKM}}$ and β using Equation 195. The RBE-weighted dose, where the survival fraction is computed from the deposited dose in each voxel, is computed as:

$$D_{RBE} = \left(-\frac{\alpha_r}{2\beta_r} + \sqrt{\frac{-\ln S}{\beta_r} + \left(\frac{\alpha_r}{2\beta_r}\right)^2}\right) \qquad \text{[Eq. 201]}$$

In case of a fixed reference survival fraction, the RBE-weighted dose is instead computed as:

$$D_{RBE} = \frac{\left(-\frac{\alpha_r}{2\beta_r}+\sqrt{\frac{-\ln S_r}{\beta_r}+\left(\frac{\alpha_r}{2\beta_r}\right)^2}\right)}{\left(-\frac{\overline{\alpha_{MKM}}}{2\beta}+\sqrt{\frac{-\ln S_r}{2\beta}+\left(\frac{\overline{\alpha_{MKM}}}{2\beta}\right)^2}\right)} \sum_{T,E} D(T,E)$$ [Eq. 202]

The RBE is computed from D_{RBE}, the total absorbed dose from the particle energy spectra and the clinical scaling factor F_{clin} as:

$$RBE = \frac{D_{RBE}}{\Sigma_{T,E} D(T,E)} F_{clin}$$ [Eq. 203]

The RBE-weighted dose in RayStation is finally computed as the product of the physical dose, as computed by the pencil beam dose engine, and the RBE.

7.10 RBE-WEIGHTED DOSE ALGORITHMS FOR LEM

This section describes computation of RBE-weighted dose when using a Local Effect Model.

In order to calculate the biological effect of ions, -ln S (see Equation 190 for the linear quadratic formulation), the following is required:

- $\frac{dF(E_{beam},x,T,E)}{dE}$ the differential spectra of particles of type T and energy E at water equivalent depth x for incoming primary light ions of nominal beam energy E_{beam}.
- $\alpha(T,E)$ obtained from the corresponding initial RBE value given by the RBE model (see *section 7.5 Initial RBE computation in the Local Effect Model on page 295*).

From the biological effect -ln S, the RBE-weighted dose is calculated from the inverse of Equation 190, taking only positive roots into account. The RBE-weighted dose is the photon (x-ray) dose that would have to be delivered in order to achieve the same biological effect.

$$D_{RBE} = \begin{cases} \sqrt{-\ln S/\beta_X + (\alpha_X/2\beta_X)^2} - (\alpha_X/2\beta_X) & -\ln S \leq -\ln S_{cut} \\ (-\ln S + \ln S_{cut})/s_{max} + D_{cut} & -\ln S > -\ln S_{cut} \end{cases} \quad \text{[Eq. 204]}$$

The calculation of -ln S can be carried out in RayStation by either following the "Classic" approach [94] or by using the so called "Low-Dose" approximation [93]. While the classical approach includes random sampling of the number of particle traversals in a cell nucleus as well as sampling from the local particle spectrum to accumulate the induced damage, the low dose approximation assumes a single hit probability and the survival fraction is calculated for a single "average" particle traversal.

7.10.1 The LEM "Classic" algorithm

The calculation of -ln S for a mixed radiation field using the classical approach is described in [94]. The implementation in RayStation follows these steps:

1. Determine the particle energy spectra in voxel (see *section 7.1.8 Light ion pencil beam dose algorithm on page 272*). The lateral variation of the particle species (primary and fragments) is accounted for using the trichrome approximation (see *section 7.3.3 The trichrome approximation on page 288*).
2. Calculate the average number of hits per cell nucleus as

$$\overline{N}_{hit} = F(x)A_{nucl} \quad \text{[Eq. 205]}$$

where

$$F(x) = \int \frac{dF}{dE} dE \quad \text{[Eq. 206]}$$

is the total particle fluence at water equivalent depth x and A_{nucl} is the area of the cell nucleus.

3. Sample the actual number of hits per cell nucleus, N_{hit}, from a Poisson distribution with the expected value $\overline{N}_{hit}$.
4. Sample the particles responsible for these hits from the particle energy spectra $n = N_{hit}$ times. This gives n particles of different types and energies $(T_k, E_k; k = 1, ..., n)$.
5. Accumulate the absorbed dose D_{abs} and the effect -ln S induced by the particles sampled in step 4:

$$\begin{aligned} D^0_{abs} &= 0 \\ D^k_{abs} &= D^{k-1}_{abs} + \tfrac{dE}{dx}(T_k, E_k) \cdot c \qquad k = 1...n \\ -\ln S^0 &= 0 \\ -\ln S^k &= -\ln S^{k-1} + s_k \tfrac{dE}{dx}(T_k, E_k) \cdot c \qquad k = 1...n \end{aligned}$$

[Eq. 207]

$\frac{dE}{dx}(T_k, E_k)$ is the linear energy transfer (LET) and the factor c converts LET to dose. s_k is the slope of the damage curve for particle k and depends on the absorbed dose D_{abs}. It is determined from the initial slope α_Z (see section *section 7.5 Initial RBE computation in the Local Effect Model on page 295*), the maximum slope s_{max}, and the dose transition D_t as

$$s_k = \begin{cases} \alpha_Z(T_k, E_k) + (s_{max} - \alpha_Z(T_k, E_k)) \frac{D^{k-1}_{abs}}{D_t} & D^{k-1}_{abs} < D_t \\ s_{max} & D^{k-1}_{abs} \geq D_t \end{cases}$$

[Eq. 208]

Steps 3-5 are repeated a number of times, N_{rep}, that is specified by the user in the Dose computation settings dialog (refer to the *RSL-D-RS-2024A-USM, RayStation 2024A User Manual*). The average absorbed dose is calculated from the accumulated absorbed dose

$$\overline{D_{abs}} = \frac{\sum D_{abs}}{N_{rep}}$$

[Eq. 209]

The average effect $-\ln \overline{S}$ is computed as

$$-\ln \overline{S} = -\ln \left(\frac{\sum e^{lnS}}{N_{rep}} \right)$$

[Eq. 210]

The RBE-weighted dose corresponding to physical dose D_{abs} is determined from $-\ln \overline{S}$ with Equation 204 and the RBE factor is simply the ratio of D_{RBE} to $\overline{D_{abs}}$.

$$RBE = \frac{D_{RBE}}{D_{abs}}$$ [Eq. 211]

The RBE-weighted dose in RayStation is finally computed as the product of the physical dose, as computed by the pencil beam dose algorithm, and the RBE factor.

7.10.2 The LEM low dose approximation

The low dose approximation has been developed to improve the calculation speed of biological effects [93], since the sampling procedure described above for the classic approach can be time consuming. The low dose approach assumes a 1-hit probability and the surviving fraction is calculated for a single "average" particle traversal, so sampling over the particle spectrum is not performed. In RayStation, the user can choose between the two algorithms; however, only dose calculated with the classic algorithm is considered clinical. In this section, the low dose algorithm is briefly described. For more details, refer to Krämer and Scholz (2006) [93].

The usage of a 1-hit probability is motivated by the assumption that at low doses the number of particle traversals in the cell is small. Assuming a 1-hit probability, the following expression for the initial slope of the survival curve at macroscopic doses can be derived

$$\alpha_D(T,E) = \frac{1-e^{-\alpha_Z(T,E)d_1}}{d_1}$$ [Eq. 212]

$\alpha_Z(T,E)$ is the intrinsic LEM parameter for particle of type T and energy E, and d_1 is the dose from a single traversal of such a particle. d_1 is calculated from the particle's LET, the nucleus area A and a unit conversion coeffcient C:

$$d_1 = C\frac{\mathrm{LET}}{A}$$ [Eq. 213]

A corresponding macroscopic parameter $\beta_Z(T,E)$ is determined from $\alpha_Z(T,E)$ as described by Scholz et al. [97]

The corresponding $\beta_D(T,E)$ parameter of the survival curve at macroscopic doses is estimated by scaling

$$\beta_D(T,E) = \left(\frac{\alpha_D(T,E)}{\alpha_z(T,E)}\right)^2 \beta_z(T,E)$$ [Eq. 214]

In order to take into account the mixed radiation field and the contributions to the biological effect from both primary particles and fragments, dose-averages (denoted as $\overline{\alpha_D}$ and $\overline{\sqrt{\beta_D}}$) are computed for each voxel:

$$\overline{\alpha_D} = \frac{\sum_{T,E} \alpha_D(T,E) \cdot D(T,E)}{\sum_{T,E} D(T,E)} \quad \text{[Eq. 215]}$$

$$\overline{\sqrt{\beta_D}} = \frac{\sum_{T,E} \sqrt{\beta_D}(T,E) \cdot D(T,E)}{\sum_{T,E} D(T,E)} \quad \text{[Eq. 216]}$$

where $D(T,E)$ is the dose contribution in the voxel from particle of type T and energy E. The trichrome approximation (see *section 7.3.3 The trichrome approximation on page 288*) is used to account for the lateral variation of the particle species (primary and fragments).

The biological effect, -ln S, is calculated from $\overline{\alpha_D}$ and $\overline{\beta_D}$ with Equation 190, and the RBE-weighted dose is calculated according to Equation 204. The RBE is then calculated from D_{RBE} and the total absorbed dose from all particles in the voxel:

$$RBE = \frac{D_{RBE}}{\sum_{T,E} D(T,E)} \quad \text{[Eq. 217]}$$

The RBE-weighted dose in RayStation is finally computed as the product of the physical dose, as computed by the pencil beam dose algorithm, and the RBE.

7.11 RBE MODEL LIMITATIONS

7.11.1 General RBE Model limitations

WARNING!

Clinical practices related to RBE models. The user is expected to be well informed of the relevant clinical practices that relate to the models for predicting relative biological effectiveness (RBE) and to closely follow published literature on the subject. This includes awareness of the uncertainties involved and the difficulty in directly measuring RBE-weighted dose. (261621)

WARNING!

Comparison of RBE-weighted dose calculated with different RBE models. RayStation supports different approaches to the calculation of the RBE. While each approach gives an RBE-weighted dose (in units Gy(RBE)), it is important to note that the doses are not directly comparable in terms of absolute values, and any comparison of results using different RBE models must be done very carefully. (67927)

Particle energy spectra limitations

The generic particle energy spectra used in RayStation is based on Monte Carlo simulations of light ions transported through a water phantom, see *section 7.2.2 Particle energy spectra on page 276*. Hence, there is no account taken to patient inhomogeneities or different nuclear interaction cross sections in different materials. This also applies to beam limiting devices such as ripple filters and range shifters. The user should be aware of this limitation and its potential effect on RBE-weighted dose in heterogeneous regions, and primarily in materials largely different to water.

WARNING!

Limitations in RBE-weighted dose and dose-averaged LET computation. The primary and secondary particle energy spectra used in RBE-weighted dose and dose-averaged LET calculation were simulated in water. The user should be aware of this limitation and its potential effect on RBE-weighted dose and dose-averaged LET in heterogeneous regions, and primarily in materials that differ significantly from water. (5133)

WARNING!

Limitations in RBE-weighted dose and dose averaged LET computation. The prediction of RBE-weighted dose and dose averaged LET is dependent on the mixed radiation field at each position. In RayStation, this is quantified by simulated primary and secondary particle energy spectra. Differences and uncertainties in the particle energy spectra are propagated to the dose computation in addition to the inherent uncertainties of the biological model used to calculate the RBE.

The user should be aware of the sensitivity to the input particle energy spectra in the prediction of RBE-weighted dose and dose-averaged LET.

(2222)

WARNING!

Approximate lateral dependence of the mixed radiation field for RBE weighted dose and dose-averaged LET. The lateral fluence distribution of primary particles and fragments is computed using a trichrome approximation. The trichrome approximation makes use of the MCS and nuclear halo gaussians and associates them with different particle species to achieve realistic lateral distributions of the fluence of primaries and fragments. The approximation can cause significant errors in areas of the field where the distribution of primary particles and fragments is different to where there is a lateral equilibrium in the mixed radiation field, for example, outside of the field, within a small field, or at the edge of a larger field. Note that the effect is directly visible in the dose-averaged LET, but contributes only as a secondary effect for the RBE.

(408315)

User-defined RBE models

RayStation supports user defined RBE models, for which relevant data tables can be imported from file. There is no validation of the imported data tables. Invalid or inconsistent data will not be stopped from being used.

WARNING!

User-defined RBE models. When RBE cell type parameters and data tables are imported to a user-defined RBE model, the user has the full responsibility to ensure the validity and clinical applicability of this data before the RBE model is commissioned. There is no validation of the imported data performed in RayStation. (262079)

7.11.2 Local Effect Model limitations

The Local Effect Model (LEM-I) [97] , has been implemented for the computation of RBE-weighted dose in RayStation. The computation of initial RBE in RayStation has been validated against the original model data from articles as well as against source code from GSI. The computation of RBE-weighted dose for mixed radiation fields (considering the fragmentation that occurs when high energy ions traverse matter) has been validated against TRiP98 and, for carbon ions, against syngo. Note that the evaluation of the model itself is not within the scope of the RayStation validation. Some of the known limitations of LEM-I and the computation of RBE-weighted dose are described below.

WARNING!

Variations in RBE for different LET values using LEM-I. It has been observed that LEM-I tends to overestimate the RBE at low Linear Energy Transfer (LET) values, and underestimate the RBE at high LET. From a clinical point of view for the carbon modality, these trends go in the "right" direction in the sense that the actual effect in normal tissue located in the entrance channel should be lower than predicted by the model, whereas the effect in the tumor region should be higher than predicted. However, for the helium modality, these effects make LEM-I unsuitable for clinical use. The user should be aware of these effects.

(458)

WARNING!

Number of repetitions for LEM Classic. When calculating RBE-weighted dose according to the LEM model, it is required to use at least 1000 repetitions in the LEM Classic algorithm to obtain a clinical dose in RayStation. It should be noted that more than 1000 repetitions may be required to obtain sufficient statistical accuracy. The necessary number of repetitions is dependent on modality, model parameters and fragment spectra. It is the responsibility of the user to ensure that the statistical accuracy from the LEM Classic dose computation is sufficient.

(221247)

WARNING!

The s_{max} parameter of the Low Dose approximation. In the computation of RBE in the Low Dose approximation of LEM, the slope at the transition to exponential dose-effect relation at high doses is represented by the parameter s_{max}. This can either be taken to be the slope of the reference radiation curve or of the ion radiation curve. The RayStation implementation follows the latter choice, while other implementations, such as TRiP, follow the former. The effect of this difference in the approximation is in general very small and only relevant for high doses. Although the low-dose approximation cannot be used to calculate clinical dose, the user should be aware of this difference.

(221231)

Uncertainties for high fraction doses

In the LEM, the expression for photon cell survival is based on the linear-quadratic (LQ) model. The LQ model is widely used for estimating the effects of photon radiation at low and medium doses per fraction. However, due to the continuously bending survival curve of the model, as well as the lack of data at high doses, the LQ model may not be reliable at high fraction doses. In the LEM, the expression for photon cell survival is a modification of the LQ model in order to obtain an exponential curve for high doses. Still, due to the limited data available at high doses for evaluation, the LEM may be unreliable at high fraction doses [99].

WARNING!

Limitations in the LEM model for high doses. Due to the limited availability of experimental data for high fraction doses, the Local Effect Model (LEM) has not been comprehensively evaluated and the user should be aware that the model may be unreliable at high fraction doses. (261598)

Statistical uncertainties due to resampling

Due to the stochastic nature of particle traversal and the non-linear biological response relation, random sampling from the energy spectra of particles of type and energy at location for particles of initial energy is needed to obtain a set of particles of different type and energy [94]. The higher the number of samples, the lower the statistical uncertainty. The number of sampling repetitions can be chosen in the Dose Computation Settings. At least 1000 repetitions are required for clinical dose calculations. 1000 sampling repetitions is a value suitable for clinical use because it minimizes the statistical fluctuations while keeping computation time reasonable for planning purposes [94].

Model and parameter uncertainties

The LEM and its parameters are, as all mathematical models of biological effects, subject to uncertainties. Before clinical application of LEM-I, a thorough review of recent scientific findings reported in the literature should be conducted, as well as consulting carbon centers with relevant clinical experience of the model.

Scope of validation

Track dose parameters

The LEM-I model uses track dose parameters as input to the computation of the structure around a particle track. Note that only two sets of track dose parameters have been used in the validation of initial RBE tables. Original track dose parameters [100]:

- Track core radius = 0.01 µm
- Prefactor (γ) = 0.05 µm $(\text{MeV/u})^{-\delta}$
- Exponent (δ) = 1.7

Updated track dose parameters [101]:

- Track core radius = 0.01 µm
- Prefactor (γ) = 0.062 µm $(\text{MeV/u})^{-\delta+1}$
- Exponent (δ) = 1.7
- Kiefer low energy approximation

Although it is possible to choose different parameters as input to RayStation, this should be handled with care as it lies outside the bounds of the Local Effect Model. Only the original parameters have been used clinically on a regular basis.

WARNING!

Track dose parameter limitations for RBE using LEM-I. The RBE-weighted dose according to LEM-I has only been validated using the following track dose parameters:

- Track core radius = 0.01 µm
- Prefactor (γ) = 0.05 µm (MeV/u)$^{-\delta}$
- Exponent (δ) = 1.7
- No Kiefer low energy approximation

Although it is possible to choose different parameters as input to RayStation, this should be handled with extra care as it lies outside the bounds of the current clinical use of the Local Effect Model.

(459)

Cell type parameters

The model can also use different cell type parameters as input. Initial RBE tables for different cell type parameters have been published [93], [94] and is part of the validation for RayStation.

WARNING!

Cell type parameter limitations for RBE using LEM-I. The RBE-weighted dose according to LEM-I has been validated for the carbon modality using a range of cell types with varying radio sensitivity. The user is expected to closely follow published literature with regard to which cell type parameters are suitable for clinical use. The choice of parameters to be used for clinical purposes should be made based on an extensive evaluation of the safety and the clinical efficacy.

(457)

WARNING!

Cell type parameter limitations for RBE based on LEM-IV. The RBE-weighted dose according to LEM-IV has been validated for the helium modality using the following two sets of cell type parameters:

set 1

- $\alpha_x = 0.10\ Gy^{-1}$
- $\beta_x = 0.050\ Gy^{-2}$
- $D_t = 8.0\ Gy$
- $r_n = 5.0\ \mu m$

set 2

- $\alpha_x = 0.50\ Gy^{-1}$
- $\beta_x = 0.050\ Gy^{-2}$
- $D_t = 14\ Gy$
- $r_n = 5.0\ \mu m$

These parameters have never been used in clinical practice, and extensive evaluation of safety and clinical efficacy needs to be carried out before they are applied for clinical purposes.

Extra care should also be taken if using a different set of cell type parameters.

(219180)

RBE-weighted dose computation

Note that only the original track dose parameters and Chordoma cell type parameters, as specified above, have been used in the validation of RBE-weighted dose for mixed radiation fields in patient geometries.

7.11.3 Microdosimetric Kinetic Model limitations

The modified Microdosimetric Kinetic Model (MKM) [134], [131], has been implemented for the computation of RBE-weighted dose in RayStation. The computation of RBE-weighted dose according to MKM for mixed radiation fields (considering the fragmentation that occurs when high energy ions traverse matter) has been validated against iDose [134], [135], [136], [137]. Note that the evaluation of the model itself is not within the scope of the RayStation validation. Some of the known limitations of MKM and the computation of RBE-weighted dose are described below.

Model and parameter uncertainties

The MKM and its parameters are, as all mathematical models of biological effects, subject to uncertainties. Before clinical application of MKM, a thorough review of recent scientific findings reported in the literature should be conducted, as well as consulting carbon centers with relevant clinical experience of the model.

Scope of validation

RBE dose calculation parameters

The model uses a set of calculation parameters as input to the RBE-weighted dose calculation. The parameters include a clinical RBE scale factor, fixed survival fraction and alpha/beta values for a reference radiation. The user has the option to set these freely (only the clinical scale factor is mandatory). However, only a single set of parameters have been used in the RayStation validation for carbon ions [134]. For helium, no such validation has taken place.

WARNING!

Dose calculation parameter limitations for RBE using MKM. The RBE-weighted dose according to MKM has only been validated for the carbon ion modality using the following dose calculation parameters:

- Clinical scale factor = 2.41
- Reference radiation $\alpha_r = 0.764\ Gy^{-1}$
- Reference radiation $\beta_r = 0.0615\ Gy^{-2}$

Extra care should be taken if using plans for other modalities than the carbon ion modality.

Although it is possible to choose different parameters as input to RayStation, this should be handled with extra care as it lies outside the bounds of the validation scope.

(66531)

Cell type parameters

The model can use different cell type parameters as input. However, in the validation scope of RayStation, only a single set of parameters have been used. The validation has only been done for carbon plans, and not for helium plans. The parameters correspond to the HSG cell type [134].

WARNING!

Cell type parameter limitations for RBE using MKM. The RBE-weighted dose according to MKM has only been validated for a single cell type with fixed radio sensitivity using plans for the carbon ion modality. The following cell type parameters apply, i.e., HSG:

- $\alpha_0 = 0.1720\ Gy^{-1}$
- $\beta = 0.0615\ Gy^{-2}$
- $r_d = 0.32\ \mu m$
- $r_n = 3.9\ \mu m$

Extra care should be taken if using plans for other modalities than the carbon ion modality.

Although other cell type parameters can be imported to the model in RayStation, users should not apply this for clinical purposes until an extensive evaluation of the safety and the clinical efficacy has been carried out.

(66530)

RBE-weighted dose computation

Note that only a single set of RBE dose calculation parameters together with HSG cell type parameters have been used in the validation of RBE-weighted dose calculation with MKM. Details regarding the defined parameters can be found above.

7.12 OPTIMIZATION WITH LET FUNCTIONS

For information on optimization with LET functions, see *section 6.14 Optimization with LET functions on page 262*.

8 ION MACHINE ALGORITHMS

This chapter describes Ion machine algotithms in RayStation.

In this chapter

This chapter contains the following sections:

8.1	Automatic range shifter selection	p. 324
8.2	Automatic proton beam parameters using Treat and Protect	p. 325
8.3	MLC leaf positions for ion machines	p. 329
8.4	Spot handling for ion machines	p. 331

8.1 AUTOMATIC RANGE SHIFTER SELECTION

In RayStation it is possible to choose to automatically select the range shifter thickness for PBS and Line Scanning machines that use range shifters. If the automatic range shifter function is selected, the range shifter with optimal thickness will be chosen for the beam at Start optimization and then used in the optimization. The automatic selection ensures that both the proximal and distal target edge can be reached. For machines with discrete energy levels, the automatic range shifter selection also results in a range shifter thickness that gives the best match for the distal edge with respect to the available discrete energy levels.

The range shifter selection algorithm begins by finding the range shifters that make it possible to cover both the proximal and distal target depths. This set of possible range shifters can include the "None" alternative, that is a range shifter thickness of 0. If no possible range shifters are found (including "None"), an error message is given and the optimization is canceled. For machines with continuous energy levels, the thinnest range shifter among the set of possible range shifters is selected as the optimal one. For machines with discrete energy levels, the range shifter that also results in the best match for the distal target depth, given the available discrete energy levels, is selected. The depths of the energy levels are determined at 95% of the Bragg peak proximal depth.

8.2 AUTOMATIC PROTON BEAM PARAMETERS USING TREAT AND PROTECT

The passive proton beam parameters include the aperture contour, compensator, spread out Bragg peak (SOBP) range and width and snout position. These can automatically be computed in RayStation using the concept of Treat and Protect. For each beam the user can specify one or more Treat ROIs and optionally one or more Protect ROIs (protected either with the aperture or the compensator). The user also needs to specify the lateral, distal and proximal margins, density uncertainty and air gap. It is possible, but not necessary, to set the smearing radius and maximum gradient for the compensator, in which case the corresponding filters will be used in the automatic computation.

The beam parameters can be computed all at once (**Compute beam set parameters**), for the selected beam (**Compute beam parameters**) or one by one (**Conform block/MLC**, **Compute compensator**, and **Compute SOBP**). The following sections contain descriptions on how each component is computed.

In this section

This section contains the following sub-sections:

8.2.1	Aperture	p. 326
8.2.2	Compensator	p. 326
8.2.3	SOBP field	p. 327
8.2.4	Snout position	p. 328

8.2.1 Aperture

The beam can be collimated by either an aperture block or an MLC. The collimating device is described by a contour, defined at the isocentric plane, a virtual tray position and a source axis distance (which may be different in X and Y – IEC gantry coordinate system). The source axis distance is used to scale the contour to the actual position of the collimator and is exported in DICOM as (300A,030A) – Virtual Source-Axis Distance for machines that do not allow collimator rotation. For systems that do allow collimator rotation, the average value of the source axis distances are exported in DICOM.

The collimating contour is computed by projecting the union of all Treat ROIs onto the isocentric plane and adding an anisotropic (lateral) margin. The union of all projected block Protect ROIs, including the same margin, is then subtracted from first contour. For block apertures, the contour is expanded so that it is possible to manufacture using the specified milling tool diameter. A contour will not be computed if it does not fit within the inner snout opening or if the defined targets yield multiple block apertures.

The Beams Eye view in RayStation 2024A can only handle a single SAD_{vir} when projecting a snout mounted object to the isocenter plane, which has some consequences for how the aperture contour is visualized. This will introduce a small error in the visualization of the MLC leaf positions and block contour for systems where SAD_{vir} differs significantly in X and Y SAD_{vir}.

8.2.2 Compensator

The compensator is defined by a matrix of physical thickness values, the compensator milling tool diameter, a material, a virtual tray position, and a source axis distance (which may be different in X and Y – IEC gantry coordinate system). The positions of the thickness values are defined at the isocentric plane and correspond to the physical positions of the milling tool, as exported via DICOM. The milling pattern will be set as regular or hexagonal, according to how the machine was commissioned in RayPhysics. The source axis distance is the same as for the aperture described above. The compensator is setup so that the rectangular grid covers the block aperture including a margin of the maximum value of 0.5 cm and 2 times the compensator resolution. This implies that an aperture contour (created by block or MLC) must be defined in order to automatically compute the compensator.

The compensator is computed by ray tracing through the aperture contour and only compensator pixels inside the aperture contour will initially get a value. To avoid large discontinuities at the aperture edge, an extra margin is added outside the aperture, where the compensator pixels are extrapolated from the neighboring pixels. The margin is set to be at least 2 times the compensator resolution. Outside the margin the compensator pixels are set to the maximum thickness.

When a compensator is computed it is ensured that its thinnest point will correspond to the specified minimum thickness for the current beam. If the optimal compensator thickness is larger than the specified maximum thickness, its values will be truncated. Note that no warning will be given to the user, even if this results in a suboptimal compensator.

In order to take the beam spread into account, the compensator is computed on ROIs which are expanded perpendicular to the beam axis, the expansion distance being determined by the beam spread. The effect of this is that the lateral edges and any narrow extensions of the target ROIs will be fully covered by the dose, without resulting in an unnecessary overshoot. Note that this is not

the same as smearing the compensator, described in the next section. If any position on the compensator does not intersect the expanded target ROIs, its value will be extrapolated from neighboring pixels in the same way as for compensator pixels outside the aperture contour.

Smearing filter

The smearing of a compensator is performed after the Treat and Protect ROIs margins and density uncertainty have been taken into account. The main reason for smearing is to be robust against position uncertainties, ensuring that an undershoot will never occur if the position error is within the specified smearing radius. Note that this will result in an overshoot of the dose in the nominal case.

The smearing algorithm will set the thickness of each compensator pixel to the smallest thickness of all neighboring pixels whose center position fall within the smearing radius from the center of the current pixel. [76]

Maximum gradient filter

The maximum gradient filter will smooth any gradient in the compensator larger than the specified maximum gradient. The algorithm ensures that the gradient between any pair of compensator pixels does not exceed the maximum value while maintaining the minimum compensator thickness. To ensure target coverage at the distal end of the field, the thickness of compensator pixels is only reduced by the filtering. This handling may however result in overshoots and, for some cases, in under dosage at the proximal end of the target.

Note that the lack of target coverage may be addressed by clicking the **Compute beam SOBP** button after the smearing or maximum gradient filtering has been performed.

8.2.3 SOBP field

The SOBP range is computed as the largest radiological depth *section 6.4.2 Energy loss and radiological depth on page 182* to the distal edge of the target for all points within the collimating contour of the aperture. For each point, the distal edge of the target is defined as the radiological depth to the distal edge of all Treat ROIs, plus the distal target margin and density uncertainty, or the radiological depth of the proximal edge of all Protect ROIs, minus the distal protect margin and density uncertainty factor, whichever is smallest. Note that the radiological depth through the compensator will always be added to the SOBP range since this affects the actual range in the patient. This implies that a compensator must be defined in order to automatically compute the SOBP range and width.

The SOBP width (modulation) is computed as the SOBP range minus the smallest radiological distance to the proximal edge of all Treat ROIs, including the specified proximal treat margin and density uncertainty. This ensures that the whole target will be covered by the SOBP. The SOBP range is adjusted so that the 95% isodose exactly (disregarding beam spread) matches the distal target edge, including the defined margins and density uncertainty.

Density uncertainty

The distal treat and protect margins are specified in water equivalent thickness (cm water). The density uncertainty (%) will result in a scaling of the radiological distance to the distal and proximal edge of the Treat and Protect ROI:s respectively, where the scaling factors are computed as

Distal factor = (1 + density uncertainty / 100)

Proximal factor = (1 - density uncertainty / 100)

This will result in a margin dependent of the radiological depth in the patient, i.e. a larger margin for deeper points.

8.2.4 Snout position

When adding a new beam the snout position will automatically be set to its most retracted value. When Compute Beam Set Parameters, Compute Beam Parameters or Compute Compensator are used, the snout position will automatically be set so that the smallest distance between the most downstream device and the patient will correspond to the specified air gap. If the snout position falls outside of the defined limits, the system will revert to its previous state.

8.3 MLC LEAF POSITIONS FOR ION MACHINES

Ion treatment machines that are equipped with an MLC can be used to collimate fields for all proton delivery techniques in RayStation. It is also possible to use the MLC leaves as a secondary collimator for beams with block to avoid leakage in the outer area of the block used for mounting. Depending on how the machine is commissioned, the leaves can then either be positioned as a fixed opening (e.g. a 10x10 cm opening), or to form a rectangle around the block contour with certain margin, e.g. 2 cm defined on the downstream MLC physical plane. If the margin is used, the dimensions of the rectangle formed by the MLC is automatically updated whenever the block contour geometry is modified, either by the Treat and Protect functions, or manually. Leaves are closed according to default closed leaves position in the machine but can, for some cases be placed along the beam axis.

In RayStation, the MLC leaves are only taken into account by the proton dose engines if the MLC is regarded as collimating. The MLC leaves are regarded as non-collimating if the MLC leaves are in their most retracted position (outside the snout inner dimension) or if the MLC leaves are positioned outside a block opening. Any effect on the dose distribution from such MLC setups are not reflected in the dose computation. The dose difference between the computed plan and the delivered plan needs to be assessed by the user in the commissioning of RayStation as well as during patient-specific QA.

The smallest allowed margin for the MLC leaves to the snout inner dimension or block contour is 2 mm. If one of the MLC leaves would be positioned at a distance closer than 2 mm outside the snout inner dimension or block contour edge, or extend into the field, RayStation will detect this and stop dose calculation for that field. The safety margin is added since MLC leaves positioned outside the snout inner dimension or block contour edge will not be taken into account in the RayStation dose calculations.

In the RayStation proton dose engines, a collimating MLC is regarded as an aperture block with a jagged contour, i.e., actual leakage between adjacent leaves or closed leaf tips are not handled by the dose engines. The dose difference between the computed plan and the delivered plan needs to be assessed by the user in the commissioning of RayStation as well as during patient-specific QA.

In RayStation, the MLC leaf positions for an ion treatment machine are defined at the downstream physical plane of the MLC, and not at the isocenter (SAD_{vir}). In the DICOM export, the physical MLC leaf positions, x_{ph} , are projected to the isocenter plane position, x_{iso} , using the following formula:

$$x_{iso} = x_{ph} \times \frac{SAD_{vir}^{X}}{SAD_{vir}^{X} - d_{MLC}} \; ; \; y_{iso} = y_{ph} \times \frac{SAD_{vir}^{Y}}{SAD_{vir}^{Y} - d_{MLC}} \qquad \text{[Eq. 218]}$$

where SAD_{vir}^{X} , and SAD_{vir}^{Y} are the virtual source axis distances along the IEC Gantry X and Y directions, respectively, and d_{MLC} is the isocenter to MLC physical tray distance. In RayStation, only collimator angles of 0 are supported for light ion machines and Mevion Hyperscan. For machines that support a collimator angle different from zero the average value of SAD_{vir}^{X} and SAD_{vir}^{Y} is used as SAD_{virs} in Equation 218.

If the leaves are positioned in their most retracted position, the physical MLC leaf positions are moved inwards by 0.0001 cm in order to avoid the machine not being able to position the leaves after DICOM export due to floating point rounding issues.

8.4 SPOT HANDLING FOR ION MACHINES

This chapter describes spot selection for ion active scanning beams (Pencil Beam Scanning and Line Scanning) as well as spot sorting and spot filtering for ion Pencil Beam Scanning.

In this section

This section contains the following sub-sections:

8.4.1	Spot selection	p. 331
8.4.2	Spot selection for robust optimization	p. 332
8.4.3	Spot sorting and filtering	p. 333

8.4.1 Spot selection

As a prerequisite for optimization of ion active scanning beams (Spot Scanning and Line Scanning), energy layers and spots (or line segments) are selected and given an initial weight. The spot selection is based on the patient geometry and target optimization functions, machine constraints such as energy limits and maximum field size and beam computation settings maximum number of energy layers.

Initially the minimum and maximum radiological depth of the proximal and distal target union edges are computed respectively using the target union occupancy per voxel. If two or more target ROIs partially occupy a single voxel, the target union occupancy of the voxel will be the sum of the ROI occupancies, or at most 100%.

Note: *If the ROIs do not only occupy the same voxel but also overlap within this voxel, the target union occupancy is overestimated. This may affect where the target union edges fall within a voxel.*

The energy layers are chosen so that all Bragg peaks (as defined by the proximal 95% dose level) fall within the target union limits. The highest energy is computed to match the maximum radiological depth, while the remaining energies will depend on the energy spacing. By default, the distance between the energy layers are computed so that the Bragg peaks overlap at 80% of the max dose; however, this distance can also be scaled by a user defined factor, or set to a fixed water equivalent distance in cm. In addition, the user can specify a number of distal and proximal energy layers that will be added as margins. The user also has the option to specify a maximum number of energy layers. If this limit is exceeded, energy layers will be removed starting from the lowest energies.

The target union is then expanded perpendicularly to the beam direction by a distance of one average sigma in the Bragg peaks at the distal edge. The reason for this is to take into account the loss of dose due to lateral beam spread, making it necessary to have spots laterally outside the target region. The expansion distance can be scaled using a user-defined factor, or set to a fixed value in cm. Note that this expansion is performed on the dose grid resolution, and the actual expansion will often be to the nearest voxel size above the intended distance.

In the next step, Bragg peak positions and average beam sigma are computed on a high resolution grid for all available energy layers, and it is noted if the Bragg peak falls within the expanded target

union. Spots for each layer are placed in a hexagonal or square pattern, depending on the user's selection, with orientation based on the spot pattern angle specified in the machine. The angle shall be measured counter clockwise starting from the fixed gantry X1 axis in the IEC61217 system. By default, the spot distance is equal to 1.06 times the average projected sigma in the Bragg peak. If a square pattern is selected, the spots will be aligned so that there will always be a (potential) spot in the isocenter. As for the energy layer spacing, the spot distance can be scaled by a user-defined factor, or set to a fixed value in cm. All spots which fall within the projected region are kept and given an initial weight, as described below. Note that since the spot positions do not align perfectly with the grid pixels, the range may not exactly correspond with the intended target margins. This is especially true in regions with high gradients in density.

The initial spot weight distribution is computed to give a flat dose in the target union. For a set of spots lying on a line along the beam direction (i.e., having approximately the same x-y position), the relative weight, w, for a spot with energy E [MeV] and energy layer spacing δ [MeV] is given by ([102]):

$$w(E,\delta) = \left(E_{max}^2 - \left(E - \frac{\delta}{2}\right)^2\right)^{\mu} - \left(E_{max}^2 - \left(E + \frac{\delta}{2}\right)^2\right)^{\mu}, \quad E_{min} \leq E < E_{max}$$

$$w(E,\delta) = \left(E_{max}^2 - \left(E - \frac{\delta}{2}\right)^2\right)^{\mu}, \quad E = E_{max}$$

$$\mu = \left(0.43 - 0.05\frac{E_{max}}{E_p}\right) - 0.4\left(\frac{E_{max}}{E_p}\right)^2\left(1 - \frac{E}{E_{max}}\right)$$

The fitting parameter E_p is 240.0 MeV for protons, 500 MeV/u for helium ions and 1250 MeV/u for carbon ions. Spots within the proximal and distal margins are given an initial weight of zero.

Note that no spots will be added outside the inner snout dimension or the defined maximum field size of the machine. If an aperture block or MLC is used, the outer limit is defined by the block contour plus a margin of 1.4x sigma in air of the spot. For Mevion Hyperscan this margin is zero, that is, no spots are placed with their central axis outside the block contour. It is also ensured that the minimum range is given by the range shifter thickness, if present in the beam.

The spot selection can be modified by a minimum/maximum radiological depth override, an OAR range margin or a distal edge tracking technique. This is further described in the *RSL-D-RS-2024A-USM, RayStation 2024A User Manual*. For Line Scanning, line segment end points are chosen in the same way as spots in Spot Scanning.

8.4.2 Spot selection for robust optimization

If any target optimization function is defined as robust, the initial spot distribution will be expanded according to the robustness uncertainty settings in position, range and image. A lateral expansion is performed on the projected points on the ray trace grid per energy layer, so that all points which are within the position uncertainty will also be considered to fall within the target union. Additionally, positions in neighboring energy layers which are within the range uncertainty will also be included.

If multiple images are included in the optimization, a target projection is performed on each image. An expansion according to the position and range uncertainty is performed as described above, and finally the union of all projected points are taken over all images. Combined, this ensures that the initial spot distribution will have spots that cover the entire target, regardless of what image or robustness scenario is active. As a result, some spots may miss the patient or exit the patient before the Bragg peak in the nominal scenario.

8.4.3 Spot sorting and filtering

After a given number of iterations the spot pattern can optionally be post-processed with respect to scan pattern and/or spot metersets.

Spot sorting

Sorting spots to minimize the scan path is solved as a traveling salesperson problem. The method implemented in RayStation is based on the Lin-Kernighan-Helsgaun heuristic [79], 399. The distance between two scanning positions p and q is calculated using the distance function

$$d(p,q) = \sqrt{(w_x^2(p_x - q_x)^2 + w_y^2(p_y - q_y)^2}$$

where the weight for the x-direction is equal to 1 and y-direction is equal to the penalty factor for leaving the spot pattern angle. The formula is implemented by first rotating the coordinate system of the spot pattern with the spot pattern angle, such that the spot pattern is aligned with the x-direction in the formula.

Spot and energy layer filtering

Spots can optionally be filtered with respect to a minimum spot meterset limit and/or a minimum energy layer meterset limit after a given number of iterations.The weights of removed spots are added to the immediately following retained spot. Similarly, a maximum spot meterset limit can be applied. For subsequent iterations these limits are used as bounds for the remaining spots and/or energy layers. An optional margin can also be applied to the limits in order to allow some smaller modifications of the spot metersets after optimization without making the plan undeliverable (e.g., allow scale dose to primary prescription).

Minimum spot weight calculation for Mitsubishi Proton and Toshiba Carbon-Ion PBS

The Mitsubihi Proton and Toshiba Carbon-Ion PBS machines can not deliver plans where the dose from a spot is less than the spill dose delivered when scanning to that spot. The minimum deliverable relative weight w_i for spot i (corresponding to the spill dose delivered when scanning to that spot) in energy layer E is calculated according to:

$$w(E)_i = I(E) \times Max\left(Max(\frac{x_i}{v_{x(E)}}, \frac{y_i}{v_{y(E)}}) + t_c, t_r + t_c\right)/BeamMeterset \qquad \text{[Eq. 219]}$$

where $I(E)$ is the intensity of the number of particles or MU delivered per time unit, x_i (y_i) is the distance in x (y) between spot i and spot i-1, v_x (v_y) is the scan speed in the corresponding

direction (which may or may not depend on energy), t_c is the time taken to issue an instruction to start a scan from one spot to another indepent of scan distance, t_r is the minimum scan time taken to scan from one spot to another and $BeamMeterset$ is the total number of particles or MU delivered for the beam. The minimum relative weight w_0 for the first spot within an energy layer is given by:

$$w(E)_0 = I(E) \times (t_r + t_c)/BeamMeterset \qquad \text{[Eq. 220]}$$

The limit for the minimum deliverable weight for each spot is applied in addition to the filtering described in *Spot and energy layer filtering on page 333* after the given number of iterations. Also in this case the weights of removed spots are added to the immediately following retained spot.

Since the minimum deliverable spot weight is dependent on the scan length between two consecutive spots, the spots are sorted as described in *Spot sorting on page 333* before filtering. After filtering the remaining spots are sorted again. Spot weights that violate the minimum deliverable weight after the second sorting are adjusted so they are within limits.

For subsequent iterations the spot weight limits are used as bounds for the remaining spots.

Since the minimum deliverable spot weight is also dependent on scan direction, the filtering is applied for both directions when number of paintings are set to more than one.

Intensity calculation for Toshiba Carbon-Ion PBS

For Toshiba Carbon-Ion PBS machines, the beam intensity to be used in Equation 219 can either be set manually by the user or calculated automatically. The automatic intensity calculation option makes use of a procedure provided by the National Institute of Radiological Sciences (NIRS) in Chiba, Japan, in order to obtain the maximum intensity that maintains a flat dose in the target in the presence of a spill-dose. This maximum intensity, calculated independently for each beam in the plan, is given by the following expression:

$$I_{max} = \frac{f}{N_r}\frac{\Delta_x}{3}\frac{\Delta_z}{3}\Big((A_1 + A_2 d_p + A_3 d_p^2) + (B_1 + B_2 d_p + B_3 d_p^2)T_t + (C_1 + C_2 d_p + C_3 d_p^2)T_t^2 + (D_1 + D_2 d_p + D_3 d_p^2)T_t^3\Big) \qquad \text{[Eq. 221]}$$

The terms entering this calculation are defined as follows:

- N_r: Number of repaintings, as set by the user, per beam
- Δ_x: Average spot distance across all energy layers
- Δ_z: Average water-equivalent distance between energy layers, per beam
- A_i, B_i, C_i, D_i, f: Parameters of the calculation procedure, defined in the Machine Model
- T_t: Difference between the minimum and maximum target water equivalent depths in the direction of the beam

- d_p: Minimum dose of all min-dose optimization functions (min Dose, min DVH or uniform dose) of RBE-dose type, divided by the number of beams

The result, constrained to be within the intensity bounds specified in the Machine Model, corresponds to the intensity at a nominal beam energy of 350 MeV/u. For any other energy, E, the intensity is obtained by scaling this value by the corresponding stopping power (SP), according to the following:

$$I_m(E) = I_{max} \cdot SP(350MeV/u)/SP(E) \qquad \text{[Eq. 222]}$$

This is the value used in Equation 219. If the user chooses to manually enter an intensity value, rather than to have it calculated automatically, the same scaling to different energies is performed, with the manually entered intensity taking the place of I_{max}. In both cases, the resulting value $I_m(E)$ is used for the intensity in Equation 219, and for the calculation of the final irradiation intensity described below.

To determine the final intensity I_{irr} used for irradiation, one more step is performed to achieve an irradiation time for each energy layer that is as uniform as possible: The quantity $I_t = NP(n)/t_{irr}$ is calculated, where $NP(n)$ is the number of particles to be delivered to energy layer n according to the optimized plan, and t_{irr} is the irradiation time per slice. If respiratory motion synchronization with gating is used, the value of t_{irr} depends on the Respiratory Phase Gating Duty Cycle Values (G_1 and G_2) and the Respiratory Interval Time (R) entered by the user, according to the following relationship:

$$t_{irr} = \frac{G_2 - G_1}{100} \cdot R \cdot f_{gate} \qquad \text{[Eq. 223]}$$

where f_{gate} is a correction factor defined in the machine model definition. If gating is not used, a default value for t_{irr} is used, specified in the machine model definition.

The final irradiation intensity I_{irr} for each energy layer is then obtained from I_t, the SP-scaled intensity $I_m(E)$ from Equation 222, and the machine's lower bound on intensity for the given energy layer, $I_{lim_min}(E)$. As follows:

- If $I_t > I_m(E)$, then $I_{irr}(E) = I_m(E)$
- If $I_m(E) \geq I_t > I_{lim_min}(E)$, then $I_{irr}(E) = I_t$
- If $I_m(E) > I_{lim_min}(E) \geq I_t$, then $I_{irr}(E) = I_{lim_min}(E)$

When the plan is subsequently DICOM-exported, it is the irradiation intensities $I_{irr}(E)$ that will be exported per control point.

Note that since $I_{irr}(E)$ is only calculated after the optimization, the minimum spot weight calculation is performed for $I_m(E)$, not $I_{irr}(E)$. However, by construction $I_{irr}(E) \leq I_m(E)$, meaning that the

minimum spot weight will never be underestimated. It may, however, lead to a higher minimum spot weight than necessary, possibly resulting in a less optimal plan.

Further note that I_m will not be recalculated if the user selects to **Continue** optimization. On the other hand, the calculation of I_{irr} will always be performed at the end of each optimization. Hence, if the user manually edits the intensity of individual energy layers before clicking **Continue**, the modified values will be used for calculating I_{irr} at the end of the optimization (provided that the values are within the limits of the machine model). If, after optimization, changes have been made to the plan that would affect the calculation of I_{max} in Equation 221, it is advised to **Reset** and **re-Start** the optimization, rather than to press **Continue**, in order to repeat the I_{max} calculation.

Also note that if the "exclude beam" optimization option is used (refer to the *RSL-D-RS-2024A-USM, RayStation 2024A User Manual* section *Beam optimization settings*), the intensities are recommended to be set manually as there is no special treatment for excluded beams in the automatic intensity calculation.

9 ROBUST OPTIMIZATION

This chapter describes the basis for the robust optimization in RayStation.

In this chapter

This chapter contains the following sections:

9.1	Precautions	p. 338
9.2	Optimization formulation	p. 339
9.3	Scenarios	p. 343
9.4	Robust dose mimic	p. 345

9.1 PRECAUTIONS

WARNING!

Evaluate the dose after robust optimization. After a robust optimization has been performed, the user is strongly advised to evaluate the dose using Robust evaluation, Plan evaluation or the scripting functionality in RayStation to verify that the plan is robust with regards to all relevant uncertainties during delivery.

(10775)

WARNING!

Be aware how the different types of robustness affect the plan optimization. Different robustness types (systematic, interfraction, intrafraction) depend on different assumptions of underlying uncertainty and will result in different types of plans. The user needs to be aware of the effect of the robustness setting, and evaluate the plan with respect to the type of uncertainty it is set to be robust against.

Note that the integrated robustness evaluation tools in the Robust evaluation module only considers systematic uncertainties with the same uncertainty for all beams and isocenters. For plans optimized robustly with independent beams, independent isocenters, interfractional or intrafractional uncertainties, the user needs to assess the robustness through other means, for example by combinations of evaluation doses from the Plan evaluation module.

(283855)

9.2 OPTIMIZATION FORMULATION

9.2.1 Systematic errors

The basis for the robust optimization with respect to systematic errors in RayStation is minimax optimization [78], in which the optimization functions that have been selected to be robust are considered in the worst case scenario. The set of scenarios forms a discretization of the errors against which the plan should be robust. If patient setup errors, density errors, and patient image uncertainty are considered, each scenario determines a specific setup error, density error, and patient image.

The "worst case scenario" is the scenario in which a robust function attains its highest value. If several functions are selected to be robust, their weighted sum in the worst case scenario is considered. Minimax optimization of n functions $f_1, ..., f_n$ which are all required to be robust in the scenarios in the set S, and which have nonnegative importance weights $w_1, ..., w_n$, can be formulated as an optimization problem on the form

$$\min_{x \in X} \max_{s \in S} \sum_{i=1}^{n} w_i f_i(d(x;s)), \qquad \text{[Eq. 224]}$$

where X is the set of feasible variables (e.g., MLC leaf positions and segment weights for IMRT with photons or spot weights for IMPT), and $d(x;s)$ is the dose distribution as a function of the variables x and the scenario s. Functions considering only the nominal scenario, which corresponds to no error, can also be added to the objective. Moreover, nominal and robust constraints can be used in combination with formulation (Equation 224).

For the gradients of the robust optimization problem to be continuous, the maximum operator in the optimization problem (Equation 224) is approximated by the smooth power mean operator. The optimization problem that is solved by RayStation thus takes the form

$$\min_{x \in X} \left(\frac{1}{|S|} \sum_{s \in S} (\sum_{i=1}^{n} w_i f_i(d(x;s)))^p \right)^{1/p}, \qquad \text{[Eq. 225]}$$

in which the power p is set to 8.

9.2.2 Interfraction (random) uncertainty

When patient position uncertainty or organ motion uncertainty is selected to be handled as interfraction (random) uncertainty, RayStation will generate simulated treatment courses and perform the robust optimization taking these into account. A scenario is then defined as a possible realization of the treatment over the full treatment course. If there are n_f fractions, a scenario s can then be represented by a vector $(s_1, \ldots, s_{n_f})$, where s_i represents the patient position error and organ motion in fraction i for $i = 1, \ldots, n_f$. The number of fractions n_f is defined in the beam set.

The optimization is then performed on the average value of the objective functions over the simulated treatment courses, which means that the following optimization problem is solved:

$$\min_{x \in X} \frac{1}{|S|} \sum_{s \in S} \sum_{i=1}^{n} w_i f_i(d(x;s)) \qquad \text{[Eq. 226]}$$

where $d(x;s) = \sum_{i=1}^{n_f} d_f(x;s_i)$, in which $d_f(x;s_i)$ is the fraction dose (deformed to the planning image if necessary) under the realization s_i of the random variables.

Interfraction organ motion uncertainty requires deformations between the planning image and the included additional images.

When interfraction uncertainty is considered, the resulting plan may underdose the target or overdose the OARs in the nominal scenario, i.e., when no uncertainty is considered. To avoid this, robust functions applied to targets and OARS may be complemented with nominal functions applied to the same structures. For a target, a robust minimum dose function may thus be complemented by a nominal minimum dose function.

9.2.3 Intrafraction (e.g., breathing) organ motion

When the organ motion is selected to be handled as intrafraction organ motion, RayStation will generate scenarios in which all included patient images are included with equal weight. The optimization then solves the following problem:

$$\min_{x \in X} \sum_{i=1}^{n} w_i f_i(d(x)) \qquad \text{[Eq. 227]}$$

where $d(x)$ is the dose defined by $d(x) = \frac{1}{n_p} \sum_{i=1}^{n_p} d_i(x)$, in which n_p is the number of patient images and $d_i(x)$ is the dose to image i deformed to the planning image.

Intrafraction organ motion requires deformations between the planning image and the included additional images.

When intrafraction organ motion is considered, the resulting plan may underdose the target or overdose the OARs in the nominal scenario, i.e., when no organ motion is considered. To avoid this, robust functions applied to targets and OARS may be complemented with nominal functions applied to the same structures. For a target, a robust minimum dose function may thus be complemented by a nominal minimum dose function.

9.2.4 Combinations of systematic and interfraction errors

When there are simultaneously systematic errors and interfraction errors, the systematic errors are handled in the worst case and the interfraction errors are handled in the average case. This means that the following optimization problem is solved:

$$\min_{x \in X} \max_{s \in S} \frac{1}{|R_s|} \sum_{r \in R_s} \sum_{i=1}^{n} w_i f_i(d(x;r)) \qquad \text{[Eq. 228]}$$

Here, S is the set of systematic errors and R_s is the set of treatment course scenarios under the systematic error s. Hence, r in the above optimization problem can be represented by a vector $(r_1, \ldots, r_{n_f})$, where r_i represents the patient position error and organ motion in fraction i for $i = 1, \ldots, n_f$, which in turn depends on the systematic error scenario s. For example, if position uncertainty is handled as a systematic error and organ motion is handled as interfraction motion, then r_i corresponds to the systematic position error s in combination with a randomly selected patient image (which can differ in each fraction). The dose $d(x;r)$ is given by $d(x;r) = \sum_{i=1}^{n_f} d_f(x;r_i)$.

The approximation described in Equation 225 is used for the maximum over the systematic error scenarios.

This type of optimization is described by Fredriksson [Fredriksson, A. A characterization of robust radiation therapy treatment planning methods—from expected value to worst case optimization, Medical Physics 39(8): 5169–5181, 2012].

9.2.5 Combinations of systematic errors and intrafraction organ motion

When there are simultaneously systematic errors and intrafraction organ motion, the systematic errors are handle din the worst case and the interfraction organ motion is handled by the inclusion of all patient images equally weighted in each systematic error scenario. The following optimization problem is solved:

$$min_{x \in X} \max_{s \in S} \sum_{i=1}^{n} w_i f_i(d(x;s)) \qquad \text{[Eq. 229]}$$

where S is the set of systematic error scenarios and $d(x;s) = \frac{1}{n_p} \sum_{i=1}^{n_p} d_i(x;s)$, in which n_p is the number of patient images and $d_i(x;s)$ is the dose to image i under systematic error s deformed to the planning image.

The approximation described in Equation 225 is used for the maximum over the systematic error scenarios.

9.2.6 Combinations of interfraction uncertainty and intrafraction organ motion

When interfraction uncertainty is used in combination with intrafraction organ motion, the interfraction errors are handled in the average case, and the intrafraction organ motion is handled by the inclusion of all patient images equally weighted in each random error scenario. The optimization problem is formulated according to:

$$\min_{x \in X} \frac{1}{|S|} \sum_{i=1}^{n} w_i f_i(d(x;s)) \qquad \text{[Eq. 230]}$$

where S is the set of random error scenarios and

$d(x;s) = \sum_{i=1}^{n_f} d_f(x;s_i)$, in which $d_f(x;s_i)$ is the fraction dose under the realization s_i of the random variables, which is calculated from the intrafraction organ motion according to

$d_f(x;s_i) = \frac{1}{n_p} \sum_{j=1}^{n_p} d_j(x;s_i)$, in which n_p is the number of patient images and $d_j(x;s_i)$ is the dose to image i under random error s_i deformed to the planning image.

9.2.7 Treatment course scenario dose calculation

The dose of a treatment course scenario is the sum of the fraction doses. Since interfraction errors are considered, the fraction doses will generally be different from each other. For accumulation of the fraction doses to be possible, the fraction doses must be on the same patient image. For a simulated treatment course where in each fraction only the patient position differs, the doses are on the same image and can be directly summed. For a simulated treatment course where the patient image is different in different fractions, the doses need to be deformed to the same image before the dose accumulation.

9.3 SCENARIOS

The scenarios are combinations of setup error scenarios, density error scenarios, and patient image scenarios. If n_s setup error scenarios, n_d density error scenarios, and n_i patient image scenarios are considered, then the total number of scenarios considered by the robust optimization is $n_s n_d n_i$.

9.3.1 Setup error scenarios

If the patient position uncertainties specified in the Robustness Settings dialog are denoted by the nonnegative numbers $u_1, ..., u_6$ (for the directions left, right, inferior, superior, posterior, and anterior), the setup error scenarios are determined in the following way:

- The nominal setup error scenario, corresponding to no setup error, is always included.
- Setup error scenarios shifted the distance u_i cm, for $i = 1, ..., 6$ from the nominal patient position in the direction corresponding to i are included. The number m of intermediate setup error scenarios, between the nominal setup error and that of distance u_i cm, is determined by $m = \left\lfloor \frac{u_i}{0.75+\epsilon} \right\rfloor$, where $\epsilon > 0$ is small.
- If the setup errors in the directions (±1,±1,±1), which are computed as lying on ellipsoids with radii determined by $u_1, ..., u_6$, are strictly larger than 0.5 cm, then these setup error scenarios are included. For each additional 0.75 cm, an intermediate setup error scenario is added.
- If the setup errors in the directions (0,±1,±φ),(±1,±φ,0),(±φ,0,±1) where $\varphi = \frac{(1+\sqrt{5})}{2}$ is the golden ratio, which are computed as lying on ellipsoids with radii determined by $u_1, ..., u_6$, are strictly larger than 1 cm, then these setup error scenarios are included. For each additional 0.75 cm, an intermediate setup error scenario is added.

When independent beams or independent isocenters are used, all combinations of setup error scenarios for the different beams (isocenters) are included, leading to n_s^b setup error scenarios, where b is the number of beams (isocenters). The number of dose and gradient computations are $n_s n_d$ for the independent as well as for the dependent case, but the total number of scenarios is $n_s^b n_d$ for independent beams (isocenters). The exponential dependency on the number of independent beams or isocenters can lead to a large number of scenarios. Because the optimization functions are evaluated under each scenario, this can lead to long optimization times. The numbers of scenarios can be reduced considerably by considering independent beams (isocenters) only in specific directions, in which case the uncertainties are treated as universal in the other directions.

Note: *Setup errors are modeled as displacements of the isocenter. This means that any Fixation, Support or Bolus ROIs will move with the patient.*

9.3.2 Density error scenarios

The number n_d of density error scenarios is given by $n_d = 1 + 2\left\lfloor 1 + \frac{r}{5+\epsilon} \right\rfloor$ if $r > 0$ and 1 otherwise, where the nonnegative number r is the density uncertainty in percent. These scenarios are evenly spaced in the interval $[-r, r]$.

The density uncertainty is modeled by scaling the mass density of the patient and is universal for all beams.

Note: *Density scaling is applied equally to the patient and the support structures. This means that the density of any Fixation or Support ROIs will be scaled together with the patient. Density scaling also applies to ROIs with material override.*

Note: *Density uncertainty is supported only for protons and light ions.*

9.3.3 Patient image scenarios

The n_i patient image scenarios are selected from the list of available patient images for which the frame of reference is the same as that of the planning image, or for which there exists a rigid registration to the planning image.

9.3.4 Scenario dose computation

In order to evaluate robust optimization functions, a dose must be computed on each robustness scenario. If the **Accurate scenario doses** option is selected, this is done by explicitly computing each scenario dose with the selected dose engine. While being more accurate, the computation time before optimization will increase linearly with the number of scenarios.

If the **Accurate scenario doses** option is not selected, they will be computed by means of interpolation. The dose of a perturbed spot, represented by a shifted position, will be computed by linear interpolation of the neighboring spots. In addition, the perturbation in density results in an interpolation from neighboring spots with higher and lower energy.

In order to minimize the interpolation error, auxiliary spot doses are computed in areas (in position and range) where there are perturbed spots, but no neighboring nominal spots. They are temporary and will not be part of the final plan.

Note that no interpolation is possible between other images that are included in the optimization (i.e. 4D optimization), however all robustness scenario doses (resulting from position and range uncertainty) for a particular image can be interpolated.

Due to the non-linearity of the RBE models, it is not possible to compute interpolated spot doses for carbon ions, and accurate scenario doses are required. This is also true for proton plans using a block or multi-layer aperture, since the aperture edge scatter will affect the dose in a way that is not applicable to perturbed spot doses, since they do not have the same relative position to the aperture edge.

9.4 ROBUST DOSE MIMIC

Several types of reference functions are supported in RayStation. These functions generally base their penalties on a reference dose distribution rather than a dose level. Where a standard Min Dose function penalizes voxels whose dose is below the given dose level, a Min Dose reference function penalizes voxels whose dose is below its dose in the reference dose distribution. This allows for setting up an optimization problem that tries to mimic a given dose distribution.

A subset of the reference functions is supported as robust. During robust optimization, the reference dose will be assumed to be the same for all scenarios, meaning that each scenario dose will be directly compared with the same reference dose. No deformation of the reference dose will be done to take into account ,e.g., organ motion.

10 VOLUME HANDLING

This chapter describes the algorithms used in RayStation for visualization of region of interests (ROI) in 2D and 3D. It also describes the algorithms used to convert user-defined or imported ROIs to dose grid ROIs. It also describes how the slice indicator is visualized in the BEV/DRR views.

In this chapter

This chapter contains the following sections:

10.1	Algorithms for visualization of ROIs	p. 348
10.2	Algorithms for representing ROIs in the dose grid	p. 355
10.3	Slice indicator gadget in BEV/DRR	p. 358

10.1 ALGORITHMS FOR VISUALIZATION OF ROIS

10.1.1 General information

When visualizing ROIs, conversions between ROI shapes have to be performed. In RayStation 2024A, a 2D visualization is always the shape of a contour, and a 3D visualization is always the shape of a triangle mesh. Since the ROI being visualized can be of any of the shapes contour set, voxel ROI or triangle mesh conversions between the different ROI shapes have to be performed for visualization. The conversions between shapes used for visualization are shown in Figure 81.

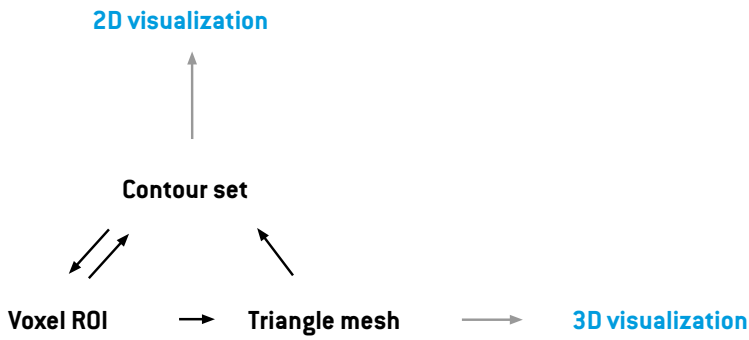

Figure 81. The conversions used for visualization in RayStation 2024A.

In RayStation 2024A, ROIs can be of three different shapes:

- contour set
- voxel ROI
- triangle mesh

Contour sets

A contour set is a set of contours where each contour is defined as a sequence of points all lying in the same plane.

A contour set is either created using various contouring tools, e.g. brush, polygon, spline, freehand, smart contour, or imported. In RayStation 2024A all contours that could be imported must lie in a plane that corresponds to a slice of the image stack. Reconstructed contours in sagittal or coronal planes are also used when visualizing ROIs in 2D. It is also possible to draw contours in sagittal and coronal slices. In that case the entire contour set is converted to contours in that direction. Voxel volumes can be reconstructed from sagittal or coronal contours in the same manner as for transversal contours.

Voxel ROIs

A voxel ROI is defined by its corner (a point given in patient coordinates), resolution, size, and an array of voxel values. Voxel ROIs in RayStation 2024A use relative volumes.

Voxel ROIs are typically generated with the margin tools (expansion and contraction). Gray-level thresholding operations also generates voxel ROIs.

Triangle meshes

Triangle meshes are defined as a set of triplets of vertices given in patient coordinates. The geometrical shapes of ROIs created with model based segmentation and atlas based segmentation are triangle meshes. Triangle meshes are also used for 3D visualization of structures and when modifying structures with 3D interaction tools.

Primary shape and reconstructed shapes

An ROI geometry in RayStation 2024A has a primary shape, which may be either contour set, voxel ROI or triangle mesh. Which primary shape the ROI geometry has depends on the last operation performed on it. Different operations are performed on different shapes and hence the geometry has to be converted to a new primary shape to be able to perform the operation. For example, when applying margins to an ROI geometry that has contour set as primary shape, the primary shape is converted to voxels. Manual drawing operations in 2D will convert the primary shape to a contour set and manual operations in 3D will convert the primary shape to a triangle mesh.

In RayStation 2024A there is also the concept of reconstructed shapes. These shapes are not saved when saving the case, but generated when needed and then reused as long as the case is open. This implies that an ROI has a primary shape may also have reconstructed shapes of the other shape types. This is used in visualization, so that the primary shape does not have to be changed when visualizing the ROI.

ROI volume

In RayStation 2024A, the volume of an ROI is always calculated from its voxel ROI shape. Thus, if the primary shape of an ROI is contour set or triangle mesh the voxel ROI reconstructed shape is used when retrieving the volume of the ROI.

Note: *Volume is not well defined for non-closed surfaces and therefore will not be calculated for open triangle mesh ROIs.*

10.1.2 Input

The algorithms needs the following input communicated according to the DICOM standard [47]:

- A patient or phantom description, normally CT images (optionally cone beam CT, MR or PET).
- Regions of interest (ROIs).
- The type of visualization, i.e. 2D or 3D.
- For 2D visualization the plane, in which to visualize the ROIs, is required.

10.1.3 Output

For 2D visualization the output is 2D contours in the stated plane. Most commonly the planes of visualization are the transversal, sagittal and coronal planes.

For 3D visualization the output is triangle meshes.

10.1.4 Description

When visualizing ROIs the reconstructed shape needed for the visualization is generated as a reconstructed shape.

Converting voxel ROIs to contour sets

To visualize voxel ROIs in 2D they are converted to contours. This is performed using Marching squares [48].

The primary shape for a voxel ROI is converted to a contour set using the same algorithm when performing 2D operations e.g. rotating or scaling the 2D object, or when using the manual drawing tools.

The contours will be created as isocontours at an approximated 50% level of the surface voxels of the voxel ROI in the contour plane. An example of the points generated at the surface voxels is shown in Figure 82.

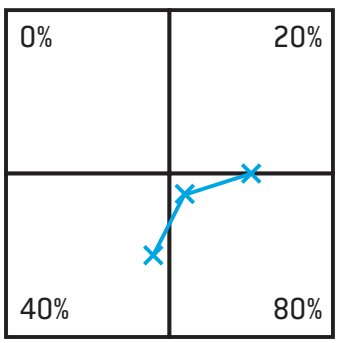

Figure 82. The blue crosses are the contour points generated from the surface voxels having the relative volumes according to the percentages in the image.

Note: *When converting from voxel ROIs to contours the geometry between the contours (i.e., image slices) will be lost. Thus small structures between slices may be lost. Also, due to the loss of information between slices, the conversion from voxel ROI to contour set may affect the volume of the ROI.*

As mentioned in *Converting contour sets to voxel ROIs on page 352*, hats are added when converting from contour sets to voxel ROI. Depending on how the original voxel ROI looked between the slices, the volume might increase or decrease when converting from voxel ROI to contour set. Figure 83 and Figure 84 show scenarios where the volume of the ROI increase and decrease when converting from voxel ROI to contour set.

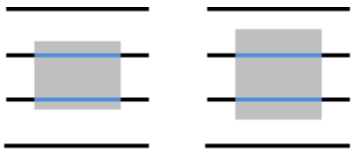

Figure 83. The gray rectangles are voxel ROI, the black lines are slices and the blue lines are the contours generated when converting to contour ROI. The left image shows the original voxel ROI and the right image shows the reconstructed voxel ROI used for volume calculation of the contour set. The volume of the reconstructed voxel ROI is greater than that of the original voxel ROI.

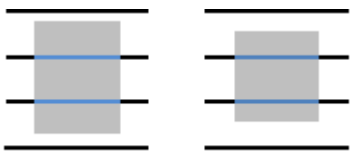

Figure 84. The gray rectangles are voxel ROI, the black lines are slices and the blue lines are the contours generated when converting to contour ROI. The left image shows the original voxel ROI and the right image shows the reconstructed voxel ROI used for volume calculation of the contour set. The volume in the reconstructed voxel ROI is smaller than that of the original voxel ROI.

Converting triangle meshes to contour sets

When visualizing triangle meshes in 2D they are converted to contours. This is done by computing the intersection between the selected plane and the triangles, and then connecting the intersections into closed contours.

Note: *If an ROI is represented as an open triangle mesh, it will be visualized in 2D with open contours on slices intersecting with mesh openings. An open triangle mesh can never be converted to contour sets.*

Note: *When converting from triangle meshes to contours the geometry between the contours (i.e. image slices) will be lost. The contours will be the true intersections of the triangles and the plane so no information will be lost in the plane.*

Converting voxel ROIs to triangle meshes

Voxel ROIs are converted to triangle meshes when visualizing them in 3D. The triangulation algorithm used will create more and smaller triangles on the high curvature parts of the objects, and fewer and larger triangles on the flatter parts.

The same conversion is performed on the primary shape of an ROI when performing 3D operations, e.g. rotating or deforming the 3D object.

Note: *As triangulation is a time-consuming task RayStation 2024A performs the triangulation of ROIs multi-threaded. This implies that all 3D renderings of ROIs may not display at the same time.*

An alternative algorithm when converting voxel ROIs to triangle meshes is Marching Cubes [48]. Marching cubes is faster, but the surfaces of the resulting meshes are not as smooth.

Converting contour sets to triangle meshes

This conversion is made when rendering contour sets in 3D. This is not a direct conversion but the contour set are first converted to a voxel ROIs and then converted to triangle meshes.

The conversion from contour sets to voxel ROIs is explained in *Converting contour sets to voxel ROIs on page 352*, and the conversion voxel ROIs to triangle meshes was described in *Converting voxel ROIs to triangle meshes on page 351*.

The triangulation of contour sets does not guarantee that the triangle meshes match the original contours exactly. This is a consequence of making the intermediate conversion to voxel ROIs.

Note: *The triangle mesh representation of the patient outline geometry is used for computing physical depth and SSD. There are many factors contributing to the uncertainty in this computation, the actual position of the contours being the primary one. If we assume ideal outline contours, the uncertainty comes from discretization effects in the voxelization and triangulation. Both algorithms work with sub-pixel resolution and the maximum error is less than half a voxel. For SSD and physical depth, the worst case would be the sum of these errors which is less than one voxel. A typical patient outline is discretized on a grid with a voxel size of 1-2 mm^3.*

There are algorithms for creating triangle meshes directly from contours without creating an intermediate voxel ROI. However, this is not implemented in RayStation 2024A and the main reasons for this are that when creating reconstructed contours it is probably faster to create a voxel ROI than to create a triangle mesh, and the reconstructed voxel ROI is often needed for other tasks, e.g. to be able to compute the volume of the ROI.

Converting contour sets to voxel ROIs

To convert contour sets to voxel ROIs shape-based interpolation [49] is used. The algorithm for shape-based interpolation is originally used to convert contour sets to binary voxel ROIs hence, in RayStation 2024A, adaptations have been made to the algorithm to be able to support voxel ROIs with relative volumes.

The algorithm for shape-based interpolation must have input regarding properties of the resulting voxel ROI grid:

- Voxel size: The default voxel size for contour voxelization is selected to be (1) as close as possible to 0.5^3 mm^3 and (2) a fraction 1/(2k) (k>=1) of the slice distance (in the reconstruction direction). If this voxel size would result in an object having more than 300^3 voxels (~25 MB), a larger voxel size is calculated (still fulfilling (2) if possible). The voxel size upper limit is 2.5^3 mm^3 and the lower limit is 0.1^3 mm^3.
- The number of voxels in each direction, i.e. the size of the bounding box of the contours, plus a margin of 3.5 voxels
- Corner, i.e. the corner of the bounding box of the contours, plus the margin of 3.5 voxels

The aim is to define a grid that satisfies the Nyquist sampling criterion and produces a well-aligned reconstruction where the ROI "hats" (see description below) are located exactly on the slice boundaries. The extra 0.5 voxel in the margin is used for aligning the grid voxel centers with the contours.

The algorithm consists of the following major steps:

1. The contours are binarized to the selected resolution.
2. The binary contours are filled using a seed fill algorithm.
3. For all pixels that are intersected by the contours, the area fraction within the contour is computed and the pixel gets a value corresponding to this area fraction. Pixels inside gets 100% and pixels outside gets 0%.*
4. A signed distance transform is computed. The original algorithm uses binary input, but we have used the Fast marching distance transform [50] using relative values as input.*
5. A linear interpolation between each pixel and the corresponding pixel on the next slice is performed to get values for the voxels in between the slices.
6. For all contours that do not have an overlapping contour on the slice above or below, a “hat” will be added. This hat reaches half-way to the next slice and has somewhat rounded edges.

* Steps modified from the original algorithm in order to get relative volumes.

The algorithm will make sure, for all voxels that covers the plane of a contour, that if the voxel that has a relative volume > 0% and < 100% then the contour is touching the voxel, i.e. the distance from the center of the voxel to the contour is ≤ the length of the voxel side/√2.

Conversion from contour representation to voxel representation is performed implicitly for use in computations (ROI algebra with expansion/contraction) and visualization (non-transversal reconstructions). It is also performed explicitly when using tools such as keep/delete component in the Structure Definition module.

Note: *The quality of the resulting voxel representation depends on the input contour set and the resolution of the reconstruction grid. If the contour set contains irregularities, e.g., contours on neighboring slices that differ very much from each other, the algorithm may produce a result that does not capture the original contour set completely. In general, when performing a contours-voxels-contours roundtrip, the difference compared to the original contours is less than the size of a reconstruction grid voxel.*

When converting from contour sets to voxel ROIs a new representation of the geometry is generated that might differ somewhat from the original. How much it will differ depends mainly on the resolution. When reconstructing contours that have been converted to voxel ROIs the difference compared to the original contour is always less than one voxel. Note that it is impossible to know what the real data would look like in between the CT slices, so the resolution and quality of the input image is of course very important.

To be able to perform ROI algebra on two voxel ROIs they must be in the same grid, hence the ROI in the voxel ROI in the grid with the higher resolution is resampled to the grid with the lower resolution before performing the ROI algebra.

Image set slice spacing and extrapolation of contours

In RayStation, the 3D reconstruction of an ROI from contours assumes that the first and last contours extend half a slice distance. The first and last contours of an ROI are therefore extrapolated half a slice distance from the outermost drawn contours. Note that there is no limit for this extrapolation, it is always half a slice distance. For typical image sets with a slice distance of about 2-3 mm this means that RayStation extrapolates 1-1.5 mm, but in an image set with wide slice spacing, this extrapolation may lead to unexpected behavior. It is therefore highly recommended to always use planning CTs reconstructed with a slice spacing less than or equal to 3 mm.

Converting triangle mesh ROI to voxel object ROI

The algorithm for converting a triangle mesh to a voxel object is based on inside/outside testing of voxels using ray intersection counting with the mesh. For an infinite long ray starting at the voxel center, the voxel is determined to be inside if there is an odd number of ray intersections with the mesh. If the number of intersections with the mesh is even, the voxel is determined to be outside of the mesh. To improve accuracy at the border voxels, relative volumes are used. It is assumed that the triangles are in general larger than the voxel size so if the algorithm finds a triangle passing through a voxel, the partial volume of the voxel determined to be inside the mesh is approximated as the part of the voxel that is on the inside of the triangle determined by its orientation. The mesh is required to have a consistent orientation of the triangles, either all triangles counter-clockwise (recommended) or all triangles clockwise (not recommended). If the algorithm detects that triangles seem to be oriented clockwise, all triangles will be changed to counter-clockwise. The default voxel size of the voxel object is 0.05 cm. For a larger object, the voxel size can be higher. The allowed maximal voxel size is 0.25 cm. Because of this, structures of the mesh smaller than 0.25 cm are not guaranteed to be preserved in the conversion. In most cases, 0.05 cm is the limit.

10.2 ALGORITHMS FOR REPRESENTING ROIS IN THE DOSE GRID

10.2.1 Introduction

ROIs are used as relative volume distributions in the dose grid when computing dose and also when computing DVHs, dose statistics and optimization function values. *section 10.2.2 Converting ROIs to dose grid ROIs on page 355* describes how ROIs are converted to relative volume distributions (dose grid ROIs), *section 10.2.3 Computing dose statistics on page 356* describes how dose statistics are computed, *section 10.2.4 Visualizing dose on page 357* describes how dose is visualized and *section 10.2.5 Summary on page 357* summarizes the previous sections.

10.2.2 Converting ROIs to dose grid ROIs

General information

RayStation can convert the three different shapes of ROIs to dose grid ROIs. The conversion from ROI shapes to dose grid ROIs used in RayStation shown in Figure 85.

Figure 85. The conversions used for converting ROIs to dose grid ROIs in RayStation 2024A.

Input

The algorithm needs the following input communicated according to the DICOM standard [47]:

- A patient or phantom description, normally CT images (optionally cone beam CT, MR or PET).
- Regions of interest (ROI).
- Dose grid settings, i.e.
  - Resolution
  - Size
  - Corner, i.e. a point given in patient coordinates.

Output

Dose grid ROIs, which are voxel ROIs having relative volume voxel values in the dose grid. The resolution of the dose grid ROIs is that of the dose grid.

Converting contour sets to dose grid ROIs

The main algorithm in RayStation 2024A to convert ROIs in to dose grid ROIs in the dose grid is shape-based interpolation [49] which converts contour sets to dose grid ROIs. The algorithm was

described in *Converting contour sets to voxel ROIs on page 352*. The difference is the resolution of the target grid, and that a 3x super-sampling is performed in the axial direction in order to get better accuracy when moving to a lower resolution grid.

Converting voxel ROIs to dose grid ROIs

When converting a voxel ROI to dose grid ROI representation, the shape is first converted to a contour set according to *Converting voxel ROIs to contour sets on page 350*. This intermediate conversion to contours is independent of the image set slices and is made at twice the dose grid resolution (the distance between generated contours is half a voxel size in the sup-inf direction). The resulting contour set is then converted to a dose grid ROI according to *Converting contour sets to dose grid ROIs on page 355*.

Converting triangle meshes to dose grid ROIs

When converting a triangle mesh to dose grid ROI representation, the shape is first converted to a voxel object according to *Converting triangle mesh ROI to voxel object ROI on page 354*. To increase the accuracy, the reconstruction grid is super sampled in x,y,z-directions by a factor of 2. The resulting voxel object is then interpolated onto dose grid.

10.2.3 Computing dose statistics

The dose volume computation in RayStation assumes the following:

- Dose is constant within each dose grid voxel.
- Dose at volume, $D(v)$, is the minimum dose received by a sub-volume of an ROI, where this sub-volume is accumulated from the highest to lower voxel doses and has size v.
- Volume at dose, $V(d)$, is the accumulated volume in an ROI that receives at least dose d.

These assumptions are used for DVHs, dose statistics, clinical goals, prescription evaluation and objective function evaluation. Scripting methods for calculating dose statistics also make use of the above assumptions.

When the number of voxels within an ROI is small, the discretization of the volume will become apparent in the resulting dose statistics. Multiple dose statistics measures (e.g., D5 and D2) may get the same value when there are steep dose gradients within the ROI, and similarly, the dose ranges lacking volume will appear as horizontal steps in the DVH.

Consequently, the minimum dose to an ROI will be the lowest voxel dose taken over all voxels that have non-zero relative volumes, as computed according to *section 10.2.2 Converting ROIs to dose grid ROIs on page 355*. The maximum dose is analogously determined by the highest voxel dose within the ROI. If there are dose gradients close to the ROI boundaries, the minimum and maximum dose values become very sensitive to interpolation effects, and it is recommended to consider the near-minimum and near-maximum doses represented by the D98 and D2 respectively, see ICRU 83.

Note that point doses in RayStation are trilinearly interpolated from the neighboring voxels and will not simply report the voxel dose within which the point falls. This means that a point dose within the min or max dose voxel may be different from the reported min and max dose for the ROI.

For large ROIs with an extremely wide dose range (difference between minimum and maximum dose larger than 500 Gy), dose statistics will become less accurate for the highest part of the dose. As an example, DoseAtVolume evaluations for an ROI with dose range 1250 Gy will, for the dose region above 250 Gy, be correct within 2 cGy. For an ROI with dose range 10250 Gy, for the dose region above 250 Gy, the same figure is 20 cGy. It is expected that these effects are only relevant for evaluation distributions (e.g., EQD2) or when looking at user defined data (i.e., when set via scripting).

10.2.4 Visualizing dose

The default dose visualization uses tri-linear interpolation from the dose grid to the screen resolution. The interpolation is such that the true dose value of a voxel is obtained only at the voxel center. Since dose statistics is computed without interpolation, the position of an iso-dose line, as calculated by the tri-linear interpolation, does not coincide with the extent of a certain dose level as far as the dose statistics are concerned. In order to see the dose as the dose statistics sees it, interpolation should be turned off.

10.2.5 Summary

There are differences in how the volumes and doses are handled when computing dose statistics compared to how they are visualized. The underlying reason for these differences lies in the interpolation effects which are created when representing the smooth nature of anatomy and dose in the jagged representation of Cartesian grids. The impact of these differences is most pronounced when considering, for instance, the minimum dose to a structure, as reported by the dose statistics, and comparing that to what the minimum dose would seem to be according to the visualized contours and iso-dose lines. According to *Converting contour sets to dose grid ROIs on page 355*, a voxels can get a non-zero relative volume if a contour touches the voxel in any of the involved slices, i.e. in slices within or close to the voxels extent. And, according to *section 10.2.4 Visualizing dose on page 357*, the iso-dose lines are visualized according to a tri-linear interpolation of the dose, so, depending on the dose values of neighboring voxels, the position of the iso-dose line can be offset with as much as half a voxel diagonal. In total, a dose value can be included in the dose statistics although there is a distance in the order of one voxel diagonal between the associated contours and iso-dose lines.

10.3 SLICE INDICATOR GADGET IN BEV/DRR

The slice indicator gadget in the BEV views displays the intersection p between the (infinite) slice plane (blue line) and the isocenter plane, as illustrated below.

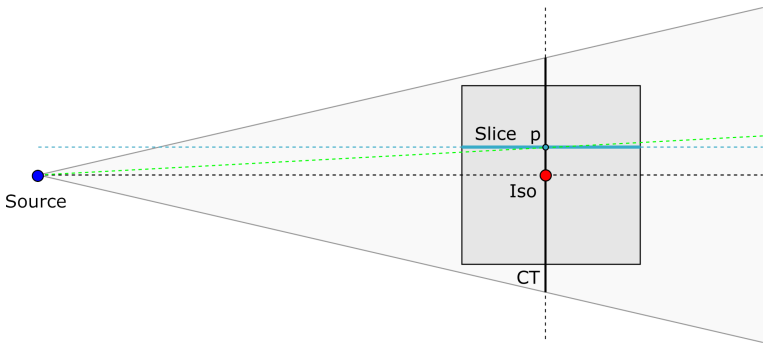

The green dashed line in the illustration represents the projection of p towards the X-ray source. Note that if the CT image is located far away from the isocenter, the projection of p might not necessarily match the actual location of the slice:

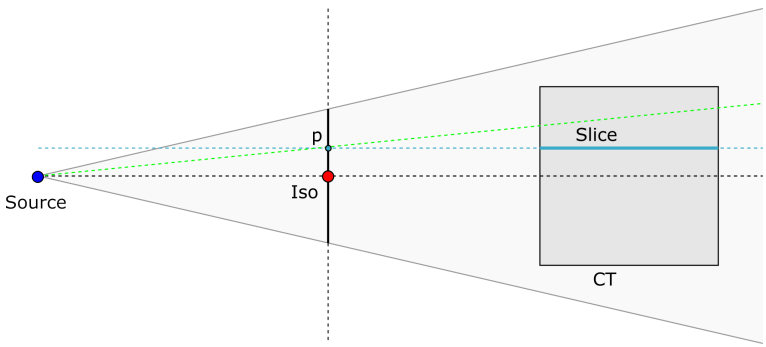

This discrepancy between the slice indicator and the actual slice location becomes larger when scrolling further up or down in the CT stack:

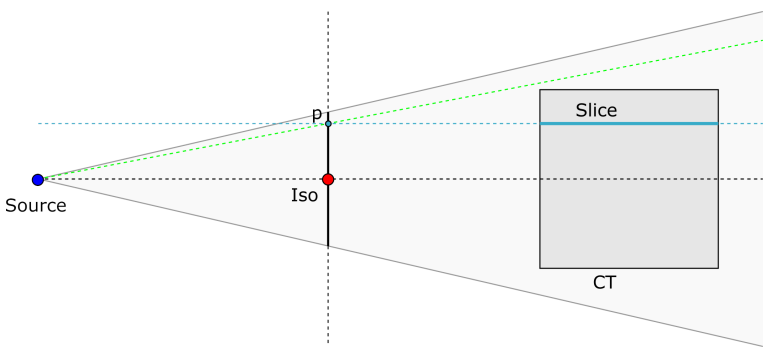

The discrepancy between the slice indicator and the actual slice location also becomes larger when the BEV is generated from a direction that is not parallel to the slice direction:

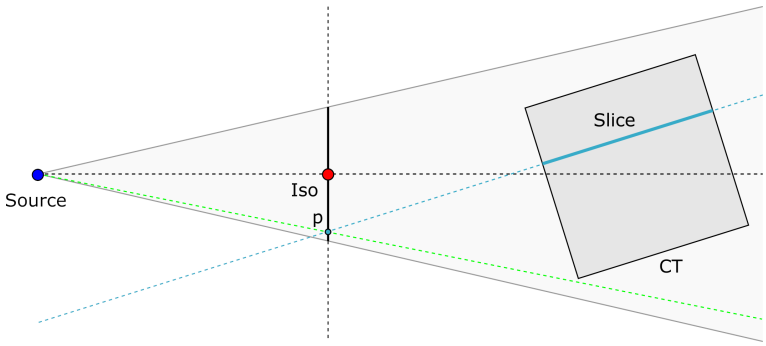

The slice indicator gadget is designed for the normal use case where the isocenter is located inside the patient, i.e., inside the CT image.

11 BIOLOGICAL MODELS REFERENCE INFORMATION

Radiobiological models are used in radiobiological treatment planning to estimate the tumor control probability (TCP) and the normal tissue complication probability (NTCP). One TCP model, TCP-PoissonLQ, and two NTCP models, NTCP-PoissonLQ and NTCP-LKB, are presented in this chapter.

In this chapter

This chapter contains the following sections:

11.1	Precautions	p. 362
11.2	Summary	p. 363
11.3	Introduction to biological models	p. 365
11.4	Cell survival models	p. 366
11.5	EQD2	p. 371
11.6	Protons	p. 376
11.7	Dose-response model	p. 377
11.8	Tumor and normal tissue response	p. 383
11.9	Composite TCP and NTCP models	p. 386
11.10	Parameters of the biological models	p. 388

11.1 PRECAUTIONS

WARNING!

Always evaluate the dose distribution when using biological functions. Biological functions can be used as tools to create and evaluate a plan, but the resulting dose distribution must always be evaluated. (508965)

WARNING!

Biological models. When using biological models, carefully review the selection of model parameters before clinical use. (508966)

WARNING!

Biological model parameters. The biological model parameters are only valid if the correct reference volume is outlined when creating the ROI. (508967)

WARNING!

Factory default biological models. The database of factory default biological model parameters comes from published clinical and pre-clinical studies for photons. Still, this is an evolving field of science and more recent studies may provide evidence for other biological model parameters to be more suitable for clinical use.

The user shall always review the literature and base their usage of biological model parameters on the current state of knowledge in the field and clinic-specific treatment techniques and modalities. (508968)

WARNING!

Biological evaluation and optimization for protons. The biological models used for evaluation and optimization in RayStation are based on studies for photons. Photon equivalent dose must be used when performing biological evaluation and optimization for protons, so the machine model must either include an RBE factor in the absolute dosimetry or be used together with an RBE model. (508969)

11.2 SUMMARY

Radiobiological models are used in radiobiological treatment planning to estimate the tumor control probability (TCP) and the normal tissue complication probability (NTCP). One TCP model, TCP-PoissonLQ, and two NTCP models, NTCP-PoissonLQ and NTCP-LKB, are presented in this manual and are summarized here.

11.2.1 The TCP-PoissonLQ model

The TCP-PoissonLQ model is defined as:

$$TCP(D) = \prod_{i=1}^{M}\left[\exp\left(-\ N_0 \exp\left(\sum_{k=1}^{n}\{-\alpha d_{k,i} - \beta d_{k,i}^2\}\right)\right)\right]^{\frac{v_i}{V_{ref}}}$$
$$= \prod_{i=1}^{N_v}\left[\exp\left(-\ \exp\left[e\gamma - \frac{EQD_{2,i}}{D_{50}}\left(e\gamma - \ \ln(\ln(2))\right)\right]\right)\right]^{\frac{v_i}{V_{ref}}} \qquad \text{[Eq. 231]}$$

where M denotes the total number of voxels, D denotes the total dose, $d_{k,i}$ is the dose of the kth fraction to voxel i and n is the total number of fractions. N_0 denotes the initial number of cells, α and β are the parameters of the LQ model and v_i/V_{ref} is the relative volume of voxel i compared to the reference volume for which the parameters are obtained. D_{50} denotes the dose giving a 50% response probability, γ is the maximum normalized gradient of the dose response curve and $EQD_{2,i}$ is the equivalent dose in voxel i given in 2 Gy-fractions. The equality in the equation is derived in *Appendix B Rewriting of linear dose-response models*.

11.2.2 The general EQD_2

The general EQD_2 is defined as:

$$EQD_{2,i,general} = \frac{\sum_{k=1}^{n}\left\{\ d_{k,i}\left(1 + \frac{d_{k,i}}{\alpha/\beta}\right)\right\}}{1 + \frac{2}{\alpha/\beta}} \qquad \text{[Eq. 232]}$$

where n, $d_{k,i}$, α and β are defined as in *section 11.2.1 The TCP-PoissonLQ model on page 363*.

11.2.3 The NTCP-PoissonLQ model

The **NTCP-PoissonLQ** model, based on the relative seriality model by [43], is expressed as:

$$NTCP_{P-LQ}(D) =$$

$$= \left(1 - \prod_{i=1}^{M}\left(1 - \left[\exp\left(-\ N_0 \exp\left(\sum_{k=1}^{n}\{-\alpha d_{k,i} - \beta d_{k,i}^2\}\right)\right)\right]^s\right)^{\frac{v_i}{V_{ref}}}\right)^{\frac{1}{s}}$$

$$= \left(1 - \prod_{i=1}^{M}\left(1 - \left[\exp\left(-\exp\left[e\gamma - \frac{EQD_{2,i}}{D_{50}}\ (e\gamma - \ln(\ln(2)))\right]\right)\right]^s\right)^{\frac{v_i}{V_{ref}}}\right)^{\frac{1}{s}}$$

[Eq. 233]

where M, D, $d_{k,i}$, n, N_0, α, β, v_i/V_{ref}, D_{50}, γ and EQD_2 are defined as in *section 11.2.1 The TCP-PoissonLQ model on page 363*. s denotes the relative seriality.

11.2.4 The NTCP-LKB model

The NTCP-LKB model is expressed as:

$$NTCP_{LKB}\,(D) = \frac{1}{2\pi}\int_{-\infty}^{t} \exp\left(\frac{-\ u^2}{2}\right)\,du$$

[Eq. 234]

where

$$t = \frac{D_{eff} - D_{50}}{m \cdot D_{50}}$$

[Eq. 235]

and

$$D_{eff} = \sum_{i=1}^{M}\left(\frac{v_i}{V_{ref}}\ EQD_{2,i}^{1/n}\right)^n$$

[Eq. 236]

D_{50} denotes the dose giving a response probability of 50%, m is the slope of the response curve and n specifies the volume dependence. M denotes the total number of voxels, v_i/V_{ref} is the relative volume of voxel i compared to the reference volume and $EQD_{2,i}$ is the equivalent dose in voxel i given in 2 Gy-fractions.

11.3 INTRODUCTION TO BIOLOGICAL MODELS

The main goal in radiation therapy is to deliver a sufficiently high dose to the tumor so that all tumor cells are killed while avoiding radiation induced damage to the surrounding normal tissue. Radiobiological models are used in radiobiological treatment planning to estimate the probability of eradicating the tumour and the probability of inducing damage to the normal tissue. In this manual, one model for estimating tumor control probability, TCP-PoissonLQ, and two models for estimating normal tissue complication probability, NTCP-PoissonLQ and NTCP-LKB, are presented. The TCP-PoissonLQ model and the NTCP-PoissonLQ model are based on cell survival models and Poisson statistics and some background to these models is given. The NTCP-LKB model, on the other hand, is based on a probit function.

11.4 CELL SURVIVAL MODELS

A cell survival curve describes the relationship between the absorbed dose and the fraction of cells that survive. The meaning of cell survival is different in different contexts. For proliferating cells, the term clonogenic cell survival is often used and in this context surviving cells are cells that have retained their reproductive capacity i.e. cells still capable of undergoing cell divisions. Conventionally, the survival fraction is plotted on a log-linear scale with dose on the linear x-axis. The clonogenic cell survival as a function of dose shows an exponential decrease at high doses. At low doses (around 2 Gy) there is usually a curvature or, as it is commonly called, a shoulder region on a log-linear plot which is explained by cellular repair mechanisms. Cell survival models aim to describe the shape of survival curves and two of the most commonly used models are described here.

11.4.1 The linear cell survival model

The clonogenic cell survival as a function of dose is in a first approximation an entirely exponential process. The simple linear cell survival model is expressed as

$$S_L(D) = e^{\frac{D}{D_0}} \qquad \text{[Eq. 237]}$$

where D denotes the total dose and D_0 is the dose that reduces the survival by a factor 0.37 (e^{-1}). In this model cellular repair is not considered as it is done in the linear-quadratic cell survival model.

11.4.2 The linear-quadratic (LQ) cell survival model

The fraction of surviving cells as a function of dose is usually not an entirely exponential process as it is assumed by the linear cell survival model described in *section 11.4.1 The linear cell survival model on page 366*, but there is a curvature or shoulder on the log-linear survival curve at low doses due to the influence of cellular repair mechanisms. The linear quadratic (LQ) model can handle this type of response and takes fractionation effects into account. Figure 86 shows examples of a linear and a LQ cell survival curve with equal cell survival fraction at 2 Gy, where the curvature of the LQ model is clearly shown using log-linear axes.

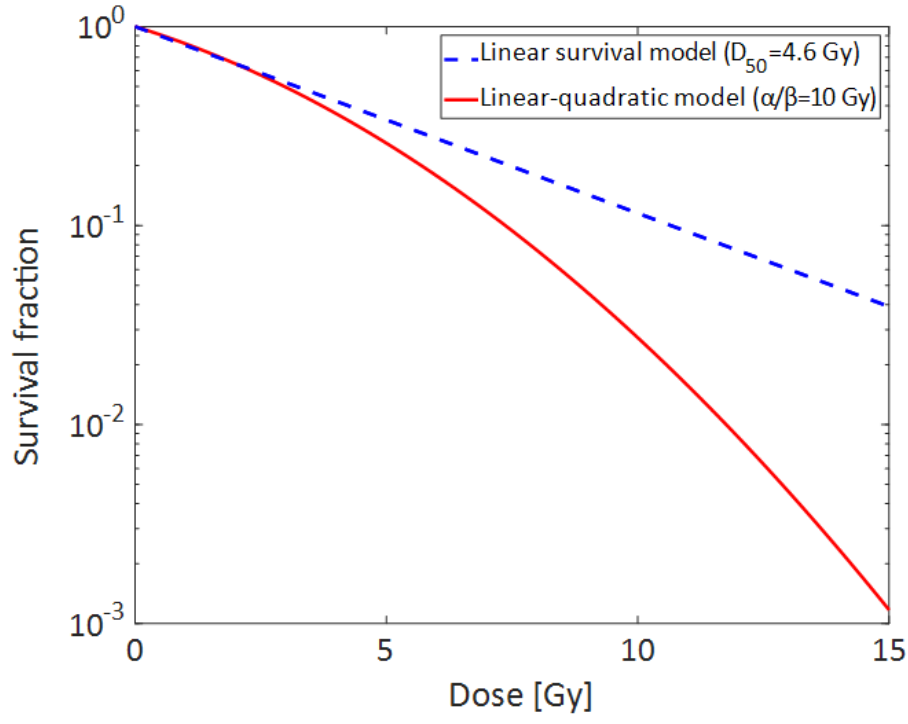

Figure 86. Illustration of a linear and a linear-quadratic (LQ) cell survival curve for a single dose. The model parameters were arbitrary selected to generate equal cell survival at 2 Gy, and the graph has a logarithmic scale on the y-axis and a linear scale on the x-axis.

The LQ model is expressed as

$$S_{LQ}(D) = \prod_{k=1}^{n} S_{LQ}(d_k) =$$

$$= \prod_{k=1}^{n} \exp\left(-\alpha d_k - \beta n d_k^2\right) = \exp\left(\sum_{k=1}^{n}\{-\alpha d_k - \beta d_k^2\}\right) = \qquad \text{[Eq. 238]}$$

$$= \exp\left(\sum_{k=1}^{n} - d_\alpha\left(1 + \frac{d_k}{\alpha/\beta}\right)\right)$$

where D denotes the total dose ($D = \sum_{k=1}^{n} d_k$), d_k is the dose of the kth fraction, n is the total number of fractions, and α and β are the parameters of the LQ model. The α/β ratio describes the fractionation sensitivity of the tissue. For late responding tissues the α/β value is low (commonly

around 3 Gy) while acutely responding normal tissue and most tumors have a larger α/β value (around 10 Gy). A small α/β value indicates that large fractional doses are not well tolerated. Figure XX schematically illustrates this with LQ cell survival curves assuming α/β ratios of 3 Gy and 10 Gy. Note that the cell survival fraction for a low α/β value (3 Gy here) is generally smaller compared to the high α/β value (10 Gy here) for large single doses, whereas the relation is the opposite for a fractionation scheme of 2 Gy per fraction.

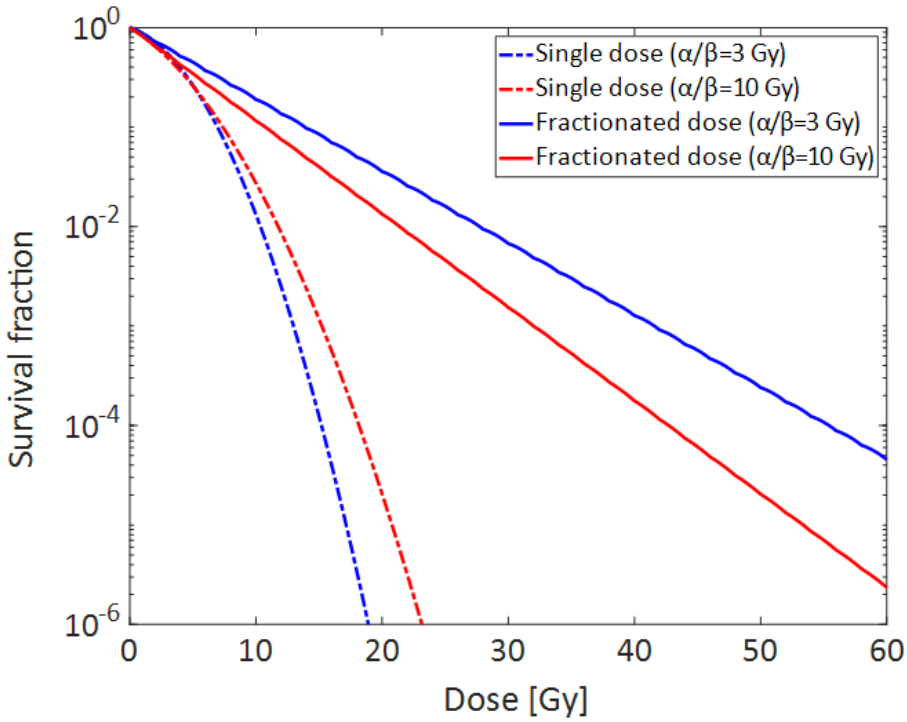

Figure 87. Illustration of LQ cell survival curves following a single dose, and for a schedule of equal fractionation doses of 2 Gy per fraction assuming no repopulation and complete repair between the fractions. Generic values of α = 0.1 Gy-1 and α/β = 3 Gy were assumed for the blue lines, and α = 0.18 Gy-1 and α/β = 10 Gy for the red lines. The graph has a logarithmic scale on the y-axis and a linear scale on the x-axis.

When the fractional doses are equal this expression in [NO STYLE FOR THIS OBJECT] is simplified to

$$S_{LQ}(D) = \exp(-\ \alpha nd - \beta nd^2) = \exp\left(-\ \alpha D\left(1 + \frac{d}{\alpha/\beta}\right)\right) \qquad \text{[Eq. 239]}$$

The LQ cell survival model including incomplete repair

In the simple LQ cell survival model (*section 11.4.2 The linear-quadratic (LQ) cell survival model on page 366*) it is assumed that the time between dose fractions is sufficient for completely repairing the sublethal damage. In bi-exponential repair models, incomplete repair is accounted for and it is assumed that the repair process has a fast and a slow component. The LQ-model is then expanded to the following expression [44]

$$\ln S_{LQ\,repair}(D) =$$

$$= \sum_{k=1}^{n}\left\{-\alpha d_k - \beta d_k^2 - 2\,(1-l)\beta d_k \sum_{p=1}^{k-1}\left(d_p \prod_{q=p}^{k-1}\theta_{s,q}\right) - 2l\beta d_k \sum_{p=1}^{k-1}\left(d_p \prod_{q=p}^{k-1}\theta_{l,q}\right)\right\} = \qquad \text{[Eq. 240]}$$

$$= \sum_{k=1}^{n}\left\{-\alpha d_k\left(1 + \frac{d_k}{\alpha/\beta} + \frac{2}{\alpha/((1-l)\beta)}\sum_{p=1}^{k-1}\left(d_p \prod_{q=p}^{k-1}\theta_{s,q}\right) + \frac{2}{\alpha/(l\beta)}\sum_{p=1}^{k-1}\left(d_p \prod_{q=p}^{k-1}\theta_{l,q}\right)\right)\right\}$$

where D denotes the total dose, d_k is the dose of the kth fraction and n is the total number of fractions. α and β are the parameters of the LQ model, l refers to the fraction of the total repair that is due to long repair times and

$$\theta_{s,q} = \exp\left(-\frac{\ln(2)}{T_{(1/2),s}}\,\Delta\,t_q\right)$$

$$\theta_{l,q} = \exp\left(-\frac{\ln(2)}{T_{(1/2),l}}\,\Delta\,t_q\right) \qquad \text{[Eq. 241]}$$

where Δt_q is the time between fraction q and $q+1$ and $T_{(1/2),s}$ and $T_{(1/2),l}$ are the repair half-times for the short and long repair, respectively.

The LQ cell survival model including accelerated repopulation

There are studies showing that cells start to divide at a higher rate after some time following irradiation. This phenomenon can be taken into account by modifying the LQ cell survival model as [41]

$$S_{LQrepop}(D) = \exp\left(\sum_{k=1}^{n}\{-\alpha d_k - \beta d_k^2\}\right) 2^{\frac{T-T_{start}}{T_p}} =$$

$$= \exp\left(\sum_{k=1}^{n}\{-\alpha d_k - \beta d_k^2\}\right) \cdot \exp\left(\ln\left(2^{\frac{T-T_{start}}{T_p}}\right)\right) \qquad \text{[Eq. 242]}$$

After some rewriting this gives:

$$S_{LQrepop}(D) = \sum_{k=1}^{n}\left\{-\alpha d_k\left(1+\frac{d_k}{\alpha/\beta}\right)\right\}+\left(\frac{T-T_{start}}{T_p}\right)\ln(2) \qquad \text{[Eq. 243]}$$

where D denotes the total dose, d_k is the dose of the kth fraction, n is the total number of fractions and α and β are the parameters of the LQ model. T is the total treatment time, T_{start} is the time point when the accelerated repopulation sets in and T_p is the potential cell doubling time. When $T < T_{start}$, it is assumed that no repopulation occurs. The fraction of surviving cells is not allowed to become larger than one even if there is a major contribution of accelerated repopulation.

The LQ cell survival model including both incomplete repair and accelerated repopulation

When both incomplete repair and accelerated repopulation is taken into account the expression for cell survival becomes

$$\begin{aligned} &S_{LQrandr}(D) = \\ &= \sum_{k=1}^{n}\{-\alpha d_k(1+\frac{d_k}{\alpha/\beta}+\frac{2}{\alpha/((1-l)\beta)}\sum_{p=1}^{k-1}(d_p\prod_{q=p}^{k-1}\theta_{s,q}) \\ &+\frac{2}{\alpha/(l\beta)}\sum_{p=1}^{k-1}(d_p\prod_{q=p}^{k-1}\theta_{l,q}))\}+\left(\frac{T-T_{start}}{T_p}\right)\ln(2) \end{aligned} \qquad \text{[Eq. 244]}$$

where D denotes the total dose, d_k is the dose of the kth fraction and n is the total number of fractions. α and β are the parameters of the LQ model, l refers to the fraction of the total repair that is due to long repair times. $\theta_{s,q}$ and $\theta_{l,q}$ are defined in [NO STYLE FOR THIS OBJECT]. T denotes the total treatment time, T_{start} is the time point when the accelerated repopulation sets in and T_p is the potential cell doubling time. When $EQD_{general} = -\frac{\ln S_{LQ}(D)/\alpha}{1+\frac{d_{ref}}{\alpha/\beta}} = \frac{\sum_{k=1}^{n}\left\{d_k\left(1+\frac{d_k}{\alpha/\beta}\right)\right\}}{1+\frac{d_{ref}}{\alpha/\beta}}$, it is assumed that no repopulation occurs. The fraction of surviving cells is not allowed to become larger than one even if there is a major contribution of accelerated repopulation.

11.5 EQD$_2$

EQD$_2$, the equivalent dose in 2 Gy-fractions, is based on the linear quadratic (LQ) cell survival model and can be used for comparing fractionation schedules. It estimates the total dose delivered in 2 Gy-fractions that gives the same biological effect as the total dose obtained using the fractionation schedule of interest. The general EQD is expressed as

$$EQD_{general} = -\frac{\ln S_{LQ}(D)\ /\alpha}{1+\frac{d_{ref}}{\alpha/\beta}} = \frac{\sum_{k=1}^{n}\left\{d_k\left(1+\frac{d_k}{\alpha/\beta}\right)\right\}}{1+\frac{d_{ref}}{\alpha/\beta}} \qquad \text{[Eq. 245]}$$

where D denotes the total dose, d_k is the dose of the kth fraction and n is the total number of fractions. α and β are the parameters of the LQ model. d_{ref} is the reference fractional dose and is usually 2 Gy. Henceforth, d_{ref} is set to 2.

If equal fractional doses are used this expression reduces to

$$EQD_2 = \frac{D\left(1+\frac{d}{\alpha/\beta}\right)}{1+\frac{2}{\alpha/\beta}} \qquad \text{[Eq. 246]}$$

EQD$_2$ is a tool for comparing treatment plans qualitatively. If for example two fractionation schedules are to be compared and both are rescaled using EQD$_2$, the treatment plan with the highest EQD$_2$ will according to the model give more damage than the other plan.

11.5.1 Computing EQD$_2$ dose distribution

In Plan evaluation, it is possible to compute an EQD2 dose distribution. The EQD2 dose for one fraction is computed as

$$d_{EQD2} = \frac{d\left(1+\frac{d}{\alpha/\beta}\right)}{1+\frac{2}{\alpha/\beta}} \qquad \text{[Eq. 247]}$$

where d is the physical fraction dose. For dose grid voxels intersected by several ROIs with a defined α/β, the α/β value of the ROI with the highest priority is used.

To get the total EQD2 for several fractions, several EQD2 fraction doses can be summed. If the fraction doses are defined on different image set, the individual EQD2 fraction doses must first be deformed to one image set.

11.5.2 EQD$_2$ including incomplete repair

In the general EQD$_2$ it is assumed that the time between dose fractions is sufficient for completely repairing the sublethal damage. When incomplete repair is taken into account the EQD$_2$ is then expanded to (see *The LQ cell survival model including incomplete repair on page 369*)

$$EQD_{2,repair} = -\frac{\ln S_{LQ}(D)\ /\alpha}{1+\frac{2}{\alpha/\beta}} =$$

$$= \frac{\sum_{k=1}^{n}\left\{d_k\left(1+\frac{d_k}{\alpha/\beta}+2\,\frac{1}{\alpha/((1-l)\beta)}\sum_{p=1}^{k-1}(d_p\prod_{q=p}^{k-1}\ \theta_{s,q})+2\frac{1}{\alpha/(l\beta)}\sum_{p=1}^{k-1}(d_p\prod_{q=p}^{k-1}\ \theta_{l,q})\right)\right\}}{1+\frac{2}{\alpha/\beta}} \qquad \text{[Eq. 248]}$$

where D denotes the total dose, d_k is the dose of the kth fraction and n is the total number of fractions. α and β are the parameters of the LQ model. l refers to the fraction of the total repair that is due to the long repair times and

$$\theta_{s,q} = \exp\left(-\frac{\ln(2)}{T_{(1/2),s}}\ \Delta\ t_q\right)$$

$$\theta_{l,q} = \exp\left(-\frac{\ln(2)}{T_{(1/2),l}}\ \Delta\ t_q\right)$$

where $\Delta\ t_q$ is the time between fraction q and $q+1$ and $T_{(1/2),s}$ and $T_{(1/2),l}$ are the repair half-times for the short and long repair, respectively.

11.5.3 EQD$_2$ including accelerated repopulation

In the general EQD$_2$, accelerated repopulation is not taken into account. The expression for EQD$_2$ when repopulation is included becomes [41]

$$EQD_{2,repop} = -\frac{\ln S_{LQrepop}(D)\ /\alpha}{1+\frac{2}{\alpha/\beta}}$$

$$= \frac{\sum_{k=1}^{n}\left\{d_k\left(1+\frac{d_k}{\alpha/\beta}\right)\right\}-\frac{\ln(2)}{\alpha}\left(\frac{T-T_{start}}{T_p}\right)}{1+\frac{2}{\alpha/\beta}} \qquad \text{[Eq. 249]}$$

where d_k is the dose of the kth fraction, n is the total number of fractions and α and β are the parameters of the LQ model. T is the total treatment time, T_{start} is the time point when the accelerated repopulation sets in and T_p is the potential cell doubling time. When $T < T_{start}$, it is

assumed that no repopulation occurs. If the accelerated repopulation term becomes very large this would give a negative EQD_2 value. In this case EQD_2 is set to zero.

11.5.4 EQD_2 including both incomplete repair and accelerated repopulation

When both incomplete repair and accelerated repopulation is taken into account the EQD_2 becomes

$$EQD_{2,randr} = \\ = \frac{\sum_{k=1}^{n}\left\{d_k\left(1+\frac{d_k}{\alpha/\beta}+2\,\frac{1}{\alpha/((1-l)\beta)}\sum_{p=1}^{k-1}(d_p\prod_{q=p}^{k-1}\theta_{s,q})+\,2\,\frac{1}{\alpha/(l\beta)}\sum_{p=1}^{k-1}(d_p\prod_{q=p}^{k-1}\theta_{l,q})\right)\right\}}{1+\frac{2}{\alpha/\beta}} \\ \frac{-\frac{\ln(2)}{\alpha}\left(\frac{T-T_{start}}{T_p}\right)}{1+\frac{2}{\alpha/\beta}} \qquad \text{[Eq. 250]}$$

where d_k is the dose of the kth fraction and n is the total number of fractions. α and β are the parameters of the LQ model. l refers to the fraction of the total repair that belongs to the long repair times and

$$\theta_{s,q} = \exp\left(-\frac{\ln(2)}{T_{(1/2),s}}\,\Delta\,t_q\right) \\ \theta_{l,q} = \exp\left(-\frac{\ln(2)}{T_{(1/2),l}}\,\Delta\,t_q\right) \qquad \text{[Eq. 251]}$$

where $\Delta\,t_q$ is the time between fraction q and $q+1$ and $T_{(1/2),s}$ and $T_{(1/2),l}$ are the repair half-times for the short and long repair, respectively. T is the total treatment time, T_{start} is the time point when the accelerated repopulation sets in and T_p is the potential cell doubling time. When $T < T_{start}$, it is assumed that no repopulation occurs. If the accelerated repopulation term becomes very large this would give a negative EQD_2 value. In this case EQD_2 is set to zero.

WARNING!

Limitations of the EQD2 formalism. The equivalent dose in 2-Gy fractions (EQD2) implemented in RayStation is based on the standard linear-quadratic (LQ) model, which has the following implications that the user should be aware of:

- The model assumes complete repair between fractions and disregards repopulation of tumor cells. Therefore, in cases where complete repair between fractions is not achieved, the biological effects will not be adequately modeled. Furthermore, when repopulation of tumor cells becomes important, for example due to interruptions in the treatment or for rapidly proliferating tumors, the EQD2 dose will not be fully correct.
- The uncertainties in the LQ model become larger for low prescribed doses (below 1 Gy) and high prescribed doses (8 Gy) per fraction. Consequently, the EQD2 doses are less reliable for such dose levels.
- The EQD2 doses are strongly dependent on the α/β-values used in the evaluation. The user is advised to consider a range of α/β-values in the evaluation and investigate worst-case scenarios for EQD2, especially when normal tissue tolerance may be compromised.
- EQD2 doses do not depend linearly on the physical dose, which means that cold and hot spots are enhanced when translating physical dose to EQD2 and gradients in the EQD2 distribution are higher than in the physical dose distribution. It is therefore advised to not evaluate EQD2 in a single point only but use multi-point evaluations to account for differences throughout the volume. Furthermore, when the EQD2 evaluation is based on volumes in the DVH, it is advised to use more than one clinical goal. For example, a clinical goal on EQD2(D90) could be complemented with clinical goals for other accumulated volumes than 90% of the total ROI volume. Volume effects can be analyzed further in the full EQD2 distribution, as obtained from the EQD2 computation in Plan Evaluation.

(406776)

WARNING!

Interpretation of EQD2 distributions. An EQD2 distribution differs from the corresponding physical dose distribution in several aspects and special care must be taken when interpreting EQD2 dose distributions:

- Evaluation criteria for physical dose cannot be used directly when evaluating EQD2 distributions. The physical dose criteria must always first be converted to the EQD2 domain. This is essential also for treatments prescribed at 2 Gy per fraction to the tumor: even if the prescribed dose in the tumor will be 2 Gy per fraction both in physical dose and in EQD2, cold and hot spots inside the tumor will be enhanced in the EQD2 domain. More importantly, normal tissue tolerances can differ significantly between the physical dose and the EQD2 distribution also for 2 Gy-fractionated treatments.
- For an EQD2 distribution computed in Plan Evaluation, adjacent or overlapping ROIs can be assigned with different α/β-values and the EQD2 distribution will be discontinuous across boundaries between ROIs with different α/β-values. For overlapping ROIs, a priority between the ROIs in the EQD2 computation determines which α/β-value to be used in a voxel belonging to more than one ROI. The result is that the α/β-value specified for an ROI may only be used in part of the ROI.
- To ensure that a specific α/β-value is used to evaluate a clinical goal in the EQD2 domain, it is recommended to first extract the clinical goal for the physical dose and then convert it to EQD2 with the α/β-value of choice, rather than extracting the clinical goal directly from the EQD2 distribution. Reporting of EQD2 metrics is common in brachytherapy, and RayStation supports EQD2 clinical goals in the brachytherapy module, which automatically performs the recommended conversion.

(408774)

11.6 PROTONS

For photons $EQD2(D)$ is a function of the dose D, but for protons the $EQD_2(RBE * D)$ is a function of the dose weighted with the Relative Biological Effectiveness (RBE-weighted dose). This is also valid for the TCP and NTCP models where for photons $TCP(D)$ and $NTCP(D)$ are functions of the dose, but for protons the $TCP(RBE * D)$ and $NTCP(RBE * D)$ are functions of the RBE-weighted dose. The user must verify that the RBE-weighted dose is used when applying the models to protons. This can be achieved by either including the RBE in the absolute dosimetry of the machine model, or by using an RBE model in the plan.

11.7 DOSE-RESPONSE MODEL

A dose-response model describes the probability of response (biological effect) as a function of dose. The dose-response curve usually has a sigmoid shape. At low doses the probability of response is small but increases with increasing dose. A dose-response model can be derived from a cell survival model, seeking to estimate the probability that no clonogenic tumor cells (or functional subunits) survives. Assuming N_0 clonogenic cells, all with the same probability of survival at a given dose, $S(D)$, and that the survival of each cell is independent of the survival of other cells, then the process of survival follows the binominal distribution (an irradiated cell either survive or is killed). Typically, there is a large number of clonogenic cells, each with a small probability of survival. This allows for the use of Poisson statistics as an approximation of the binominal process. For a Poisson distribution, the probability P of zero surviving cells (or functional subunits) given the expected value of N_s surviving cells for a given dose D results in the following relation:

$$P(D) = P(N_S, 0) = \frac{N_S^0 \exp(-N_S)}{0!} = \exp(-N_s) = \exp(-N_0 S(D)) \qquad \text{[Eq. 252]}$$

where N_0 is the initial number of cells and $S(D)$ is the probability of survival at a given dose D using an arbitrary cell survival model. This type of dose-response curve usually has a sigmoid shape, which is frequently described by the dose giving a 50% response, D_{50}, and the maximum normalized gradient of the dose response curve, γ. The parameter γ is defined as $\gamma = \max(D\frac{\delta P}{\delta D})$, as described in [40]. Figure 88 shows a schematic representation of a sigmoidal dose-response curve with D_{50} and the maximum gradient related to γ indicated.

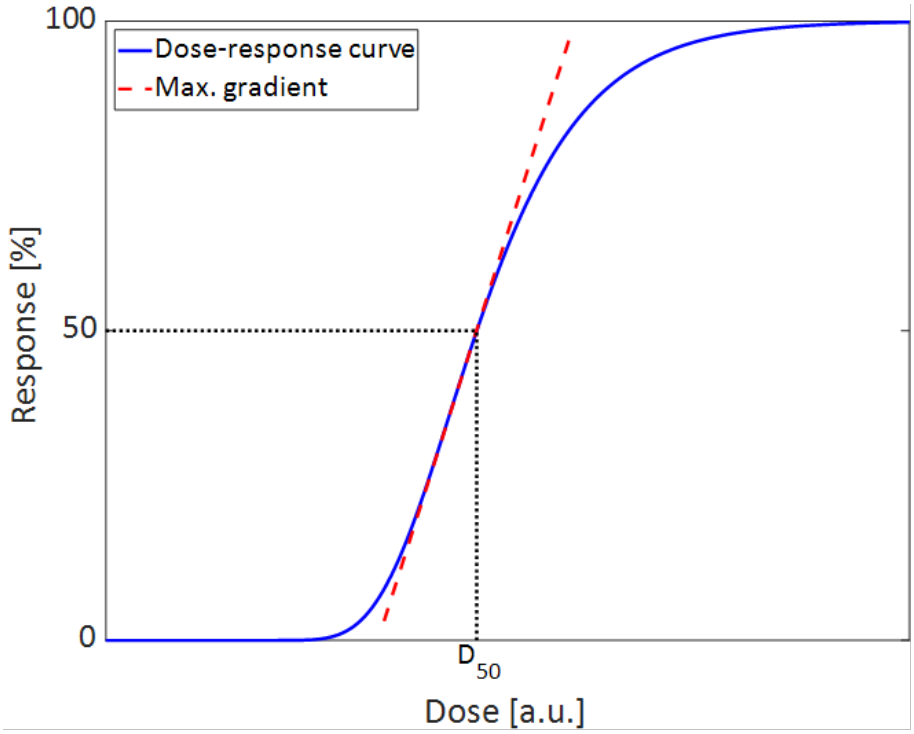

Figure 88. Schematic illustration of the sigmoidal dose-response curve as the blue solid line. D_{50} is indicated with the black dotted line as the dose leading to 50% probability of response, and the red dashed line show the maximum gradient of the dose-response curve which is closely related to γ.

The initial number of cells can be expressed as [45]:

$$N_0 = \exp(e\gamma) \qquad \text{[Eq. 253]}$$

where e is Euler's number (2.71828).

11.7.1 The linear dose-response model

Using the linear cell survival model (see *section 11.4.1 The linear cell survival model on page 366*) we obtain the following expression for the response as a function of dose

$$P_L(D) = \exp(-\ N_0 S_L(D)) =$$
$$= \exp\left(-\ N_0 \exp\left(-\ \frac{D}{D_0}\right)\right) = \exp\left(-\ \exp\left[e\gamma - \ \frac{D}{D_0}\right]\right) \qquad \text{[Eq. 254]}$$

where D denotes the total dose, D_0 is the dose that reduces the survival by a factor 0.37 (e^{-1}), N_0 is the initial number of cells and γ is the maximum normalized gradient of the dose response curve.

By inserting the dose giving a response value of 0.5 (D_{50}) we obtain

$$\begin{aligned}
&P_L(D_{50}) = \exp\left(-\ \exp\left[e\gamma - \frac{D_{50}}{D_0}\right]\right) \Leftrightarrow \\
&\Leftrightarrow\ \exp\left(\ln\left(\frac{1}{2}\right)\right) = \exp\left(-\ \exp\left[e\gamma - \frac{D_{50}}{D_0}\right]\right) \Leftrightarrow \\
&\ln(\ln(2)) = e\gamma - \frac{D_{50}}{D_0} \\
&\Rightarrow D_0 = \frac{D_{50}}{e\gamma - \ \ln(\ln(2))}
\end{aligned}$$

[Eq. 255]

The linear dose response model can thus be expressed with the parameters D_{50} and γ:

$$P_L = \exp\left(-\ \exp\left[e\gamma - \frac{D}{D_{50}}\left(e\gamma - \ \ln(\ln(2))\right)\right]\right)$$

[Eq. 256]

The parameters D_{50} and γ are only valid if the dose D is delivered using the same reference dose per fraction, d_{ref}, as the one that was used when these parameters were estimated. By using EQD_2 instead of the physical dose D, the physical dose is rescaled to an isoeffective dose delivered in fractions of 2 Gy. In this way the parameters of the linear dose-response model derived for 2 Gy per fraction can be used even if the dose per fraction is not equal to 2 Gy. By replacing the total dose D by EQD_2 the following expression is obtained

$$P_{LQ} = \exp\left(-\ \exp\left[e\gamma - \frac{EQD_2}{D_{50}}\ (e\gamma - \ \ln(\ln(2)))\right]\right)$$

[Eq. 257]

where one of the four expressions for EQD_2 defined in *section 11.5 EQD_2 on page 371* can be used.

11.7.2 The linear-quadratic (LQ) dose-response model

When the dose-response model is based on the linear-quadratic (LQ) cell survival model (see *section 11.4.2 The linear-quadratic (LQ) cell survival model on page 366*) the following expression is obtained:

$$P_{LQ}(D) = \exp\left(-\ N_0 S_{LQ}(D)\right) =$$
$$= \exp\left(-\ N_0 \exp\left(\sum_{k=1}^{n}\{-\ \alpha d_k - \ \beta d_k^2\}\right)\right) \qquad \text{[Eq. 258]}$$

where N_0 is the initial number of cells, D denotes the total dose, d_k is the dose of the kth fraction and n is the total number of fractions. α and β are the parameters of the LQ model.

When the fractional doses are equal this expression can be simplified to

$$P_{LQ}(D) = \exp\left(-\ \exp\left[e\gamma - \alpha D\ \left(1 + \frac{d}{\alpha/\beta}\right)\right]\right) \qquad \text{[Eq. 259]}$$

where γ is the maximum normalized gradient of the dose response curve.

The clinically important D_{50} parameter can be included in the LQ model by having $P_{LQ}(D) = P_L(D)$ for a given fractional dose d_{ref} , usually 2 Gy, which gives [45] :

$$\alpha = \frac{e\gamma - \ \ln(\ln(2))}{D_{50}\left(1 + \frac{d_{ref}}{\alpha/\beta}\right)} = \frac{e\gamma - \ \ln(\ln(2))}{D_{50}\left(1 + \frac{2}{\alpha/\beta}\right)} \qquad \text{[Eq. 260]}$$

This equality holds only for the constant fractional dose d_{ref} for which the parameters were estimated or when $\alpha/\beta\ \rightarrow\ \infty$. Using this expression for the parameter α, the LQ dose-response model, $P_{LQ}(D)$, is equivalent to the linear dose-response model using $EQD_2, P_L(EQD_2)$, as shown in *Appendix B Rewriting of linear dose-response models*.

The LQ dose-response model including incomplete repair

The dose-response model obtained using the LQ cell survival model including cellular repair is expressed as [44]

$$P_{LQrepair}(D) = \\ = \exp\left(-\exp\left[e\gamma - \sum_{k=1}^{n}\{\alpha d_k(1 + \frac{d_k}{\alpha/\beta} + \frac{2}{\alpha/((1-l)\beta)}\sum_{p=1}^{k-1}(d_p\prod_{q=p}^{k-1}\theta_{s,q}) \\ + \frac{2}{\alpha/(l\beta)}\sum_{p=1}^{k-1}(d_p\prod_{q=p}^{k-1}\theta_{l,q})\}\right]\right) \qquad \text{[Eq. 261]}$$

where d_k is the dose of the kth fraction and n is the total number of fractions. α and β are the parameters of the LQ model, and γ is the maximum normalized gradient of the dose response curve. l refers to the fraction of the total repair that is due to the long repair times. Moreover,

$$\theta_{s,q} = \exp\left(-\frac{\ln(2)}{T_{(1/2),s}}\Delta t_q\right)$$

$$\theta_{l,q} = \exp\left(-\frac{\ln(2)}{T_{(1/2),l}}\Delta t_q\right)$$

where Δt_q is the time between fraction q and $q+1$ and $T_{(1/2),s}$ and $T_{(1/2),l}$ are the repair half-times for the short and long repair, respectively.

The LQ dose-response model including accelerated repopulation

Using the LQ cell survival model including repopulation the following dose-response expression is obtained (see *The LQ cell survival model including accelerated repopulation on page 369*):

$$P_{LQrepop}(D) = \\ = \exp\left(-\exp\left[e\gamma - \sum_{k=1}^{n}\left\{\alpha d_k\left(1 + \frac{d_k}{\alpha/\beta}\right)\right\} + \left(\frac{T - T_{start}}{T_p}\right)\ln(2)\right]\right) \qquad \text{[Eq. 262]}$$

where d_k is the dose of the kth fraction, n is the total number of fractions and α and β are the parameters of the LQ model and γ is the maximum normalized gradient of the dose response curve. T is the total treatment time, T_{start} is the time point when the accelerated repopulation sets in and T_p is the potential cell doubling time. When $T < T_{start}$, it is assumed that no repopulation occurs.

The LQ dose-response model including both incomplete repair and accelerated repopulation

When both incomplete repair and accelerated repopulation is taken into account the dose-response expression becomes

$$P_{LQandr} = \exp(-\ \exp[e-\sum_{k=1}^{n}\{\ \alpha d_k(1+\frac{d_k}{\alpha/\beta}+\frac{2}{\alpha/((1-l)\beta_s)}\sum_{p=1}^{k-1}(d_p\prod_{q=p}^{k-1}\ \theta_{s,q})$$

$$+\frac{2}{\alpha/(l\beta_l)}\sum_{p=1}^{k-1}(d_p\prod_{q=p}^{k-1}\ \theta_{l,q}))\}+\left(\frac{T-T_{start}}{T_p}\right)\ln(2)]) \qquad \text{[Eq. 263]}$$

where d_k is the dose of the kth fraction and n is the total number of fractions. α and β are the parameters of the LQ model, and γ is the maximum normalized gradient of the dose response curve. l refers to the fraction of the total repair that is due to the long repair times. Moreover,

$$\theta_{s,q} = \exp\left(-\ \frac{\ln(2)}{T_{(1/2),s}}\ \Delta\ t_q\right)$$

$$\theta_{l,q} = \exp\left(-\ \frac{\ln(2)}{T_{(1/2),l}}\ \Delta\ t_q\right)$$

where $\Delta\ t_q$ is the time between fraction q and $q+1$ and $T_{(1/2),s}$ and $T_{(1/2),l}$ are the repair half-times for the short and long repair, respectively. T denotes the total treatment time, T_{start} is the time point when the accelerated repopulation sets in and T_p is the potential cell doubling time. When $T < T_{start}$, it is assumed that no repopulation occurs.

11.8 TUMOR AND NORMAL TISSUE RESPONSE

The main goal in curative radiation therapy is to deliver a sufficiently high dose to the tumor so that all tumor cells are killed while avoiding damage to the surrounding normal tissue. The tumor control probability, TCP, and normal tissue complication probability, NTCP, can be estimated by the expressions presented here. The TCP-PoissonLQ model and the NTCP-PoissonLQ model are based on cell survival models and Poisson statistics while the NTCP-LKB model is based on a probit function.

11.8.1 TCP-PoissonLQ

In order to eradicate a tumor it is generally believed that all clonogenic tumor cells have to be killed. Using the LQ dose-response model (with or without incomplete repair and/or repopulation) or, equivalently (see *Appendix B Rewriting of linear dose-response models*), using the linear dose-response model with EQD_2 (with or without incomplete repair and/or repopulation) the probability of tumor control, TCP, can be obtained. The TCP for target (tumor) j is calculated according to

$$TCP_j\left(D\right) = \prod_{i=1}^{M} \left(P_{LQ,j}\left(D_i\right)\right)^{\frac{v_i}{V_{ref}}} = \\ = \prod_{i=1}^{M} \left[\exp\left(-\ N_0 \exp\left(\sum_{k=1}^{n}\{-\ \alpha d_{k,i} - \beta d_{k,i}^2\}\right)\right)\right]^{\frac{v_i}{V_{ref}}} \qquad \text{[Eq. 264]}$$

$$TCP_j\left(D\right) = \prod_{i=1}^{M} \left(P_{L,j}\left(EQD_{2,i}\right)\right)^{\frac{v_i}{V_{ref}}} = \\ = \prod_{i=1}^{M} \left[\exp\left(-\ \exp\left[e\gamma - \frac{EQD_{2,i}}{D_{50}}\ \left(e\gamma - \ln(\ln(2))\right)\right]\right)\right]^{\frac{v_i}{V_{ref}}} \qquad \text{[Eq. 265]}$$

where $P_{LQ}(D)$ is the LQ dose-response model (see *section 11.7.2 The linear-quadratic (LQ) dose-response model on page 380*) and $P_L(EQD_2)$ is the linear dose-response model using EQD_2, the equivalent dose given in 2 Gy-fractions (see *section 11.7.1 The linear dose-response model on page 378*). D denotes the total dose, $d_{k,i}$ is the dose of the kth fraction to voxel i and n is the total number of fractions and M denotes the total number of voxels. N_0 denotes the initial number of cells, α and β are the parameters of the LQ model and v_i/V_{ref} is the relative volume of voxel i compared to the reference volume for which the parameters are obtained. D_{50} denotes the dose giving a 50% response probability and γ is the maximum normalized gradient of the dose response curve.

11.8.2 NTCP

NTCP-PoissonLQ model

The normal tissue complication probability for tissue j, $NTCP_j$, can be calculated using the relative seriality model defined by Källman and co-workers [43] together with the LQ dose-response model (with or without incomplete repair). Equivalently (see *Appendix B Rewriting of linear dose-response models*), $NTCP_j$ can be calculated using the relative seriality model together with the linear dose-response model with EQD2 (with or without incomplete repair).

$$NTCP_{P-LQ,j}\,(D) = \left(1-\prod_{i=1}^{M}\,(1-\,P_{LQ,j}\,(D_i)^s)^{\frac{v_i}{V_{ref}}}\right)^{\frac{1}{s}}$$
$$= \left(1-\prod_{i=1}^{M}\left(1-\left[\exp\left(-\,N_0\exp\left(\sum_{k=1}^{n}\{-\,\alpha d_{k,i}-\,\beta d_{k,i}^2\}\right)\right)\right]^s\right)^{\frac{v_i}{V_{ref}}}\right)^{\frac{1}{s}} \qquad \text{[Eq. 266]}$$

$$NTCP_{P-LQ,j}\,(D) = \left(1-\prod_{i=1}^{M}\,(1-\,P_{L,j}\,(EQD_{2,i})^s)^{\frac{v_i}{V_{ref}}}\right)^{\frac{1}{s}}$$
$$= \left(1-\prod_{i=1}^{M}\left(1-\left[\exp\left(-\exp\left[e\gamma-\frac{EQD_{2,i}}{D_{50}}\left(e\gamma-\ln(\ln(2))\right)\right]\right)\right]^s\right)^{\frac{v_i}{V_{ref}}}\right)^{\frac{1}{s}} \qquad \text{[Eq. 267]}$$

where $P_{LQ}(D)$ is the LQ dose-response model (see *Appendix B Rewriting of linear dose-response models*) and $P_L(EQD_2)$ is the linear dose-response model using EQD_2, the equivalent dose given in 2 Gy-fractions (see *section 11.7.1 The linear dose-response model on page 378*). D denotes the total dose, $d_{k,i}$ is the dose of the kth fraction to voxel i and n is the total number of fractions and M denotes the total number of voxels. N_0 denotes the initial number of cells, α and β are the parameters of the LQ model and v_i/V_{ref} is the relative volume of voxel i compared to the reference volume for which the parameters are obtained. D_{50} denotes the dose giving a 50% response probability, γ is the maximum normalized gradient of the dose response curve and $EQD_{2,i}$ is the equivalent dose in voxel i given in 2 Gy-fractions. Parameter s is the relative seriality parameter describing the volume dependence of the dose-response relation by specifying the internal organization of the organ. For a so called parallel organ, such as the lung, the parameter s is small. This means that the organ is not that sensitive to high local doses (hot-spots) but both low and high doses are important to consider. On the other hand, a so called serial organ such as the spinal cord has a high s value and is very sensitive to high local doses even if the mean dose is low.

NTCP-LKB model

The normal tissue complication probability, NTCP, based on the LKB model [46], [42] is defined as

$$NTCP_{LKB}\left(D\right) = \frac{1}{2\prod} \int_{-\infty}^{t} \exp\left(\frac{-\ u^2}{2}\right) du \qquad \text{[Eq. 268]}$$

where

$$t = \frac{D_{eff} - D_{50}}{m \cdot D_{50}}$$

and

$$D_eff = \left(\sum_{i=1}^{M} \frac{v_i}{V_{ref}} EQD_{2,i}^{1/n}\right)^n$$

where D_{50} denotes the dose giving a response probability of 50%, m is the slope of the response curve and n specifies the volume dependence. M denotes the total number of voxels, v_i/V_{ref} is the relative volume of voxel i compared to the reference volume and $EQD_{2,i}$ is the equivalent dose in voxel i given in 2 Gy-fractions.

11.9 COMPOSITE TCP AND NTCP MODELS

Individual TCPs can be combined into an overall (composite) TCP if there are several tumors. Similarly, individual NTCPs for different organs can be combined into a composite NTCP. Composite TCP and NTCP models are used to estimate the overall probability of eradicating all tumors of interest and the overall probability of injuring any of the normal tissues of interest, respectively.

11.9.1 Composite TCP

The composite TCP for all tumors is calculated according to

$$TCP(D) = \prod_j TCP_j(D) \qquad \text{[Eq. 269]}$$

assuming that all tumors j have to be eradicated in order to be cured.

11.9.2 Composite NTCP

The overall probability of injury is obtained by combining NTCPs for different organs at risk:

$$NTCP(D) = 1 - \prod_j (1 - NTCP_j(D)) \qquad \text{[Eq. 270]}$$

assuming that it is sufficient for only one of the organs j included in the composite NTCP to collapse to severely harm the patient. It is important to carefully consider which NTCPs that should be included in the composite NTCP. The risk of inducing severe damage to normal tissue cannot be compared with the risk of minor complications.

11.9.3 P+

The probability of complication-free tumor control, P_+, is an attempt to combine the individual TCPs and NTCPs into a single measure of the quality of the treatment plan [45]:

$$P_+ = TCP(D)\,(1 - NTCP(D)) \qquad \text{[Eq. 271]}$$

Which NTCPs that are included into the P_+ expression is highly essential. Loss of tumor control cannot be compared with the risk of minor normal tissue complications. Only NTCPs of severe complications should be considered to be included in the calculation of P_+. Figure 89 shows a schematic graphical representation of P_+ calculated with Eq. 254 for schematic sigmoidal dose-response curves for TCP and NTCP.

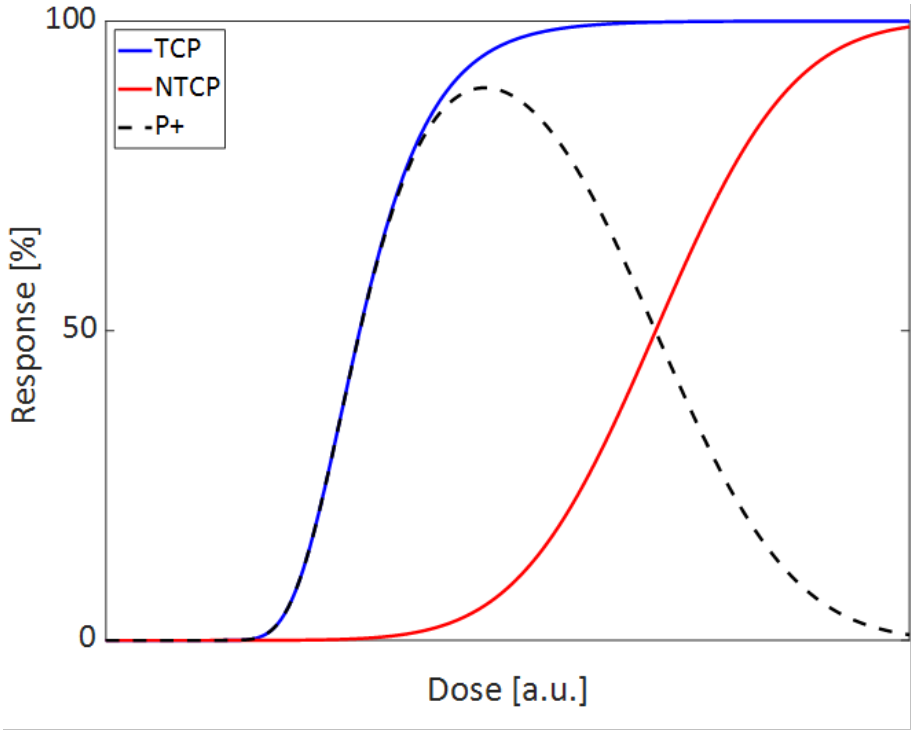

Figure 89. Schematic illustration of sigmoidal dose-response curves for tumor control probability (TCP) and normal tissue complication probability (NTCP) together with the resulting complication-free tumor control (P+) response curve using the equation above.

11.10 PARAMETERS OF THE BIOLOGICAL MODELS

It is important to be aware of that the parameters listed as default parameters can only be considered for the endpoint and reference volume for which they have been derived for. Some of the parameters are derived from another linear dose-response model, here labeled with a star (*), than the one presented in this manual. These parameters cannot be used by the models implemented in this manual unless they are transformed as described below.

The linear dose response model described in this manual is expressed as (see *section 11.7.1 The linear dose-response model on page 378*):

$$P_L(D) = \exp\left(-\exp\left[e\gamma - \frac{D}{D_{50}}(e\gamma - \ln(\ln(2)))\right]\right) \quad \text{[Eq. 272]}$$

whereas the other linear dose response model* has the following form

$$P_L(D)^* = 2^{-\exp\left(e\gamma\left(1-\frac{D}{D_{50}}\right)\right)} = \\ = \exp\left(-\exp\left[e\gamma^* - \frac{D}{D_{50}}e\gamma^* + \ln(\ln(2))\right]\right) \quad \text{[Eq. 273]}$$

These two expressions are equal if

$$\gamma = \gamma^* + \frac{\ln(\ln(2))}{e} \quad \text{[Eq. 274]}$$

Hence, by simply rescaling the $\gamma*$ of the other linear dose response model* by the term $\ln(\ln(2))/e$, these parameters can be used by the linear dose response model used in this manual.

If the estimated parameters D_{50} and γ are not derived from a dose per fraction of 2 Gy in the entire volume of interest (i.e. uniform dose), a fraction size correction to 2 Gy per fraction is performed for these parameters using EQD_2.

A DEFINITIONS

Term	Meaning
BEV	Beam's Eye View
CBCT	Cone Beam Computed Tomography
CPB	Carbon Pencil Beam ***Note:*** *The Carbon Pencil Beam dose engine is used for light ions, i.e. carbon and helium.*
CT	Computed Tomography
DCR	Digitally Composited Radiograph
DVH	Dose Volume Histogram
deg	When the term deg is seen in RayStation 2024A this refers to degrees
DMLC	Dynamic Multi-Leaf Collimator
DRR	Digitally Reconstructed Radiograph
External ROI	The ROI used to define patient outline. Defines the region used for dose computation, together with BOLUS for beam, SUPPORT and FIXATION ROIs.
GUI	Graphical User Interface
IMRT	Intensity Modulated Radiation Therapy
LINAC	Linear accelerator, conventional radiation therapy treatment unit.
LS	Line Scanning
MBS	Model-Based Segmentation
MCO	Multi-Criteria Optimization
MU	Monitor Units
NP	Number of Particles. For protons the MU fields are replaced with Number of particles (NP) if the machine has Primary Dosimetry Unit set to Number of Particles.
NTCP	Normal tissue complication probability

Term	Meaning
OAR	Organ at risk
P+ or PPLUS	Probability of complication free tumor control
PBS	Pencil Beam Scanning
PHY	Physical dose
POI	Point of Interest
RBE	Relative Biological Effectiveness
RBE dose	RBE-weighted dose is in RayStation and this manual referred to as RBE dose.
ROI	Region of Interest
ROI Geometry	The image set-specific geometric representation of an ROI
SMLC	Segmental Multi-Leaf Collimator
SOBP	Spread Out Bragg Peak
SSD	Source to Skin Distance
SUV	Standardized Uptake Value
TCP	Tumor control probability
UI	User Interface
VMAT	Volumetric Modulated Arc Therapy

B REWRITING OF LINEAR DOSE-RESPONSE MODELS

The linear dose-response model using EQD_2 (*section 11.7.1 The linear dose-response model on page 378*) and the linear-quadratic (LQ) dose-response model using a rewriting of the parameter α (*section 11.7.2 The linear-quadratic (LQ) dose-response model on page 380*) are equivalent. This can be shown by the following steps:

The linear dose-response model can be expressed as

$$P_L(EQD_2) = \exp\left(-\exp\left[e\gamma - \frac{EQD_2}{D_{50}}\left(e\gamma - \ln(\ln(2))\right)\right]\right)$$

where

$$EQD_2 = \frac{D\left(1 + \frac{d}{\alpha/\beta}\right)}{1 + \frac{d_{ref}}{\alpha/\beta}}$$

By combining the previous two equations, the following expression is obtained

$$P_L(EQD_2) = \exp\left(-\ \exp\left[e\gamma - \frac{D}{D_{50}}\ \frac{1 + \frac{d}{\alpha/\beta}}{1 + \frac{d_{ref}}{\alpha/\beta}}\ \left(e\gamma - \ln(\ln(2))\right)\right]\right)$$

The LQ dose-response model is defined as

$$P_{LQ}(D) = \exp\left(-\ \exp\left[e\gamma - \alpha D\ \left(1 + \frac{d}{\alpha/\beta}\right)\right]\right)$$

where α can be defined as [45]

$$\alpha = \frac{e\gamma - \ \ln(\ln(2))}{D_{50}\left(1 + \frac{d_{ref}}{\alpha/\beta}\right)}$$

By combining the previous two equations, the following expression is obtained

$$P_{LQ}(D) = \exp\left(-\ \exp\left[e\gamma - \frac{D}{D_{50}}\ \frac{1 + \frac{d}{\alpha/\beta}}{1 + \frac{d_{ref}}{\alpha/\beta}}\ \left(e\gamma - \ln(\ln(2))\right)\right]\right)$$

which is the same expression as the one obtained for the linear dose-response model above.

Here the equivalence between the linear dose-response model and the LQ dose-response model was only shown for the “simple” case where incomplete repair and accelerated repopulation were

not considered. However, by using the same approach using the EQD_2 including repair and/or repopulation (see *section 11.5 EQD_2 on page 371*) and the corresponding LQ dose-response model (see *section 11.7.2 The linear-quadratic (LQ) dose-response model on page 380*), the equivalence in these cases can be showed as well.

C DOSE ENGINE VERSION NUMBER

The version number of the dose engine consists of two parts, major and minor version number. For example, dose engine version 1.2 has major version number 1 and minor version number 2.

The major version number is increased when there are large enough changes to the dose engine to require treatment machine models to be updated. This means that previously existing treatment machines need to be re-commissioned if the major dose engine version number is increased before usage in a new RayStation version.

The minor version number is increased when there are no changes to the dose engine (i.e., no changes that require re-commissioning of the treatment machine in beam commissioning), but there may still be changes in the 3D dose computation in patients due to for example changes in the density or voxel volume calculation. When only the minor version number has been increased, no re-commissioning of machines is necessary and it is allowed to use any machine which has the correct major version number for dose calculation in RayStation.

As an example, if a machine has been commissioned for version number 1.0, it is allowed to use it for dose calculation in a RayStation application with dose engine version 1.2. The computed patient dose will have dose engine version 1.2.

It is always required that patient dose has been computed with the latest version of both major and minor version number to allow approval in RayStation.

REFERENCES

[1] Ahnesjö A, Collapsed cone convolution of radiant energy for photon dose calculation in heterogeneous media, Med. Phys. 16 (1989) 577-59.

[2] Amsler C et al., The Review of Particle Physics, Physics Letters B667, 1 (2008).

[3] Aspradakis M.M., Morrisson R.H., Richmond N.D., and Steele A., Experimental verification of convolution/superposition photon dose calculation for radiotherapy treatment planning, Phys. Med. Biol. 48 (2003) 2873-2893.

[4] Berger M.J., Coursey J.S., Zucker M.A., and Chang J., Stopping-Power and Range Tables for Electrons, Protons, and Helium Ions, National Institute of Standards and Technology, Physical Reference data, NISTIR 4999, http://physics.nist.gov.

[5] Chaney E.L., Cullip T.J., A Monte Carlo study of accelerator head scatter, Med. Phys. 21 (1994) 1383-1390.

[6] Grosswendt B., Determination of Electron Depth-Dose Curves for Water, ICRU Tissue, and PMMA and Their Application to Radiation Protection Dosimetry, Radiat. Prot. Dosimetry 54 (1994) 85-97.

[7] Hoban P.W., Murray D.C., Round W.H, Photon beam convolution using polyenergetic energy deposition kernels, Phys. Med. Biol. 39 (1994) 669-685.

[8] Hubbel J.H., and Seltzer S.M., Tables of X-Ray Mass Attenuation Coefficients and Mass Energy-Absorption Coefficients from 1 keV to 20 MeV for Elements Z=1 to 92 and 48 Additional Substances of Dosimetric Interest, National Institute of Standards and Technology, Physical Reference data, NISTIR 5632, http://physics.nist.gov.

[9] Hughes D.B., Karznarj C.J., Levy R.M., Conventions for Wedge Filter Specifications, Br. J. of Radiol. 45 (1972) 868.

[10] Jaffray D.A., Battista J.J., X-ray sources of medical linear accelerators: focal and extra focal radiation, Med. Phys. 20 (1993) 1417-1427.

[11] Kawrakow, IE. Mainegra-Hing, D.W.O. Rogers, F. Tessier and B.R.B. Walters, "The EGSnrc code system: Monte Carlo simulation of electron and photon transport," NRC Report No. PIRS-701, 2016.

[12] Kawrakow I., Accurate condensed history Monte Carlo simulation of electron transport. I. EGSnrc, the new EGS4 version, Med. Phys. 27, 485 - 498 (2000).

[13] Khan Faiz M., (2003), The Physics of Radiation Therapy, 3rd edition, Lippincott, Williams & Wilkins.

[14] Leavitt D.D., Martin M., Moeller J.H., Lee W.L., Dynamic Wedge Field Techniques Through Computer-Controlled Collimator Motion and Dose Delivery, Med. Phys. 17 (1990) 87-91.

[15] Ma C-M., and Li J., Dose specification for radiation therapy: dose to water or dose to medium?, Phys. Med. Biol. 56 (2011) 3073-3089.

[16] Mackie T.R., Bielajew A.F., Rogers D.W.O., and Battista J.J., Generation of photon energy deposition kernels using the EGS Monte Carlo code, Phys. Med. Biol. 33 (1988) 1-20.

[17] Mackie T.R., El-Khatib E., Battista J., Scrimger J.W., Van Dyk J., Cunningham J.R., Lung dose corrections for 6- and 15-MV X-rays, Med. Phys. 12 (1985) 327-332.

[18] Mackie T.R., Scrimger J.W., and Battista J.J., A convolution method of calculating dose for 15-MV x rays, Med. Phys. 12 (1985) 188-196.

[19] Metcalfe P., Kron T., Hoban P., The Physics of Radiotherapy X-Rays and Electrons, Medical Physics Publishing, 2007, ISBN: 978-1-930524-36-1.

[20] Miften M, Fraass B., McShan D., Analysis of the accuracy of various approximations in convolution dose calculation methods, Med. Phys. 6 (1996) 1128.

[21] Nisbet A., Beange I., Vollmar H-S., Irvine C., Morgan A., Thwaites D.I., Dosimetric verification of a commercial collapsed cone algorithm in simulated clinical situations, Radiother. Oncol. 73 (2004) 79-88.

[22] Papanikolaou N, Mackie T.R., Meger-Wells C., and Gehring M, Investigation of the convolution method for polyenergetic spectra, Med. Phys. 20 (1993) 1327-1336.

[23] Rogers D. W. O, Kawrakow I., Seuntjens J.P., Walters B.R.B., Mainegra-Hing E., NRC User Codes for EGSnrc, Technical Report PIRS-702(revB), National Research Council of Canada, Ottawa, Canada, 2010.

[24] Seco J., and Evans M., Assessing the effect of electron density in photon dose calculations, Med. Phys. 33 (2006) 540-552. Erratum in Med. Phys. 34 (2007) 3121.

[25] Sharp M.B., and Battista J.J., Dose calculations using convolution and superposition principles: The orientation of dose spread kernels in divergent x-ray beams, Med. Phys. 20 (1993) 1685-1694.

[26] Sterling T.D., Perry H., and Katz L., Automation of radiation treatment planning, Br. J. Radiol, 37 (1964) 544-550.

[27] van't Veld A.A., van Luijk P., Praamstra F., and van der Hulst P.C., Detector line spread function determined analytically by transport of Compton recoil electrons, Med.Phys. 28 (2001) 738-751.

[28] Yang J, Li J S, Qin L, Xiong W and MA C-M, Modelling of electron contamination in clinical photon beams for Monte Carlo dose calculation, Phys. Med. Biol. 49 (2003) 2657-2673.

[29] Information transfer from beam data acquisition systems, Report of Task Group 11 Computer Committee, http://www.aapm.org/pubs/reports/or_01.pdf.

[30] ICRU, Stopping Powers for Electrons and Positrons, Report 37 of the International Commission of Radiation Units and Measurements, 1984.

[31] ICRU, Tissue Substitutes in Radiation Dosimetry and Measurement, Report 44 of the International Commission on Radiation Units and Measurements, 1989.

[32] ICRU, Photon, Electron, Proton and Neutron Interaction Data for Boyd Tissues, Report 46 of the International Commission on Radiation Units and Measurements, 1991.

[33] ICRP, Report of the Task Group on Reference Man (ICRP 23): anatomical, physiological and metabolic characteristics, 1975.

[34] International Electrotechnical Commission, IEC 61217 Radiotherapy equipment – Coordinates, movements and scales, 2008.

[35] Siemens physics handbook, Physics Primer Linear Accelerator 73 48 332 Revision B Software Version 8.0.

[36] Siyong Kim, Timothy C. Zhu and Jatinder R. Palta, An equivalent square field formula for determining head scatter factors of rectangular fields, Med.Phys. 24 (1997) 1770-1774.

[37] Yu M. K., Analytical representation of enhanced dynamic wedge factors for symmetric and asymmetric photon fields, Med. Phys. 29 (2002) 2606-1610.

[38] Ansbacher, W. and Neath, C., Comment on "Analytical representation of enhanced dynamic wedge factors for symmetric and asymmetric fields", Med. Phys. 30 (2003) 722-723.

[39] Ahnesjö, Weber, Nilsson, Modeling transmission and scatter for photon beam attenuators, Med phys 22(11) Pt. 1, November 1995.

[40] Brahme, A. (1984). Dosimetric precision requirements in radiation therapy. Acta Radiologica: Oncology, 23(5), 379-391.

[41] Fowler JF. The linear-quadratic formula and progress in fractionated radiotherapy. Br J Radiol. 1989 Aug;62(740):679-94.

[42] Kutcher GJ, Burman C, Brewster L, Goitein M, Mohan R. Histogram reduction method for calculating complication probabilities for three-dimensional treatment planning evaluations. Int J Radiat Oncol Biol Phys. 1991;21(1):137-46.

[43] Källman P, Ågren A, Brahme A. Tumour and normal tissue responses to fractionated non-uniform dose delivery, Int J Radiat Biol. 1992;62:249-262.

[44] Levin-Plotnik D, Hamilton RJ, Niemierko A, Akselrod S. A model for optimizing normal tissue complication probability in the spinal cord using a generalized incomplete repair scheme. Radiat Res. 2001;155(4):593-602.

[45] Lind BK, Mavroidis P, Hyödynmaa S, Kappas C. Optimization of the dose level for a given treatment plan to maximize the complication-free tumor cure. Acta Oncol. 1999;38(6):787-98.

[46] Lyman JT. Complication probability as assessed from dose-volume histograms. Radiat Res Suppl. 1985;8:S13-9.

[47] National Electrical Manufacturers Association, DICOM Standards Committee, Digital imaging and communications in Medicine (DICOM) – Part 3.

[48] William E. Lorensen, Harvey E. Cline, Marching cubes: A high resolution 3D surface construction algorithm, Computer Graphics, Vol. 21, Nr. 4, July 1987

[49] Gabor T. Herman, Jingsheng Zheng, Carolyn A. Bucholtz, Shape-Based Interpolation, IEEE Computer Graphics and Applications, Volume 12 Issue 3, May 1992

[50] J.A Sethian, Fast Marching Methods, SIAM Review, 41,2, 1999, pp. 199-235.

[51] The International Commission on Radiation Units and Measurements, Journal of the ICRU Vol 10 No 1 (2010) Report 83

[52] Podgorsak, E.B., Metcalfe, P., Van Dyk, J., "Medical accelerators", The Modern Technology in Radiation Oncology (Van Dyk, J., Ed.), Medical Physics Publishing, Madison, WI (1999) 349–435.

[53] Kawrakow, I., "Accurate condensed history Monte Carlo simulation of electron transport. I. EGSnrc, the new EGS4 version", Med. Phys., vol. 27, no. 3, pp. 485-498, 2000.

[54] A. Kling, F. Barão, M. Nakagawa, L. Távora and P. Vaz (Eds.), Advanced Monte Carlo for Radiation Physics, Particle Transport Simulation and Applications - Proceedings of the Monte Carlo 2000 Conference, Lisbon 23-26 October 2000. Springer Science & Business Media 2014.

[55] With, A., "Investigations of a beam phase-space model for multi-leaf collimated electron fields", Master of science thesis, Stockholm University, 2010.

[56] Sorcini B., Hyödynmaa S., and Brahme A, "The role of phantom and treatment head generated bremsstrahlung in high-energy electron beam dosimetry", Phys. Med. Biol 41 2657-2677, 1995

[57] Clasie, Depauw, Fransen, et al. Phys. Med Biol. 57 (2012) 1147

[58] J.O. Deasy, Med. Phys. 25 (1998) 476

[59] L. Eyges, Physical Review (1948) 1534

[60] B. Gottschalk, A.M. Koehler, R.J. Schneider et al, Nucl. Intrum. Methods. Phys. Research B 74 (1993) 467.

[61] B. Gottschalk, Med Phys. 37 (2010) 352

[62] V. L. Highland, Nucl. Instrum. Method. (1975) 497

[63] M. Hollmark et al. Phys. Med. Biol. 49 (2004) 3247

[64] L Hong, M. Goitein, M. Bucciolini et al. Phys.Med.Biol. 41 (1996) 1305

[65] ICRU Report 49, ISBN 0-913394-47-5

[66] ICRU Report 35

[67] Pedroni, Scheib, and Böhringer et al. Phys. Med. Biol. 50 (2005) 541

[68] P. Petti, Med. Phys. 19 (1992) 137

[69] Råde and Westergren, Mathematical Handbook for Science and Engineering, fifth edition (2004), Studentlitteratur, ISBN 91-44-03109-2

[70] In house study comparing different scattering power expressions in water, where more energies than that used in [Gotttschalk 2010] were investigated.

[71] K.R. Russel, E. Grusell, A. Montelius, Phys.Med. Biol. 40 (1995) 1031

[72] B. Schaffner, Phys. Med. Biol. 53 (2008) 1545

[73] Soukup, M., Fippel, M. & Alber, M. A pencil beam algorithm for intensity modulated proton therapy derived from Monte Carlo simulations. Phys. Med. Biol. 50, 5089-5104 (2005).

[74] Y.S. Tsai, Rev. Mod. Phys. 46 (1974) 815

[75] W. K. Weyrather, J. Debus, Clinical Oncology 15(2003) S23

[76] Urie M, Goitein M, Wagner M., Phys. Med. Biol. 29 (1984) 553

[77] B. Schaffner, E. Pedroni, A. Lomax, Phys. Med. Biol. 44 (1999) 27

[78] Fredriksson, A., Forsgren, A., Hårdemark, B., Minimax optimization for handling range and setup uncertainties in proton therapy, Medical Physics 38(3): 1672–1684, 2011.

[79] K Helsgaun. An effective implementation of the Lin-Kernighan traveling salesman heuristic. Eur. J. Oper. Res., 126(1):106-130, 2000.

[80] K Helsgaun. General k-opt submoves for the Lin-Kernighan TSP heuristic. Math. Prog. Comp., 1(2-3):119-163, 2009.

[81] Scholz, M., Kellerer, a. M., Kraft-Weyrather, W., & Kraft, G. (1997). Computation of cell survival in heavy ion beams for therapy. Radiation and Environmental Biophysics, 36(1), 59–66. doi:10.1007/s004110050055.

[82] Scholz, M., & Kraft, G. (2004). The Physical and Radiobiological Basis of the Local Effect Model: Radiation Research, 620, 612–620.

[83] Friedrich, T., Grün, R., Scholz, U., Elsässer, T., Durante, M., & Scholz, M. (2013). Sensitivity analysis of the relative biological effectiveness predicted by the local effect model. Physics in Medicine and Biology, 58, 6827–49. doi:10.1088/0031-9155/58/19/6827.

[84] D. Schardt, T. Elsässer, and D. Schulz-Ertner, Rev. Mod. Phys. 82 (2010) 383.

[85] ICRU Report 73, ISBN 0198570120.

[86] Böhlen, T. T. et al. The FLUKA Code: Developments and Challenges for High Energy and Medical Applications. Nucl. Data Sheets 120, 211-214 (2014).

[87] Ferrari, A., Sala, P. R., Fasso, A. and Ranft, J. FLUKA: A Multi-Particle Transport Code. CERN-2005-10, INFN/TC 05/11, SLAC-R-773 (2005).

[88] Inaniwa, T. & Kanematsu, N. A trichrome beam model for biological dose calculation in scanned carbon-ion radiotherapy treatment planning. Phys. Med. Biol. 60, 437-451 (2015).

[89] Inaniwa, T. et al. Implementation of a triple Gaussian beam model with subdivision and redefinition against density heterogeneities in treatment planning for scanned carbon-ion radiotherapy. Phys. Med. Biol. 59, 5361-5386 (2014).

[90] Fuchs, H., Ströbele, J., Schreiner, T., Hirtl, A. & Georg, D. A pencil beam algorithm for helium ion beam therapy. Med. Phys. 39, 6726 (2012).

[91] Gottschalk, B., Cascio, E. W., Daartz, J. & Wagner, M. S. Nuclear halo of a 177 MeV proton beam in water: theory, measurement and parameterization. arXiv: 1409.1938 (2014).

[92] Parodi, K. et al. Monte Carlo simulations to support start-up and treatment planning of scanned proton and carbon ion therapy at a synchrotron-based facility. Phys. Med. Biol. 57, 3759-3784 (2012)

[93] Krämer, M. & Scholz, M. Rapid calculation of biological effects in ion radiotherapy. Phys. Med. Biol. 51, 1959-70 (2006).

[94] Krämer, M. & Scholz, M. Treatment planning for heavy-ion radiotherapy: calculation and optimization of biologically effective dose. Phys. Med. Biol. 45, 3319-30 (2000).

[95] Parodi, K., Mairani, A. & Sommerer, F. Monte Carlo-based parametrization of the lateral dose spread for clinical treatment planning of scanned proton and carbon ion beams. J. Radiat. Res. 54, i91-i96 (2013).

[96] International Commission of Radiation Units and Measurements. ICRU Report 49. Stopping Powers and Ranges for Protons and Alpha Particles. ICRU (1993)

[97] Scholz, M. et al. Computation of cell survival in heavy ion beams for therapy. Radiat. Environ. Biophys. 36, 59-66 (1997)

[98] Elsässer, T., Krämer, M., & Scholz, M. Accuracy of the local effect model for the prediction of biologic effects of carbon ion beams in vitro and in vivo. International Journal of Radiation Oncology* Biology* Physics, 71, 866-872 (2008).

[99] Karger, C. P., Peschke, P., Sanchez-Brandelik, R., Scholz, M., & Debus, J. Radiation tolerance of the rat spinal cord after 6 and 18 fractions of photons and carbon ions: Experimental results and clinical implications. International Journal of Radiation Oncology* Biology* Physics, 66, 1488-1497 (2006).

[100] Scholz, M., & Kraft, G. Track structure and the calculation of biological effects of heavy charged particles. Advances in Space Research, 18(1), 5-14 (1996).

[101] Friedrich, T., Grün, R., Scholz, U., Elsässer, T., Durante, M., & Scholz, M. Sensitivity analysis of the relative biological effectiveness predicted by the local effect model. Physics in medicine and biology, 58(19), 6827 (2013).

[102] Fourkal, E., Velchev, I., Fan, J., Luo, W., & Ma, C.-M. (2007). Energy optimization procedure for treatment planning with laser-accelerated protons. Medical Physics, 34(2), 577. http://doi.org/10.1118/1.2431424.

[103] "Secondary electron spectra from charged particle interactions", ICRU Report 55, International Commission on Radiation Units and Measurements (1995).

[104] S. A. Goudsmit and J. L. Saunderson. Multiple scattering of electrons. Phys. Rev., 57:24 - 29, 1940.

[105] S. A. Goudsmit and J. L. Saunderson. Multiple scattering of electrons. II. Phys. Rev., 58:36 - 42, 1940.

[106] I. Kawrakow and A. F. Bielajew. On the representation of electron multiple elasticscattering distributions for Monte Carlo calculations. Nuclear Instruments and Methods, 134B:325 - 336, 1998.

[107] I. Kawrakow. Accurate condensed history Monte Carlo simulation of electron transport. I. EGSnrc, the new EGS4 version. Med. Phys., 27:485 - 498, 2000.

[108] M. Fippel and M. Soukop. A Monte Carlo dose calculation algorithm for proton therapy. Medical Physics 31, 2263 (2004).

[109] R. A. Arndt, I. I. Strakovsky, and R. L. Workman, "Nucleon–nucleon elastic scattering to 3 GeV," Phys. Rev. C 62, 034005 (2000).

[110] "Nuclear Data for Neutron and Proton Radiotherapy and for Radiation Protection", ICRU-Report 63, International Commission on Radiation Units and Measurements (2000).

[111] F. Salvat, J.M. Fernández-Varea and J. Sempau PENELOPE-2011: A Code System for Monte Carlo Simulation of Electron and Photon Transport OECD NEA Data Bank/NSC DOC(2011)/5 (OECD Nuclear Energy Agency, Issy-les-Moulineaux, 2011).

[112] Bernard Gottschalk (Harvard) BGtalks.zip at http://lppc.physics.harvard.edu/~gottschalk/

[113] Ma, C-M and Li J, Dose specification for radiation therapy: dose to water or dose to medium? Phys. Med. Biol. 56 (2011) 3073-3089.

[114] Andreo P, Dose to 'water-like' media or dose to tissue in MV photons radiotherapy treatment planning: still a matter of debate, Phys. Med. Biol. 60 (2015) 309-337.

[115] Gladstone D.J., et al. Dose specification for NRG radiation therapy trials, Int. J. Oncol. Biol. Phys. 2016 1344-1345.

[116] Kry S.F. et al, AAPM Task Group 329: Reference dose specification for dose calculations: Dose-to-water or dose-to-muscle? Med. Phys. 47 (3) March 2020.

[117] AAPM TG-105, Issues associated with clinical implementation of Monte Carlo-based photon and electron external beam treatment planning, Chetty I J, et al, 2007, Med. Phys. 34 (12) 4818.

[118] Zifodya J.M el al, From AAA to Acuros XB-clinical implications of selecting either Acuros XB dose-to-water or dose-to-medium, Australas Phys. Eng. Sci. Med, DOI 10.1007/s13246-016-0436-z, 2015.

[119] AAPM Medical Physics Practice Guideline 5.a: Commissioning and QA of Treatment Planning Dose Calculations – Megavoltage Photon and Electron Beams, J. of Appl. Clin. Med. Phys. 16 (2015).

[120] Walters BRB, Kramer R and Kawrakow I, Dose to medium versus dose to water as an estimator of dose to sensitive skeletal tissue, Phys. Med. Biol. 55 (2010) 4535-4546.

[121] Westerly DC, Soisson E, Chen Q, Woch K, Schubert L, Olivera G and Mackie TR, Treatment planning to improve delivery accuracy and patient throughput in helical tomotherapy, Int J Radiat Oncol Biol Phys. 74(4) (2009) 1290–1297.

[122] Sarkar V, Lin L, Shi C, Papanikolaou N, Quality assurance of the multileaf collimator with helical tomotherapy: design and implementation. Med Phys. 2007 Jul;34(7):2949-56.

[123] Whitmode N, Nalichowski A, Burmeister J, Effects of dose scaling on delivery quality assurance in tomotherapy. J Appl Clin Med Phys. 2012 Jan 5;13(1):3621. doi: 10.1120/jacmp.v13i1.3621.

[124] XCOM: Photon Cross Sections Database, NIST Standard Reference Database 8 (XGAM), M.J. Berger, J.H. Hubbell, S.M. Seltzer, J. Chang, J.S. Coursey, R. Sukumar, D.S. Zucker, and K. Olsen, https://www.nist.gov/.

[125] R. M. Sternheimer, S. M. Seltzer, and M. J. Berger. Density effect for the ionization loss of charged particles in various substances. Phys. Rev., B26:6067, 1982.

[126] T. Bortfeld, W. Schlegel, B. Rhein, Decomposition of pencil beam kernels for fast dose calculations in three-dimensional treatment planning, Med. Phys., 20(2), 311, 1993.

[127] Hawkins, R. B. (1994). A Statistical Theory of Cell Killing by Radiation of Varying Linear Transfer Energy, 140(3), 366–374.

[128] Hawkins, R. B. (2003). A Microdosimetric-Kinetic Model for the Effect of Non-Poisson Distribution of Lethal Lesions on the Variation of RBE with LET, 160(1), 61–69.

[129] Kellerer, a. M., & Rossi, H. H. (1978). A Generalized Formulation of Dual Radiation Action. Radiation Research, 75, 471–488.

[130] Kase, Y., Kanai, T., Matsumoto, Y., Furusawa, Y., Okamoto, H., Asaba, T., … Shinoda, H. (2006). Microdosimetric measurements and estimation of human cell survival for heavy-ion beams. Radiat. Res., 166(4), 629–638, https://doi.org/10.1667/RR0536.1.

[131] Inaniwa, T., Furukawa, T., Kase, Y., Matsufuji, N., Toshito, T., Matsumoto, Y., … Noda, K. (2010). Treatment planning for a scanned carbon beam with a modified microdosimetric kinetic model. Physics in Medicine and Biology, 55, 6721–6737, https://doi.org/10.1088/0031-9155/55/22/008.

[132] Chatterjee, a, & Schaefer, H. J. (1976). Microdosimetric structure of heavy ion tracks in tissue. Radiation and Environmental Biophysics, 13(3), 215–227, https://doi.org/10.1007/BF01330766.

[133] Kiefer, J., & Straaten, H. (1986). A model of ion track structure based on classical collision dynamics. Physics in Medicine and Biology, 31, 1201–1209, https://doi.org/10.1088/0031-9155/31/11/002.

[134] Inaniwa, T., Kanematsu, N., Matsufuji, N., Kanai, T., Shirai, T., Noda, K., … Tsujii, H. (2015). Reformulation of a clinical-dose system for carbon-ion radiotherapy treatment planning at

the National Institute of Radiological Sciences, Japan. Physics in Medicine and Biology, 60(8), 3271–3286, https://doi.org/10.1088/0031-9155/60/8/3271.

[135] Inaniwa, T., Kanematsu, N., Hara, Y., Furukawa, T., Fukahori, M., Nakao, M., & Shirai, T. (2014). Implementation of a triple Gaussian beam model with subdivision and redefinition against density heterogeneities in treatment planning for scanned carbon-ion radiotherapy (Phys. Med. Biol. 59 5361). Physics in Medicine and Biology, 59, 6305–6305, https://doi.org/10.1088/0031-9155/59/20/6305.

[136] Inaniwa, T., & Kanematsu, N. (2015). A trichrome beam model for biological dose calculation in scanned carbon-ion radiotherapy treatment planning. Physics in Medicine and Biology, 60, 437–451, https://doi.org/10.1088/0031-9155/60/1/437.

[137] Inaniwa, T., Kanematsu, N., Hara, Y., & Furukawa, T. (2015). Nuclear-interaction correction of integrated depth dose in carbon-ion radiotherapy treatment planning. Physics in Medicine and Biology, 60(1), 421–435, https://doi.org/10.1088/0031-9155/60/1/421.

[138] Inaniwa T, Lee SH, Kota M, Sakata D, Iwata Y, Kanematsu N and Shirai T. Nuclear-interaction correction for patient dose calculations in treatment planning of helium-, carbon-, oxygen-, and neon-ion beams. Phys. Med. Biol. 65 025004 (2019).

[139] Sihver L, Tsao CH, Silberberg R, Kanai T and Barghouty AF. Total reaction and partial cross section calculations in proton–nucleus (Zt ≤ 26) and nucleus–nucleus reactions (Zp and Zt ≤ 26) Phys. Rev. C 47 1225–36 (1993).

[140] I. Kawrakow, Phys. Med. Biol. 47 (2002) 3087.

[141] Huang, J. Y., Dunkerley, D., & Smilowitz, J. B. (2019). Evaluation of a commercial Monte Carlo dose calculation algorithm for electron treatment planning, J Appl Clin Med Phys. 20.6 (May 2019),184-193. doi: 10.1002/acm2.12622

[142] Elsässer, T., Weyrather, W.K., Friedrich, T., Durante, M., Iancu, G., Krämer, M., ... Scholz, M. Quantification of the relative biological effectiveness for ion beam radiotherapy: direct experimental comparison of proton and carbon ion beams and a novel approach for treatment planning. International Journal of Radiation Oncology Biology Physics, 78, 1177-1183 (2010).

[143] Joao Seco, Frank Verhaegen, Monte Carlo Techniques in Radiation Therapy, CRC Press, (2016), ISBN: 9781138199903

[144] Graf M. et al. SU-D-213AB-04: Evaluation of the Dose Calculation in a Commercial Planning System for a Breast Cancer Brachytherapy Technology Using Monte Carlo Simulation. Med Phys. 2012.

[145] Jacob D. et al. Clinical transition to model-based dose calculation algorithm: A retrospective analysis of high-dose- rate tandem and ring brachytherapy of the cervix. Brachytherapy. 2017

[146] Mikell J. et al. Impact of heterogeneity-based dose calculation using a deterministic grid-based Boltzmann equation solver for intracavitary brachytherapy. Int J Radiat Oncol Biol Phys. 2012.

[147] Mikell J, Klopp A, Price M, Mourtada F. SU-E-T-425: Impact of Model Based Dose Calculation Algorithm for Ir-192 Intracavitary Brachytherapy with Shielded Applicator. Med Phys. 2012

[148] Nath R. et al. Dosimetry of interstitial brachytherapy sources: recommendations of the AAPM Radiation Therapy Committee Task Group No. 43. American Association of Physicists in Medicine. Med Phys. 1995. Erratum in: Med Phys 1996.

[149] Perez-Calatayud J. Dose calculation for photon- emitting brachytherapy sources with average energy higher than 50 keV: report of the AAPM and ESTRO. Med Phys. 2012.

[150] Rivard M.J. et al. Update of AAPM Task Group No. 43 Report: A revised AAPM protocol for brachytherapy dose calculations. Med Phys. 2004. Erratum in: Med Phys. 2004.

[151] I. Kawrakow and M. Fippel. Investigation of variance reduction techniques for Monte Carlo photon dose calculation using XVMC. Phys. Med. Biol. 2000; 45(8): 2163-83. https://doi.org/10.1088/0031-9155/45/8/308.

[152] Wilkens, J. J., & Oelfke, U. (2003). Analytical linear energy transfer calculations for proton therapy. Medical Physics, 30(5), 806–815.

[153] ICRU, Fundamental Quantities and Units for Ionizing Radiation, Report 60 International Commission on Radiation Units and Measurements, Bethesda, MD, 1998.

[154] Looe et al., The dose response functions of ionization chamber in photon dosimetry – Gaussian or non-Gaussian?, Zeischrift fur Medizinishe Physik 23 (2013)

[155] Ketelhult et al., Measurement of spatial response functions of dosimetric detectors, Phys. Med. Biol. 60 (2015) 6177.

[156] AAPM's TG-51 protocol for clinical reference dosimetry of high-energy photon and electron beams, Almond et. al., Med. Phys. 26 (1999) 1847

[157] Addendum to the AAPM's TG-51 protocol for clinical reference dosimetry of high-energy photon beams, McEwen et. al., Med. Phys. 41 (2014) 041501-1

[158] Tessier, Kawrakow, Effective point of measurement of thimble ion chambers in megavoltage photon beams, Med. Phys. 37 (2010)

[159] Looe et al, Experimental detemination of the effective point of measurement for various detectors used in photon and electron dosimetry, Phys. Med. Biol. 56 (2011) 4267-4290

[160] McEwen et al, The effective point of measurement of ionization chamber and the build-up anomaly in MV x-ray beams, Med Phys. 35 (2008) 950

[161] Battistoni Giuseppe, Bauer Julia, Boehlen Till T., Cerutti Francesco, Chin Mary P. W., Dos Santos Augusto Ricardo, Ferrari Alfredo, Ortega Pablo G., Kozłowska Wioletta, Magro Giuseppe, Mairani Andrea, Parodi Katia, Sala Paola R., Schoofs Philippe, Tessonnier Thomas, Vlachoudis Vasilis. The FLUKA Code: An Accurate Simulation Tool for Particle Therapy. Frontiers in Oncology 6 (2016)

[162] A. Marti, Cobalt-base alloys used in bone surgery, Injury, Int. J. Care Injured, Volume 31, Supplement 4 (2000)

[163] U.S. Titanium Industry Inc.. (2020, September 02). Titanium Alloys - Ti6Al4V Grade 5. AZoM. Retrieved on March 17, 2022 from https://www.azom.com/article.aspx?ArticleID=1547

[164] Inaniwa T, Kanemetsu N. A trichrome beam model for biological dose calculation in scanned carbon-ion radiotherapy treatment planning. Phys Med Biol. 60(1) (2015) 437-451 doi: 10.1088/0031-9155/60/1/437

CONTACT INFORMATION

RaySearch Laboratories AB (publ)
Eugeniavägen 18C
SE-113 68 Stockholm
Sweden

Contact details head office
P.O. Box 45169
SE-104 30 Stockholm, Sweden
Phone: +46 8 510 530 00
Fax: +46 8 510 530 30
info@raysearchlabs.com
www.raysearchlabs.com

RaySearch Americas
Phone: +1 877 778 3849

RaySearch China
Phone: +86 137 0111 5932

RaySearch Japan
Phone: +81 3 44 05 69 02

RaySearch UK
Phone: +44 2039 076791

RaySearch Australia
Phone: +61 411 534 316

RaySearch France
Phone: +33 1 76 53 72 02

RaySearch Korea
Phone: +82 01 9492 6432

RaySearch Belgium
Phone: +32 475 36 80 07

RaySearch India
Phone: +91 9995 611361

RaySearch Singapore
Phone: +65 81 28 59 80

RSL-D-RS-2024A-REF-EN-1.0-2023-12-19
RayStation 2024A Reference Manual

RaySearch Laboratories